



UNIVERSITAT_{DE}
BARCELONA

Self-organization and cooperativity of cytoskeletal molecular motors

David Oriola Santandreu

ADVERTIMENT. La consulta d'aquesta tesi queda condicionada a l'acceptació de les següents condicions d'ús: La difusió d'aquesta tesi per mitjà del servei TDX (www.tdx.cat) i a través del Dipòsit Digital de la UB (diposit.ub.edu) ha estat autoritzada pels titulars dels drets de propietat intel·lectual únicament per a usos privats emmarcats en activitats d'investigació i docència. No s'autoritza la seva reproducció amb finalitats de lucre ni la seva difusió i posada a disposició des d'un lloc aliè al servei TDX ni al Dipòsit Digital de la UB. No s'autoritza la presentació del seu contingut en una finestra o marc aliè a TDX o al Dipòsit Digital de la UB (framing). Aquesta reserva de drets afecta tant al resum de presentació de la tesi com als seus continguts. En la utilització o cita de parts de la tesi és obligat indicar el nom de la persona autora.

ADVERTENCIA. La consulta de esta tesis queda condicionada a la aceptación de las siguientes condiciones de uso: La difusión de esta tesis por medio del servicio TDR (www.tdx.cat) y a través del Repositorio Digital de la UB (diposit.ub.edu) ha sido autorizada por los titulares de los derechos de propiedad intelectual únicamente para usos privados enmarcados en actividades de investigación y docencia. No se autoriza su reproducción con finalidades de lucro ni su difusión y puesta a disposición desde un sitio ajeno al servicio TDR o al Repositorio Digital de la UB. No se autoriza la presentación de su contenido en una ventana o marco ajeno a TDR o al Repositorio Digital de la UB (framing). Esta reserva de derechos afecta tanto al resumen de presentación de la tesis como a sus contenidos. En la utilización o cita de partes de la tesis es obligado indicar el nombre de la persona autora.

WARNING. On having consulted this thesis you're accepting the following use conditions: Spreading this thesis by the TDX (www.tdx.cat) service and by the UB Digital Repository (diposit.ub.edu) has been authorized by the titular of the intellectual property rights only for private uses placed in investigation and teaching activities. Reproduction with lucrative aims is not authorized nor its spreading and availability from a site foreign to the TDX service or to the UB Digital Repository. Introducing its content in a window or frame foreign to the TDX service or to the UB Digital Repository is not authorized (framing). Those rights affect to the presentation summary of the thesis as well as to its contents. In the using or citation of parts of the thesis it's obliged to indicate the name of the author.

Self-organization and cooperativity of cytoskeletal molecular motors

DAVID ORIOLA SANTANDREU

- Ph.D. Thesis -

Ph.D. advisor:

JAUME CASADEMUNT VIADER

Barcelona, September 2015

Programa de Doctorat en Física
Departament d'Estructura i Constituents de la Matèria
Facultat de Física



David Oriola Santandreu
Departament d'Estructura i Constituents de la Matèria
Facultat de Física
Universitat de Barcelona
Barcelona, E-08028
Spain
oriola@ecm.ub.edu

**Self-organization and cooperativity
of cytoskeletal molecular motors**

Ph.D. Thesis
Programa de Doctorat en Física
Línia de Recerca en Física de la Matèria Condensada
Memòria presentada per a optar al títol de Doctor en Física
Quatreni 2011-2015
Barcelona, Setembre de 2015

The work described in this thesis was financed by the Ministerio de Economía y Competitividad, under the FPU program (Formación de Profesorado Universitario).

The work presented had also financial support from Ministerio de Economía y Competitividad under projects FIS2010-21924-C02-02 and FIS2013-41144-P, the Generalitat de Catalunya under projects 2009 SGR 14, 2014 SGR 878, the Foundation for Fundamental Research on Matter (FOM), which is part of the Netherlands Organization for Scientific Research (NWO) and an EMBO Short Term Fellowship with ASTF number 314-2014.

“The world is full of obvious things which nobody
by any chance ever observes”

— Sir Arthur Conan Doyle, *The Hound of the Baskervilles*

Al meu pare

Acknowledgements

I would like to thank everyone I have met during these four years and all the people who has contributed in many different ways to make this thesis possible.

En primer lloc voldria agrair en especial a en Jaume per obrir-me les portes al món de la Biofísica. M'és difícil expressar tot el meu agraïment en poques línies. Moltes gràcies per tot el que m'has ensenyat, per confiar en mi, per el teu suport a totes hores, per la teva paciència, i sobretot, per la teva amistat.

Marileen, thank you very much for accepting me as a member of your group in my stay at AMOLF. I guess that few people would have bet on a four-month experimental project carried out by a theorist by training student. Thank you for your support and time on the project, and your kindness at all times.

Hermes! Obrigado por tudo, amigo! Thank you for your trust and support, and all the Skype meetings and failed connections. Thank you for always cheering me up in our quest with flagella. I had a wonderful time in the Mathematical Institute, and I learned a lot from you during our long discussions, both scientifically and personally. Most importantly, thank you for being a friend.

També vull agrair a tota la gent de dins i fora de la facultat amb la que he tingut ocasió de coincidir durant aquests anys: Alejandro, Carles, Clàudia, David(s), Eli, Enric, Genís, Guillermo, Irina, Javier, Jordi, Laura, Marc, Paco, Paul, Pau(s), Ricard, Sara, Sérgio, Xavier, gent del Grup de Física No Lineal i del Consolider, professors, personal del departament, etc. Als amics de carrera: Arnau, Carlos, Jordi(s), Marc i Teresa, per els nostres sopars i

les recursives converses sobre els nostres futurs, i en especial a l'Antoni, el qual ha sigut el nostre nexa d'unió. Al Ricard, perquè la història i la física no estan tan lluny si hi ha la música que les uneix. A l'Isaac, per ajudar-me inconscientment a decidir el meu futur predoctoral. A l'Èric, per infiltrar-se a les classes de física. A tots els meus amics d'ara i de sempre.

For making my stay at AMOLF an experience I'll remember throughout my life, I would like to specially thank Clara, Feng, Florian, Georges, Ioana, Jacopo, Johannes, Joris, José, Marileen, Nicola, Núria, Simone, Sophie, Stephen, Thomas and Vanda. Thank you Sophie for teaching me all I know in the lab and to spend part of your precious time purifying not one, not two but three times our "beloved" kinesin. Gràcies Núria per ajudar-me amb tot i més durant l'estància. Thank you Georges for having lots of laughs (and beers) together.

I would also like to thank all the people I came across in Oxford, undoubtedly and idyllic place to work and live. Thank you Wanda for the nice time I spent in your place and for being such a kind host. Francis, thank you for all the nice dinner discussions and for the nice friendship. Maria, moltes gràcies per donar-me consells durant la meva estada. Ramsès, gràcies per totes les converses a l'hora de dinar i la vostra amabilitat.

A la meva família, que ha estat en tot moment al meu costat. Gràcies Ester per tot l'esforç durant aquests anys, per aguantar les meves històries incomprensibles i en definitiva, la meva estranya (i apassionant) feina. Gràcies per estimar-me i compartir la teva vida amb mi, ets un sol. També vull donar-vos les gràcies a vosaltres, Toni, Anna i iaia, per acollir-me sempre. Vull agrair als meus pares i a la meva àvia, tot l'esforç, paciència i confiança, ara i sempre. A la meva mare, per cuidar-me a totes hores i escoltar-me en els bons i mals moments, i al meu pare, per transmetre'm la passió per la ciència i la curiositat per totes les coses que ens envolten. Finalment, gràcies iaia i tieta, per haver-me cuidat i estimat com ningú. Sense vosaltres no hauria arribat mai fins aquí.

This thesis is based on the following articles:

- D. Oriola and J. Casademunt.
Cooperative force generation of KIF1A Brownian motors.
Physical Review Letters, **111**, 048103 (2013). (Chapter 3)
- D. Oriola and J. Casademunt.
Cooperative action of KIF1A Brownian motors
with finite dwell time.
Physical Review E, **89**, 032722 (2014). (Chapter 3)
- D. Oriola, S. Roth, M. Dogterom and J. Casademunt.
Formation of helical membrane tubes around microtubules by
single-headed kinesin KIF1A.
Nature Communications, **6**, 8025 (2015). (Chapter 4)
- D. Oriola, H. Gadêlha, C. Blanch-Mercader and J. Casademunt.
Subharmonic oscillations of collective molecular motors.
EPL (Europhysics Letters), **107**, 18002 (2014). (Chapter 6)
- D. Oriola, H. Gadêlha and J. Casademunt.
Nonlinear dynamics of flagella driven by molecular motors.
In preparation. (Chapter 7)

Contents

1	General Introduction	1
Part I Cooperative force generation by molecular motors		
2	Introduction	17
2.1	Vesicular traffic	18
2.2	Intracellular transport	19
2.3	Axonal transport	21
2.4	Coordination of motor teams	22
2.5	A model motor: the kinesin KIF1A	23
2.6	Modelling intracellular transport	24
2.6.1	The two-state model	26
3	Theoretical modeling of KIF1A	31
3.1	Ratchet model for KIF1A dynamics	31
3.1.1	Hard-core repulsive interactions	35
3.1.1.1	The dwell time effect	35
3.1.1.2	Staircase-shaped VF curves for large N	37
3.1.1.3	Convergence to mean-field	40
3.1.1.4	Cluster force distribution	42
3.1.1.5	Coordinated motion of large clusters	44
3.1.1.6	Efficiency and randomness	45
3.1.2	Confining interactions	47
3.1.2.1	Rigidly coupled motors	47
3.1.2.2	Raft-induced interactions	49
3.1.2.3	Transition between rigid coupling and hard-core repulsion	51

3.1.3	Conclusions	53
3.2	Lattice model for KIF1A dynamics	54
3.2.1	Dynamics on a 1D lattice	56
3.2.1.1	Cases $N = 1$ and $N = 2$	57
3.2.1.2	Monte Carlo simulations	62
3.2.1.3	N interacting motors	63
3.2.2	Dynamics on a 2D lattice	64
3.2.3	Conclusions	67
4	Membrane tube formation by KIF1A	69
4.1	Formation of membrane tubes	69
4.2	Minimal experimental <i>in vitro</i> system	71
4.2.1	Experimental methods	72
4.2.1.1	Microtubule preparation	72
4.2.1.2	KIF1A preparation	72
4.2.1.3	Gliding assays	73
4.2.1.4	Electroformation of GUVs	74
4.2.1.5	Tube pulling assay	76
4.2.2	Image acquisition and data analysis	77
4.2.3	Results	78
4.2.3.1	Parallel tubulation	78
4.2.3.2	Helical tubulation	81
4.3	<i>In silico</i> model for longitudinal tube pulling	85
4.3.1	Description of the model	85
4.3.1.1	Tube region	85
4.3.1.2	Vesicle region	89
4.3.1.3	Parameters for the <i>in silico</i> model ...	90
4.3.2	Results	91
4.3.3	Mean-field model for helical tube formation ..	93
4.3.4	Conclusions	96

Part II Dynamical instabilities of motor assemblies

5	Introduction	101
5.1	Muscle contraction	102
5.2	Flagellar and ciliary beating	105
5.3	Positive feedback and negative damping	108
5.3.1	Two-state rigid model	108
5.3.2	‘Tug-of-war’ model	111

6	Spontaneous oscillations of motor assemblies	113
6.1	Two-state model with an elastic element	114
6.2	Three-variable system	115
6.3	Comparison with a minimal actomyosin system	118
6.4	Subharmonic oscillations	120
6.5	Conclusions	123
7	Flagellar beating	125
7.1	Continuum flagella equations	126
7.2	Linear stability analysis	130
7.3	Parameter choice	134
7.4	Nonlinear motor dynamics	135
7.5	Principal component analysis	137
7.6	Bending initiation	140
7.7	Conclusions	141
8	General conclusions	143
9	Resum en català	147
A	Analytical VF relationship for KIF1A	155
B	Simulation of stochastic processes	159
B.1	Langevin dynamics	159
B.2	Gillespie algorithm	160
C	Cell culture and purification of KIF1A	163
C.1	Mediums and buffers	163
C.2	Protocol	164
D	Theoretical description of a tubular helix	167
D.1	Geometry and energetics of a tubular helix	167
D.2	Superhelical effect on the tube pitch	169
D.3	Estimation of the off-axis force	170
E	Elastohydrodynamic flagella equations	171
E.1	Derivation of the equations	171
E.2	Boundary conditions	173

F	Integration of the nonlinear flagella equations	175
	F.1 Tangent angle dynamics	175
	F.2 Dynein dynamics	177
	References	179

Chapter 1

General Introduction

Molecular motors are ubiquitous in biology and they are in charge of a variety of mechanical functions inside cells, such as force generation and motility in living systems. They move, divide and spatially organize the crowded interior of a cell. These molecules constitute the basis of the elementary processes in cells, such as cell division or RNA transcription. Molecular motors may be classified in two major groups, namely cytoskeletal or nucleic acid motors, depending on whether they act on protein or nucleic acid based structures (Fig. 1.1)¹. Cytoskeletal motors are in charge of many different processes inside the cell such as intracellular traffic, mitosis, meiosis, muscular contraction or flagellar beating. On the other hand, nucleic acid motors are involved in DNA replication and repair, RNA transcription, chromatin remodeling or genome packaging [Alberts et al., 2002].

Molecular motors are proteins capable of transforming chemical energy into mechanical work. The two main sources of chemical energy are the hydrolysis of nucleotide triphosphate (NTP) molecules and ionic/proton gradients. The first energy source is most commonly used by cytoskeletal and nucleic acid motors whereas the second energy source is typically used by rotatory motors such as ATP-synthase or the rotatory motor of bacterial flagella. The hydrolysis of NTP results into a nucleotide diphosphate (NDP) molecule and an inorganic phosphate, providing an

¹ Other molecular motor examples are the F_1 -ATP synthase or the bacterial flagellar motor which are involved in ATP synthesis and bacterial propulsion, respectively.

energy of $\sim 10k_B T$, where $k_B T$ is the thermal energy. The most common forms of NTPs are adenosine triphosphate (ATP) being the major source of cellular energy and guanosine triphosphate (GTP), which is a frequent cofactor of enzymes and proteins. The chemical energy released during ATP hydrolysis is converted into mechanical work, producing nanometer ranged displacements ($1 \text{ nm} = 10^{-9} \text{ m}$). Hence, the order of magnitude of the forces generated by cytoskeletal motors is $\sim 10k_B T/\text{nm}$, in the range of piconewtons ($1 \text{ pN} = 10^{-12} \text{ N}$).

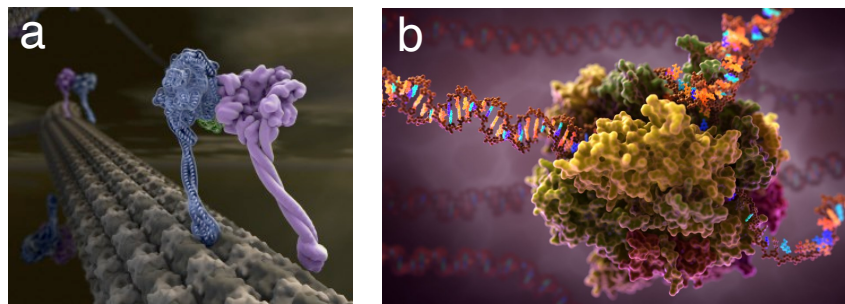


Fig. 1.1 Artistic 3D rendering of molecular motors based upon X-ray crystal structure. a) Cytoskeletal motor: dynein walking along a microtubule. Image created by Graham Johnson of The Scripps Research Institute (grahamj.com). b) Nucleic acid motor: RNA polymerase transcribing a DNA template. (Art of the Cell, Medical & Scientific 3D animation, www.artofthecell.com).

From a physical perspective, molecular motors can be suitably described using overdamped mechanics in a noisy environment. Therefore, a first fundamental question is: *Which type of forces act on a molecular motor?* The relevant forces are of four different types: elastic, viscous, thermal and electrostatic² [Howard, 2001]. These forces are found in the range of 1 to 10^3 pN. Elastic forces have their origin on the molecular bonds which form a molecule. The elasticity of such proteins is usually described by means of Hooke's law, which yields a good approximation in many situations. Viscous forces are of transcendental importance in the molecular scale, since the hydrodynamics of micro

² Covalent forces are also important ($\sim 10^4$ pN) but they will not be our main focus of attention.

and nanosized objects are described in the limit of *low Reynolds number* [Howard, 2001, Lauga and Powers, 2009]. The Reynolds number is a dimensionless quantity which is defined as the ratio of inertial forces to viscous forces. This number can be expressed as $Re = \rho v L / \eta$, where ρ is the density of the fluid, v and L are the velocity and the size of the object respectively, and η is the viscosity of the medium. Let us consider a motor protein of size $L \simeq 10$ nm in water ($\rho \simeq 10^3$ kg/m³ and $\eta \simeq 10^{-3}$ Pa·s), moving with speed $v \simeq 1$ μ m/s. In this case, $Re \simeq 10^{-8}$! Hence, for our purposes $Re \ll 1$ and therefore inertial forces are negligible in front of viscous forces. Additionally, friction forces can be typically considered to be proportional to the velocity of the system v , via a drag coefficient. Unlike macroscopic motors, molecular motors work in a thermal bath where thermal fluctuations are significant. Thermal forces have their origin on the random collisions of water and other molecules on proteins. The resulting random forces drive diffusion and play a crucial role in many processes in the cell. Finally, electrostatic and Van der Waals forces determine protein folding and the chemical kinetic rates involved in the motor cycle.

In this thesis, we will focus on cytoskeletal motors and refer to them as simply ‘motors’. Next, we will study how motors are able to transfer force and directed movement to the environment by interacting with the cytoskeleton, a complex architecture inside the cell composed of polar filaments which are able to actively assemble and disassemble.

Cytoskeletal filaments

Two major classes of cytoskeletal filaments are found within the cell to which molecular motors can interact, namely actin filaments and microtubules (MTs)³ [Alberts et al., 2002, Howard, 2001].

³ A third class of cytoskeletal filaments are intermediate filaments, which confer further mechanical consistency to the cell.

Actin filaments

Actin filaments are composed of actin monomers, which assemble in a right-handed double helix with a full period of 72 nm and a diameter of 7 nm. Actin monomers are structurally polar, and monomers assemble in a head-to-tail arrangement which confer an overall polarity to the filaments, being the two ends structurally different. Actin polymerization is mediated by ATP. Actin monomers can be in three different states depending on whether they are bound to ATP, ADP-P_i or ADP (yellow, orange and red monomers in Fig. 1.2). The thermodynamically limiting step for actin assembly, nucleation, is the formation of dimers and trimers. ATP-bound monomers assemble faster than ADP-bound monomers and the resulting structure is more stable. Hence, actin filaments with ADP-bound monomers depolymerize faster. The ATP-containing end is referred to as plus-end (or barbed end) and the ADP-containing end is referred to as minus-end (or pointed end).

In eukaryotic cells, actin filaments usually assemble in networks. This process is highly regulated by actin associated proteins which control the nucleation, growth and interaction of actin filaments [Alberts et al., 2002]. Actin nucleation is a slow process. The Arp 2/3 complex triggers actin nucleation whenever activated by nucleation promoting factors (NPFs) [Mullins et al., 1998, Blanchoin et al., 2014]. In addition to this nucleating activity, the Arp 2/3 complex can also attach to pre-existing actin filaments and initiate the nucleation of another actin filament, with a preferred angle of 70 degrees [Mullins et al., 1998], leading to branched actin networks (Fig. 1.2b,1). On the other hand, polymerization activity can be enhanced by actin monomer binding proteins such as profilin or formin, which promote polymerization at the barbed end [Blanchoin et al., 2014, Schlüter et al., 1997]. The network is further modeled by capping proteins which regulate the length of actin filaments, and crosslinker proteins which structure and confer further consistence to the network (Fig. 1.2b) [Blanchoin et al., 2014].

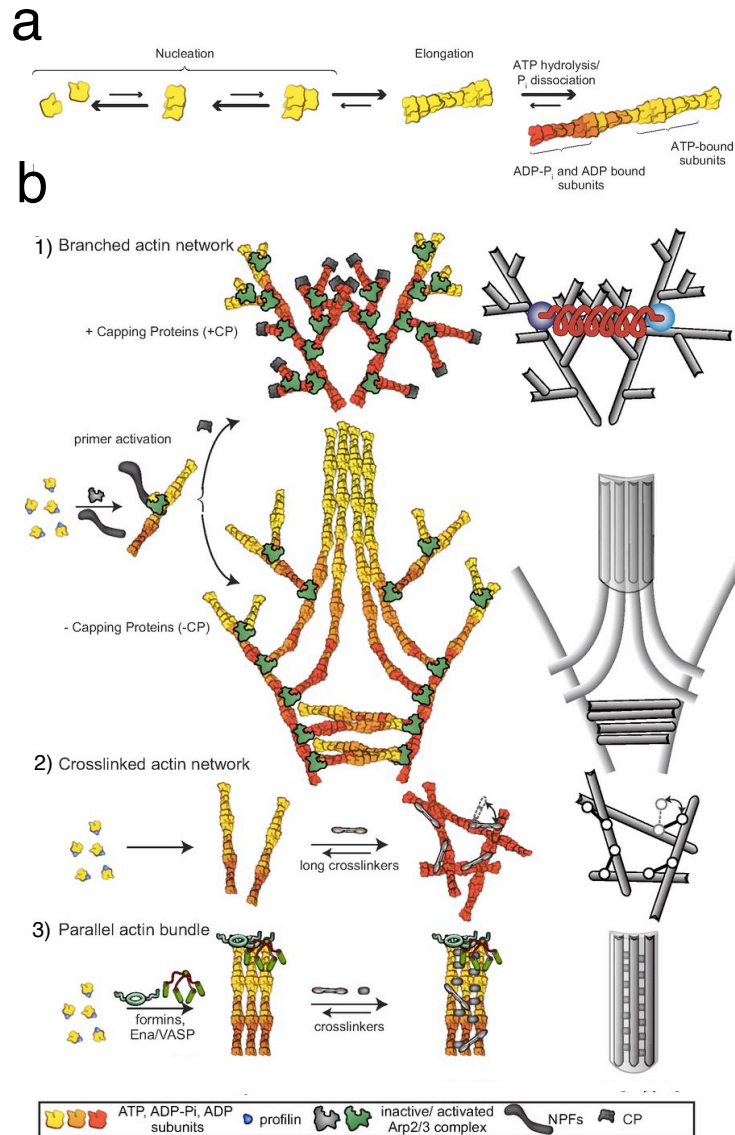


Fig. 1.2 Actin filaments. a) Actin filaments (F-actin) are composed of globular actin monomers (G-actin) which assemble in a right-handed double helix. b) Distinct actin filament organizations: 1) Branched actin network. The entanglement of filament subnetworks leads to mechanical interactions represented by a spring (in red) connecting the barycenters of adjacent subnetworks. 2,3) Long and short crosslinkers organize actin filaments into networks. On the right, gray diagrams represent mechanical analogs of the molecular structures. (Adapted from [Blanchoin et al., 2014]).

Microtubules

Microtubules are hollow cylindrical tubes of typically 24 nm in diameter and several micrometers long (Fig. 1.3). They are composed of α and β tubulin protein subunits, which assemble in $\alpha\beta$ dimers of 8 nm in length. At the same time, the dimers associate head-to-tail forming linear *protofilaments* (pfs) with the dimer periodicity. Protofilaments associate laterally to form a sheet that closes forming the cylindrical tube, described as a B-type lattice with a seam (Fig. 1.3a, long arrow) [Conde and Cáceres, 2009]. During lateral association, there exist a rise between adjacent pfs [Chrétien and Wade, 1991], such that the tubulin subunits arrange in a left-handed helix with a pitch of 12 nm. On the other hand, the head-to-tail association of the dimers provides a polarity on the microtubules, which have different polymerization rates at the two ends. β -tubulin monomers are oriented towards the faster-growing end (plus end) while α -tubulin monomers are exposed at the slower-growing end (minus end) (Fig. 1.3a,b). Each subunit forming the tubulin dimer has a binding site for GTP, but only that exposed to the exterior in the β -tubulin subunit can be hydrolyzed into GDP. The GTP molecules are hydrolyzed quickly after assembly; consequently, the microtubule is characterized by a GTP cap at the plus end, and a GDP tubulin region in the rest of the microtubule. When the GTP cap is stochastically lost, the protofilaments splay apart and the microtubule rapidly depolymerizes, in a process known as a catastrophe. If a GTP-cap is newly formed, the microtubule can slowly grow again, known as a rescue (Fig 1.3b). A dynamic instability is known as the switching between growing (polymerizing) and shrinking (depolymerizing) states. The case in which a microtubule grows at the plus end and shrinks in the minus end is known as treadmilling.

Finally, most cellular microtubules typically contain 13 protofilaments, although microtubules with 8 pfs and as many as 19 pfs have been observed *in vitro* and *in vivo* [Amos and Schlieper, 2005, Chrétien and Wade, 1991]. 13 pf microtubules run straight with respect to the microtubule axis. However, when the number of protofilaments differs from 13, the structure rearranges in such a

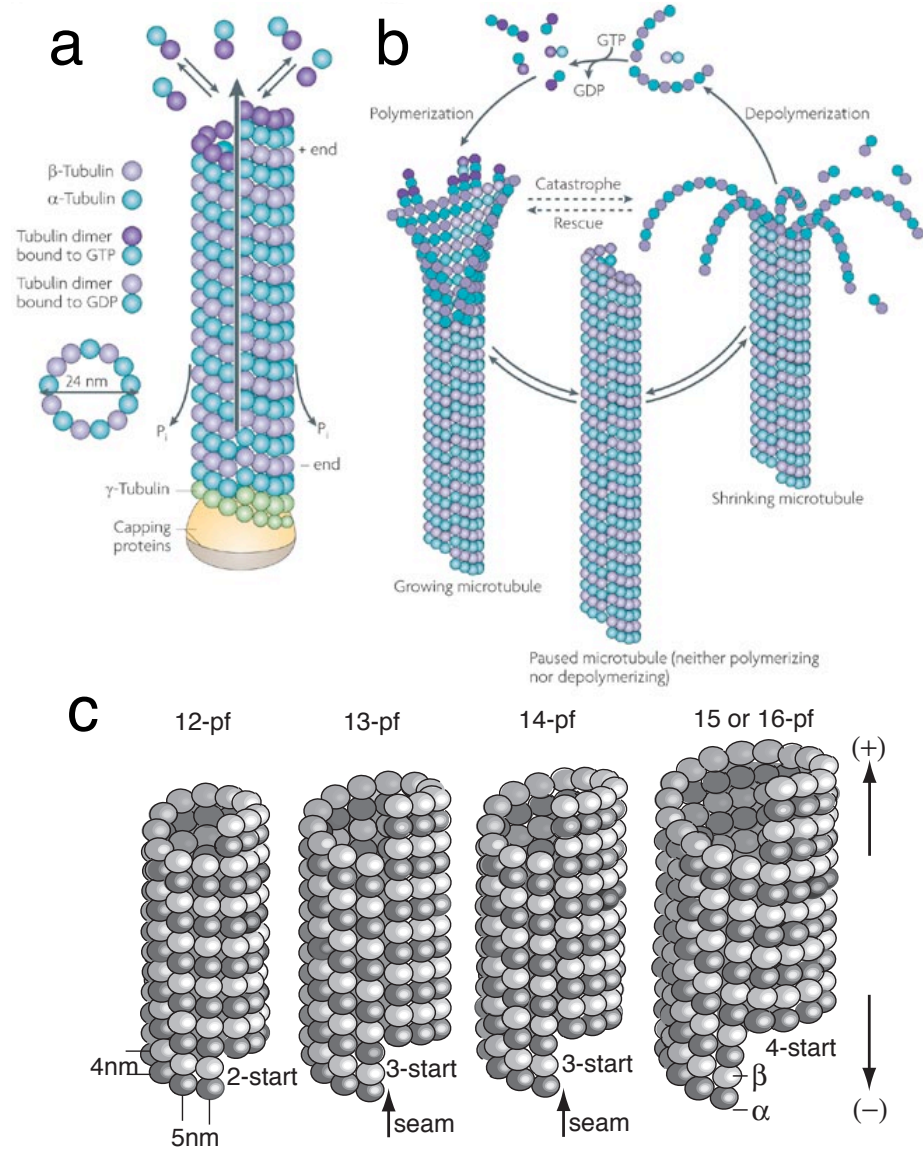


Fig. 1.3 Microtubule filaments. Microtubules are hollow cylindrical tubes of typically 24 nm in diameter composed of α and β tubulin subunits which assemble in $\alpha\beta$ dimers of 8 nm in length. b) Microtubules can rapidly grow (polymerize) or shrink (depolymerize) in size, depending on how many tubulin molecules they contain. (Adapted from [Conde and Cáceres, 2009]) c) A single microtubule typically contains 10 to 15 protofilaments (13 in mammalian cells) that wind together to form a 24 nm wide hollow cylinder. (Adapted from [Amos and Schlieper, 2005]).

way that protofilaments wind around the microtubule axis (see Fig. 1.3c), and form a shallow helix known as *superhelix*.

Cytoskeletal motor proteins

There exist three large superfamilies of cytoskeletal molecular motors: kinesins, myosins and dyneins, which are involved in many force generating processes in cells [Alberts et al., 2002, Howard, 2001]. The representative protein structures of the three superfamilies are shown in Fig. 1.4. Kinesins and dyneins move along microtubules typically to the plus and minus ends respectively, while myosin motors move along actin filaments to the plus end (barbed end). Their protein structure is characterized by the presence of binding regions to the filament (heads), a tail region to bind specifically to a cargo and a coiled-coil domain connecting both regions. On the other hand, the motor domain is the region where ATP molecules bind to produce a conformational change on the protein which triggers the *power stroke*. In the case of kinesin and myosin, the binding domains and motor domains physically coincide; however, this is not the case for dynein (see Fig. 1.4c). From a physical perspective, directed motion is achieved by virtue of ATP hydrolysis and the polarity of the filament tracks. ATP supply drives the system out of equilibrium and breaks time reversal symmetry, while the polarity of the filaments breaks reflection symmetry [Jülicher et al., 1997].

Kinesin (from the Greek *kinein*) was first isolated from squid nervous tissue [Vale et al., 1985], while a microtubule ATPase with the same molecular weight and properties as kinesin was independently discovered in the chicken brain [Brady, 1985]. Kinesin motors are involved in a large variety of cell processes such as intracellular transport, mitosis or meiosis. The kinesin superfamily is constituted by 15 kinesin families according to phylogenetic analyses [Hirokawa et al., 2009]. These families can be classified in three main groups, depending on the position of the motor domain in the molecule: N-kinesins, M-kinesins and C-kinesins, where

in each case the motor is located at the amino-terminal region, in the middle of the protein or in the carboxyl-terminal region. N-kinesins and C-kinesins drive microtubule plus- and minus-end-directed motilities, respectively, whereas M-kinesins depolymerize microtubules. N-Kinesins (hereinafter referred as simply kinesins) are composed of a relatively small globular motor domain (~ 400 aa) which is connected to stalk and tail regions that are used for kinesin dimerization and/or kinesin binding to cargos, adaptors or scaffolding proteins. Cargos can bind to the tail region and be transported when the motor attaches to a microtubule track.

Kinesins can act as monomers (single-headed), dimers (two-headed) or tetramers (four-headed). The kinesin-3 KIF1A can work in a monomeric form *in vitro* [Okada et al., 2003]. The simplicity of the single-headed form serves as a motor paradigm to understand the mechanochemistry of the kinesin motor domain. However, kinesins are usually found to act as dimers, being the kinesin-1 KIF5 (also known as conventional kinesin) the most studied motor. This motor moves using a ‘hand-over-hand’ mechanism [Yildiz et al., 2004]. This model postulates that the two heads alternate so that the kinesin is always attached to the microtubule by at least one motor domain during the movement, and the two heads alternate the leading/trailing position. Finally, the tetrameric kinesin-5 motor KIF11 (also known as Eg5) is able to crosslink anti-parallel microtubules and it is essential for mitosis in most organisms [Kapitein et al., 2005].

Myosin (from the Greek *muós*) was discovered in the XIX century [Kühne, 1859] and subsequently identified as an actin-activated ATPase almost a century later [Engelhardt and Ljubimowa, 1939, Straub, 1943]. The myosin superfamily contains at least 18 families [Thompson and Langford, 2002], termed myosin I to myosin XVIII. Their motor domain is slightly larger than kinesin (~ 800 aa) and shares a similar structure [Kull et al., 1996]. Myosin motors are involved in muscle contraction, cytokinesis, intracellular transport, Golgi organization and other cellular processes [Sweeney and Houdusse, 2010, Hartman and Spudich, 2012]. They are typically found in monomeric (e.g. Myosin I) or dimeric (e.g.

Myosin II, V) forms.

Finally, dynein (from the Greek *dynamis*) was first identified in protozoan cilia [Gibbons and Rowe, 1965]. Dynein can be grouped in 9 classes of dynein heavy chains [Wickstead and Gull, 2007, Roberts et al., 2013]. Dynein heavy chains are large polypeptides (~ 3000 aa), each containing a single motor domain. The first class (here referred to as simply cytoplasmic dynein) is involved in different cellular functions such as vesicular transport or positioning of the nucleus during cell division, and acts as a two-headed motor, containing two heavy chains (see Fig. 1.4c). The second class is referred to as ‘intraflagellar transport dynein’ or ‘cytoplasmic dynein 2’ for distinction. Finally, the remaining classes are classified as axonemal dyneins, since they are found in a cytoskeleton structure named *axoneme* which is the major structure composing cilia and flagella. Dyneins inside the axoneme are found in monomeric and dimeric forms in a complex arrangement [Roberts et al., 2013].

Cytoskeletal motor proteins bind and unbind stochastically to cytoskeletal filaments. An important property is their *duty ratio*, which is defined as the fraction of the time a motor spends attached to a filament [Howard, 2001]. For example, a high duty ratio (~ 1) is important for intracellular transport, since motors are able to translocate organelles over long distances before detaching from a filament. In this context, motors are referred to as being *processive*. In contrast, when the duty ratio is low ($\ll 1$), motors are referred to as *non-processive*, spending only a small fraction of time attached to filaments. Motors with low duty ratio are essential to drive dynamical instabilities [Howard, 2009]. Some prominent examples are the flagellar beat, mitotic spindle oscillations or bidirectional organelle transport [Camalet et al., 1999, Grill et al., 2005, Müller et al., 2008].

Finally, serious human and animal diseases arise from cytoskeletal motor protein dysfunctions. Kinesins are known to be involved in neural disorders, viral traffic, kidney diseases and can be used as drug targets in cancer chemotherapy [Millecamps and Julien, 2013, Mandelkow and Mandelkow, 2002]. Defects in muscular myosin cause myopathies [Oldfors et al., 2004] and dynein deficiencies

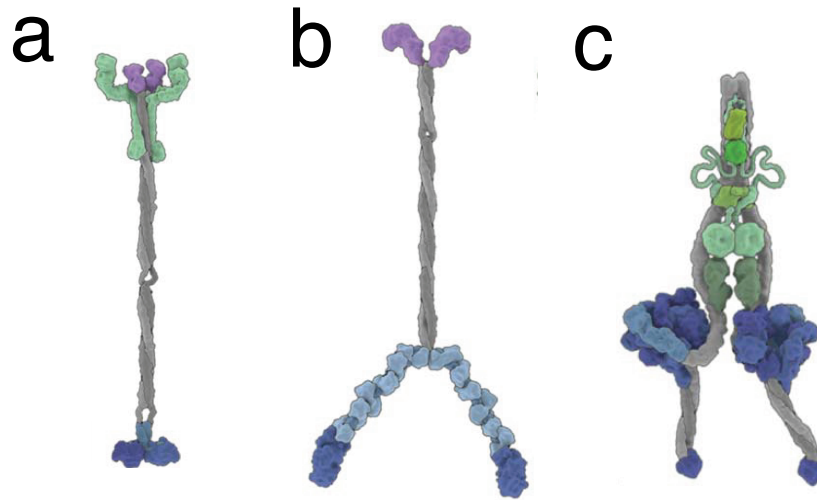


Fig. 1.4 a) Kinesin-1 (KIF5). Kinesin dimer with a coiled-coil region (grey) which connects the two motor domains (dark blue) through a neck linker region (light blue). Cargo binding is mediated by the kinesin light chains (green) and the tail region (purple). b) Myosin V. The structure is similar to the case of kinesin; however, the neck linker regions are larger c) Cytoplasmic dynein. We identify two microtubule-binding domains at the end of a coiled-coil stalk (grey). The motor domains consist of a ring of AAA+ domains (dark blue) with one and three active sites of ATP hydrolysis. The N-terminal tail of dynein (grey) is involved in dimerization and binding to dimers of intermediate chains, light intermediate chains and three light chains (different shades of green). Cargo binding is mediated by these accessory chains. (Adapted from [Carter, 2013]).

can lead to chronic respiratory diseases and male infertility [Chao et al., 1982, Khelifa et al., 2014]. Although many advances have been done in the field of molecular and cell biology, we are still rather unable to make predictive statements in these systems, for example, on how motor proteins interact and coordinate inside the cell. One of the main reasons is that we are still lacking a complete understanding of the physical principles of subcellular organization [Needleman and Brugués, 2014]. Next, we illustrate some examples of collective motor organization.

Collective dynamics of cytoskeleton motor proteins

In many cases, cytoskeletal motors operate in groups inside the cell, rather than acting as isolated entities. In intracellular transport, groups of ~ 10 motors work collectively in vesicle transport [Holzbaur and Goldman, 2010]. The beating of cilia or flagella involves roughly $\sim 10^4 - 10^5$ dynein motors [Ma et al., 2014, Nicastro et al., 2006], while in the case of a muscle, the number of myosins involved can reach $10^{19} - 10^{20}$ [Guérin et al., 2010, Cotterill, 2002].

An early approach to classify molecular motors regarding their collective behaviour was the categorization of *rowers* and *porters* [Leibler and Huse, 1993, Howard, 2001], which is related to the concept of processivity. The latter classification is based on the functionality of motors regarding their tasks in the cell, rather than their molecular structure or family. Large ensembles of myosin in muscles (or axonemal dynein in cilia and flagella), can be regarded as *rowers* such that each motor cannot work individually and it is a part of a larger assembly. Due to their low duty ratio, the action of individual molecules is not correlated over large distances. Hence, motors spend most of their time binding and unbinding without producing any power stroke. In this way, motors do not work against each other and “protein friction” is minimized. This is suitable for large cytoskeletal structures which need to perform work at high loads. On the other hand, *porters* are entities which can work individually or in small groups, such as kinesin, cytoplasmic dynein or some myosin members (e.g. Myosin V) transporting organelles. These types of motors are characterized by their high duty ratio. In this case, loads are generally small and protein friction is not an important issue.

Over the last two decades, *in vitro* and *in vivo* experiments together with theoretical descriptions, have shown that the interaction of many motors can lead to complex phenomena such as bidirectional motion, oscillations or the formation of dynamical structures. In many cases, the study of minimal reconstituted systems by using cytoskeletal filaments and motors, have provided

deep physical insights on the collective behaviour of these systems. Some prominent examples are summarized in Figure 1.5.

As previously mentioned, kinesins and cytoplasmic dyneins usually act as *porters* in vesicle transport. The motion of these motors in microtubule networks can be tracked using single-molecule techniques. Recently, superresolution microscopy has revealed how motors behave in the presence of obstacles, such as microtubule-microtubule intersections [Bálint et al., 2013]. In parallel, lattice models describing the dynamics of molecular motors in networks have just begun to emerge [Neri et al., 2011, Neri et al., 2013]. As more motors interact on the same cargo, there exist the possibility that those have opposite polarities. In this case, an interesting phenomenon emerges which is known as ‘tug-of-war’ [Hendricks et al., 2010]. From a theoretical perspective, this phenomenon can be understood as a symmetry breaking process [Müller et al., 2008]; however, the underlying *in vivo* implications are still under debate [Hancock, 2014]. If tens of motors cluster in lipid membranes, they may be strong enough to be able to form membrane tube networks [Koster et al., 2003, Leduc et al., 2004, Shaklee et al., 2008]. This process can be described by using lattice models and studying how motors self-organize at the tube tips [Campàs et al., 2008]. For larger motor assemblies ($N > 10^2$) motors are usually found to work as *rowers*. When these assemblies are coupled to an elastic element, motors are able to produce self-organized oscillations [Camalet et al., 1999, Guérin et al., 2010]. Spontaneous oscillations in actomyosin systems or the beating of cilia and flagella, are some examples that have been reproduced in minimal *in vitro* systems [Plaçais et al., 2009, Sanchez et al., 2011]. Finally, an important example of large-scale self-organization of microtubules and motors is the mitotic spindle. In this dynamical cell structure, kinesins and dyneins work collectively to segregate chromosomes during mitosis [Brugués et al., 2012, Brugués and Needleman, 2014].

In this thesis, we will study some of the previous examples. In the first part, we will mainly focus on the cooperative behaviour of *porters*, while in the second part we will study the oscillatory properties of *rowers* coupled to an elastic element.

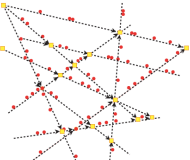
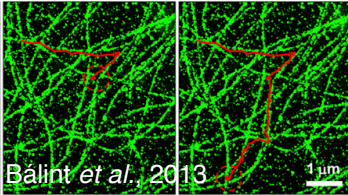
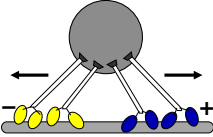
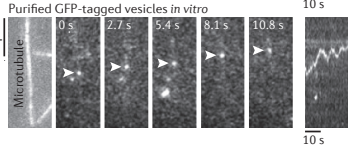
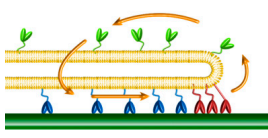
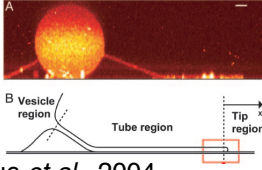
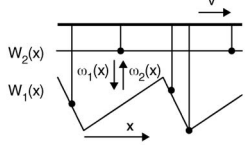
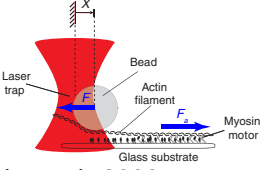
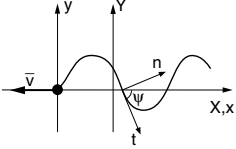
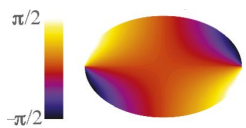
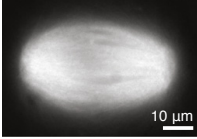
N	Theoretical models	Experiments
~ 1	 Neri <i>et al.</i> , 2013	 Bálint <i>et al.</i> , 2013
1-10	 Müller <i>et al.</i> , 2008	 Hendricks <i>et al.</i> , 2010
10-20	 Campàs <i>et al.</i> , 2008	 Leduc <i>et al.</i> , 2004
$10-10^2$	 Guérin <i>et al.</i> , 2010	 Plaçais <i>et al.</i> , 2009
$10^4 - 10^5$	 Camalet & Jülicher, 2000	 Gaffney <i>et al.</i> , 2011
$10^5 - 10^6$	 Brugués & Needleman, 2014	 Brugués <i>et al.</i> , 2012

Fig. 1.5 Examples of *in vitro* and *in vivo* systems where interacting cytoskeletal molecular motors work in groups and the corresponding theoretical and experimental approaches used in the literature. N indicates the typical number of motors working collectively in the system. From top to bottom: Intracellular traffic in the cytoskeleton, ‘tug-of-war’ in liposome transport, membrane tube extraction from giant unilamellar vesicles, spontaneous oscillations in a minimal actomyosin system, flagellar beating and mitotic spindle formation. Figures adapted from the corresponding references.

Part I
Cooperative force generation by
molecular motors

Chapter 2

Introduction

Thousands of different biochemical reactions occur every second in the crowded interior of a living eukaryotic cell. These processes are highly regulated in time and space and compose a remarkable example of self-organization in biology. The proper transport of biomolecules inside the cell is crucial for its maintenance and functioning. However, simple passive diffusion cannot meet the transport needs of a cell. In addition, transport is very specific and selective according to the needs at different regions in the cell. Hence, how is efficient transport achieved? The answer relies on active transport by ATP-fueled motor proteins which move along the cytoskeleton network, which spans the cytoplasm connecting the cell nucleus and the cell membrane. In addition, compartmentalization in cells is essential to establish physical boundaries and prevent the interference of cellular processes. Hence, proteins are usually transported in membrane-bound compartments which constitute the cargos motor proteins move along cytoskeletal filaments. Intracellular transport is particularly demanding in highly polarized cells such as neurons, where cargos need to be transported over very long distances in a dense and particularly crowded environment. In such cases, motors usually cooperate in teams to secure cargo delivery to their final destination. One of our main goals will be to understand how motors self-organize in groups and cooperate to pull on membrane-bound cargos.

2.1 Vesicular traffic

Cells must eat and communicate with their environment. Eukaryotic cells present a membrane system which enables them to take up macromolecules by a process named *endocytosis* and deliver synthesized molecules by *exocytosis* [Alberts et al., 2002]. In both cases, the material to be transported needs to be enclosed inside membrane-bound compartments or packages. We shall use the term *vesicles* to apply to all forms of packages.

The creation of small vesicles requires different proteins such as Clathrin or COP [McMahon and Mills, 2004] which locally assemble on the membrane surface and induce the formation of a membrane bud, which pinches off due to the action of other proteins (e.g. dynamin [Ferguson and Camilli, 2012]). The latter process is known as membrane fission. These vesicles are transported by motor proteins along cytoskeletal filaments up to target compartments, where they release their material through membrane fusion. In this way, cells ingest macromolecules derived from the plasma (or cell) membrane which are transported to membrane-bound organelles named lysosomes, where different enzymes digest the material [Alberts et al., 2002]. This process is known as the endocytic pathway (Fig. 2.1, green arrows). On the other hand, the biosynthetic-secretory pathway allows the cell to deliver synthesized molecules to the exterior by a process called exocytosis (Fig. 2.1, red arrows). Proteins synthesized in the cell nucleus are transported from the endoplasmic reticulum (ER) to the Golgi apparatus (see Fig. 2.1), and subsequently sorted to the lysosome or to the plasma membrane. Finally, sometimes molecules follow retrieval pathways between compartments (see Fig. 2.1, blue arrows).

The formation and maintenance of membrane organelles, like the ER or the Golgi apparatus, is known to involve the presence of microtubules and motor proteins [Alberts et al., 2002, Gurel et al., 2014]. The ER is an interconnected network of tubules of $\simeq 50$ nm in diameter and sheets (also known as cisternae) forming irregular polygons. The overall structure is held together by the cytoskeleton through the interaction of proteins such as CLIMP-

63 [Gurel et al., 2014]. ER tubules can extend by attaching themselves to the polymerizing end of microtubules via a tip attachment complex (TAC) or can be transported along microtubule filaments by motor proteins [Tripathi, 2010]. The latter process involves the cooperation of motor proteins to pull membrane tubes. We will focus on this process in Chapter 4 using a biomimetic *in vitro* system to study the cooperative action of motors.

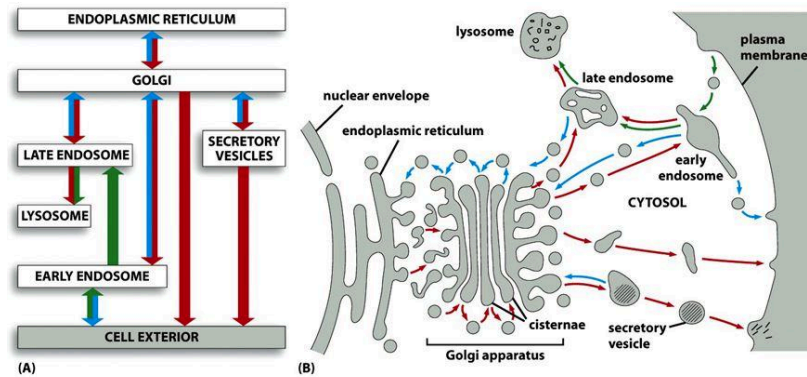


Fig. 2.1 Intracellular compartments of eukaryotic cell. a) “Road map” of the biosynthetic-secretory pathway (red), endocytic pathway (green) and retrieval pathways (blue) between the different intracellular compartments b) In the biosynthetic-secretory pathway (red arrows) protein molecules are transported from the ER to the plasma membrane or (via late endosomes) to lysosomes. In the endocytic pathway (green arrows) molecules are ingested in vesicles derived from the plasma membrane and delivered (via early and late endosomes) to lysosomes. Endocytosed molecules sometimes are retrieved from early endosomes and returned to the cell surface for reuse; similarly, some molecules are retrieved from the late endosome and returned to the Golgi apparatus, and some are retrieved from the Golgi apparatus and returned to the ER. Retrieval pathways are shown with blue arrows. Modified from [Alberts et al., 2002].

2.2 Intracellular transport

Intracellular transport corresponds to the active transport of proteins in membranous organelles, messenger RNA and protein complexes along cytoskeletal filaments [Hirokawa and Takemura, 2005, Hirokawa et al., 2009]. Transport is achieved by ATP-fueled motor proteins namely kinesin, dynein and myosin motors which carry organelles to their destinations. Kinesins and dyneins are in charge

of the plus/minus-end-directed (anterograde/retrograde) transport along microtubules, whereas myosin is in charge of short-range transport in the cell, occurring beneath the plasma membrane. Hence, microtubules play the role of two-way “highways” and actin filaments are typically one-way “roads”. Microtubule polarity arrangement varies depending on the cell type. We can classify intracellular transport in three different scenarios: neural cells, non-neural cells and cilia (see Fig. 2.2). Neurons are highly polarized cells which present three main regions: the soma (cell body), the axon, and the synaptic terminals (Fig. 2.2a). Proteins are synthesized in the soma and they must be transported all along the axon to supply synaptic terminals with proteins, lipids and mitochondria [Millecamps and Julien, 2013]. Microtubules are unipolar

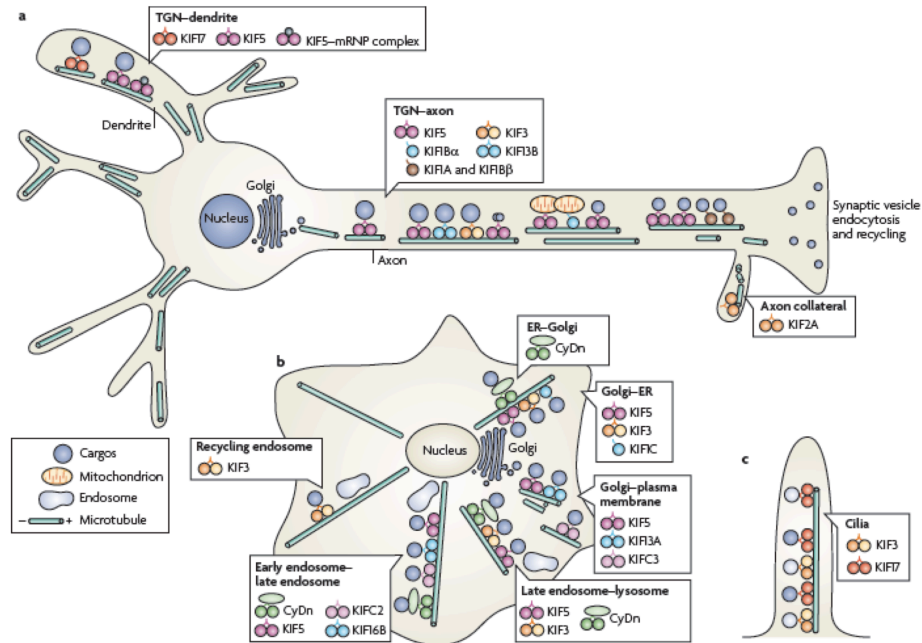


Fig. 2.2 Intracellular transport by kinesins and cytoplasmic dynein in neural cells (a), non-neural cells (b) and in cilia (c). ER, endoplasmatic reticulum, TGN, Trans-Golgi network. a) In neural axons, microtubules are unipolar and point distally, i.e. with the plus-end pointing to the synaptic terminals. In dendrites, microtubules can have mixed polarity. b) In non-neuronal cells, microtubules usually point with their plus-ends to the periphery from the microtubule organizing center. c) Bidirectional intraflagellar transport in cilia. Notice that microtubules are oriented reflecting the polarity of the different regions. Modified from [Hirokawa et al., 2009].

in the axon, with their plus-end pointing to the synaptic terminals. On the other hand, in non-neural cells microtubules are usually directed from the cell nucleus to the cell periphery (Fig. 2.2b). Finally, intraflagellar transport is required for the maintenance and assembly of cilia. Transport is bidirectional and motor proteins move along axonemal microtubules (Fig. 2.2c) [Hao and Scholey, 2009]. We will focus on axonal transport since neurons are a good model system to study intracellular transport due to the very large distances motors must translocate organelles.

2.3 Axonal transport

In neurons, membrane organelles are transported by fast axonal transport at a similar speed to kinesin motors *in vitro* (50-200 mm per day), and cytoplasmic proteins, such as tubulin and neurofilament proteins, are transported by slow axonal transport (0.1-3 mm per day) [Hirokawa et al., 2009]. Kinesin motors use adaptors/scaffolding protein complexes for cargo recognition and binding. Although most scaffolding complexes are still unknown, cargo selectivity has been extensively studied. The kinesin-1 KIF5 is able to transport a great variety of cargos such as vesicles, oligomeric tubulin and mitochondria. On the other hand, the kinesin-3 motors KIF1A and KIF1B β transport synaptic proteins such as synaptotagmin or synaptophysin [Hirokawa and Takemura, 2005].

Finally, impaired axonal transport is commonly associated to several neural disorders [Millecamps and Julien, 2013]. Neurotoxic compounds such as MPTP or Rotenone, have been shown to decrease anterograde transport and increase mitochondrial retrograde transport respectively, leading to Parkinson's disease [Morfini et al., 2007, Arnold et al., 2011]. Pathological forms of proteins such as the amyloid precursor protein (APP) or tau, affect axonal transport by various mechanisms leading to Alzheimer's disease. On the other hand, loss-of-function mutations in motor proteins may result in motor neuron diseases, but are rare and have not been linked with Alzheimer's or Parkinson's diseases [Millecamps and Julien, 2013]. Therefore, probably axonal

deficits commonly arise because motor proteins find obstacles or roadblocks along their way. How motors navigate the cell in order to overcome possible traffic jams is only now beginning to be studied thanks to state-of-the-art single molecule biophysical tools [Bálint et al., 2013, Lakadamyali, 2014]. Different strategies may be used in the axon such as bidirectional movement [Hancock, 2014] or transversal motion [Can et al., 2014].

2.4 Coordination of motor teams

Intracellular transport in cells is carried out by small motor teams pulling on cargos. The total number of kinesin and dynein motors involved in vesicle transport typically ranges from 1 to 10 motors [Gross et al., 2007, Holzbaur and Goldman, 2010] while the number of myosin motors carrying vesicles is still unclear, estimated in the range ~ 10 -100 motors in axonal transport [Tabb et al., 1998]. Some observations have shown that the necessary force to stop cargo motility increases with motor number, although not necessarily in proportion [Mallik et al., 2005, Vershinin et al., 2007, Furuta et al., 2013]. The distance a cargo is transported before dissociation is also shown to increase with motor number [Gross et al., 2007, Beeg et al., 2008, Furuta et al., 2013]. How do multiple motors coordinate and interact on a cargo? First, one should understand how single motors act individually. Although the ATP cycle of single motor domains has been studied extensively [Hackney, 1996], motor dimers which are typically the relevant forms *in vivo*, use more sophisticated mechanisms, e.g. the ‘hand-over-hand’ mechanism [Yildiz et al., 2004] for kinesin-1 or uncoordinated stepping [DeWitt et al., 2012] for cytoplasmic dynein. In terms of mathematical modelling, the detailed description of a motor dimer is involved [Shao and Gao, 2006] and the consequent study of groups of interacting motors becomes impractical. Therefore, in order to model interacting motors carrying a cargo, a good strategy is to choose a motor which is amenable to mathematical modeling. A good candidate is the monomeric form of the kinesin-3 motor KIF1A, as discussed below.

2.5 A model motor: the kinesin KIF1A

KIF1A is a kinesin motor specific of axonal transport of synaptic vesicle precursors [Okada et al., 1995, Okada et al., 2003]. The monomeric form of KIF1A was proposed as a model motor [Okada et al., 2003] (see Fig. 2.3, bottom) being a prototype of Brownian motor [Reimann, 2002]. The protein is composed of a single globular motor domain, in contrast to conventional dimeric kinesin (Fig. 1.4a and Fig. 2.3, top), which is a larger motor with two motor domains. Monomeric kinesin alternates between two different states: a strongly and a weakly-bound state to the microtubule. In the latter case, the motor is able to diffuse close to the microtubule by virtue of an electrostatic interaction between the K-loop of the motor domain and the C-terminus of tubulin [Okada and Hirokawa, 2000]. Single-molecule experiments reported zero load velocities of $0.2 \mu\text{m/s}$ and very small stall forces around 0.1 pN , fulfilling a linear velocity-force relationship [Okada et al., 2003]. Although this motor was origi-

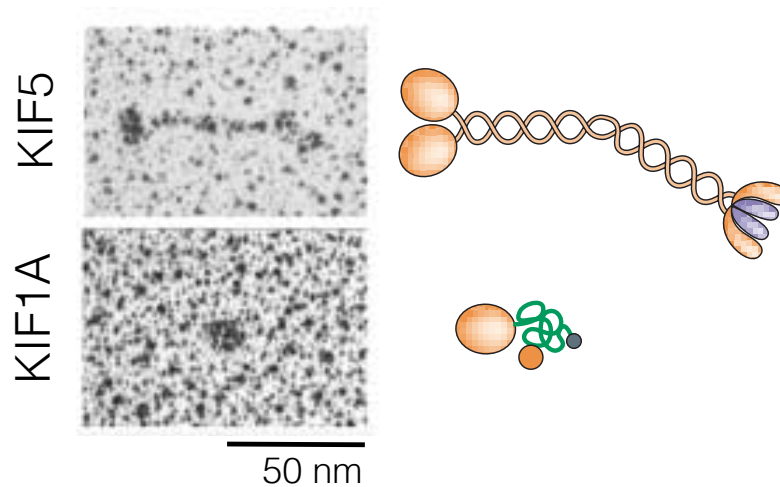


Fig. 2.3 Diagrams (right) and electron microscopy images (left) of the kinesin-1 dimer KIF5 and kinesin-3 monomer KIF1A. (Top) KIF5 forms a homodimer and kinesin light chains associate at the carboxyl terminus to form fanlike ends. (Bottom) KIF1A is monomeric and globular. Modified from [Hirokawa and Takemura, 2005].

nally reported to be a unique monomeric motor driving antero-grade transport in neurons, many studies now support the idea that KIF1A is mainly found as a dimer *in vivo* eliciting velocities of $\sim 1 \mu\text{m/s}$ [Tomishige et al., 2002, Hammond et al., 2009, Soppina et al., 2014]. However, the motor dimer has also been shown to present a diffusive state, which alternates with processive motion [Hammond et al., 2009]. Intriguingly, the intrinsic ability of KIF1A to diffuse is at odds with the demanding conditions of axonal transport, since it makes the individual motor inefficient and weak. In order to solve this apparent paradox, we may use the monomeric form of KIF1A as a model system to understand collective transport.

2.6 Modelling intracellular transport

We now aim to model intracellular transport from a physical perspective. Molecular motors can be regarded as isothermal thermodynamic machines working far from equilibrium at the nanoscale [Jülicher et al., 1997]. They can be described by overdamped mechanics in the presence of strong thermal noise, taking into account the kinetics of the motor cycle and the different relevant forces acting on the motor. First we pursue to describe the dynamics of a single molecular motor transporting a cargo along a polar filament track. We consider the motion of the motor to be one-dimensional and we denote the position of the motor over time by $x(t)$. Some molecular motors might explore the surface of cytoskeletal filaments and fail to exhibit a one-dimensional trajectory [Yajima and Cross, 2005, Brunnbauer et al., 2012] (see also Chapter 4); however, in many cases this is a good assumption. We consider the motor to be subject to a drag with an effective friction coefficient λ and to experience a force $-\partial_x U$, where U is the effective potential landscape originated by the interaction between the motor and the filament, and x is the spatial coordinate. The potential landscape can change over time since the molecule suffers different conformational changes during its ATP-cycle which affect its interaction with the filament. Therefore, we consider $U(x, t)$. Additionally, cytoskeletal filaments are periodic

and polar, therefore these properties must be reflected in the potential landscape. The first property implies $U(x, t) = U(x + l, t)$, where l is the periodicity of the filament, and the second property implies $U(x, t) \neq U(l - x, t)$. We also include a random, Gaussian distributed thermal force $\zeta(t)$, which has correlation $\langle \zeta(t)\zeta(t') \rangle = 2k_B T \lambda \delta(t - t')$ and zero mean $\langle \zeta(t) \rangle = 0$, where $\langle \cdot \rangle$ denotes ensemble average and $\delta(t - t')$ is the Dirac delta function centered at t' . Finally, we consider a constant external force F applied to the molecule. In the biological context, this force may arise as a consequence of friction forces opposing the cargo motion in constrained and constricted environments, as in the case of a neural axon. The dynamics of $x(t)$ simply reads:

$$\lambda \dot{x} = -\partial_x U - F + \zeta(t) \quad (2.1)$$

where the dot denotes time derivative. The last expression is known as Langevin equation [Langevin, 1908] and can be simulated numerically (see Appendix B.1) [García-Ojalvo and Sancho, 1999]. If we compute the ensemble average of Eq. 2.1 and define $v \equiv \langle \dot{x} \rangle$, $F_{ATP} = -\langle \partial_x U \rangle$ we obtain:

$$v(F) = \frac{1}{\lambda} (F_{ATP} - F) \quad (2.2)$$

where F_{ATP} is the active force generated by the motor in its ATP-cycle. The stall force F_s of a single motor is defined as the necessary force to stop the motor. This occurs for $F = F_{ATP}$. Since $U \sim 10 k_B T$ and $l \sim 10$ nm, we get F_s on the order of a few pN, which is a good stall force estimate for cytoskeletal motors. For the case of constant F_{ATP} , Eq. 2.2 gives a linear relationship between velocity and force. This approximation is quite accurate for a single-motor [Svoboda and Block, 1994, Okada et al., 2003]. Next we consider the case of N molecular motors pulling on a membranous cargo. We may call it a *soft* cargo, since motors are not anchored at the surface but they can move freely due to the liquid-like nature of the lipid membrane. Considering N motors pulling on the same cargo, only the foremost motor experiences the force F , while the rest of the motors experience unequal loading due to the transmission of the force through motor-motor interactions. Hence, motors accumulate at the front where they share the force, while

in the rear motors may barely experience any force at all. In order to describe the collective dynamics of the motors, we associate a Langevin equation to each motor i :

$$\lambda \dot{x}_i = -\partial_x U_i - \sum_{k \neq i} W'(\xi) - F \delta_{1i} + \zeta_i(t) \quad (2.3)$$

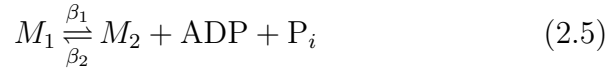
where $\xi = x_i - x_k$ and δ_{ij} is the Kronecker delta, which reads 1 if $i = j$ and 0 otherwise. $W(\xi)$ stands for the interaction potential between motor pairs. The sum indicates that the i -th motor can interact with all motors except with itself. In this case, the velocity-force relationship will be in general nonlinear, and its dependence may be quite complex [Brugués and Casademunt, 2009, Orlandi et al., 2010]. In our description, $U(x, t)$ encodes the periodicity and polarity of the filament, but also the kinetics and free energy excess released during the motor cycle. Next, we introduce a two-state model providing a simple description of a motor ATP-cycle.

2.6.1 The two-state model

The two-state model was first proposed to describe muscle contraction and flagellar beating [Huxley, 1957, Brokaw, 1975]. Years later, increasing interest arise on *Brownian motors* [Magnasco, 1993, Hänggi and Marchesoni, 2009] which were inspired by the celebrated Brownian ratchet [Smoluchowski, 1912, Feynman, 1963], and two-state models were used to describe the motion of Brownian particles in asymmetric environments which constituted a minimal description of an ATP motor cycle. Here, we present a common description of the ATP cycle used for molecular motors [Jülicher et al., 1997].

We consider a molecular motor which can be found in two different states: a “ground” state, in which the motor is found in a strongly bound conformation to the filament ($k = 1$) or an “excited” state, where the motor can be detached or weakly bound to the track ($k = 2$). k is a dichotomic discrete stochastic variable whose value can be 1 or 2 depending on the state of the motor.

In state k , the motor feels the periodic landscape potential $U_k(x)$, where now the subscript k refers to the state of the motor. $U_1(x)$ will be an asymmetric periodic potential describing the polarity and periodicity of the system, and we will consider U_2 as a flat potential, describing the energy landscape in the weakly bound state. The motor can switch to the “excited” state by using the chemical energy gain of ATP hydrolysis or by using thermal energy. In the most general case we consider these two different processes and write down the corresponding chemical reactions:



where α_i, β_i denote the chemical rates and M_1, M_2 are the two possible states of the motor corresponding to $k = 1, 2$, respectively. The first pathway (Eq. 2.4) requires the consumption of ATP and therefore there is a chemical potential difference $\Delta\mu$ which measures the free energy change per ATP molecule consumed. On the other hand, the second pathway (Eq. 2.5) uses the energy from the thermal bath to excite the molecule. Chemical kinetics in the steady state follow:

$$\frac{\alpha_1}{\alpha_2} = \exp\left(\frac{-\Delta U + \Delta\mu}{k_B T}\right); \quad \frac{\beta_1}{\beta_2} = \exp\left(\frac{-\Delta U}{k_B T}\right) \quad (2.6)$$

Where $\Delta U = U_1 - U_2$ is the difference between the periodic potential profiles. Since the motor can jump to a given state using two different processes, the total transition rates for the system $\omega_1(x)$ and $\omega_2(x)$ will be the sum of the rates for each process:

$$\omega_1(x) = \exp\left(-\frac{\Delta U}{k_B T}\right) \left[\alpha \exp\left(\frac{\Delta\mu}{k_B T}\right) + \beta \right] \quad (2.7)$$

$$\omega_2(x) = \alpha + \beta \quad (2.8)$$

where $\alpha \equiv \alpha_2$ and $\beta \equiv \beta_2$. In principle, $\alpha(x)$ and $\beta(x)$ are unknown l -periodic functions which may depend on space. We notice that when $\Delta\mu = 0$ we recover detailed balance. Let us construct a quantity Ω measuring the local deviation from detailed balance,

such that if $\Delta\mu = 0$, $\Omega = 0$:

$$\Omega(x) = \frac{\omega_1(x)}{\omega_2(x)} - \exp\left(-\frac{\Delta U}{k_B T}\right) \quad (2.9)$$

Using Eqs. 2.7 and 2.8 we obtain:

$$\Omega(x) = \Omega\theta(x) \quad (2.10)$$

where $\Omega \equiv \exp[\Delta\mu/k_B T] - 1$ is the amplitude of the perturbation and $\theta(x) \equiv \alpha/(\alpha + \beta) \exp[-\Delta U/k_B T]$ its modulation. Therefore, we have:

$$\frac{\omega_1(x)}{\omega_2(x)} = \exp\left(-\frac{\Delta U}{k_B T}\right) + \Omega\theta(x) \quad (2.11)$$

The first term in the right-hand side accounts for thermal activations from state 1 to state 2. The second term is due to the action of ATP which drives the system out of equilibrium. In the case of molecular motors $\Delta U \gg k_B T$, and thus we can typically neglect thermal excitations from state 1 to state 2. In this limit, Eq. 2.11 reduces to:

$$\frac{\omega_1(x)}{\omega_2(x)} = \Omega\theta(x) \quad (2.12)$$

Normally, the total decay rate ω_2 is taken to be delocalized, i.e. $\omega_2(x) = \omega$. On the other hand, ATP driven excitations are likely to happen when the motor is waiting in the U_1 minima rather than when the motor diffuses in the “excited” state or it is performing the power stroke. Therefore $\omega_1(x)$ should be maximum when $U(x)$ is minimum and viceversa. As we will see, possible practical implementations are to choose a rectangular form of $\omega_1(x)$ and approximate ω_2 to be constant, or to choose particular sinusoidal forms of $\alpha(x)$ and $\beta(x)$ such that ω_2 is constant and use Eq. 2.12 to find $\theta(x)$.

In summary, we shall describe the motor ATP-cycle as follows:

1. Initially, the motor is found in one of the $U_1(x)$ minima. This state corresponds to a strongly bound conformation of the motor protein to the filament. The motor waits a certain dwell time until it captures an ATP molecule. Usually, the dwell time is

approximated to be exponentially distributed with mean $1/\omega^*$, such that ω^* is the mean excitation rate. This rate will be dependent on the ATP concentration present in the medium.

2. Once an ATP molecule is captured, the motor switches to an “excited” state. In the case of myosin, this state corresponds to a completely detached state from the filament. However, in the case of KIF1A for example, the motor is weakly bound to the filament. In this state, hydrolysis takes place and ATP is converted to ADP and an inorganic phosphate P_i . Associated to this reaction, there is a chemical potential difference $\Delta\mu$ which measures the free energy excess.

3. In the “excited” state the motor is able to diffuse and explore the filament.

4. After a mean time $1/\omega$, the motor releases the inorganic phosphate P_i and binds again to the filament, where ω is defined as the mean decay rate. This transition is thermally driven and consequently passive.

5. Finally the motor performs the power stroke releasing the ADP molecule and moving in average to the next binding site.

Chapter 3

Theoretical modeling of KIF1A

In this chapter we study in detail the cooperative action of small groups of KIF1A motors within an arrangement relevant to vesicle traffic or membrane tube extraction. In particular, we analyze the cooperative effects which arise in motor teams due to the presence of a finite dwell time in their motor cycle. We first formulate the problem as one-dimensional in terms of Langevin dynamics, and we further complement our study using a lattice formulation for the case of one and two interacting KIF1A motors. The latter approach provides a deeper insight into the minimal ingredients for cooperative force generation and it enables us to obtain analytical expressions for the velocity-force relationships in certain limits. We also consider a first extension of the problem to an arbitrary number of motors. Finally, motivated by the experiments in Chapter 4, we also study the case of a single KIF1A motor moving in two dimensions on the MT surface lattice.

3.1 Ratchet model for KIF1A dynamics

We consider the general problem of N KIF1A motors moving along a one-dimensional track. The dynamics of the system is defined by a set of N Langevin equations as described in Eq. 2.3 with positions $x_i(t)$, $i = 1, \dots, N$. On the other hand, $k_i(t) = \{1, 2\}$ is a discrete stochastic variable that describes the state of the i -th motor. The two possible states correspond to two different conformations of the motor domain, with their respective potential

landscapes $U(x_i, k_i)$. When KIF1A captures an ATP molecule, the motor switches to a weakly bound state ($k_i = 2$). In this state, KIF1A diffuses along the filament with diffusion coefficient D feeling a constant potential $U_2 \equiv U(x_i, 2)$. In contrast, in the absence of ATP, the motor is strongly bound to the filament ($k_i = 1$) and it feels a periodic ratchet potential $U_1 \equiv U(x_i, 1)$ similar to the one depicted in Fig. 3.1a. Each motor switches its state independently and it follows its particular kinetics. Since KIF1A carries soft cargos, motors are not fixed in the cargo reference frame and they interact via a given potential $W(\xi)$. Finally, F is the tangential load originated by the cargo. This force is applied only to the foremost motor which conveys the load to the rest. This non-equal loading has already been shown as the main reason for the appearance of cooperativity in the system [Brugués and Casademunt, 2009, Orlandi et al., 2010].

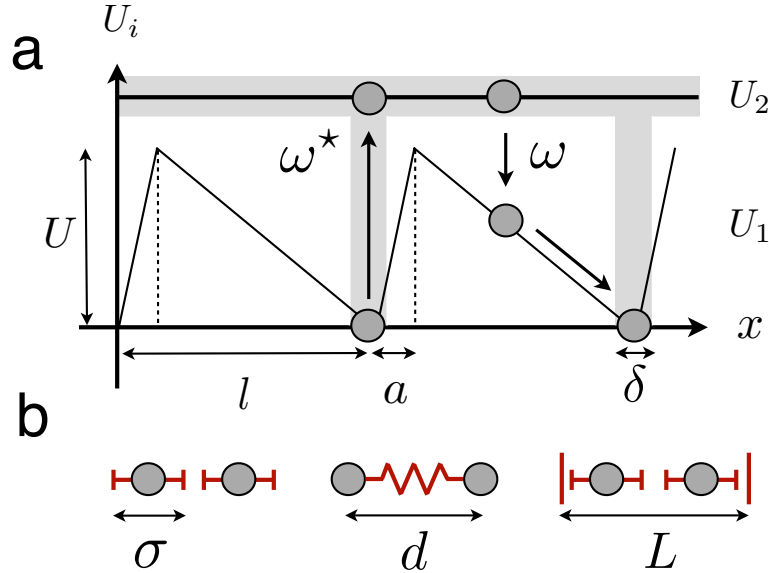


Fig. 3.1 Description of the model. a) Two-state ratchet model for monomeric KIF1A. Motors switch stochastically between the states $k = 1, 2$ with potentials U_1 and U_2 respectively. Excitations are localized in regions of size δ around the minima of U_1 whereas decays are delocalized. The average excitation and decay rates read ω^* and ω respectively. Gray zones depict where transitions are allowed. b) Main motor-motor interactions: hard-core repulsion (left), rigid coupling (center) and raft-induced interactions (right) (see Sections 3.1.1 and 3.1.2). Small circles indicate the motor position and the red drawings indicate the type of interaction.

Next we need to describe the state kinetics. We define the average excitation rate ω^* , which depends essentially on the time required to capture an ATP molecule. We assume that the molecule is allowed to get excited only in a small neighborhood of size δ around the potential minima, being $\delta \ll l$. This condition follows from the fact that the motor is not likely to capture an ATP molecule during the power stroke (i.e. sliding down the sawtooth potential). On the other hand, we assume that thermal decays are delocalized, with an average decay rate ω (Fig. 3.1a). Motors get excited and decay stochastically, with exponential distributed times having average values $1/\omega^*$, $1/\omega$ respectively.

The presence of an external load F applied to the foremost motor drives the spontaneous formation of a fluctuating cluster. When the steady state is reached, the velocity of a N -motor cluster coincides with that of the first motor $V_N(F) = \langle \dot{x}_1 \rangle$. On the other hand, the collective stall force is usually defined as the necessary force to stall the cluster. However, it is quite common that for large numbers of motors the collective VF curves fall to very small values at forces significantly smaller than the stall force, implying the existence of an apparent stall force that scales differently with N respect to the actual stall force [Campàs et al., 2006]. In such cases it is useful and convenient to define an apparent stall force F_s by a condition of the type $V_N(F_s) = V_c$ where V_c is a small cut-off velocity. Hereinafter we will use the term ‘stall force’ and the notation $F_s(N)$ to denote the apparent stall force of a N -motor cluster, unless otherwise indicated. Finally, the collective efficiency $\eta_N(F)$ in the biological context is usually defined as [Parmeggiani et al., 1999]:

$$\eta_N(F) = \frac{FV_N(F)}{r_N(F)\Delta\mu} \quad (3.1)$$

where $r_N(F)$ is the collective chemical reaction rate dependent on the applied force. In our case the calculation of this rate equals the number of excitations per unit time for all the motors and $\Delta\mu$ corresponds to the chemical potential difference for ATP hydrolysis. Since we will work in far from equilibrium conditions (i.e.

$\Delta\mu \gg k_B T$) we neglect thermal activations.

Next we discuss the proper parameters to model a single-headed KIF1A motor *in vitro*. Table 3.1 shows the main selected parameters in our study. The most salient feature of single-headed KIF1A

Parameter	Value
MT periodicity	$l = 8 \text{ nm}$
Ratchet asymmetry	$a = 1.6 \text{ nm}$
Diffusion coefficient	$D = 20 \text{ nm}^2/\text{ms}$
Excitation rate	$\omega^* \leq 250 \text{ s}^{-1}$
Decay rate	$\omega = 250 \text{ s}^{-1}$
Ratchet potential maximum	$U = 20k_B T$

Table 3.1 Realistic values of the main parameters for the modeling of monomeric KIF1A motors *in vitro*. The values are extracted mainly from [Okada and Hirokawa, 1999, Nishinari et al., 2005, Okada et al., 2003].

is that the ability to advance along the MT relies on thermal diffusion in the weakly bound state. *In vitro* experiments have reported diffusion coefficients in the range of 20 to 40 nm^2/ms which involve motor excursions much larger than the ratchet periodicity of 8 nm [Okada and Hirokawa, 1999, Okada et al., 2003]. We will consider 20 nm^2/ms as a reasonable value. The characteristic rates ω and ω^* are found in the literature within the range of hundreds of Hz. Whereas ω is a parameter coming from the affinity between the motor domain and the MT, ω^* depends on ATP concentration in the solvent. Experimental data suggest that $\omega^* \leq 250 \text{ s}^{-1}$ and $\omega \simeq 250 \text{ s}^{-1}$ [Nishinari et al., 2005, Okada and Hirokawa, 1999, Okada et al., 2003]. The asymmetry a of the ratchet is an adjustable parameter for the model which is difficult to grasp from experiments. The asymmetry reduces the overall velocity of the system and it can lead to non-trivial effects specially in the limit of weak noise [Orlandi et al., 2010]. For our purposes, we adjust this parameter to 20 % of the periodicity length. Finally, the motor size σ is carefully chosen to avoid possible commensurability effects [Brugués and Casademunt, 2009, Orlandi et al., 2010]. In Section

3.1.2.3 we will study in detail the implications of this parameter in the study of the collective stall force of the system.

3.1.1 *Hard-core repulsive interactions*

To study the dynamics of N interacting motors, we first consider hard-core repulsion between them. For practical reasons we use a truncated Lennard-Jones potential:

$$W_{HC}(\xi) = 4\epsilon \left[\left(\frac{\sigma}{\xi} \right)^{12} - \left(\frac{\sigma}{\xi} \right)^6 \right] \quad (3.2)$$

for $\xi < 2^{1/6}\sigma$ and zero otherwise, where ϵ is taken large enough to ensure that the interaction is effectively hard-core for $\xi < \sigma$.

3.1.1.1 The dwell time effect

Excitations of motors are localized in regions of size $\delta \ll l$ centered in the minima of the ratchet potential. Once a motor enters this region, it waits a certain amount of time given by an exponential dwell time distribution with average dwell time $1/\omega^*$. We define $\beta \equiv \omega/\omega^*$ so that the previous studies in Refs. [Brugués and Casademunt, 2009, Orlandi et al., 2010] with negligible dwell time correspond to the case $\beta = 0$. In a first approximation, we will consider that once the motor enters the region δ it stays in the minimum of the ratchet without fluctuating and hence, it cannot escape from the region by thermal fluctuations. This condition will be loosened and further discussed. In Fig. 3.2a we show the velocity-force (VF) relationship for $N = 1, 2$. KIF1A velocity at zero load is $V_1 = 0.15 \mu\text{m/s}$ for $\beta = 2.5$ and the stall force is $\simeq 0.1 \text{ pN}$, consistently with experimental values [Okada and Hirokawa, 1999]. An analytical expression for the VF curve of a single KIF1A motor is possible in the limit of large noise strength (see Appendix A). Upon the addition of a second motor, we find a remarkable enhancement of the VF curve with a consequent increase on the stall force of the cluster. If the dwell time is set to zero ($\beta = 0$), the naive extensive scaling $F_s(N) = NF_s(1)$ is

approximately correct, consistently with the validity of the mean-field (MF) description discussed in Ref. [Orlandi et al., 2010] for sufficiently large diffusion (Fig. 3.2a, inset). However, for $\beta \neq 0$, we find that $F_s(2)$ may be up to three times larger than $F_s(1)$ (Fig. 3.2a). The stall force of the cluster grows with β until saturation while the velocity at zero load rapidly decreases (Fig. 3.2b). The reason for the enhancement of the stall force can be explained in simple terms by considering two interacting motors.

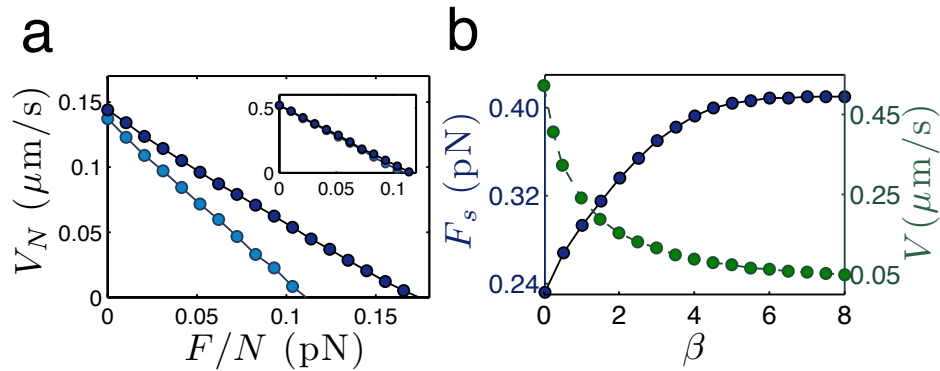


Fig. 3.2 a) VF curves for $N = 1$ (light blue) and $N = 2$ (dark blue) for $\beta = 2.5$. Inset: Same curves for $\beta = 0$ showing the mean-field behavior. b) Stall force and velocity at zero load for $N = 2$ as a function of β . $U = 20k_B T$, $D = 20 \text{ nm}^2/\text{ms}$, $\omega = 250 \text{ s}^{-1}$, $\sigma/l = 0.512$, $\delta/l = 0.02$, $a/l = 0.2$.

Let us consider the configuration in Fig. 3.3a, which was first discussed in [Brugués and Casademunt, 2009]. Initially, the motor in the back decays and slides over the potential pushing the foremost motor to the next period of the MT. This mechanism is sensitive to the external force since both motors can drift backwards when they are found in the initial configuration and holds only for $F \leq 2F_s(1)$. Therefore, it cannot be responsible for the stall force enhancement. Moreover, the strength of this mechanism is proportional to the ATP concentration in the solvent since the initial state requires the two motors to be found in state $k = 2$. Consequently, when β increases the mechanism loses strength, in contradiction to the curve in Fig. 3.2b. We shall call this mechanism a “down-push”. Now let us focus on the mechanism initiated from the configuration in Fig. 3.3b. We notice that this configuration is only possible if

$\beta \neq 0$ since the two motors are found together in state $k = 1$. The leading one is waiting for ATP, while the second one is blocked on the ratchet slope. Once the leading motor is excited, the second motor pushes the foremost in the same way as before. We shall call this mechanism an “up-push”. However, in this case the initial configuration remains unaffected for small forces $F \sim k_B T l / l_D^2$, where $l_D = \sqrt{2D/\omega}$ and the ‘up-push’ mechanism is able to work for $F > 2F_s(1)$. Furthermore, this mechanism is ATP dependent and its strength saturates for very low concentrations, as shown in Fig. 3.2b. The same results will be derived more precisely using a lattice model in Section 3.2.

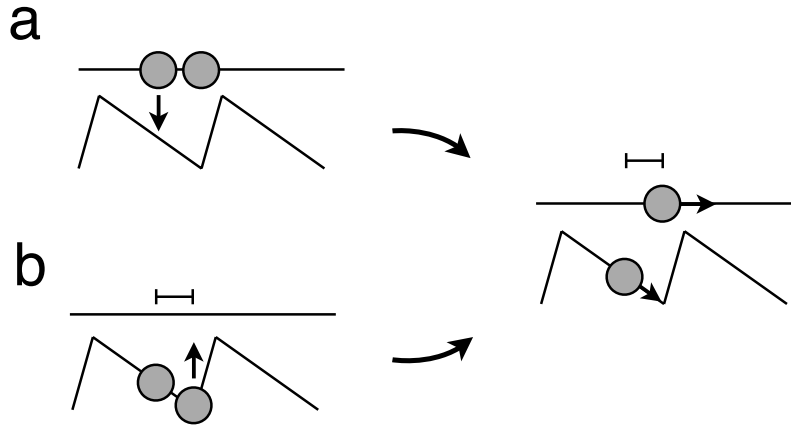


Fig. 3.3 Schematic description of the two cooperative mechanisms for the case of hard-core repulsion. (a) ‘Down-push’ mechanism: Initially, the motor in the back decays and slides down the potential pushing the foremost motor to the next site. (b) ‘Up-push’ mechanism: The leading motor is waiting for an ATP molecule while the second one is blocked in the ratchet slope. Once the leading motor is excited, the second motor pushes the foremost like in mechanism (a). The segment indicates that motors are found in contact.

3.1.1.2 Staircase-shaped VF curves for large N

Next we study the VF relationship for an arbitrary number of motors. In Fig. 3.4 we find a dramatic enhancement of the force at finite non-negligible velocities as we increase N . Although the velocity at zero load is the same for different N , the stall force is largely increased. We also note a remarkable complex shape of the

curves, which resemble a staircase. This effect is a consequence of the inhomogeneous motor density distribution in the cluster and the particular high noise intensity in the system. For relatively low forces, the external force is conveyed only to a reduced fraction of “active” motors in the center of the cluster (see Section 3.1.1.4), while those in the rear behave much more diffusively and remain loosely bound to the active group (Fig. 3.4b). The successive plateaus correspond to the recruitment of new motors by the active group. Indeed, as the force is increased, the new motor interacts more often with the active group and thus becomes progressively more cooperative. This partially compensates the decrease of velocity for a certain range of forces. This phenomenon becomes ineffective whenever the force reaches a multiple of $\sim U/l$, which is the typical ratchet force. At this point, both cooperative mechanisms in Fig. 3.3 fail and motors can be dragged back over the ratchet slope. Therefore, each plateau in Fig. 3.4a can be identified as the recruitment of a new motor by the active part of the cluster. For instance, for $N = 5$ the first plateau corresponds to typically three active motors and the second plateau to four active motors, as shown in Fig. 3.4b. This mechanism also persists for backward movement until the recruitment of the totality of motors (see Section 3.1.1.3, Fig. 3.6, inset).

In Fig. 3.5, we study in detail the scaling of F_s with N for different possible values of β (circles) and also in the case of allowing fluctuations of the motors in the ratchet minima (dashed curve). We notice a steep enhancement for low N and saturation of the stall force for large N . The presence of noise in the minima changes effectively the average excitation rate to an effective average rate ω'^* . Once a motor is drifted out of the region δ by thermal fluctuations, it soon falls back in the minimum again, thus waiting again for ATP. Consequently, the addition of noise in the ratchet minima corresponds to a smaller effective excitation rate $\omega'^* < \omega^*$ (or equivalently $\beta' > \beta$). In Fig. 3.5 (inset) we observe the saturation of the VF curves and the occurrence of long tails for large N which makes convenient to define the apparent stall force as discussed above. We also notice that for small forces ($F < 10$ pN), the velocity for $N = 10, 15, 20$ is slightly greater than $V_1(0)$. This effect is a numerical artifact, due to the existence of very long

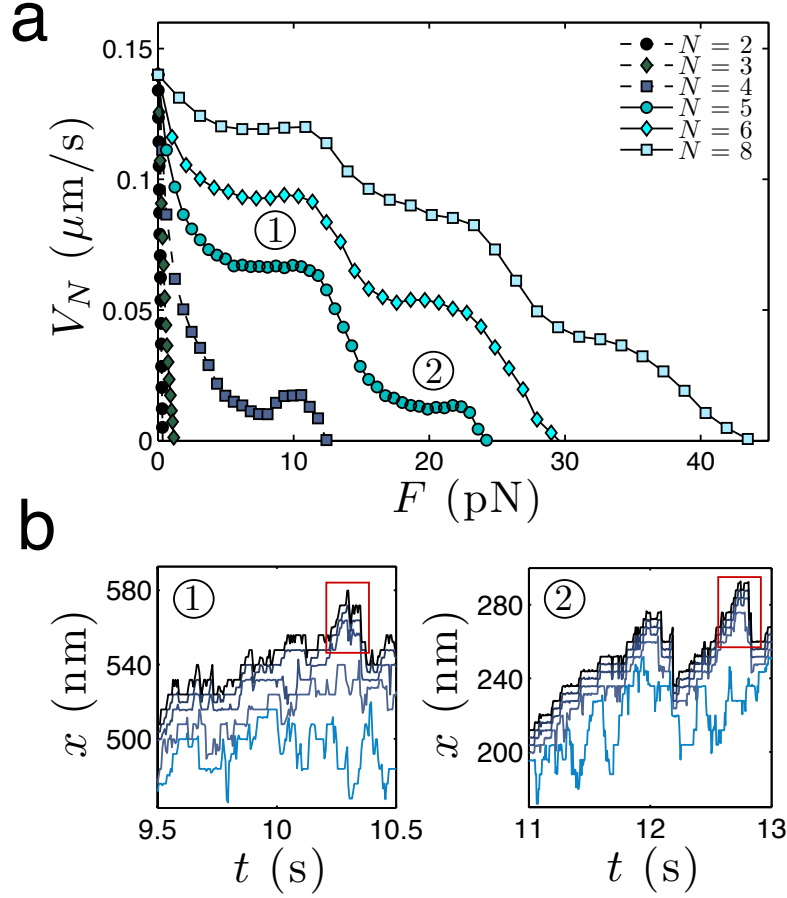


Fig. 3.4 a) VF curves for different N . $\beta = 2.5$, $\sigma/l = 0.521$ and $\delta/l = 0.02$. The collective stall force grows rapidly with N in a nonlinear fashion. Moreover, the high diffusive environment induces a staircase shape of the VF curves. Data correspond to the case where motors cannot fluctuate in ratchet minima. b) Typical motor trajectories for cases 1 ($F = 8$ pN) and 2 ($F = 20$ pN) in panel a). Red squares show the active motors in the front, which are generally three in case 1 and four in case 2.

transients for large clusters under the action of small forces which bias the statistics to larger velocities. A simple argument shows that this effect cannot be present for purely repulsive potentials. In fact, let us consider a cluster of N motors under an external force F which moves at $V_N(F) > V_1(0)$. The last motor will only be slowed down by the motors in the front since the interaction is repulsive, thus the last motor will have a velocity smaller than $V_1(0)$ and it will fall behind the cluster. By repeating the same

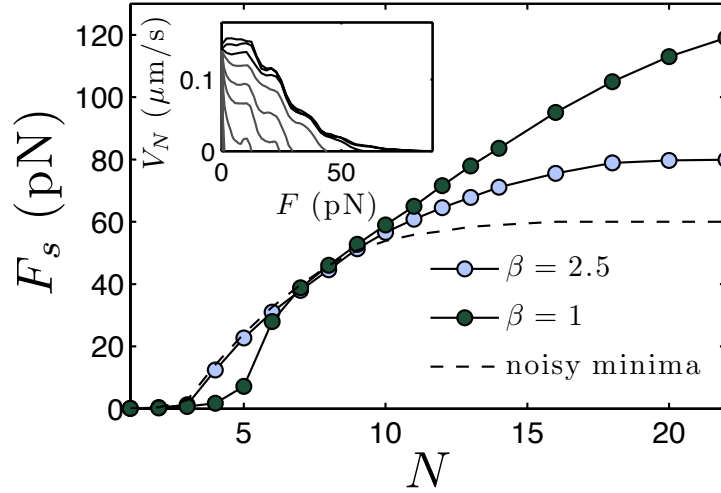


Fig. 3.5 F_s vs N for $\beta = 1, 2.5$ (circles) and for noise in the minima ($\beta = 2.5$ and $\delta/l = 0.02$, dashed line). We differentiate a steep enhancement for small clusters and a saturation regime for large clusters assuming a cut-off velocity $V_c \simeq 10^{-4} \mu\text{m/s}$. Inset: VF curves for $N = 2 - 8$ (grey) and $N = 10, 15, 20$ (black) for $\beta = 2.5$. We notice the long tails near stall force conditions.

reasoning, the cluster will lose all motors except the leading one which will move at $V_1(0)$, hence $V_1(0) \geq V_N(F)$, $\forall N, F > 0$ for the case of a repulsive interaction.

3.1.1.3 Convergence to mean-field

We have shown that the cooperative action of motor clusters outperforms the simple addition of individual forces, i.e. the extensive scaling $V_N(F) = V_1(F/N)$ or $F_N(V) = NF_1(V)$. This scaling is the one predicted by a mean-field ansatz, which assumes that correlations between positional and internal degrees of freedom of the motors are neglected. In Ref. [Orlandi et al., 2010] it was established that the extensive scaling was obtained in the limits of large noise intensity or long-ranged repulsive interaction between motors. For the case of hard-core repulsion and typical noise in-

tensity values for KIF1A, the latter arguments implied that the mean-field ansatz was essentially correct in the case $\beta = 0$. We have thus shown that $\beta \neq 0$ is responsible for a stronger violation of the mean-field ansatz in the constructive direction, that is for further enhancement of cooperativity. Here, we explicitly show how the introduction of a soft, long-ranged repulsion interaction restores the mean-field scaling. To this aim we add to the hard-core part W_{HC} , an exponential repulsive tail of the form:

$$W_L(\xi) = \kappa \Lambda e^{-\xi/\Lambda} \quad (3.3)$$

where κ measures the strength of the interaction and Λ denotes its range. In Fig. 3.6 we study the loss of cooperativity for the $N = 5$ curve of Fig. 3.4 as Λ is increased. We notice that the stall

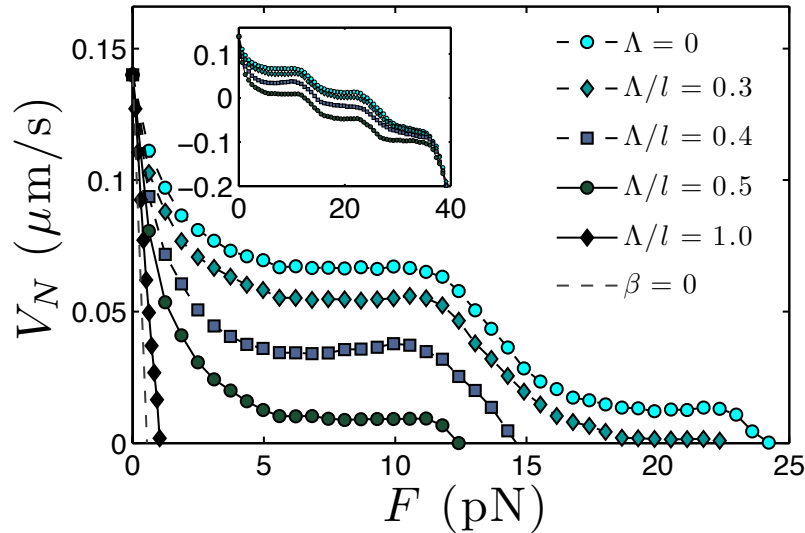


Fig. 3.6 Convergence to mean-field in the presence of long-ranged repulsion with strength $\kappa l/k_B T = 5$ and different Λ . The curve studied corresponds to the case $N = 5$ in Fig. 3.4. Symbols are calculated for $\beta = 2.5$ and the dashed line corresponds to the case $\beta = 0$. Inset: VF curves including negative velocities. The staircase behaviour persists during backward motion until the recruiting of the totality of motors.

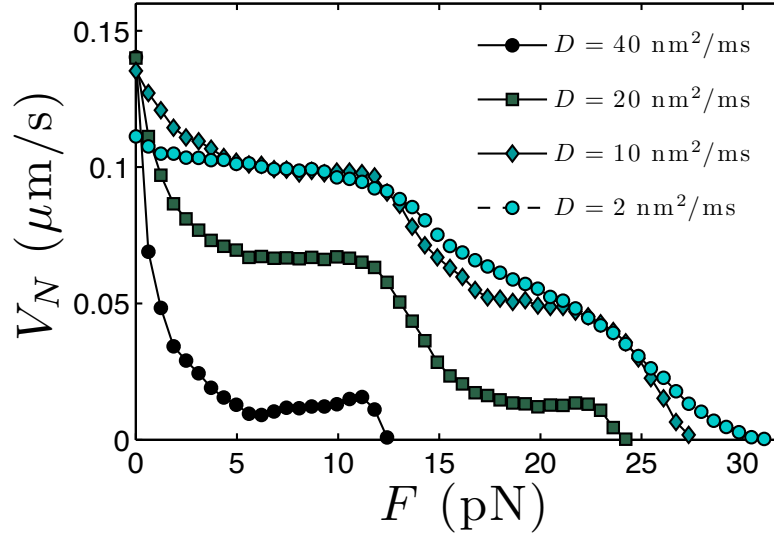


Fig. 3.7 VF curves for different noise intensities. The curve studied corresponds to the case $N = 5$ in Fig. 3.4. As diffusion strength is lowered, the staircase behaviour smooths out.

force decreases for increasing Λ and the cooperative mechanism induced by the finite dwell time disappears for sufficiently large Λ , converging to the case $\beta = 0$. Interestingly, the staircase behavior persists for negative velocities and it is not much sensitive to the long-range interaction for $\Lambda/l < 0.5$ (Fig. 3.6, inset). Now we study the effect of noise strength in the VF curves. Fig. 3.7 shows the same $N = 5$ curve for four different noise intensities. We notice that oscillations smooth out for low noise intensity. As diffusion is lowered, the external force is able to cluster motors more easily and the recruitment effect is not so pronounced. Hence, sufficiently high diffusivity is required, together with $\beta \neq 0$, to produce staircase shaped VF curves.

3.1.1.4 Cluster force distribution

Each motor in the cluster feels “active” and “passive” forces. Active forces are those forces driven by ATP hydrolysis which

allow motors to perform their power stroke. In our context, the power stroke corresponds to the sliding over the ratchet potential when motors decay. Therefore, the average active force for the i -th motor reads $F_i^{act} = -\langle U'(x_i, k_i) \rangle$. On the other hand, passive forces correspond to the forces motors feel due to the transmission of the external force F via the potential W , therefore the average passive force the i -th motor feels reads $F_i^{pas} = -\langle \sum_{k \neq i} W(x_i - x_k) \rangle - F\delta_{1i}$. Hence, computing the ensemble average in Eq. 2.3 we have:

$$\lambda \langle \dot{x}_i \rangle = F_i^{act} + F_i^{pas} \quad (3.4)$$

Since the average velocity of each motor in the cluster is the same,

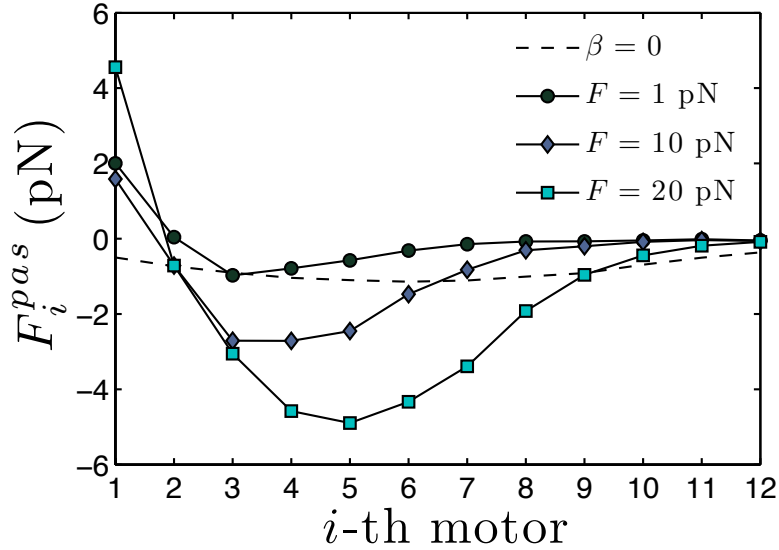


Fig. 3.8 Passive force distribution F_i^{pas} for $N = 12$, $\beta = 1$ with different forces (symbols) and for $\beta = 0$, $F = 10$ pN (dashed line). The force distribution in the cluster shows a pronounced dip which reflects an enhanced activity of the central part of the cluster in the presence of dwell time.

the last equation tells us that the sum of active and passive forces for each motor is constant in average. In Fig. 3.8, we measure passive forces F_i^{pas} inside a $N = 12$ cluster for different external forces. By virtue of Eq. 3.4, the complementary active forces

can be obtained by subtraction of the passive ones from the constant term. For $\beta = 0$, the force distribution among motors is fairly homogeneous for our choice of noise intensity and force. However, when $\beta \neq 0$, the force is much more unevenly distributed. Interestingly, the first motor is not active, but is passively pushed by a central group of motors which mostly originate the active forces. This central group of active motors grows as F is increased. The last motors rarely interact with the main cluster and thus they have a minor contribution. The emergence of a nontrivial structure in the internal distribution of forces is a signature of cooperativity in this system and was already noted in Ref. [Orlandi et al., 2010] for $\beta = 0$. However, in this case the effect is still present for large noise intensities due to the addition of dwell time.

3.1.1.5 Coordinated motion of large clusters

In the case of large clusters under heavy loads, the cluster adopts a characteristic stepwise coordinated mode, already reported in Ref. [Orlandi et al., 2010] for $\beta = 0$. In this configuration, the cluster waits for some collective dwell time before performing a step as a whole, with an almost synchronous stepping of all motors, superposed to the small fluctuations of the individual motors. Steps are totally asymmetric i.e. no backward stepping occurs. The synchronous displacement is clearer for the leading motors than for the ones in the rear. Fig. 3.9 shows the logarithm of the step size distribution $P(\Delta x)$ measured at each $\Delta t \sim 1$ ms for the leading motor of a $N = 40$ cluster with an external force $F = 30$ pN. The large central peak reflects the small fluctuations of the motor. The small peak around 4 nm corresponds to the synchronous displacement, which for our choice of σ is roughly half the period of the ratchet. We may identify a collective step as a displacement $\Delta x \geq 2$ nm of the first motor, so that we can obtain the time distribution $P(\tau_c)$ for the collective dwell time τ_c . This is shown in Fig. 3.9 (inset). The distribution appears to be very close to exponential and has a mean collective dwell time $\langle \tau_c \rangle \simeq 60$ ms, implying a rather small velocity of $\simeq 70$ nm/s. This mode of transport could be relevant to overcome very large forces

in the presence of obstacles or traffic jams, by the recruitment of a sufficient number of motors.

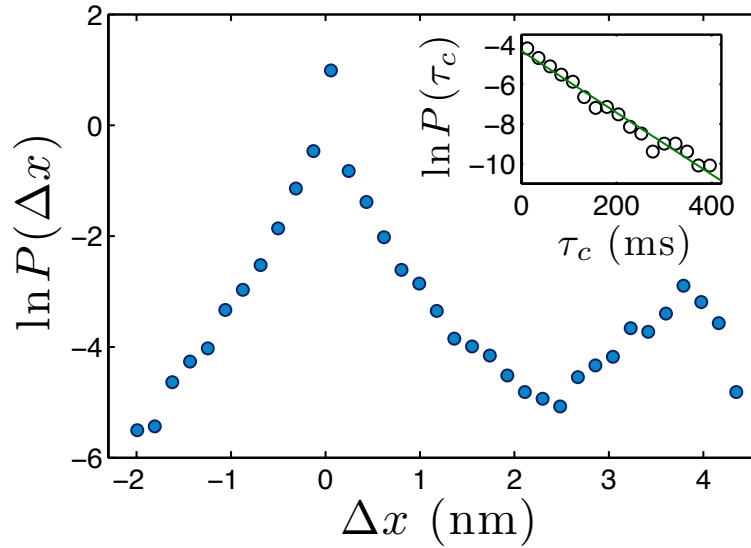


Fig. 3.9 Logarithm of the step size distribution $P(\Delta x)$ measured at each time step for the leading motor of a $N = 40$ cluster with a load of $F = 30$ pN. Inset: Logarithm of the collective dwell time distribution $P(\tau_c)$. The green line shows a good fit to an exponential distribution. Measures are taken at each time elapsed between steps $\Delta x \geq 2$ nm, which from $P(\Delta x)$ are assumed to contribute to a net movement of the cluster.

3.1.1.6 Efficiency and randomness

To further characterize the collective properties of motor clusters, we briefly discuss their collective efficiency and randomness. In Fig. 3.10 we show the collective efficiency defined in Eq. 3.1 normalized to the maximum value for a single motor. A remarkable increase on the efficiency was already reported for the case of no dwell time in Refs. [Brugués and Casademunt, 2009, Orlandi et al., 2010], where clusters of 10 motors increased the single-motor efficiency by a factor 10. In the presence of dwell time we find that the maximum efficiency for similar clusters may increase up to a factor 100 that of a single motor. As shown in

Fig. 3.10, the efficiency in our case also exhibits complex behavior, as a consequence of the staircase shaped VF curves. If we take $\Delta\mu \simeq 20 k_B T$ as a reasonable value [Parmeggiani et al., 1999], the maximum efficiency of a single motor is $\eta_1^{max} \sim 10^{-4}$. The low value is clearly associated to the diffusive part of the motor cycle, which introduces an important number of backward events. In this sense, the presence of other motors contributes to further rectify possible diffusive backward excursions. Notice that the efficiency of a noise-driven motor such as KIF1A is necessarily very small compared to the case of dimeric KIF5, exploiting the ‘hand-over-hand’ mechanism. Accordingly, the low efficiency of the motor is also associated to a high randomness. This parameter is defined as the ratio of the diffusive versus ballistic displacements of the motor, at the scale of the track periodicity l [Kolomeisky and Fisher, 2007]. We find that the collective randomness decreases very fast with the

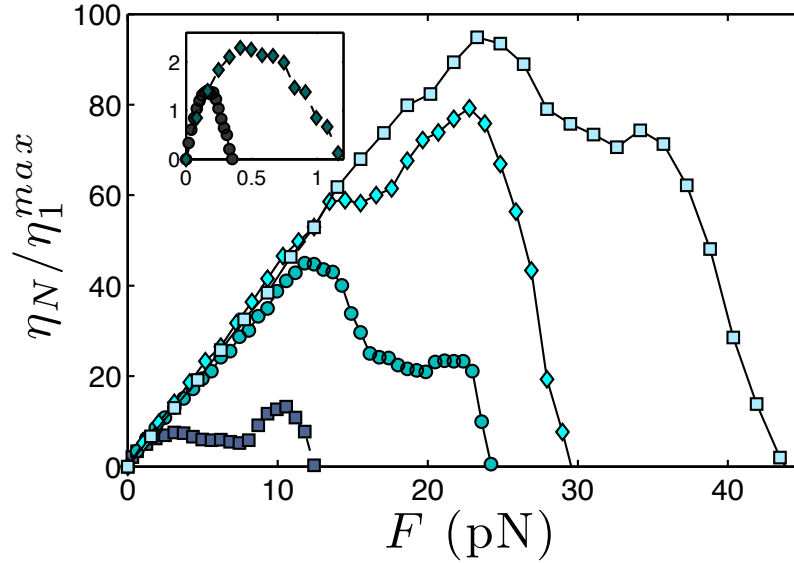


Fig. 3.10 Collective efficiency normalized to the maximum value for $N = 1$. The addition of motors in the cluster greatly enhances the efficiency of the system. Inset: Efficiencies for $N = 2$ and $N = 3$. The different parameter values and symbols are the same as in Fig. 3.4.

addition of motors. For the stepwise coordinated mode discussed above, the randomness parameter remains close to 1, that is, the case of a totally biased random walker performing unit steps with an exponentially distributed time.

3.1.2 *Confining interactions*

3.1.2.1 **Rigidly coupled motors**

Pure hard-core repulsion between motors appears to be a good description to account for excluded volume interactions in the transport of soft cargos, where motors move freely and motors are unequally loaded. However, the case of rigidly coupled motors separated by a fixed distance is also of important interest in the transport of rigid cargos and to other situations relevant for biotechnological applications, which can be designed using rigid assemblies of motors [Korten et al., 2010]. Following Ref. [Orlandi et al., 2010] to describe rigid interaction between motors we will use a harmonic potential $W_S(\xi) = \frac{1}{2}k(\xi - d)^2$, where d is the motor-motor distance. We define the dimensionless constant $\bar{k} \equiv k_B T / kl^2$ as a measure of the stiffness of the assembly. Therefore, the limit of rigid coupling will be $\bar{k} \ll 1$. As discussed in Ref. [Orlandi et al., 2010], non-trivial dynamic effects can happen when d and l are commensurable. Additionally, for the case $\beta \neq 0$, the strength of the binding interaction can produce a nonmonotonic behavior of the VF curves for a certain force range (Fig. 3.11, inset). In order to be able to compare our results to the case of non-bounded motors, we typically choose values of \bar{k} and d that minimize such commensurability effects in the rigid limit. In general we observe that velocities at a given force are typically larger than in the hard-core case. This effect is expected since rigid coupling not only enables pushing but also pulling of adjacent motors. The force enhancement due to the presence of dwell time is also found for rigid coupling. In Fig. 3.11 we show several VF curves for different numbers of motors. Note that for $\beta \neq 0$ the displacement of one motor is strongly conditioned to the motion of the rest. This means that a significant number of motors must be either in the weakly bound state, or sliding down the ratchet

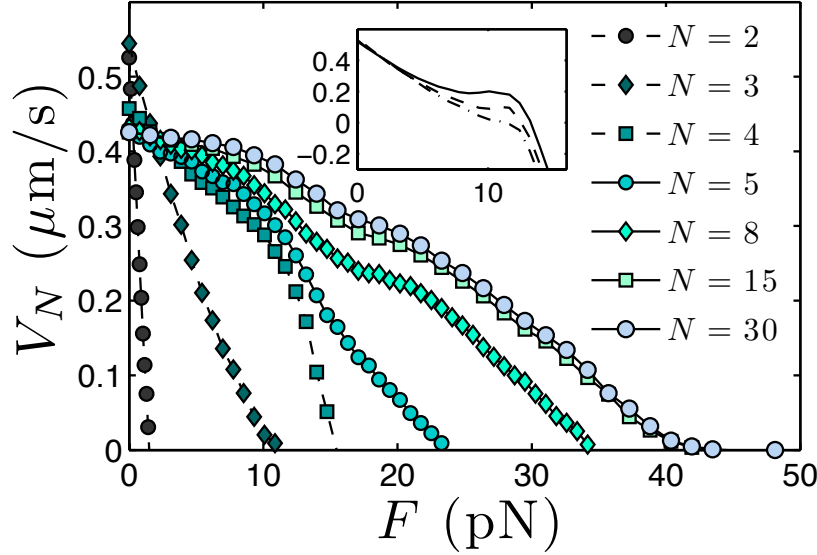


Fig. 3.11 VF curves for the case of rigid coupling. $d/l = 1.341$, $\beta = 1.25$ and $\bar{k} = 4 \cdot 10^{-3}$. Inset: $N = 3$ VF curve for $\bar{k} = 10^{-3}, 3 \cdot 10^{-3}, 4 \cdot 10^{-3}$ (ordered from more to less bumped).

potential. This fact implies an effectively larger dwell time which in turn implies a faster growth of the stall force with the number of motors. However, the stall force of the system saturates for $N > 15$ at $\simeq 35 - 40$ pN (Figs. 3.11 and 3.12). On the other hand, we notice that the velocity at null force $V_N(0)$ presents an overshoot for $N = 2, 3$ motors and stabilizes for $N \geq 5$ (Fig. 3.12, inset). This effect is due to the fact that the minimum number of consecutive motors over the lower ratchet slope needed to remove a motor from the minima must be greater than $\lfloor l/a - 1 \rfloor$ ¹ which in our case are 5 ($a/l = 0.2$). For the case $a = 0$, a given motor in the minima could not be removed by any number of motors and $V_N(0)$ would decay with N until vanishing, since the motion of the foremost motor is constrained to the dynamics of the rest.

¹ The floor function of a certain quantity x , $\lfloor x \rfloor$ is the largest integer not greater than x .

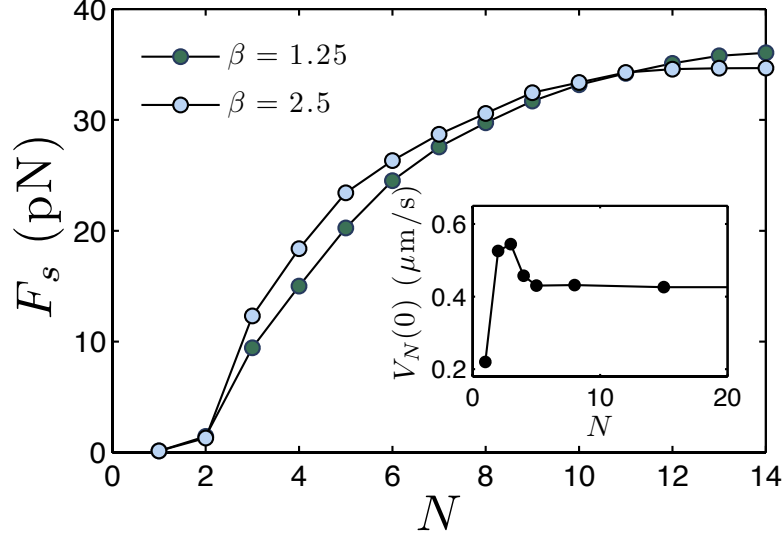


Fig. 3.12 F_s vs N for $\beta = 1.25, 2.5$, $\bar{k} = 5 \cdot 10^{-3}$ and $V_c \simeq 10^{-4} \mu\text{m/s}$. The stall force of the system saturates around 35 pN for $N \simeq 15$ motors. Inset: $V_N(0)$ vs N using the data in Fig. 3.11. We appreciate an overshoot on the velocity around $N = 3$ and a rapid stabilization as N increases.

3.1.2.2 Raft-induced interactions

Lipid rafts are membrane microdomains which float freely in the membrane bilayer. When groups of motors bind specifically to lipid raft domains in vesicles, their motion is constrained by the size of the microdomain [Klopfenstein et al., 2002]. In this section we incorporate such raft-induced confining interactions in our model motivated by the experiments in Ref. [Klopfenstein et al., 2002], where the liposome movement driven by the collective action of Unc104 motors (the analogous kinesin of KIF1A for *C. elegans*) showed a very steep dependence on phosphatidylinositol 4,5-biphosphate (PIP₂) concentration due to the formation of lipid rafts. Two different hypothesis were proposed to explain such phenomenon: dimerization of Unc104 motors or cooperativity between the monomeric form of the motors. The aim of this section is to re-

produce raft-like conditions and to study the velocity dependence on the parameters describing this effective interaction.

Let us consider a raft of length L which contains N motors of size σ . In order to confine the movement of motors, we will use a truncated Lennard-Jones potential which will depend on the distance between the first and last motor $\phi \equiv x_N - x_1 > 0$. Since motors can only move in a region $L - \sigma$, the potential reads:

$$W_R(\xi_r) = 4\epsilon \left[\left(\frac{\sigma}{\xi_r} \right)^{12} - \left(\frac{\sigma}{\xi_r} \right)^6 \right] \quad (3.5)$$

where $\xi_r \equiv L - \phi$ and the expression is only valid for $\phi > L - 2^{1/6}\sigma$ and is zero otherwise. This potential will be added to the hard-core part only for $i = 1, N$. We define the dimensionless density of the raft as $\rho \equiv N\sigma/L$. In Fig. 3.13 we study how VF curves change as a function of the raft motor density ρ for $N = 2$, varying L for a fixed motor size σ . The presence of raft-induced interactions confines the motion of the two motors and establishes a well defined mean motor distance as ρ increases.

The stall force is greatly enhanced similarly as in the hard-core and rigid coupling cases. Actually, in the limit $\rho \rightarrow 1$ the system converges to the rigid coupling case as expected. However, this convergence does not follow a simple monotonous growth but an irregular dependence on ρ (Fig. 3.13, inset). This dependence is difficult to interpret given the large number of length scales that could lead to commensurability effects with L , namely a , l , σ and $\langle \xi \rangle$. The velocity of the cluster already converges to the rigid coupling case around $\rho \simeq 0.6$; however, this property is missed for $N = 3$. For $N > 2$, the system shows an intermediate behaviour between hard-core repulsion and strong-coupling. Consequently, raft-like interactions can speed up the system eliciting velocities of $\sim 0.3 - 0.5 \mu\text{m/s}$ but these are still far from typical liposome velocities ($\sim 1 \mu\text{m/s}$) of Unc104 [Klopfenstein et al., 2002]. This suggests that the switching behavior of the liposome movement found in Ref. [Klopfenstein et al., 2002] is probably due to dimerization of Unc104 motors.

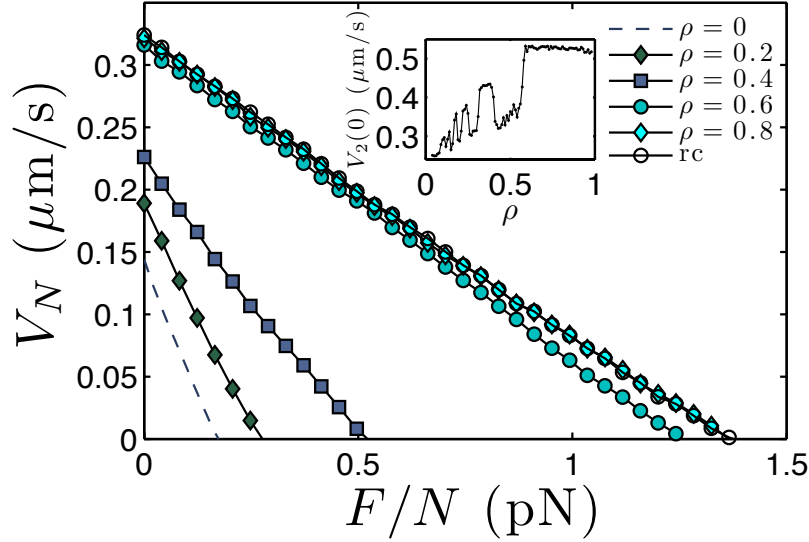


Fig. 3.13 VF curves for the case of $N = 2$ and raft-induced interactions with $\sigma/l = 0.341$, $\beta = 2.5$ and different raft density ρ . Empty circles denote the VF relationship for the same parameter values and rigid coupling interaction with $\bar{k} = 10^{-3}$. Inset: evolution of the velocity of the cluster at null force as a function of ρ for $\beta = 1.25$.

3.1.2.3 Transition between rigid coupling and hard-core repulsion

We have previously seen that both rigid and hard-core interactions produce a nonlinear enhancement on the stall force of the system. In this section, we explore the transition between these two regimes by changing the parameter \bar{k} in the limit of large N . In order for the transition to be smooth, we use $W_{HC-S}(\xi) = W_{HC}(\xi) + W_S(\xi)$ by setting a motor-motor distance d and a motor size σ . In Fig. 3.14 we study the dependence of $F_s(15)$ on \bar{k} for three values of the motor size σ . The strength of motor fluctuations $\langle(\xi - d)^2\rangle$ determines the appearance of commensurability effects. Two main factors change the strength of these fluctuations: the rigidity of the interaction \bar{k} and the external load F . For very strong spring constants motors barely fluctuate and commensurability effects are predominant, thus the system is very sensitive to σ and we find strong resonances on the stall force. On the other hand, as we

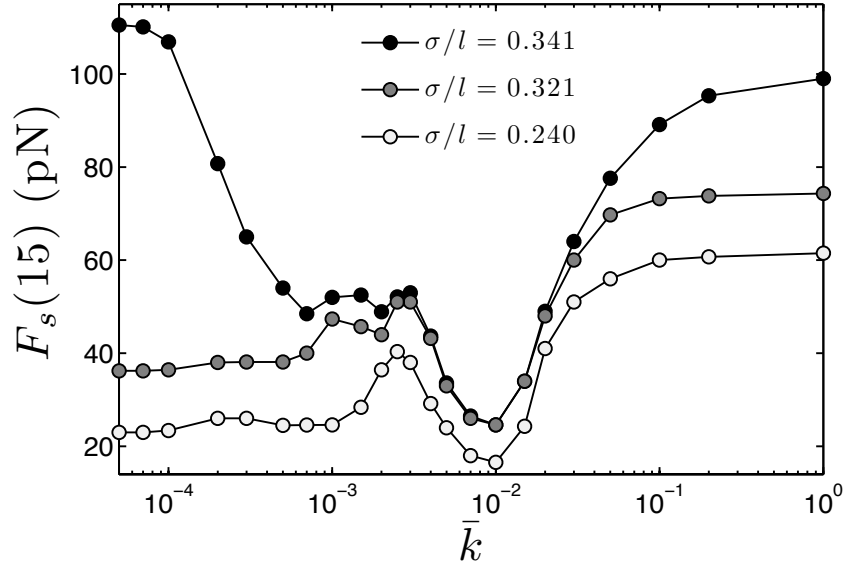


Fig. 3.14 Stall force for $N = 15$ vs \bar{k} showing the transition between rigid coupling and hard-core interaction for different motor sizes σ and $\beta = 1.25$. A pronounced dip appears for a certain \bar{k} range in which the stall force is considerably reduced.

approach the hard-core limit, fluctuations are still small since we are found near stall conditions. In this case, the system resembles the rigid case except for some long excursions of the motors in the rear of the cluster. Thus, motor size effects are present both in the rigid and hard-core limits near stall conditions, however in the hard-core limit resonances are less pronounced. We notice the presence of a pronounced dip around $\bar{k} \simeq 10^{-2}$. Hence, a weak binding interaction between motors leads to a decrease of the collective stall force in the large N limit. This can be explained in simple terms. Let us consider a large cluster of weakly bound motors in stall conditions, such that the cluster is compressed in the front and only the last motors can fluctuate significantly. Suppose that a fluctuation drives the last motor one step backwards and the binding interaction is sufficiently strong that the cluster feels a restoring force which adds to the external force. Consequently, fluctuations in the rear of the cluster will tend to destabilize it. For this situation to occur, the energy of the interaction must be

comparable to the energy scale of the ratchet for $\xi \sim l$, that is $\bar{k}_c \sim k_B T/U \sim 10^{-2}$. However, if motors do not feel any binding interaction, fluctuations do not affect the cluster.

3.1.3 Conclusions

We have provided a thorough numerical study of the collective action of single-headed KIF1A motors based on Brownian dynamics. We have predicted a dramatic improvement of the collective performance of these motors for tasks associated to the transport of membrane-bound cargos. The results rely on a two-state noise-driven model that successfully explains the motion of a single motor.

The presence of finite dwell time in the system ($\beta \neq 0$) reveals a great enhancement of the collective force generation of motors. This effect is able to produce a two-order of magnitude gain on the collective efficiency up to values of $\sim 10^{-2}$. The collective stall force at a given velocity grows faster than proportional to N up to around 5 KIF1A motors. This behaviour is remarkably different for KIF5, whose collective forces are weakly dependent on the number of motors in this regime [Furuta et al., 2013, Rai et al., 2013]. For $N \sim 5-10$ the force scaling of KIF1A remains roughly proportional to the number of motors, a property that is missed by conventional kinesin according to lattice models [Campàs et al., 2006]. Finally, for large N the total force produced by the motor ensemble eventually saturates.

A salient feature of our results for relatively small motor clusters is that the collective VF curves have staircase shapes, that effectively count the number of active motors in the cluster. This could potentially be used to infer the number of motors in a cluster by directly measuring forces. From a biological point of view, our results reinforce the hypothesis that the specificity of KIF1A to axonal vesicular trafficking is due to its unique adaptation to cooperative force generation. From a fundamental physics point of view, we have shown that Brownian motors based on two-state

ratchets with independent switching and under unequal loading are remarkably adapted to cooperative force generation. Within this spirit, rectification mechanisms and spatial confinement in ratchet systems may be deeply related to the emergence of cooperativity in nanoscopic transport [Malgaretti et al., 2013]. Additionally, hydrodynamic coupling in thermal ratchet motion might also play an important role [Malgaretti et al., 2012].

So far, we have conceptually introduced two cooperative mechanisms, namely the ‘up-push’ and ‘down-push’ mechanisms. In order to get a clear understanding of these mechanisms it is convenient to switch to a lattice model approach, grounded on the Langevin formulation, which allows analytical treatment in some limits.

3.2 Lattice model for KIF1A dynamics

Asymmetric simple exclusion process (ASEP) models have been extensively used to study non-equilibrium phase transitions, where particles jump in a lattice [Spitzer, 1970, Krug, 1991, Evans, 1996]. In the context of intracellular transport, molecular motors are treated as particles which jump on a lattice, where each lattice site corresponds to a binding site for the motor. These models are useful to study large numbers of motors which interact via simple exclusion interactions [Lipowsky et al., 2001, Parmeggiani et al., 2003]. We understand by simple exclusion interactions the fact that a motor can not jump to a lattice site which is already occupied by another motor. The latter assumption is reasonable provided that motors are found always in a strongly bound conformation to the filament. The underlying reason is the lack of force transmission. This type of interaction seems to apply to conventional kinesin, which walks following a ‘hand-over-hand’ mechanism [Rai et al., 2013]. Dimeric kinesin moves the two heads in a highly coordinated manner such that one head is always strongly bound to the filament. Consequently, this fact difficult any kind of force transmission between neighbouring dimeric kinesins. However, other types of molecular motors like KIF1A or cytoplasmatic dynein, seem to be able to transfer force from one motor to the other

[Okada et al., 2003, Rai et al., 2013]. One could think that the power stroke of a motor can be transmitted to a neighbouring motor, thus forcing the second one to move. This may be possible if the second motor is diffusing near the filament e.g. in a weakly bound state. In the latter case, motors may be able to cooperate in teams and a simple excluded volume process is not appropriate to describe their movement.

In this section, we will introduce an appropriate generalization of the ASEP approach in order to gain further insights on the cooperative effects shown in Section 3.1 for the collective dynamics of KIF1A motors. From the Langevin formulation, it is clear that the key elements that enhance cooperativity beyond mean-field involve simultaneous motion of different motors, namely, when a motor sliding down the ratchet slope in state 1 pushes a motor in state 2 (assuming $a < \sigma < l - a$) (see Fig. 3.3). Furthermore, simulations of many motors under large forces give rise to very packed motor clusters which advance with a high degree of coordination as shown in Section 3.1.1.5. These observations suggest that an appropriate discrete model should incorporate transitions of blocks of adjacent motors, with rules that should be grounded on the Langevin formulation. Next, we introduce such a model for the simplest and most illuminating case $N = 2$. An extension of the model to an arbitrary number of motors can be done with qualitatively similar results to the Langevin model; however, in the latter case there exist some complications in the way multi-particle transition rates are chosen which we will briefly discuss in Section 3.2.1.3.

Finally, so far we have studied the motion of KIF1A along a single protofilament on the microtubule lattice; however, the weakly bound state of KIF1A may enable lane changing. Motivated by the experiments in Chapter 4 we model the motion of a single KIF1A motor in a two-dimensional lattice.

3.2.1 Dynamics on a 1D lattice

We consider a 1D lattice with each site associated to a period of the ratchet potential of length l and asymmetry a , with two possible states. Single-motor transitions are shown in Fig. 3.15a,b: in state 2, a motor labeled μ can undergo biased diffusion along the lattice with rates u_μ, v_μ . Since the external load is applied only to the leading motor, we will have:

$$u_\mu = \frac{d}{2}(1 - \delta_{1\mu}f); \quad v_\mu = \frac{d}{2}(1 + \delta_{1\mu}f) \quad (3.6)$$

where $f \equiv Fl/k_B T$ and $d \equiv k_B T/\lambda^2$ is the diffusion rate. On the other hand, the motor can decay from state 2 to state 1 either at the same site, or into the next one on the right (Fig. 3.15b, upper panel), reflecting the distinct probability of falling into the red or green regions of the ratchet potential (Fig. 3.15a), with respective rates q_μ and p_μ . Consistently with the Langevin picture we take:

$$p_\mu \equiv p = \frac{\omega}{2}(1 - 2\bar{a}); \quad q_\mu \equiv q = \frac{\omega}{2}(1 + 2\bar{a}) \quad (3.7)$$

where $\bar{a} \equiv a/l$. Finally, we assume for simplicity that the excitation rate r_μ is essentially independent of the external load, with a dwell time in state 1 that is dominated by the time the motor needs to capture an ATP molecule, thus neglecting the sliding time along the slope ($r_\mu \simeq \omega^*$). These assumptions are realistic for KIF1A for small loads $f \ll f_r$ where $f_r \equiv U/(1 - \bar{a})k_B T$ and $d \gg p$ [Okada and Hirokawa, 1999]. For isolated motors this model is a simple extension of those of Refs. [Nishinari et al., 2005, Chowdhury, 2006] including unequal loading. In our model, however, we relax the simple exclusion principle and allow for coordinated steps when one motor attempts to move into an occupied site. Two adjacent motors in the diffusive state 2, will thus be allowed to move together one step forward or backward with hopping rates $u'_2 = u_1/2$ and $v'_1 = v_1/2$ respectively (Fig. 3.15c,d). The crucial processes are those in which adjacent motors undergo a change of state, in particular the p -transitions, which are the ones that contribute to motion and power generation.

Consider the case when the second motor attempts a p -decay from state 2 while the next site is occupied by the first motor. If the latter is also in state 2, then we must allow the simultaneous step forward of both. This is what we call a ‘down-push’ (see Fig. 3.15e), and corresponds to the cooperativity mechanism identified in Refs. [Brugués and Casademunt, 2009, Orlandi et al., 2010]. Only if $\beta \neq 0$, a new situation occurs when the p -decay is attempted while the first motor is occupying the adjacent site in state 1 (Fig. 3.15b, lower panel). As suggested by the Langevin dynamics, the proper way to model this case is that the second motor must wait until the first one is excited, and then both will move forward together one step. This is the new key feature that is introduced by the finite dwell time. In order to keep a Markovian description, without memory effects, this situation may be handled in practice by defining a new state 3, as the waiting state of the second motor after a p -decay when the adjacent site is occupied in state 1. This state is depicted in green in Fig. 3.15b,f and has no counterpart in the single-motor problem, or when hydrolysis dwell time is neglected. We call such an event an ‘up-push’ (Fig. 3.15f) and provides the new mechanism required to enhance cooperativity beyond MF.

3.2.1.1 Cases $N = 1$ and $N = 2$

To pursue this model analytically, we first consider the case $N = 1$. If we define the probability of finding the motor in state $s = 1, 2$ as $\sigma_s(t)$ then we have:

$$\dot{\sigma}_1 = (q_1 + p_1)\sigma_2 - r_1\sigma_1 \quad ; \quad \dot{\sigma}_2 = -\dot{\sigma}_1 \quad (3.8)$$

In the steady state we find $\sigma_1^{ss} = \beta/(1 + \beta)$ and $\sigma_2^{ss} = 1/(1 + \beta)$. Since the motor can only advance from state 2, we have $V_1(f) = l\sigma_2^{ss}(u_1 + p - v_1)$, that is,

$$V_1(f) = \frac{v_d}{1 + \beta} (f_1 - f) \quad (3.9)$$

where $v_d \equiv ld$ and $f_1 \equiv p/d$ is the stall force $f_s(1) = f_1$. The linear VF curve coincides with the prediction of the Langevin model for

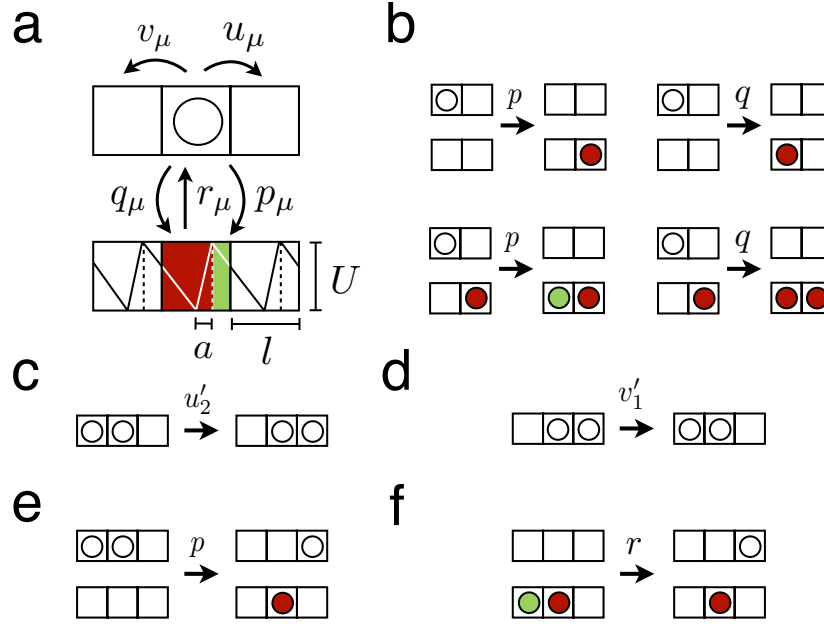


Fig. 3.15 Lattice model in 1D. a) Elementary transitions in the lattice model and their correspondence with the ratchet picture. b) p and q -decays reflecting the distinct probability of falling into the green or red regions shown in a). If the second motor attempts a p -decay from state 2 while the next site is occupied in state 1, the first is trapped in the “green” state (state 3 in the text). c,d) Coordinated diffusion of two motors in state 2. e) ‘Down-push’: The second motor makes a p -decay and pushes the first one. f) ‘Up-push’: the first motor excites and it is pushed by the second one in state 3.

large noise strength (see Appendix A and Ref. [Orlandi et al., 2010]).

The case $N = 2$ can be easily solved numerically, but some analytical approximations are illuminating. We define a generic configuration state $\mathcal{C} = \{s_1, s_2, n\}$ by the conditions of the first and second motors being respectively in states s_1 and s_2 having n vacant sites in between. The space of possible configurations can be enumerated as $\{1, 1, n\}$, $\{1, 2, n\}$, $\{2, 1, n\}$, $\{2, 2, n\}$ with $n \geq 0$ plus the configuration $\{1, 3, 0\}$, the only one that involves state 3. The Master equation for the probability $P(\mathcal{C}, t)$ of a configuration $\mathcal{C} = \{s_1, s_2, n\}$ can be written as [van Kampen, 1981, Gardiner, 1985]:

$$\dot{P}(\mathcal{C}, t) = \sum_{\mathcal{C}' \neq \mathcal{C}} \Gamma(\mathcal{C}|\mathcal{C}')P(\mathcal{C}', t) - \Gamma(\mathcal{C}'|\mathcal{C})P(\mathcal{C}, t) \quad (3.10)$$

where $\Gamma(\mathcal{C}'|\mathcal{C})$ is the transition rate from \mathcal{C} to \mathcal{C}' . We then define a decoupling approximation as $P(\mathcal{C}, t) \simeq \sigma_s(t)\tau_s(t)\rho_n(t)$ for $s = 1, 2$, $n \geq 0$ while keeping $P(\{1, 3, 0\}, t) \simeq \tau_3(t)$, where $\tau_s(t)$ is the probability of finding the second motor at state s and $\rho_n(t)$ is the vacant probability distribution within our approximation. This decoupling neglects correlations between spatial and internal degrees of freedom but is not quite a MF ansatz due to specific treatment of the configuration $\{1, 3, 0\}$. As in the MF ansatz, though, it is expected to be reasonable for large noise-strength, i.e. large diffusivity and relatively small forces. The dynamics of $\sigma_s(t)$ are the same as for a single motor. Moreover, this probability fulfills $\sigma_s(t) = \sum_{s_2, n} P(\mathcal{C}, t)$ ². The dynamics of $\tau_s(t)$ reads:

$$\begin{aligned} \dot{\tau}_1(t) &= (q + p(1 - \sigma_1\rho_0))\tau_2 + r(\tau_3 - \tau_1) \\ \dot{\tau}_2(t) &= r\tau_1 - (p + q)\tau_2 \\ \dot{\tau}_3(t) &= p\sigma_1\rho_0\tau_2 - r\tau_3 \end{aligned} \quad (3.11)$$

where $\tau_s(t) \simeq \sum_{s_1, n} P(\mathcal{C}, t)$ for $s = 1, 2$. In the steady state we find:

$$\tau_2^{ss} = \frac{1}{1 + \beta(1 + c\sigma_1^{ss}\rho_0^{ss})} \quad (3.12)$$

$$\tau_1^{ss} = \beta\tau_2^{ss} \quad (3.13)$$

$$\tau_3^{ss} = \beta c\sigma_1^{ss}\rho_0^{ss}\tau_2^{ss} \quad (3.14)$$

On the other hand, the dynamics of $\rho_n(t)$ takes the form:

$$\begin{aligned} \dot{\rho}_0 &= \rho_1[\sigma_2v_1(\tau_1 + \tau_2) + (d/2 + p)\tau_2] \\ &\quad - \rho_0[\sigma_2(u_1 + p)(\tau_1 + \tau_2) + \tau_2d/2] \end{aligned} \quad (3.15)$$

² This is an exact equality in which the state dynamics $\sigma_s(t)$ of the first motor is independent of the presence of the second motor.

$$\begin{aligned}
\dot{\rho}_n &= \rho_{n+1}[\sigma_2 v_1(\tau_1 + \tau_2) + (d/2 + p)\tau_2] \\
&+ \rho_{n-1}[\sigma_2(u_1 + p)(\tau_1 + \tau_2) + \tau_2 d/2] \\
&- \rho_n[\sigma_2(u_1 + p + v_1)(\tau_1 + \tau_2) + (d + p)\tau_2] \quad n > 0
\end{aligned} \tag{3.16}$$

where $\rho_n(t) \simeq \sum_{s_1, s_2} P(\mathcal{C}, t)$. The steady state solution reads:

$$\rho_n^{ss} = \rho_0^{ss} \chi^n \tag{3.17}$$

$$\rho_0^{ss} = \frac{f}{1 + f_1 + f/2} \tag{3.18}$$

$$\chi = 1 - \rho_0^{ss} \tag{3.19}$$

In order to calculate the approximate velocity of the first motor $V_2^{(1)}$, we define the probability of finding the first motor at position x at time t as $\eta_1(x, t)$ within our approximation. The dynamics reads:

$$\begin{aligned}
\partial_t \eta_1(x, t) &= \sigma_2[\eta_1(x - l, t)(u_1 + p) - \eta_1(x, t)(u_1 + p)] \\
&+ \sigma_2(1 - \rho_0)[\eta_1(x + l, t)v_1 - \eta_1(x, t)v_1] \\
&+ \sigma_2 \tau_2 \rho_0[\eta_1(x - l, t)(p + u'_2) + \eta_1(x + l, t)v'_1] \\
&- \sigma_2 \tau_2 \rho_0[\eta_1(x, t)(p + u'_2 + v'_1)] \\
&+ \tau_3[\eta_1(x - l, t)r - \eta_1(x, t)r]
\end{aligned} \tag{3.20}$$

As we are interested in the behavior at large length scales (larger than l), we expand the probability up to first order $\eta_1(x + \Delta x, t) = \eta_1(x, t) + \partial_x \eta_1(x, t)\Delta x + \mathcal{O}(\partial_x^2 \eta_1)$. In the long-time limit Eq. 3.20 takes the form $\partial_t \eta_1 = -V_2^{(1)} \partial_x \eta_1 + \mathcal{O}(\partial_x^2 \eta_1)$ where the drift term $V_2^{(1)}$ reads:

$$V_2^{(1)} = l\sigma_2^{ss}[u_1 + p - (1 - \rho_0^{ss})v_1 + \tau_2^{ss}\rho_0^{ss}(p + u'_2 - v'_1)] + l\tau_3^{ss}r \tag{3.21}$$

The velocity of the second motor can be similarly calculated and we find:

$$V_2^{(2)} = l\tau_2^{ss}[(d/2 + p)(1 - \rho_0^{ss}) - d/2] + l\sigma_2^{ss}\tau_2^{ss}\rho_0^{ss}(p + u'_2 - v'_1) + l\tau_3^{ss}r \tag{3.22}$$

We choose $V_2 \simeq V_2^{(1)}$ for the sake of clarity of the algebraic expressions. This particular choice is not inconsistent since any choice is equivalent in the exact problem. In our case, the results are not equivalent because we work within an uncontrollable approximation. However, the main dependences are captured in these expressions. Inserting the above approximate values we get:

$$\begin{aligned} V_2(f) &\simeq \frac{v_d}{1+\beta} (f_1 - f + \rho_0^{ss} g(f)) \\ g(f) &= \tau_2^{ss} \left(f_1 - \frac{f}{2} \right) + f_1 \tau_1^{ss} + \frac{1}{2}(1+f) \end{aligned} \quad (3.23)$$

At zero load $\rho_0^{ss}(f=0) = 0$ and from Eq. (3.23) we recover the single motor velocity. The first term in $g(f)$ accounts for the ‘down-push’ transitions (Fig. 3.15e) considered in Refs. [Brugués and Casademunt, 2009, Orlandi et al., 2010]. Note that this contribution is decreasing with β , and it is negative for $f \geq 2f_1$ so it cannot cause the stall force enhancement beyond the MF value. Conversely, the second term, which vanishes if $\beta = 0$ (i.e. $\tau_3^{ss} = 0$) comes from the ‘up-push’ transition (Fig. 3.15f), and it grows with β up to a saturation value. This term, which originates from the finite-time kinetics of ATP hydrolysis, is the only one that allows for an increase of the stall force beyond MF. Interestingly, a shortage of ATP results in a decrease of velocity but, up to a point, to a significant increase of the strength of the motor pair. The last term is due to purely excluded volume interactions between the motors, that is, coming solely from the interaction potential W , as opposed to the two first terms which are due to the filament force (i.e. the potential U_1). For $\beta = 0$ this last term yields the MF stall force of two motors $f_s(2) = 2f_1$. In order to get more insight on the stall force dependences, we use Eq. 3.22 to calculate the stall force of the second motor which takes the form $f_s(2) \simeq f_s^{(2)}(2)$ again for the sake of clarity of the algebraic expressions:

$$f_s(2) = \frac{\gamma}{2} \left(\sqrt{1 + \kappa/\gamma^2} - 1 \right) \quad (3.24)$$

where $\gamma = (1+\beta)(1-f_1)$ and $\kappa = 8f_1(1+\beta)(1+f_1)$. In the limit of $\beta \gg 1$, this expression reads:

$$\frac{f_s(2)}{2f_s(1)} = \frac{1 + f_1}{1 - f_1} > 1 \quad (3.25)$$

Hence, in the limit of low ATP supply, we obtain a simple analytical expression for the stall force of two motors which depends solely on the single motor stall force f_1 . Specifically, the cooperative factor in this limit reads $(1 + f_1)/(1 - f_1)$ which is always positive and larger than one, indicating the presence of force cooperativity beyond MF.

3.2.1.2 Monte Carlo simulations

Next, we test the validity of our analytical approximations by solving Eq. 3.10 numerically. In Fig. 3.16, we compare our analytical results to Monte Carlo (MC) simulations of the complete system by using an appropriate formulation of the Gillespie algorithm for spatially extended systems and with time dependent transition rates (see Appendix B.2). We find that the analytical

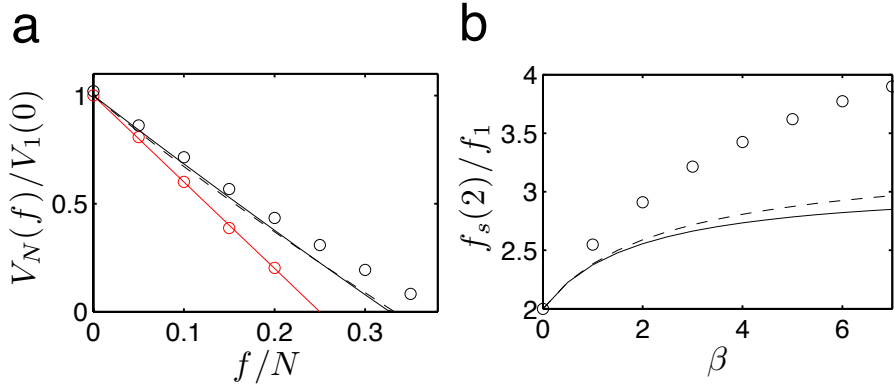


Fig. 3.16 a) VF curves for $N = 1$ (red) and $N = 2$ (black) with $\beta = 2.5$. b) Stall force of the motor pair versus β . Open circles correspond to MC simulations, the solid red line shows the exact result for $N = 1$ and the solid and dashed black lines are the analytical approximations for $\mu = 1, 2$ respectively. $d = 300 \text{ s}^{-1}$, $\omega = 250 \text{ s}^{-1}$ and $\bar{a} = 0.2$.

approximation yields actually an underestimation of $V_2(f)$. Due to our decoupling approximation, the VF curves for each of the two motors become slightly different, specially as β is increased

³ (Fig. 3.16b). Despite the discrepancy, both VF and stall force curves remain below the exact solution for $\beta > 0$ and $f > 0$ until stall for $f_1 = 0.25$. This underestimation is possibly due to neglected correlations during the decoupling approximation which may be relevant for the enhancement of the VF curves. Therefore, we might expect this underestimation to hold for $f_1 \ll 1$ as we approach to MF conditions.

3.2.1.3 N interacting motors

In Sections 3.2.1.1 and 3.2.1.2, we have demonstrated both analytically and numerically that two interacting motors can enhance the collective stall force of the system beyond MF by cooperation. However, we still ignore to what extent the lattice description successfully captures the nonlinear scaling of the stall force with N , or the staircase-shaped VF curves observed in the Langevin description. Hence, we should generalize the previous lattice model to the case of an arbitrary number of interacting KIF1A motors in a 1D lattice.

A first consideration is that the formulation used in Section 3.2.1.1 is only valid for small forces (i.e. $f \ll f_r$). Under the presence of large loads ($f \gg f_r$), a single motor can be dragged backwards in state 1. This effect also applies for a cluster of motors in state 1 sharing the external load. Hence, a force-dependent backward rate for the motors must be included in the model to ensure the linear growth of the stall force with N in the absence of cooperative effects. This rate will only apply to the consecutive motors forming the leading cluster and sharing the external load. On the other hand, single motor transitions can trigger collective transitions of motor clusters. In this way, motor transitions can be regarded as cluster transitions with rates which depend both on the size of the cluster and the external force. u and v transitions will only produce rearrangements on motor clusters in state 2, while p and r transitions can lead to “avalanches” of motor clusters.

³ In the exact calculation both VF curves must coincide with the center of mass VF curve i.e. $V_2 = V_2^{(1)} = V_2^{(2)} = V_2^{(CM)}$.

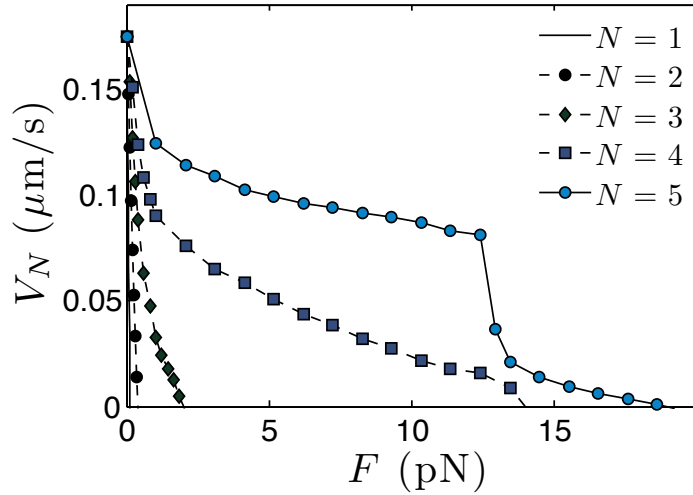


Fig. 3.17 VF curves for the different number of interacting motors N on a lattice. $\beta = 2.5$, $d = 300 \text{ s}^{-1}$, $p = 75 \text{ s}^{-1}$, $q = 175 \text{ s}^{-1}$, $U = 20 k_B T$, $\bar{a} = 0.2$.

In Fig. 3.17 we show VF curves for different number of motors N , using a particular set of rules in the Gillespie algorithm regarding cluster transitions. The choice of the transition rules is not unique and some *ad hoc* assumptions must be taken into account to simplify the problem. Remarkably, the different trends in stall force scaling and shape of the VF curves are similar to the ones in the Langevin description (Fig. 3.4). Hence, we conclude that a lattice description with multi-particle transitions captures the stall force enhancement of KIF1A motor clusters.

3.2.2 Dynamics on a 2D lattice

Finally, some molecular motors fail to follow a single protofilament and they can change pf tracks [Yajima and Cross, 2005, Brunnbauer et al., 2012]. Motivated by the experiments in Chapter 4, in which we find that single-headed KIF1A motors are able to change pf tracks, we aim to describe the motion of a single KIF1A motor on a 2D MT lattice. We extend the previous lattice description by considering a 2D oblique Bravais lattice (Fig. 3.18a) with directions \mathbf{r}_1 and \mathbf{r}_2 forming an angle θ . The vector

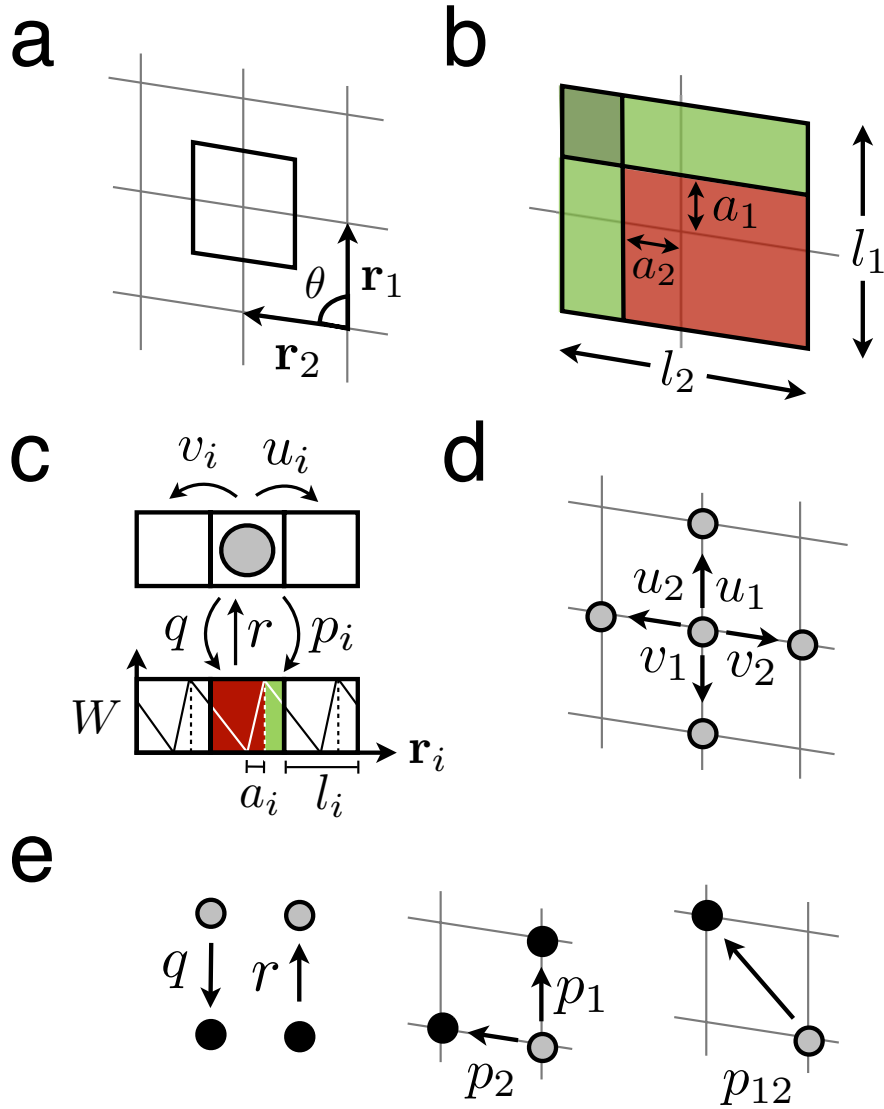


Fig. 3.18 Lattice model in 2D. a) Two-dimensional oblique Bravais lattice representing the MT surface with directions $\mathbf{r}_1, \mathbf{r}_2$, forming an angle θ . The lattice unit is centered in each node of the lattice. b) Lattice unit of lengths l_1 and l_2 and ratchet asymmetries a_1, a_2 . c) Schematic description of a two-state noise driven ratchet for the direction i and its equivalence in a lattice. Motors can diffuse with rates u_i, v_i and advance with rates p_i, q along the i -th direction. d) Two-dimensional diffusion on the lattice in the weakly bound state. e) Possible transitions between the strongly bound state (black circles) and the weakly bound state (gray circles) and its corresponding transition rates.

\mathbf{r}_1 describes the on-axis motion of kinesin reflecting the polarity of the MT. On the other hand, the vector \mathbf{r}_2 describes the off-axis motion determined by the bias due to the interaction of the motor domain and the MT lattice when the motor is diffusing in the weakly bound state. The mechanism of motion can be understood by considering a two-state model.

We define the state of the motor as $k = 1, 2$ depending on whether the motor is strongly bound ($k = 1$) or weakly bound ($k = 2$) to the MT. In the strongly bound state, the motor feels a superposition of two asymmetric ratchet potentials forming an angle θ with asymmetries a_i and periodicities l_i (Fig. 3.18b,c) where $i = 1, 2$ indicates the direction in the lattice. Each node of the Bravais lattice corresponds to the minima of the MT potential landscape. A motor in the minima can only be excited with rate $r = \omega^*$ to the weakly bound state in which it undergoes two-dimensional diffusion on the lattice with rates u_i, v_i , $i = 1, 2$ (Fig. 3.18d). These rates depend linearly on an external force $\mathbf{F} = (F_1, F_2)$ as $u_i = (d_i/2)(1 - f_i)$, $v_i = (d_i/2)(1 + f_i)$, $i = 1, 2$, where $f_i = F_i l_i / k_B T$, $d_i = D / l_i^2$ is the diffusion rate and D is the one-dimensional diffusion coefficient in the weakly bound state. When the motor decays, it can fall in one of the four possible regions depicted in Fig. 3.18b. If the motor falls in the red region, it performs a q transition binding strongly to the MT in the same node (Fig. 3.18c and 3.18e). However, if the motor falls in one of the three green regions, it will move to a new node in the lattice. The motor will make a p_1 transition if it falls in the upper green region, a p_2 transition if it falls in the left green region, and a p_{12} -transition if it falls in the dark green region. The latter probabilities are equal to the decay rate ω times the probability of falling in a given region, which can be directly obtained calculating the areas in Fig. 3.18b.

We define a given transition rate from state $\{k, \mathbf{R}\}$ to $\{k', \mathbf{R}'\}$ as $\Gamma(k', \mathbf{R}' | k, \mathbf{R})$. The different transitions read:

$$\begin{aligned}
\Gamma(1, \mathbf{R} + \mathbf{r}_1 + \mathbf{r}_2 | 2, \mathbf{R}) &= p_{12} = \frac{\omega}{4}(1 - 2\bar{a}_1)(1 - 2\bar{a}_2) \\
\Gamma(1, \mathbf{R} + \mathbf{r}_1 | 2, \mathbf{R}) &= p_1 = \frac{\omega}{4}(1 - 2\bar{a}_1)(1 + 2\bar{a}_2) \\
\Gamma(1, \mathbf{R} + \mathbf{r}_2 | 2, \mathbf{R}) &= p_2 = \frac{\omega}{4}(1 + 2\bar{a}_1)(1 - 2\bar{a}_2) \\
\Gamma(1, \mathbf{R} | 2, \mathbf{R}) &= q = \frac{\omega}{4}(1 + 2\bar{a}_1)(1 + 2\bar{a}_2) \\
\Gamma(2, \mathbf{R} | 1, \mathbf{R}) &= r = \omega^* \\
\Gamma(2, \mathbf{R} + \mathbf{r}_i | 2, \mathbf{R}) &= u_i = \frac{d_i}{2}(1 - f_i) \\
\Gamma(2, \mathbf{R} - \mathbf{r}_i | 2, \mathbf{R}) &= v_i = \frac{d_i}{2}(1 + f_i)
\end{aligned} \tag{3.26}$$

where $\bar{a}_i \equiv a_i/l_i$. The mean velocities in the \mathbf{r}_1 and \mathbf{r}_2 directions will be:

$$\begin{aligned}
v_1 &= l_1 \sigma_2^{ss} (p_{12} + p_1 + u_1 - v_1) \\
v_2 &= l_2 \sigma_2^{ss} (p_{12} + p_2 + u_2 - v_2)
\end{aligned} \tag{3.27}$$

where $\sigma_2^{ss} = 1/(1 + \beta)$ is the steady state probability of the motor to be found in state $k = 2$ and $\beta = \omega/\omega^*$. Substituting the form of the different rates, we can write the last expression as:

$$v_i = \frac{v_i^d}{1 + \beta} (f_i^s - f_i); \quad i = 1, 2 \tag{3.28}$$

where $v_i^d = l_i d_i$ and $f_i^s = \frac{\omega}{2d_i}(1 - 2\bar{a}_i)$ is the dimensionless stall force in the direction \mathbf{r}_i . Note that we recover the results for the one-dimensional case in each direction (see Section 3.2.1.1).

3.2.3 Conclusions

Inspired by the Langevin formulation, we have built up a one-dimensional lattice model to study the dynamics of two interacting KIF1A motors. Lattice models for KIF1A have been shown to be suitable to study different phenomena such as shock formation [Sparacino et al., 2011] and nonequilibrium phase transitions [Nishinari et al., 2005, Greulich et al., 2007]. In order to incorpo-

rate cooperative effects in such models, transitions of blocks of adjacent motors must be incorporated. This effect is specially relevant in the case of large clusters under heavy loads as discussed in Section 3.1.1.5. This formalism is convenient to analytical treatment and in terms of computational time by using Monte Carlo simulation; however, it has some conceptual disadvantages since the choice of the transition rules are sometimes not unique and carefulness must be taken. We have shown analytically the presence of cooperativity in the system and we have considered a first extension of the problem to an arbitrary number of motors.

We have also developed a two-dimensional lattice model to describe a single KIF1A motor moving on the microtubule surface. This is achieved by considering the microtubule lattice surface as a 2D oblique Bravais lattice where the nodes correspond to the minima of the microtubule-motor potential landscape. A single KIF1A motor follows a two-dimensional biased random walk and we recover the VF relationships for the one-dimensional case in each direction of the Bravais lattice.

Chapter 4

Membrane tube formation by KIF1A

In this chapter we set up an experimental system to verify the theoretical predictions found in Chapter 3 by challenging single-headed KIF1A motors to extract membrane tubes from giant unilamellar vesicles (GUVs) along microtubules in a minimal *in vitro* system. We briefly present the problem of tube formation, and the experimental methods used to build a minimal *in vitro* setup where motors pull membrane tubes on an underlying microtubule network. We provide a complete quantitative picture of the problem by means of the combination of experimental data, *in silico* simulation and theoretical modeling.

4.1 Formation of membrane tubes

As previously discussed in Section 2.1, biological membranes can form tubular networks. The formation of nanotubes can be provided by the cooperative action of molecular motors pulling on membranes along cytoskeletal filaments. However, these nanotubes can also be formed *in vitro* using many different experimental techniques such as hydrodynamic flow, micropipettes or optical tweezers [Waugh, 1982, Evans et al., 1996, Raucher and Sheetz, 1999]. Let us consider the formation of a tube from a planar or large spherical piece of membrane bilayer [Derényi et al., 2002]. We will study the case in which the relation between the area A and the volume V is no longer fixed, as in a closed vesicle, and we will consider an ensemble where the surface tension γ and the inside

pressure p (relative to the outside) are fixed. The free energy of the system can be written as [Helfrich, 1973]:

$$\mathcal{F} = \int \frac{\kappa}{2}(2H)^2 dA + \gamma A - pV - FL \quad (4.1)$$

where κ is the bending rigidity and H is the mean curvature of the membrane [Kamien, 2002]. First, let us study the energetics of a formed tube of length L , which is pulled with a point-like force F . Considering no difference in pressure between the inside and the outside (i.e. $p = 0$), the free energy of a tube of radius r and length L can be written as:

$$\mathcal{F}_{\text{tube}} = \left(\frac{\kappa}{2r^2} + \gamma \right) 2\pi r L - FL \quad (4.2)$$

Minimizing the previous expression respect to r and L ($\partial_r \mathcal{F}_{\text{tube}} = 0$ and $\partial_L \mathcal{F}_{\text{tube}} = 0$) we obtain:

$$r_0 = \sqrt{\frac{\kappa}{2\gamma}}, \quad F_0 = 2\pi\sqrt{2\gamma\kappa} \quad (4.3)$$

Hence, the competition of the bending rigidity and the surface tension determines the radius r_0 and the necessary force F_0 to extract a tube from a flat membrane. Typical values of these quantities are $\kappa \simeq 40$ pN nm and $\gamma \simeq 0.05$ pN/nm which correspond to a radius $r_0 \simeq 20$ nm and a force of $F_0 \simeq 13$ pN. This simple study provides us the energetics of a cylindrical tube but not how the tube is formed.

The formation process can be understood by studying how the surface of a membrane is deformed under the action of the point-like force F . The surface can be considered to be axisymmetric around the axis along the direction of the force F (Z coordinate, see Fig. 4.1). A point along the surface contour can be determined by two coordinates $\{R(s), Z(s)\}$, where s is the arclength parameter. We define the tangent angle $\psi(s)$ such that $R_s = \cos \psi$ and $Z_s = -\sin \psi$, where the subscript s denotes partial differentiation respect to the arclength parameter. Using variational methods to minimize Eq. 4.1 [Jülicher and Seifert, 1994], we can obtain a closed equation for $\psi(s)$ [Derényi et al., 2002]. For small forces

($F \ll F_0$), the membrane deformation depends linearly on F . On the other hand, for forces over the threshold ($F \gg F_0$), numerical integration of the ψ -equation shows that the membrane deforms into a cylindrical tube (Fig. 4.1). Interestingly, the force-length dependence is not monotonic, and exhibits an overshoot at a certain tube length [Derényi et al., 2002]. This fact indicates that in order to form a membrane tube, a certain force barrier must be overcome. Next we will study the formation of membrane tubes by KIF1A motors experimentally by means of a minimal *in vitro* setup.

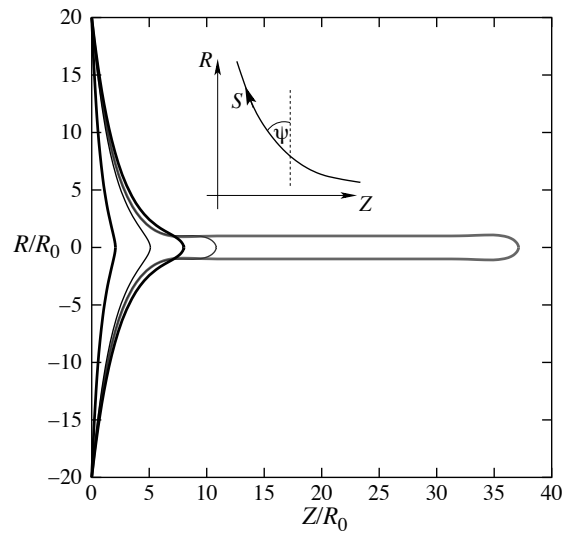


Fig. 4.1 Formation of a membrane tube under the action of a point-like force F . Shape of the emerging tube for various forces. Inset: Parametrization of the surface with arclength s and tangent angle ψ . Adapted from [Derényi et al., 2002].

4.2 Minimal experimental *in vitro* system

In order to test the theoretical results found in Chapter 3 experimentally, we will challenge KIF1A motors to collectively extract membrane tubes from giant unilamellar vesicles. This minimal *in vitro* setup has been widely used to probe the collective

action of membrane-bound molecular motors [Roux et al., 2001, Koster et al., 2003, Leduc et al., 2004, Shaklee et al., 2008], and it was originally conceived to mimic the formation of membrane tube networks *in vivo* [Waterman-Storer and Salmon, 1998]. Next, we present the experimental methods and protocols used to prepare the minimal *in vitro* system.

4.2.1 Experimental methods

We start with the description of the protocols that were used to obtain the microtubules, the motor protein KIF1A and the giant unilamellar vesicles used in the experiments. Next, the tube pulling assay is presented. Finally, the imaging acquisition and analysis techniques are described.

4.2.1.1 Microtubule preparation

Microtubules (MTs) were prepared from tubulin purchased from Cytoskeleton. Tubulin (10 mg/ml) in MRB40 (40 mM Pipes/4 mM MgCl₂/1 mM EGTA, pH 6.8) with 1 mM GTP was incubated for 45 min at 37°C to polymerize. MTs were stabilized by mixing them 1:10 (vol/vol) with MRB40 containing 10 μ M paclitaxel (taxol, Cytoskeleton Inc., USA; MRB40tax). The tubulin mixture contained 10 % of fluorescent tubulin (HiLyte Fluor 488). During experiments, taxol was added in all buffers when MTs were present.

4.2.1.2 KIF1A preparation

A construct containing the first 382 residues of KIF1A with a His-tag and a Cys residue in the N-terminal, was kindly provided by Prof. N. Hirokawa (University of Tokyo, Japan). The plasmid was expressed in *E. Coli* and was further purified using His-tag purification [Loughran and Walls, 2011], labeling the protein during the elution process. The labeling of the protein with biotin (BMCC-biotin) was realized on a nickel-nitrilotriacetic acid (Ni-NTA) matrix prior to elution. Three types of purification were

performed: no labeling, fluorescent labeling (Sulfhydryl reactive dye) (see Fig. 4.2) and labeling with biotin. The final concentrations after elution were measured with NanoDrop 2000c (Thermo scientific). The concentrations obtained were $28 \mu\text{M}$ for the unlabeled KIF1A, $42 \mu\text{M}$ for the fluorescent KIF1A and $33 \mu\text{M}$ for the biotinylated KIF1A. The detailed protocol is described in Appendix C.

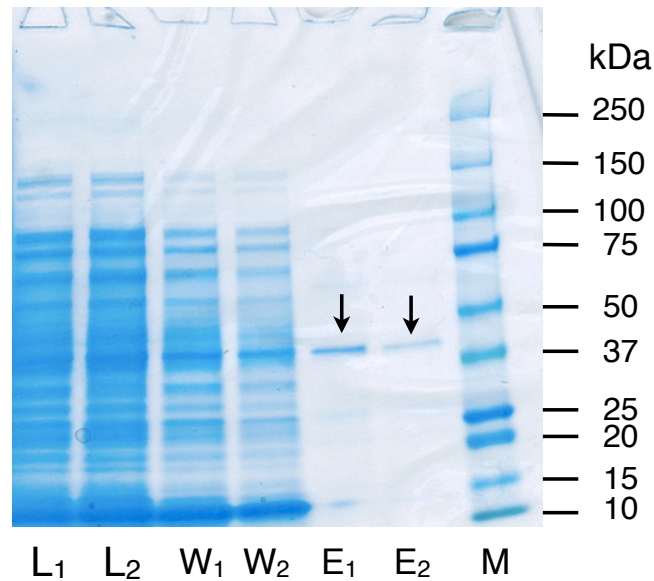


Fig. 4.2 SDS gel for fluorescently labeled (1) and unlabeled (2) KIF1A. From left to right: protein lysate (L), first wash (W), elution (E) and Kaleidoscope marker (M). The two arrows correspond to the ≈ 45 kDa band, corresponding to the KIF1A monomer molecular weight.

4.2.1.3 Gliding assays

The motility of single-headed KIF1A was tested using *in vitro* gliding assays with 1:10 dilutions of the purified motor solution in MRB40tax (pH 6.8: 40 mM PIPES, 4 mM MgCl_2 , 1 mM EGTA, $10 \mu\text{M}$ taxol). Motors were unspecifically attached to the glass surface in the case of unlabeled and fluorescently labeled KIF1A, and specifically attached in the case of biotinylated KIF1A via a

streptavidin-biotin link using Poly(L-lysine)-poly(ethylene glycol)-biotin (PLL-PEG-biotin, SUSOS AG, Switzerland) on the surface. Finally the motility solution (κ -casein 0.6 mg/mL, methylcellulose 0.1 %, glucose 50 mM, ATP 2 mM, taxol 10 μ M, diluted taxol stabilized microtubules in MRB40 and oxygen scavenger system) was flushed before observation. Unlabeled and fluorescently labeled KIF1A showed gliding velocities in the range of 100 – 200 nm/s whereas biotinylated KIF1A smoothly moved microtubules at \simeq 80 nm/s. In Fig. 4.3, gliding assay images are shown at three different times instants for the case of biotinylated KIF1A using total internal reflection fluorescent (TIRF) microscopy (see Section 4.2.2).

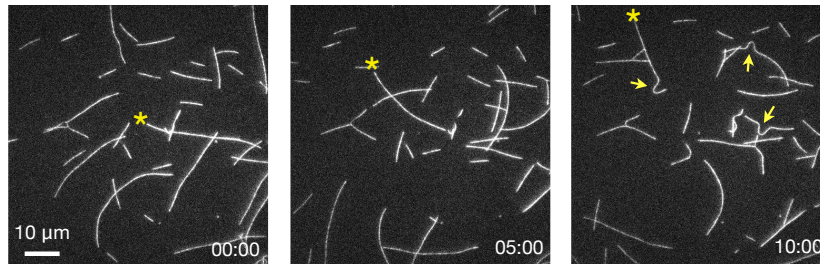


Fig. 4.3 TIRF images of a gliding assay with biotinylated single-headed KIF1A. Motors were specifically attached to the substrate via a streptavidin-biotin link using PLL-PEG-biotin. Asterisks indicate successive positions of the tip of a microtubule over time. Arrows show the presence of high curvature regions in some microtubules possibly due to the presence of defects on the surface. Microtubules moved smoothly at \simeq 80 nm/s. Each frame was acquired every 2 seconds and time is shown in minutes.

4.2.1.4 Electroformation of GUVs

Giant unilamellar vesicles were formed using the electroformation method [Angelova et al., 1992]. This method stimulates the formation of giant liposomes (typically $>$ 10 μ m diameter) by applying an external alternating field. DOPC, DOPE-Bio, and DOPE-Rh were purchased from Avanti Polar Lipids ¹. The lipid

¹ DOPC: 1,2-Dioleoyl-sn-glycero-3-phosphocoline, DOPE-Bio: 1,2-dioleoyl-sn-glycero-3-phosphoethanolamine-N-(cap biotinyl), DOPE-Rh: 1,2-dioleoyl-sn-glycero-3-phosphoethanolamine-N-(lissamine rhodamine B sulfonyl)

mixture was composed of 0.1 mol % DOPE-Rh, 0.01-1 mol % DOPE-Bio (depending on the experiment) and DOPC for the remaining fraction. 10 μl of lipids in 1:10 chloroform/methanol were dropped onto one of two indium tin oxide (ITO) coated glass slides. The lipids were locally spread on the glass slide and dried

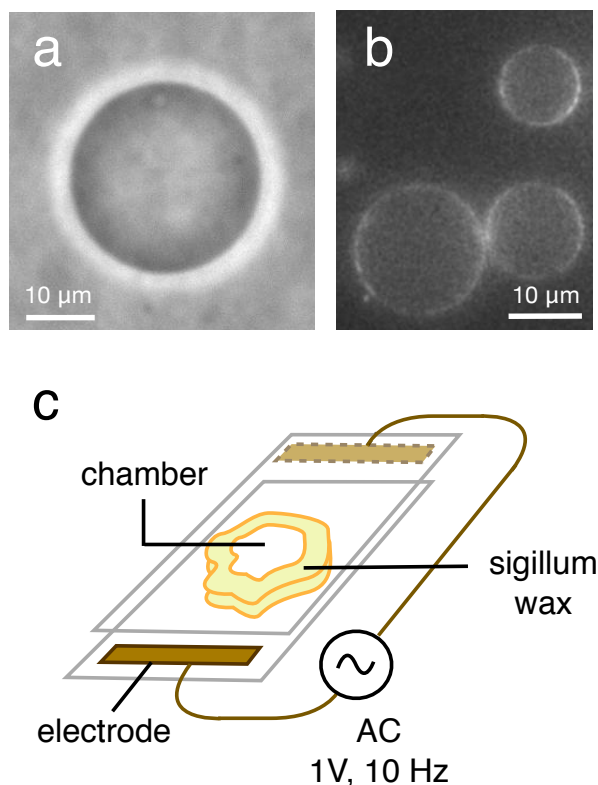


Fig. 4.4 Formation of giant unilamellar vesicles by using the electroformation method. a) Bright-field illumination of a GUV. b) TIRF image of fluorescent GUVs. c) Schematic description of the electroformation method. A chamber of $\simeq 500 \mu\text{l}$ was made with sigillum wax surrounding the dry lipid area in the center of one ITO glass. Prior to closing, the chamber was filled with a 200 mM sucrose solution. Finally, AC voltage was applied to the glass plates with the consequent formation of GUVs.

for approximately 1 hr in vacuum. A 500 μl volume chamber was made with sigillum wax (Vitrex) surrounding the dried lipid area on the bottom glass (Fig. 4.4). Prior to closing, the chamber was filled with a 200 mM sucrose solution with a 1 mL syringe. Finally,

AC voltage was applied to the glass plates (1 V, 10 Hz) during 4h, with the consequent formation of GUVs.

4.2.1.5 Tube pulling assay

The protocol used for the experiment was inspired by the experimental methods used in previous studies [Leduc et al., 2004, Shaklee et al., 2008]. Glass coverslips were sonicated in Isopropanol for 20 min, two times in deionized water for 5 min and in 1M KOH for 20 min. 200 μL of poly(-L-lysine) 1:500 in ethanol were dropped on top of the coverslip and the sample was kept in the hood until complete evaporation of the drop. A circular plastic support was placed on top of the coverslip defining a 50 μl volume chamber.

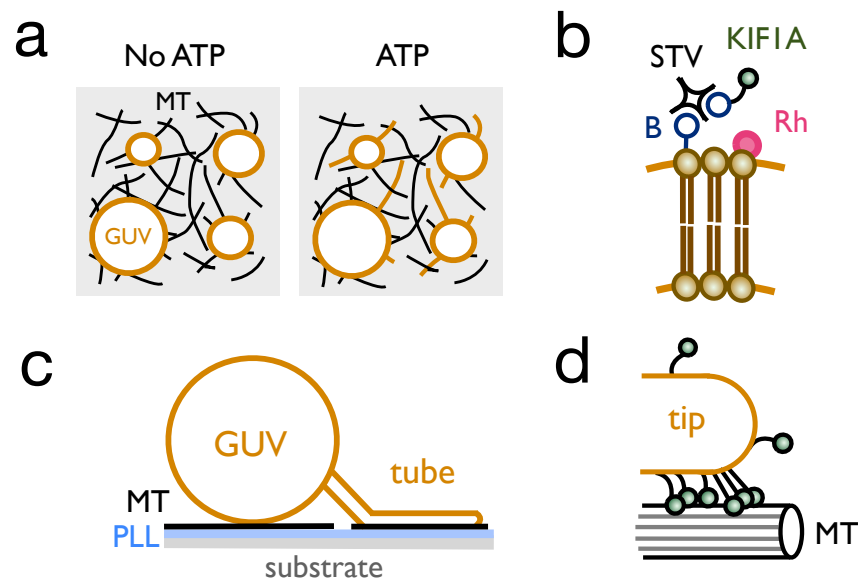


Fig. 4.5 Minimal *in vitro* experimental system. a) Top view of the system. GUVs sediment on top of a microtubule network. Tubes grow along microtubules upon the addition of ATP. b) Biotin (B) - streptavidin (STV) linkage of KIF1A with the GUV bilayer (yellow). The lipid mixture contains a small fraction of rhodamine (Rh) labeled phospholipids. c) Side view of the system. Poly-L-Lysine (PLL) is used to attach MT to the substrate and GUVs are sedimented on top. d) Tip region where motors accumulate.

MTs were dropped on the chamber and incubated for 10 min to adhere. MTs that did not stick to the surface were removed by rinsing two times with MRB40tax. Casein (Sigma) was dropped on the surface (1 mg/ml) to minimize interaction of the GUVs with the exposed glass, incubated for 10 min, and rinsed with MRB40tax. At the same time, a 5 μ l mixture of KIF1A and streptavidin (1:1 mol) was incubated for 5 min in a rotating wheel at room temperature. GUVs were mixed 1:1 in MRB40tax with 180 mM glucose to osmotically match the intravesicular osmolarity (Halbmikro Osmometer, Type M, Knauer, Germany). The KIF1A-streptavidin solution was mixed with the vesicle solution (around 50 μ l total volume) and was incubated 5 min more in the rotating wheel, in order to enable KIF1A motors to attach to the vesicles as depicted in Fig. 4.5b. 40 μ l of the vesicle solution was dropped onto the chamber. 5 μ l of MRB40tax with 180 mM glucose was dropped on top of the sample to help the vesicles to settle to the glass surface (Fig. 4.5a, left). Finally, 0.5 μ l of Oxygen Scavenger (8 mM DTT/0.4 mg/ml catalase/0.8 mg/ml glucose oxidase) and 2 μ l of 50 mM ATP were added before observation, resulting with the extraction of membrane tubes from the GUVs (Fig. 4.5a, c, d).

4.2.2 Image acquisition and data analysis

Images were acquired on a total internal reflection fluorescence microscope (TIRF; Nikon Corporation, Japan) equipped with an APO TIRF 100 \times 1.49 numerical aperture oil objective, a motorized stage, Perfect Focus System, a motorized TIRF illuminator (Roper Scientific, Tucson, AZ, USA) and a QuantEM:512SC EM-CCD camera (Photometrics, Roper Scientific). For excitation, we used a 561 nm (50 mW) Jive (Cobolt, Solna, Sweden) and a 488 nm (40 mW) Calypso (Cobolt) diode-pumped solid-state laser. Images of moving tubes were acquired every 2 s with a pixel size of 158 nm. Kymographs were built using ImageJ. The data from kymographs was exported to Matlab and a homemade program was used to fit at every time step a sigmoidal function along the nanotube to the logarithm of the intensity profile. The position

of the tube tip was determined as the inflection point of the sigmoidal function, with fitting error corresponding to 1.96 s.d. (95 % confidence interval).

4.2.3 Results

4.2.3.1 Parallel tubulation

Different fractions of biotinylated motors were studied, ranging from 0.01-1 mol %. For the case of 1 mol %, networks of tubes were formed in minutes whereas for 0.1-0.01 mol %, few tubes were formed after more than an hour (Fig. 4.6a). The 0.01 mol % case was found to be close to the threshold surface density for tube formation. This threshold value is comparable to the one for conventional kinesin [Leduc et al., 2004]. The sole fact that tubes are being extracted despite the inherent weakness of individual single-headed KIF1A motors is by itself a proof of the existence of a strong cooperative effect such as that predicted in Chapter 3, even though the precise mechanism cannot be inferred from the experiment.

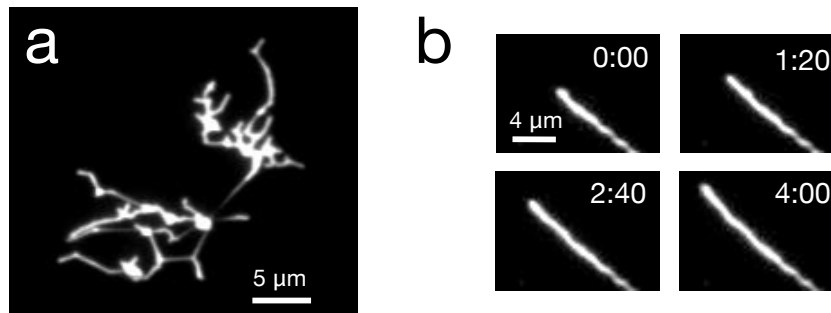


Fig. 4.6 Parallel tube growth a) TIRF fluorescent image of a membrane tube network formed on the underlying MT network. b) Time-lapse of a growing tube in minutes.

Tube growth velocities ranged from 2 to 20 nm/s, around 10 times smaller than in gliding assays. These velocities are much

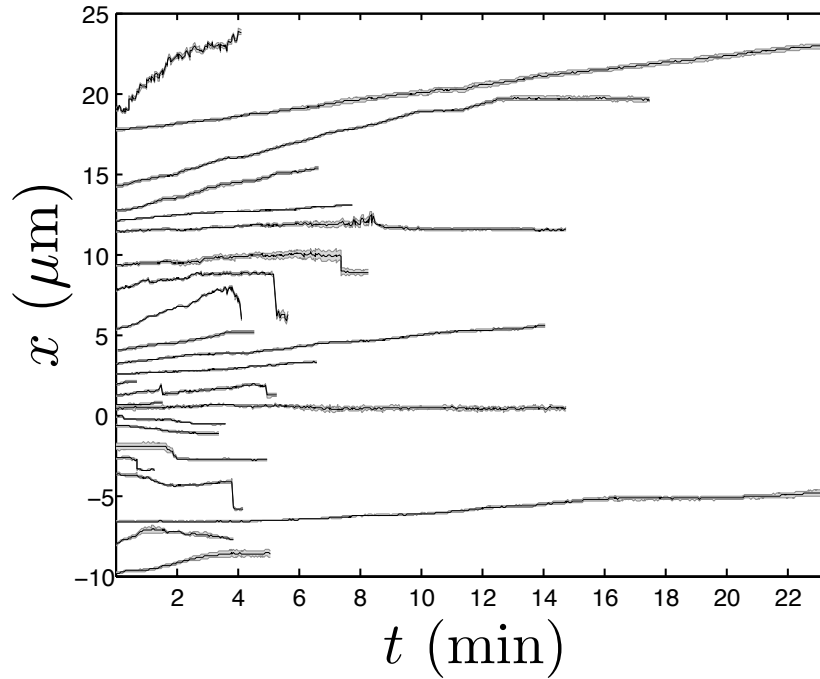


Fig. 4.7 Trajectories of nanotube growth events. The grey region surrounding the trajectory corresponds to the fitting error for each time t . For additional details on the data analysis see Section 4.2.2.

smaller than typical tube growth velocities for conventional kinesin, around 400 nm/s. This fact likely indicates that motors work near stall conditions at the tip, sharing the external load and teaming up in a cooperative manner. In some cases we observed episodes of slow backward motion, with characteristic velocities of ~ 4 nm/s indicating the presence of bidirectional movement (see Fig 4.7). Similar slow backward movements were reported in the case of non-processive Ncd motors [Shaklee et al., 2008], due to the presence of motors distributed all along the tube, typically forming motor clusters capable to withstand tube retractions. In that case, the clustering mechanism resulted from the diffusive motion of motors along the MT lattice due to their non-processivity [Shaklee et al., 2010]. Our case seems to obey a similar scenario; however, diffusion along the MT is now associated to the inherent diffusive state of KIF1A. We measured instantaneous speeds for

individual tip traces by subtracting endpoint positions of a window moving along the trace. In Fig. 4.8 the instantaneous velocity

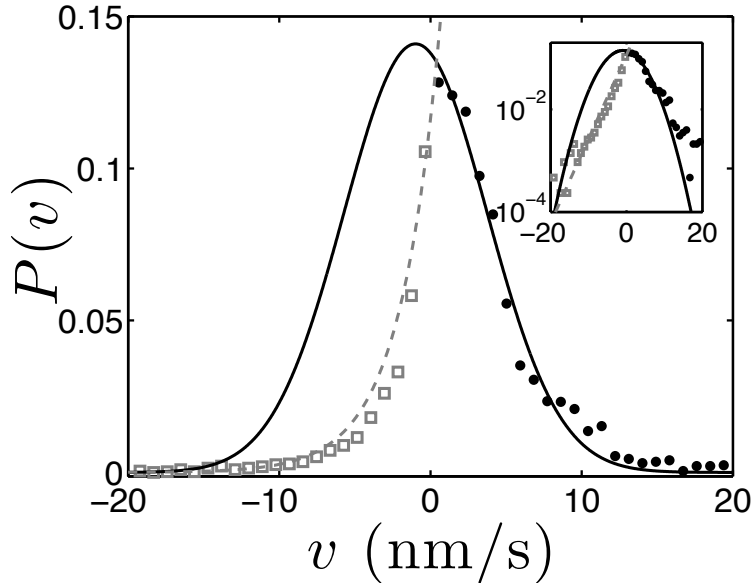


Fig. 4.8 Instantaneous velocity distribution $P(v)$ using 24 different events of longitudinal pulling. The distribution is clearly asymmetric and can be interpreted by considering retraction and growth as two differentiated processes. Lines show the best fit to the distribution for negative (\square) and positive (\bullet) velocities using exponential (dashed line) and gaussian (solid line) profiles respectively. Inset: Same distribution in the logarithmic scale.

distribution of the tube tip is shown for 24 events using a time window of 16 s. The distribution is clearly asymmetric. This fact can be understood by considering shrinkage and growth as two distinct processes. Following Ref. [Shaklee et al., 2008], the distribution for negative displacements may be explained by assuming a random cluster distribution due to the diffusive nature of KIF1A, which leads to an exponential distribution of retraction distances. For positive displacements, instead, the observed statistics reflects the interplay between a ballistic component and the diffusive spread, which suggests a Gaussian distribution.

4.2.3.2 Helical tubulation

Surprisingly, a large fraction of the extracted tubes wound around the MTs forming left-handed helical structures with well-defined pitch (Fig. 4.9a). In some cases, membrane tube networks exhibited mixed longitudinal and helical tube formation. In the case of growing helical tubes, MTs usually fluctuated close to the focal plane, indicating that they were partially anchored to the substrate and consequently tubes were able to grow underneath MTs (Fig. 4.10a). When MTs were strongly attached to the substrate, tube growth was longitudinal. Plausibly, the ability of KIF1A motors to switch pfs is facilitated by the existence of the weakly bound state (Fig. 4.10b), similarly to the case of single-headed kinesin-1 [Yajima and Cross, 2005]. Hence, this state provides a certain freedom for the motor to switch between on-axis or off-axis movements, a relevant feature when the motor runs into obstacles. The left-bias originates in the intrinsic left-right asymmetry of the motor-MT interaction, which in turn reflects MT chirality. However, it is not obvious that such an intrinsic bias is sufficient to collectively generate significant off-axis forces up to the point of twisting the membrane tubes in a counter-clockwise motion around the MT (see Fig. 4.10a.).

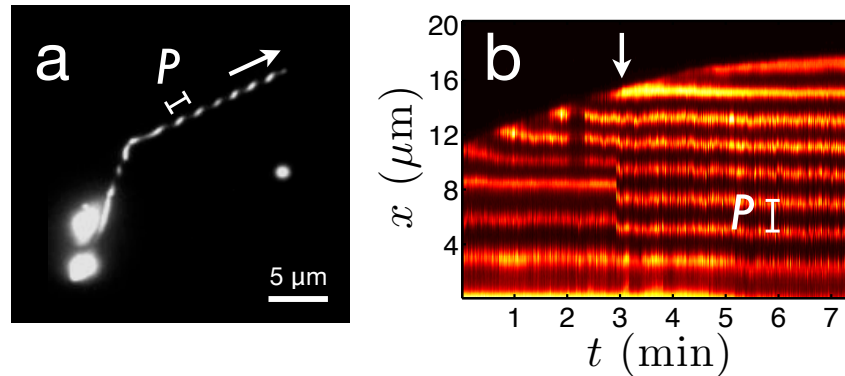


Fig. 4.9 Helical tube extraction a) Helical tube extracted from a GUV. P is a measure of the tube pitch and is defined as the peak-to-peak distance between intensity maxima along the tube. b) Kymograph of the growing helical tube in (a). Notice that around $t = 3$ min (arrow) a rapid relaxation of the pitch is observed.

In Fig. 4.9a the pitch P is measured as the distance between two consecutive fluorescence maxima. The helical pitch is observed to be relatively regular along the helix although sometimes the helical turns change dynamically via slow (minutes) or rapid (seconds) rearrangements (Fig. 4.9b) converging to a homogeneous pitch. The average value of the pitch evaluated by analyzing 57 standing helical tubes was found to be $1.4 \pm 0.1 \mu\text{m}$. Next, we study the geometry of the helical tubes. We define the pitch P as the length of MT covered per turn of the helix, and the angular pitch as $p \equiv P/2\pi$. We define ζ as the angle the tangent vector of the tube axis \mathbf{t} forms with respect to the MT axis \mathbf{z} (Fig. 4.10a). From the geometry of a helix (see Appendix D) we have $\tan \zeta = R_0/p$, where $R_0 \equiv r + R$, r is the radius of the tube and R is the radius of the MT plus the extra space occupied by the motors (see Fig. 4.10b).

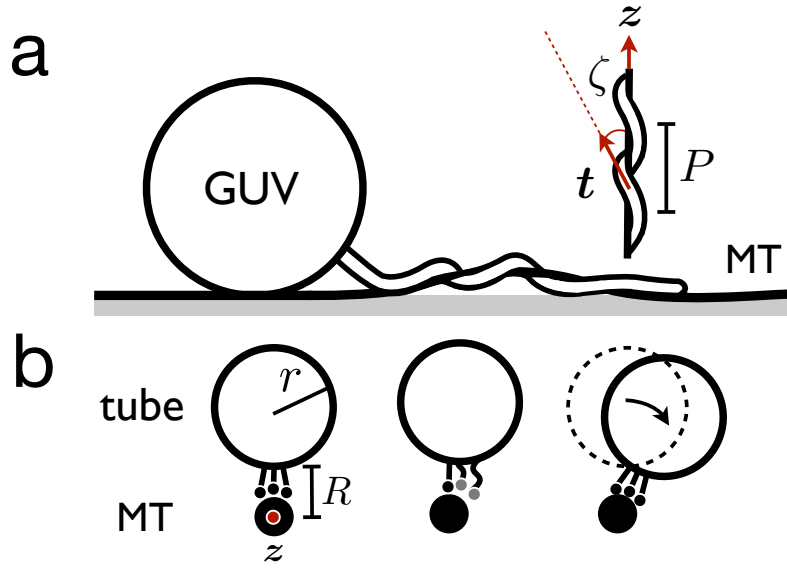


Fig. 4.10 Geometry of the helical tubes. a) Schematic description of the formation of a helical tube from a GUV around a MT. Some defects in the MT network allow motors to pull tubes through nanometer range gaps between the MT and the substrate. The angle ζ and the pitch P characterize the geometry of the helix. b) Off-axis movement of the tube: (left) Motors are found initially in a strongly bound conformation (black). (center) Some of them switch to the weakly bound state (grey) and progressively switch pfs by diffusion. (right) When motors return to the strongly bound state, the tube turns counter-clockwise.

The tube radius r results from the balance of bending energy and surface tension (see Section 4.1). For a helical tube, the twist will introduce additional bending energy due to mechanical work performed by the motors. Typically the values of both F and r from the straight case are reasonably accurate for the actual helical tubes, an exception being the point (a) in Fig. 4.11. The selection of the pitch is thus a dynamic process that results from the collective action of the motors. Once the tube is formed; however, the winding number is conserved as a topological constraint imposed by the presence of the MT, and energy minimization will only tend to leave a uniform pitch. Hence, the observed pitch inhomogeneities in Fig. 4.9b are a consequence of the motor activity.

In Fig. 4.11 (top, left) we show experimental data points of 57 tubes forming left-handed helices with pitch P and angle ζ (grey circles). *In vivo*, MTs typically contain 13 pfs, which run straight with respect to the MT axis. However, MTs grown *in vitro* may contain a similar fraction of 14 pf MT [Ray et al., 1993, Amos and Schlieper, 2005]. In the latter case, pfs wind around the MT axis, and introduce an extra pitch (superhelical pitch) in the helical tubes (see Section 1). In order to account for this effect, the red circles in Fig. 4.11 correspond to exactly the same data but subtracting the possible extra pitch introduced by 14 pf MTs. This correction is small provided that the pitch of the helix is much smaller than the superhelical pitch. The cloud of points falls into a certain sector of the parameter space bounded by a black line ($R_0 = 40$ nm) and a red line ($R_0 = 195$ nm). The scattering of points in Fig. 4.11 (top, left) reflects the variability of surface tension from vesicle to vesicle, which in turn yields a variety of tube radii. Tubes (a) and (c) in Fig. 4.11 have completely different pitches despite having similar R_0 , implying different tip velocities. In Fig. 4.11 (top, right), we see that the z -component of the tip velocity V_z grows as a function of p , suggesting that the shape of the helix roughly follows the trace of the tube tip during growth. Therefore, we conclude that the pitch grows for increasing tip velocity.

Note that from the measurement of p and ζ , the helix geometry provides a simple way to measure the tube radius r and conse-

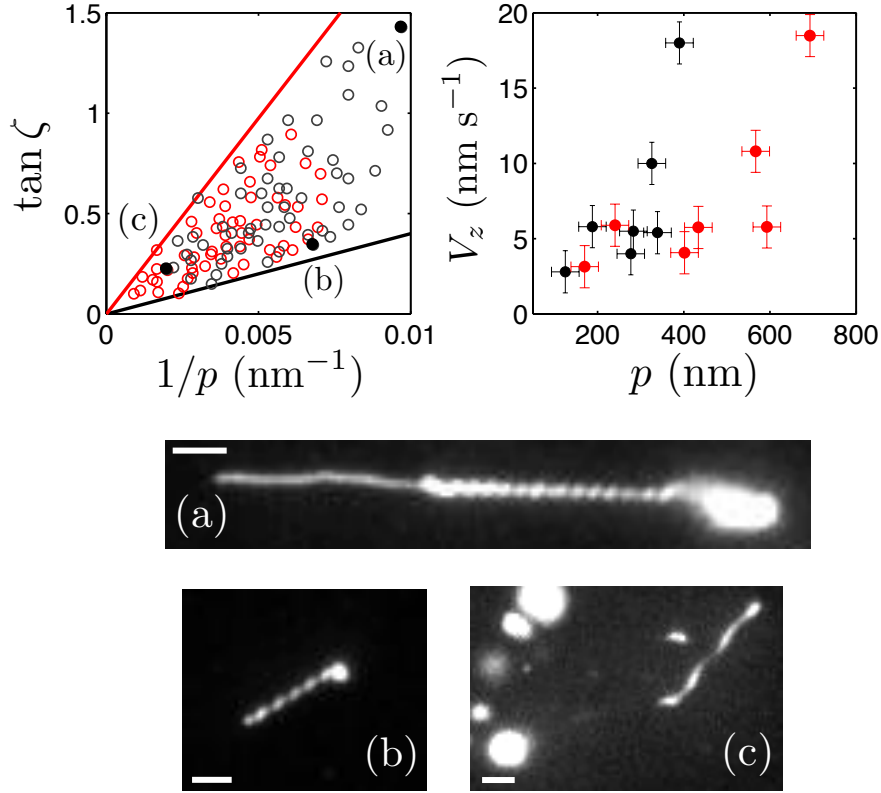


Fig. 4.11 (Top, left) $\tan \zeta$ vs $1/p$ plot showing 57 observations of helical nanotubes (grey circles) and the shifted data by assuming all MTs have 14 pf (red circles) with a superpitch of $6 \mu\text{m}$. The two straight lines show the lower limit $R_0 = 40$ nm (black line) and the upper limit $R_0 = 195$ nm (red line). The measurement error is $\pm 10^{-3} \text{ nm}^{-1}$ in the horizontal axis and ± 0.1 in the vertical axis. (Top, right) On-axis tip velocity versus the angular pitch. (Bottom) TIRF images of helical tubes for the points (a),(b) and (c) in Fig. 4.11 (top, left). Scale bars $2 \mu\text{m}$.

quently the membrane tension γ , which is usually subject to larger uncertainty than the bending rigidity, provided that the distance between the MT and the tube is known. A simple estimation based on a size ~ 5 nm for the biotin-streptavidin-biotin complex, a motor domain of KIF1A of ~ 6 nm [Okada and Hirokawa, 2000], and a contour length of the construct neck linker of ≈ 8 nm yields $R \simeq 12 - 30$ nm and thus a tube radii variability of $r \simeq 10 - 180$ nm. Assuming $\kappa = 10k_B T$ we estimate the membrane tension to be in the range $\gamma \simeq 3 \times 10^{-4} - 10^{-1}$ pN/nm and $F \simeq 1 - 20$ pN.

4.3 *In silico* model for longitudinal tube pulling

To understand at a quantitative level the on-axis cooperative force generation of single-headed KIF1A, we extend our previous theoretical approach in Section 3.1 in order to include the kinetics of attachment/detachment between the tube and the MT and to mimic the conditions of the *in vitro* system. We assume that the arrangement of motors at the tip is such as depicted in Fig. 4.10b (left) where they occupy three different pf tracks, similarly to the case of conventional kinesin, as discussed in Ref. [Campàs et al., 2006].

4.3.1 Description of the model

We illustrate the problem of tube-pulling for a tube of radius r and extraction force F , considering N motors in the vesicle reservoir and extending the model presented in Section 3.1. We distinguish two main regions in the system: the tube region and the vesicle region (Fig. 4.12b). For simplicity we will neglect interactions between motors in neighbouring pfs and assume that the on-axis cooperativity can be reduced to a single-pf problem, scaling down the total force F and the motor density ρ_∞ by a factor 3.

4.3.1.1 Tube region

A subset of motors $N_t \subset N$ are found in the tube region at time t . A motor i from this subset is found in state $k_i(t)$ at time t , where k_i is a discrete stochastic variable. Motors can be detached from the MT ($k_i = 0$), strongly bound to the MT ($k_i = 1$) or weakly bound to the MT ($k_i = 2$). In all cases, motors are also bound to the tube considered as a soft cargo. The dynamics of each motor is different depending on the region where it is found (A, B or C, see Fig. 4.12a). Next we describe the dynamics in each region:

Region A corresponds to the region in between the tube and the MT, where motors can be either weakly or strongly bound to the MT (i.e. $k_i \neq 0$). In this region the dynamics reads:

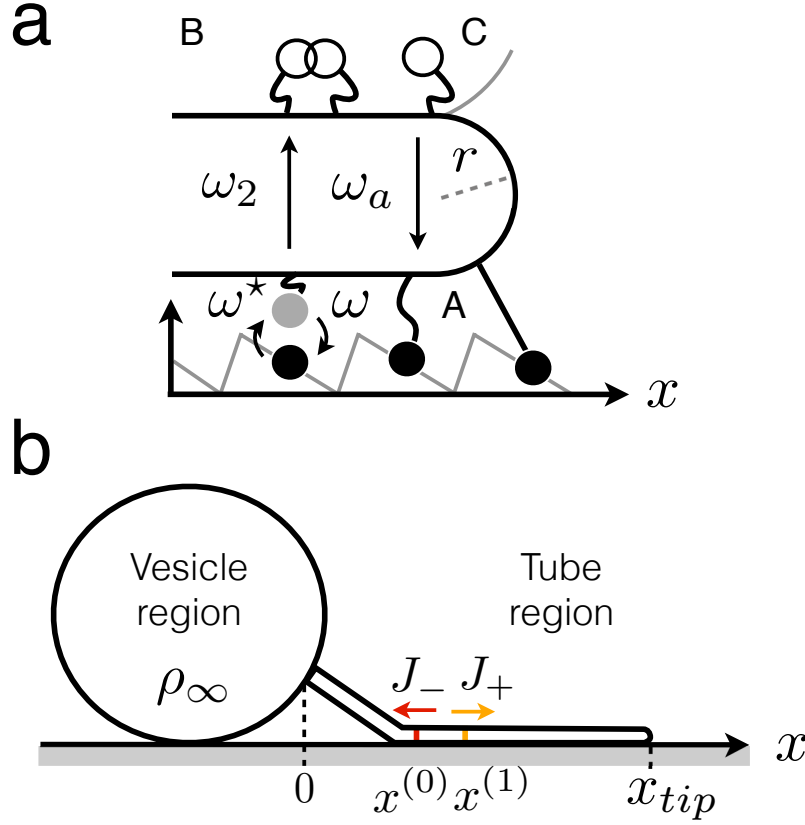


Fig. 4.12 Schematic description of the *in silico* model. a) Tube tip: three different regions can be identified in the tube region (A, B and C). In region A, motors are either strongly bound (state 1, black circles) or weakly bound (state 2, grey circles) to the MT. They get excited and decay with average rates ω^* , ω respectively. In region B, motors are detached from the MT (state 0, white circles) and diffuse freely outside the curved region of size r in the tip. Overlapping is allowed to account for the two-dimensional diffusive motion of motors on the membrane. Motors detach from state 2 and attach from state 0 with mean rates ω_2, ω_a respectively. Finally, in region C, detached motors feel a soft repulsive potential V which prevents them to enter the curved region. b) Tube extracted from a GUV with surface density of motors ρ_∞ . An influx J_+ of motors enters the tube region at $x^{(1)}$ and an outflux J_- enters back to the GUV at $x^{(0)}$.

$$\lambda \dot{x}_i = -U'(x_i, k_i) - \sum_{j \in \mathcal{S}} W'(x_i - x_j) - F \delta_{x_i, x_{\max}} + \zeta_i^{(D)}(t) \quad (4.4)$$

where λ is the friction coefficient, such that the diffusion coefficient follows the Einstein relation $D = k_B T / \lambda$. $U(x_i, k_i)$ is the potential motors feel depending on the state k_i . In the strongly bound state ($k_i = 1$), motors feel a periodic ratchet potential of

asymmetry a and periodicity l . On the other hand, in the weakly bound state ($k_i = 2$) they feel a constant potential $U(x_i, 2) = U_2$. W accounts for the motor-motor interaction potential and is taken as a truncated Lennard-Jones potential as in Section 3.1.1. The i -th motor interacts only with a subset of motors $\mathcal{S}(t)$ at time t which are bound to the MT, i.e. $\mathcal{S}(t) = \{j | j \neq i, k_j(t) \neq 0\}$. $\zeta^{(D)}(t)$ is a Gaussian white noise with delta correlation in time $\langle \zeta_i^{(D)}(t) \zeta_j^{(D)}(t') \rangle = 2k_B T \lambda \delta_{ij} \delta(t - t')$. Finally x_{\max} corresponds to the position of the foremost motor in the system.

In region B, motors are detached from the MT ($k_i = 0$) and undergo free diffusion on the membrane tube outside the curved region in the tip of size r . Defining $\xi_i = x_i - x_{\text{tip}}$ as the relative distance between the position of the i -th motor and the tip position x_{tip} , the condition for a detached motor to be in region B is $|\xi_i| > r$. The dynamics reads:

$$\lambda_t \dot{\xi}_i = \zeta_i^{(D_i)}(t) \quad (4.5)$$

where λ_t , D_t are the friction and diffusion coefficients on the membrane tube respectively. We notice there is no interaction potential for the motors in this region since we allow overlapping to account for the two-dimensional diffusive motion of motors on the tube. In this way, motors are no longer ordered respect to their label i . Region C corresponds to the curved region of the tip where $|\xi_i| < r$. In this case, we neglect noise and the dynamics simply read:

$$\lambda_t \dot{\xi}_i = -V'(\xi_i) \quad (4.6)$$

with a repulsive potential V in the form of a truncated Morse potential:

$$V(\xi_i) = \epsilon_m \left(e^{\frac{2(r_0 - |\xi_i|)}{b}} - 2e^{\frac{r_0 - |\xi_i|}{b}} \right) \quad (4.7)$$

which is valid for $|\xi_i| < r_0$ and is zero otherwise. The position $r_0 \equiv r + \sigma + b \ln 2$ is such that the potential has minimum energy $-\epsilon_m$, with b being a characteristic length. This is an *ad hoc* choice to simply prevent motors to enter in region C. We adjust the Morse parameters to ensure a soft short-ranged repulsive poten-

tial preventing the detached motors to enter the curved region ($b/l = 0.45$, $\epsilon_m/k_B T = 2 \cdot 10^{-6}$). We associate the dynamics of the tube tip with the dynamics of the foremost motor i.e. $\dot{x}_{\text{tip}} = \dot{x}_{\text{max}}$. If the foremost motor detaches, the tube retracts with a retraction velocity $\dot{x}_{\text{tip}} = -F/\lambda_m$ until a new bound motor is found. λ_m is an effective friction parameter which is inferred from the retraction velocity of motors $v_r \simeq 100 \mu\text{m/s}$ observed experimentally for $F \simeq 20 \text{ pN}$ [Campàs et al., 2008]. Finally we estimate the number of bound motors in the tip over time by counting the number of consecutive bound motors pulling on the tube, where we define two motors as consecutive if they are at a distance less than $\delta_D = \sqrt{4D/\omega}$. Also, we estimate the density of bound motors from the set of positions of the bound motors at each time step of the simulation using a smoothing technique. We define the density of motors at each point as the number of bound motors in a characteristic bandwidth divided by its length. The bandwidth size is taken $\simeq 100 \text{ nm}$, of the order of the pixel size in our experiments.

Next we describe the state kinetics. All state transitions in the system are stochastic with dwell times which are exponentially distributed. Motors are excited from state 1 to 2 from localized regions of size δ near the minima of the ratchet potential with average rate ω^* . On the other hand, decays from state 2 to 1 are delocalized with average rate ω . Attachment events occur with average rate ω_a . However, they are not always possible due to excluded volume interactions in region A. Thus, we say that a motor i will only attach if it can find a free site i.e. $\sum_{j \in \mathcal{S}} W'(x_i - x_j) = 0$. We include exponentially dependent detachment kinetics on the force. *In vitro* experiments using single-headed kinesin have shown that the detachment rate at zero load is much larger in the weakly bound state ($\sim 1 \text{ s}^{-1}$) than in the strongly bound state ($\sim 0.01 \text{ s}^{-1}$) [Uemura et al., 2002]. We choose to neglect detachment from state 1 for simplicity. The addition of detachment in state 1 leads to similar dynamics in the system. The average detachment rate from state 2 of the i -th motor at time t , will depend on the passive forces the i -th motor feels over time:

$$\omega_2(i, t) = \omega_2^0 \exp\left(\frac{|\tilde{F}_i(t)|d}{k_B T}\right) \quad (4.8)$$

where ω_2^0 is the detachment rate at zero load from state 2, $\tilde{F}_i(t)$ is local time-averaging, over an appropriate time window, of the noisy signal of the passive forces $F_i(t) = -\sum_{j \in \mathcal{S}} W'(x_i - x_j) - F\delta_{x_i, x_{max}}$ and d is a characteristic distance which is typically 2 to 4 nm for kinesin [Uemura et al., 2002, Schnitzer et al., 2000, Schroeder3rd et al., 2012]. We used a simple smoothing technique by choosing $\tilde{F}_i(t)$ as the time average of F_i in the region $[t - \tau, t]$, where τ is the window size. This is taken as $\tau = 100$ ms, which is big enough to average the passive forces a motor feels during a hydrolysis cycle (~ 10 ms), and smaller than the time scale of the tube motion (~ 1 s). Variations of τ around this value did not affect significantly the resulting dynamics of the system.

4.3.1.2 Vesicle region

The vesicle region is described as a motor reservoir with surface density of motors ρ_∞ . Motors diffuse on the vesicle and eventually they enter the tube region through the boundary $x = x^{(0)}$ (Fig. 4.12b). Hence, in the boundary we have an influx of motors $J_+(t)$ which are bound to the MT and to the tube. Experimental evidences show that it is reasonable to neglect the influx of motors only bound to the tube [Leduc et al., 2004]. On the other hand, there is also a flux of motors leaving the tube $J_-(t)$ by diffusion. Since KIF1A is able to make large backward excursions in the weakly bound state, for practical reasons it is important to ensure that motors will not fluctuate near the boundary $x = x^{(0)}$. Hence, we let motors appear at $x^{(1)} = x^{(0)} + \delta_D$, (Fig. 4.12b) and let $x = x^{(0)}$ act as an absorbing boundary condition for the motors that leave the tube region. The number of motors in this region $N_t(t)$ will depend on time through the flux balance:

$$\frac{dN_t}{dt} = J_+ - J_- \quad (4.9)$$

Experimental evidences indicate that Eq. 4.9 reaches a quasi-steady state [Leduc et al., 2004]. Far from the tip, in the quasi-steady

state the density of motors bound to the tube in the mean-field limit reads [Campàs et al., 2008]:

$$\rho_b = 2\pi r \rho_\infty \frac{\omega_a}{\omega_d^0 + \omega_a} \quad (4.10)$$

where in our case $\omega_d^0 = \omega_2^0/(1 + \beta)$ is the motor detachment rate at zero load and $\beta = \omega/\omega^*$. Therefore, at the boundary $x^{(1)}$, the average influx of motors will be $\langle J_+ \rangle = \rho_b V_0$. In our simulations, a new motor will be introduced in the system stochastically every certain time taken from an exponential distribution with mean rate $\langle J_+ \rangle$. Finally, motors crossing the boundary $x^{(0)}$ will be incorporated in the vesicle reservoir.

4.3.1.3 Parameters for the *in silico* model

The choice of parameters describing KIF1A without including attachment/detachment kinetics was already discussed in Section 3.1 and in Table 3.1. Here, we choose β such that the velocity of a single KIF1A at zero load is similar to the experimental gliding velocities ~ 80 nm/s (see Section 4.2.1.3). The resulting value is $\beta \simeq 7.5$. The detachment rate of KIF1A has been found to be $\omega_d \sim 0.1$ s⁻¹. Using our value of β we get $\omega_2^0 \simeq 1$ s⁻¹, which is in agreement with the results in Ref. [Uemura et al., 2002]. On the other hand, the allowed range of attachment rates reported in the literature is 0.1 s⁻¹ $\leq \omega_a \leq 10$ s⁻¹ [Nishinari et al., 2005], and we will take an intermediate value.

Next we discuss the parameters concerning the tube pulling system. The radius of the tube r and the threshold force to extract a tube F depend on the bending rigidity κ and the surface tension of the membrane γ through the expressions $r = \sqrt{\kappa/(2\gamma)}$ and $F = 2\pi\sqrt{2\kappa\gamma}$ as discussed in Section 4.1. κ is assumed to be roughly constant in experiments whereas γ can vary substantially. Although in principle the value of surface tension can be adjusted *in vitro* by changing the osmolarity of the solution inside the vesicle, the statistical dispersion of γ from vesicle to vesicle is large and this makes it difficult to control this parameter. The typical range of γ implicitly obtained through our data analysis

is $3 \times 10^{-4} - 10^{-1}$ pN/nm. The density of motors in the vesicle can be obtained assuming that each lipid occupies a surface of approximately 0.4 nm^2 . In the experiments, we used different molar fractions of biotinylated lipids in the range 0.01-1 mol %. This range corresponds to $250 - 25000 \mu\text{m}^{-2}$. The diffusion of motors on the tube is much larger than the typical diffusion of KIF1A motors in the weakly bound state $D_t \gg D$. Typically, $D_t \simeq 1 \mu\text{m}^2/\text{s}$ [Leduc et al., 2004]. Table 4.1 shows a summary of the selected values for the different parameters.

Parameter	Value
Periodicity length MT	$l = 8 \text{ nm}$
Motor size	$\sigma = 4.2 \text{ nm}$
Asymmetry ratchet potential	$a = 1.8 \text{ nm}$
Excitation window	$\delta = 0.16 \text{ nm}$
Characteristic detachment distance	$d = 3 \text{ nm}$
Ratchet energy maximum	$U = 10k_B T$
Vesicle tension	$\gamma = 0.05 \text{ pN/nm}$
Bending rigidity	$\kappa = 10k_B T$
Vesicle motor density	$\rho_\infty = 200 - 1000 \mu\text{m}^{-2}$
Diffusion coefficient (MT)	$D = 20 \text{ nm}^2/\text{ms}$
Diffusion coefficient (tube)	$D_t = 1 \mu\text{m}^2/\text{s}$
Excitation rate	$\omega^* = 33 \text{ s}^{-1}$
Decay rate	$\omega = 250 \text{ s}^{-1}$
Detachment rate (zero load)	$\omega_2^0 = 1 \text{ s}^{-1}$
Attachment rate	$\omega_a = 3 \text{ s}^{-1}$

Table 4.1 Parameters used in the *in silico* model.

4.3.2 Results

In Fig. 4.13 (left), the simulated dynamics of the tube tip and the motor density are shown. Motors work collectively at the tube tip against the external load by means of the cooperative mechanism previously reported in Chapter 3 for the case of no attachment/detachment kinetics. Here, the exchange kinetics controls the size of the tip cluster, together with other parameters

such as the potential height U , ω^* and γ .

Although many motors are involved in the process, the tube can be extracted provided that an average number of motors n_c are packed at the tip sharing the load. For typical values $U = 10 - 20k_B T$, $\gamma \simeq 0.1$ pN/nm and ω^* on the order of hundreds of Hz, we have $n_c \simeq 12$, only slightly larger than the typical values of 6–9 estimated for experiments with conventional kinesin [Campàs et al., 2006]. We notice that motors not only accumulate at the tube tip, but they are also present with significant density all along the tube. In Fig 4.13 (top, left), we show the tube growth for $\rho_\infty = 1000 \mu\text{m}^{-2}$ and $\gamma = 0.05$ pN/nm. The force per pf is ~ 4 pN, the average number of bound motors at the tip cluster is ~ 15 and the tube grows with a rather constant velocity ~ 15 nm/s. In this case, the number of motors at the tip fluctuates

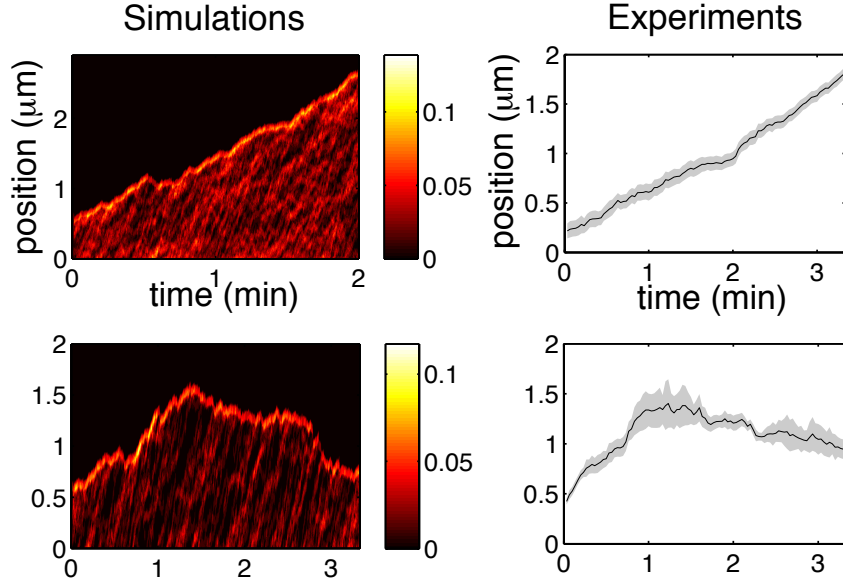


Fig. 4.13 Growth (top) and bistable motion (bottom) of a membrane tube. (Left) Simulation of the motor density plot with $\rho_\infty=1000 \mu\text{m}^{-2}$ (top) and $\rho_\infty=200 \mu\text{m}^{-2}$ (bottom). The parameters of the model are specified in Table 4.1. The color bar indicates the density of bound motors (arbitrary units). (Right) Experimental trajectories of the tube tip for 0.1 % of biotin binding sites. The grey region depicts the uncertainty of the tip position from the fitting procedure.

with an average value which is above the threshold value for tube extraction. However, in Fig. 4.13 (bottom, left), the influx of motors is reduced ($\rho_\infty = 200 \mu\text{m}^{-2}$), and the average number of motors is close to the critical value. In this case, we observe rapid and slow retractions which are rescued by motor density waves advancing along the tube. In Fig. 4.14, the instantaneous tip velocity distribution is shown for the data in Fig. 4.13 (left, bottom). We observe that the distribution qualitatively resembles the experimental results in Fig. 4.8, capturing the asymmetry of the distribution. Our *in silico* model quantitatively reproduces both the growth and the bistable motion of tubes as shown in Fig. 4.13.

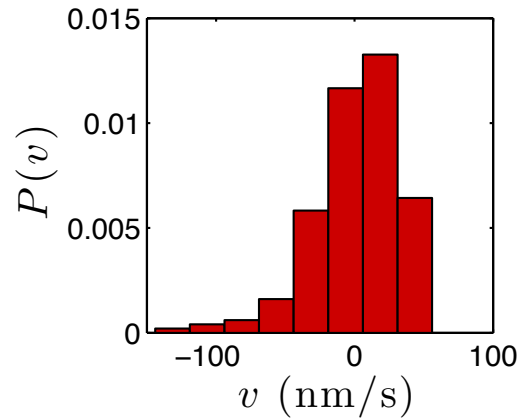


Fig. 4.14 Instantaneous tip velocity distribution using the data in Fig. 4.13 (bottom, left). For illustrative purposes, the time window was chosen 1 s to improve the statistics at the expense of increasing the dispersion.

4.3.3 Mean-field model for helical tube formation

Finally, we introduce a mean-field model to understand the role of off-axis forces in the dynamical selection of the pitch. We study the motion of a single KIF1A motor on a two-dimensional MT lattice, as described in Section 3.2.2 using a two-dimensional oblique Bravais lattice with directions \mathbf{r}_1 and \mathbf{r}_2 forming an angle

θ . The vectors \mathbf{r}_1 and \mathbf{r}_2 describe the on-axis and off-axis motion respectively. For simplicity we will consider the off-axis and on-axis movements to be independent processes, which has been shown to be a reasonable assumption for single-headed kinesin-1 [Yajima and Cross, 2005]. Motors advance along their pf tracks and share the external load. We will assume motors can change pfs whenever they are in the diffusive, weakly bound state. The motion can thus be understood as the superposition of two noise-driven ratchets of periodicities l_1 and l_2 , defined by two asymmetry parameters a_1 and a_2 . For each component of the velocity, we obtain a linear velocity-force relationship with velocity at zero load $v_i(0)$ and stall force F_i^s , $i = 1, 2$ (see Section 3.2.2). Defining the ratio $\bar{v} \equiv v_1/v_2$, the average angle of a single motor helical trajectory ζ_1 can be found as a function of \bar{v} and θ through the expression $\cot \zeta_1 = \bar{v} \csc \theta + \cot \theta$. The average pitch of a helical trajectory around the MT will be given by $P_1 = 2\pi R_{MT} \cot \zeta_1$ where R_{MT} is the MT radius. Notice that approximating $\theta \simeq \pi/2$, we have $P_1 \simeq 2\pi R_{MT} \bar{v}$ and the pitch is proportional to \bar{v} . At zero load we obtain a simple expression for the single-motor average pitch $P_1(0) \simeq 2\pi R_{MT}(l_1 - 2a_1)/(l_2 - 2a_2)$. Considering the typical values for a MT lattice, we have $l_1 \simeq 8$ nm, $l_2 \simeq 6$ nm and $\theta = 81^\circ$ [Chrétien and Wade, 1991]. Assuming zero load, $R_{MT} \simeq 12$ nm and $a_1 \sim a_2$ we get $P_1 \sim 100$ nm, which coincides with the order of magnitude of the reported pitch for single-headed kinesin-1 [Yajima and Cross, 2005], a motor relatively similar to KIF1A. In order to estimate F_2^s , we adjust the asymmetries a_1 and a_2 to match the experimental pitch of single-headed kinesin-1 ($\simeq 300$ nm), thus obtaining $F_2^s \simeq 0.04$ pN for $a_1/l_1 = 0.2$ and $a_2/l_2 = 0.4$.

The pitch of the tube will result from the competition of the total on-axis and off-axis forces, a nontrivial combination of two collective effects that depend on the actual distribution of the motors at the tip cluster and the different mechanisms of cooperation for serial and parallel arrangements of motors. In contrast to the single motor case, if the applied force is exerted by the membrane, the force components F_i are dependent on ζ and θ through $F_i = F g_i(\theta, \zeta)$, where $g_1(\theta, \zeta) = \cos \zeta - \sin \zeta \cot \theta$, $g_2(\theta, \zeta) = \sin \zeta / \sin \theta$ and F is the extraction force. Since $g_i(\theta, \zeta) > 0$ due to the action of the external loads, we have $\zeta \in [0, \theta]$. For simplicity, we assume

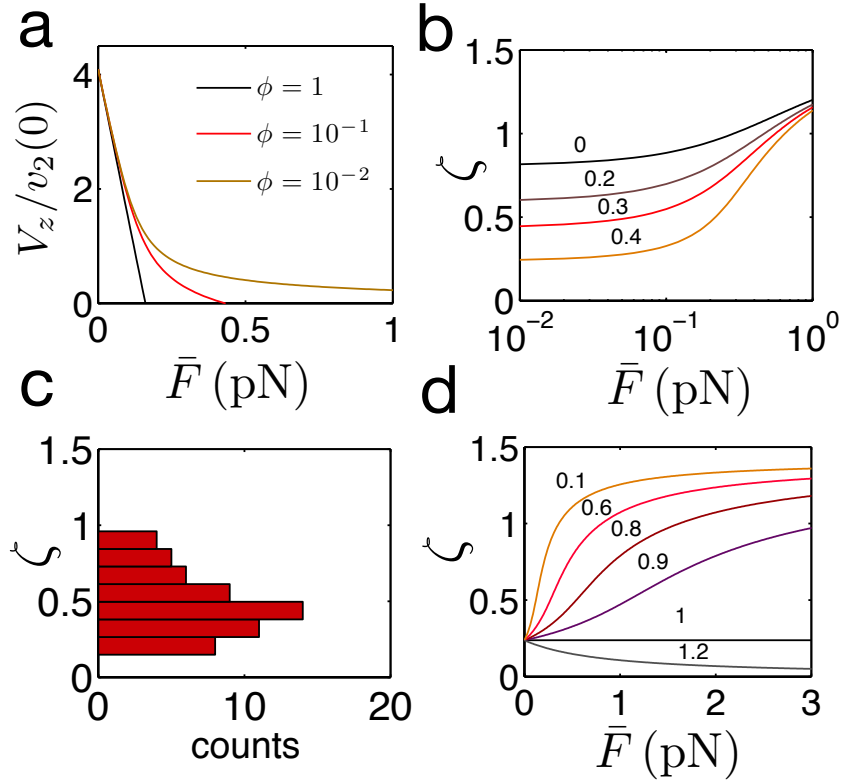


Fig. 4.15 Mean-field description of helical tube formation. a) Dimensionless on-axis velocity of the tube respect to \bar{F} for different ϕ and $a_2/l_2 = 0.4$. We notice the apparition of long-tails in the velocity-force relationship for decreasing ϕ . b) Angle dependence on the force per motor \bar{F} for different a_2/l_2 values and $\phi = 0.5$. c) Experimental angle ζ distribution of 57 standing helical nanotubes. d) Angle dependence on the force per motor \bar{F} for different ϕ values and $a_2/l_2 = 0.4$. $\theta = 81^\circ$, $F_s^1 = 0.15$ pN and $a_1/l_1 = 0.2$. Angles are shown in radians.

that each component of the total force is equally shared by a certain group of motors. Therefore, $V_i(F_i) = v_i(F_i/N_i)$, where N_i is the number of motors generating force along the i -th component. Defining $\bar{V} \equiv V_1/V_2$ we have:

$$\bar{V} = \frac{F_1^s - g_1 \bar{F}}{F_2^s - \phi g_2 \bar{F}} \quad (4.11)$$

where $\bar{F} \equiv F/N_1$ is the effective force per motor and $\phi \equiv N_1/N_2$. On the other hand, we know that $\bar{V} = -\cos \theta + \sin \theta \cot \zeta$. By combining the last expression and Eq. 4.11, we obtain a transcendental

equation for ζ which can be solved numerically. The dynamics of a helical tube and the angle selection are crucially affected by the phenomenological parameter ϕ . In Fig. 4.15a, for $\phi = 1$, the on-axis velocity-force relationship is linear and ζ is independent of the extraction force F . However, for $\phi < 1$, long tails appear on the on-axis velocity-force relationship and ζ becomes strongly dependent on F (Figs. 4.15b and d). In the latter case, the on-axis velocity may decrease by a factor four under moderately large forces, consistently with our tube-pulling data in comparison with gliding assays (see Section 4.2.1.3). In Fig. 4.15c the experimental angle distribution is shown by taking the average angle of 57 helical tubes. We compare the data with the ζ dependence on \bar{F} for different values of ϕ (Fig. 4.15d). We notice that considering $\bar{F} \simeq 1$ in the experiments, the range $\phi \simeq 0.6 - 1.2$ approximately bounds the experimental angle values. We can also infer the total off-axis force exerted by the motors F_{off} and N_2 using energetic arguments (see Appendix D), which leads to the lower bound $F_{\text{off}} \simeq 0.04 - 2$ pN and $N_2 \gtrsim 1 - 50$ motors. On the other hand, surprisingly no helical tube retractions were observed. This fact may be a signature of the long-tails in the velocity-force curves as shown in Fig. 4.15a, and consequently an indirect evidence that typically $\phi < 1$.

4.3.4 Conclusions

In this chapter we have shown that, despite the extreme inefficiency of individual single-headed KIF1A, these motors are able to cooperate collectively to extract membrane tubes, thus validating our initial theoretical predictions. Additionally, we found the surprising formation of helical tubes around microtubules. This entails an impressive capability of single-headed KIF1A motors to exert significant off-axis by virtue of the diffusive state. Accordingly, this state affords two complementary strategies to overcome obstructions: brute force and manoeuvring capability. In a series configuration (in line) it enables the generation of large forces by accumulation of motors, a possibility not available for conventional kinesin [Rai et al., 2013, Furuta et al., 2013]; in a

parallel configuration (side by side) it enables lateral displacement of the cargo. We have restricted ourselves to the monomeric form of KIF1A, as the simplest and most amenable case study, but at the same time, the weakest and most inefficient form. Many evidences now support the fact that KIF1A is largely regulated by a monomer-to-dimer transition and acts as a dimer *in vivo* [Tomishige et al., 2002, Soppina et al., 2014]. We expect dimeric KIF1A to enable a trade-off between cooperative force generation and high speed due to the combination of diffusion motion and processive motility.

Altogether, our results suggest that the existence of a diffusive state is a key distinctive feature that makes KIF1A motors genuinely cooperative for membrane-bound cargo transport and could explain their specificity to axonal vesicular traffic.

Acknowledgments

The experimental work in this chapter was conducted in FOM Institute AMOLF (Amsterdam, Netherlands) in close collaboration with Dr. S. Roth and Prof. M. Dogterom. In particular, the protocols for cell culture and purification of the KIF1A construct were designed by Dr. S. Roth. We also thank Dr. F.-C. Tsai (AMOLF Institute) for her tips on GUV formation. Finally, we are specially grateful to Prof. N. Hirokawa (University of Tokyo, Japan) for kindly providing us the KIF1A construct A382.

Part II
Dynamical instabilities of motor
assemblies

Chapter 5

Introduction

Spontaneous symmetry breaking, oscillations or waves can be observed in many cellular processes. These phenomena can emerge as the result of the self-organized behaviour of interacting components inside the cell [Kruse and Jülicher, 2005]. These constitute open nonlinear dynamical systems, where there is a continuous flow of energy through the system from its environment. We will focus on self-organized mechanical oscillations in cytoskeletal structures, which play a crucial role in many cellular processes. Some prominent examples are mitotic and meiotic oscillations [Grill et al., 2005, Vogel et al., 2009], spontaneous oscillations of auditory hair cells [Camalet et al., 2000], oscillatory regimes in muscle contraction [Ishiwata et al., 2010] or the beating of cilia and flagella [Camalet et al., 1999]. In the language of dynamical systems, positive feedback loops can destabilize the non-moving state leading to oscillations or waves in spatially extended systems. The shape, amplitude and period of oscillations are then given by the particular nonlinearities in the system. In this part of the thesis, we will study the nonlinear collective action of motor assemblies in the case of a minimal actomyosin system and in the case of axonemal beating driven by dynein motors.

5.1 Muscle contraction

Muscles function as mechanical engines to produce force and motion in most animals. They are responsible for locomotion, contraction and movement in general. Their structure is mainly composed of actin and myosin, which organize in a highly ordered structure. Vertebrate and many invertebrate muscles can be categorized in three classes: skeletal, smooth and cardiac muscle [Lodish et al., 2000, Katz, 2010]. Skeletal muscles connect the bones and are used to coordinate complex activities, being able to generate rapid movements by contracting fast. By contrast, smooth muscle cells contract and relax slowly, controlling the diameter of blood vessels and propelling food along the gastrointestinal tract. Finally, cardiac muscle is in charge of the coordinated contraction of the heart.

We will focus on the structure of skeletal muscle, which is the most representative and characteristic type of muscle tissue. Skeletal muscle is formed by a bundle of muscle cells (myofibers) that are typically cylindrical (1-40 mm in length and 10-50 μm in width) [Lodish et al., 2000]. At the same time, myofibers are packed with myofibrils, filament bundles that extend along the cell. Myofibrils are further subdivided in primordial contraction units named *sarcomeres*. Sarcomeres contain thick filaments (composed of myosin) and thin (actin) filaments (see Fig. 5.1a,b). They are 2.5 μm long and upon contraction they can be shortened about 70 % of their uncontracted, resting length. Microscopic studies showed that thick and thin filaments did not change in length while the sarcomere shortened. This fact led to the “sliding filament model” for skeletal muscle contraction [Huxley and Niedergerke, 1954, Huxley and Hanson, 1954]. This model states that ATP enables myosin motors in thick filaments to walk along thin filaments, in such a way that the two sets of filaments slide past each other and the sarcomere unit contracts (Fig. 5.1c).

How is muscle contraction regulated? As in many other cellular processes, this mechanism is regulated by the concentration of Ca^{2+}

ions in the cytosol. Typically, a nerve impulse reaches a skeletal muscle cell, producing a change in the electric potential across the plasma membrane. Ion channels are able to translate the electric signal into a chemical signal, rising Ca^{2+} levels in the cytosol. Thin filaments contain two main types of actin-binding proteins namely tropomyosin and troponin [Gunning, 2008, Zot and Potter, 1987] (see Fig. 5.1a, bottom). Tropomyosin is a ropelike molecule of ~ 40 nm in length which binds to seven actin monomers on an actin filament. On the other hand, troponin is a protein complex which is able to bind to Ca^{2+} ions. In the absence of calcium, myosin motors can bind to thin filaments but the tropomyosin-troponin complex prevents them to slide along. Upon Ca^{2+} binding to troponin, the last complex triggers the motion of tropomyosin on the surface of an actin filament, enabling myosin motors to bind to the neighbouring binding sites and move the thin filaments [Lehman et al., 2001, Lehman et al., 1994, Spudich and Watt, 1971]. Hence, sufficiently high Ca^{2+} concentrations ($\gtrsim 1 \mu\text{M}$) diminish the inhibition of the tropomyosin-troponin complex to myosin, thus enabling contraction.

Calcium oscillations in the cytosol can induce the periodic contraction of sarcomeres. However, this is not a self-organized phenomenon but a periodic mechanical oscillator driven by an external stimulus. This strategy is used by butterflies or locust to generate a wing thrust which is synchronous to nervous impulses (see Fig. 5.2, bottom). In contrast, wasps, bees and some beetles are known to exhibit a wing thrust which is asynchronous to the activating nervous impulses (see Fig. 5.2, top) [Pringle, 1977, Syme and Josephson, 2002]. This type of asynchronous oscillations are also referred to as *spontaneous*, since their origin is intrinsic of the muscle. Skinned skeletal and cardiac muscle fibers have also been shown to exhibit spontaneous oscillations *in vitro* under various conditions [Fujita and Ishiwata, 1998, Ishiwata et al., 2007]. Hence, it has been proposed that molecular motors may act in some cases as auto-oscillators [Ishiwata et al., 2010]. Next we present a non-muscular example of spontaneous oscillations, the flagellar and ciliary beating.

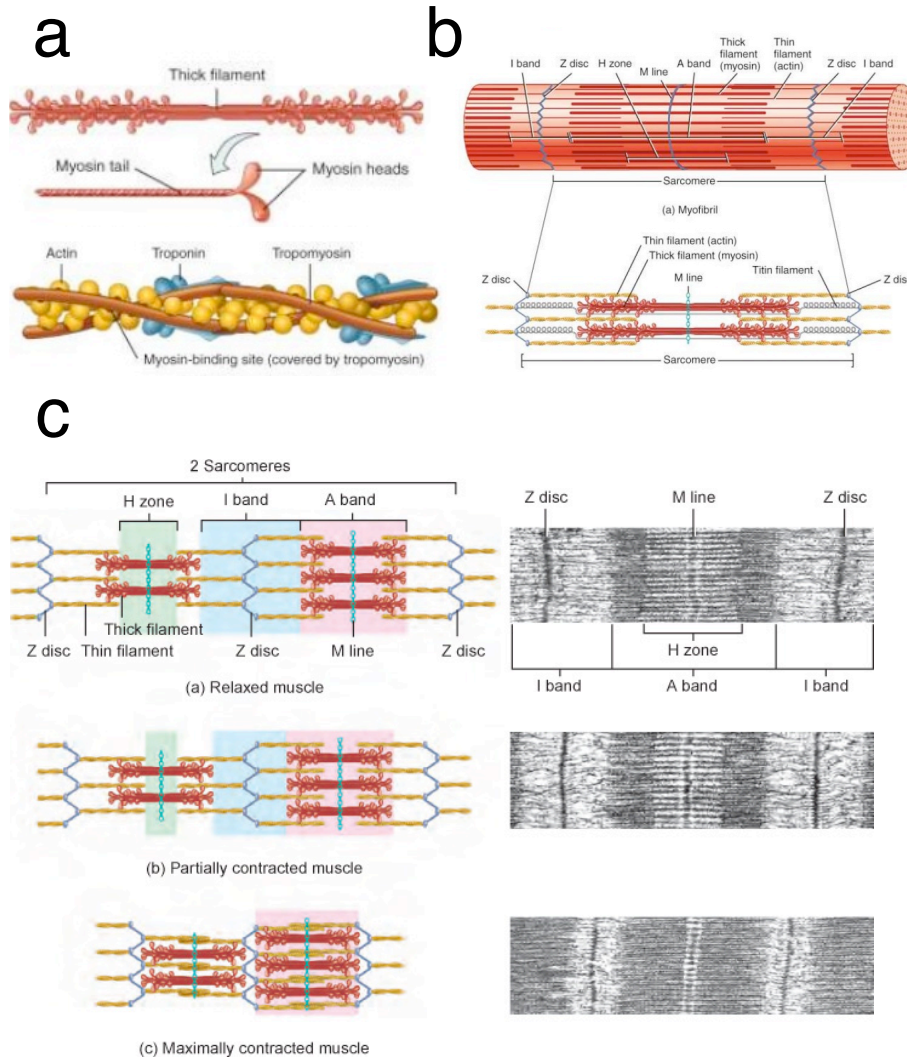


Fig. 5.1 Sarcomere contraction. a) Thick (top) and thin (bottom) filaments. Thick filaments are composed of myosin motors and thin filaments are F-actin together with tropomyosin-troponin complexes which regulate myosin binding. b) Myofiber composed of sarcomere units. Z-discs separate adjacent sarcomeres, the M-line bisects the sarcomere unit, the H-zone indicates the non-overlapped region and the I-band separates overlapped regions. c) Sarcomere contraction. (left) Sketch of the sliding filament model. (right) Electron micrograph of a contracting myofiber. Modified from [Tortora and Derrickson, 2013].

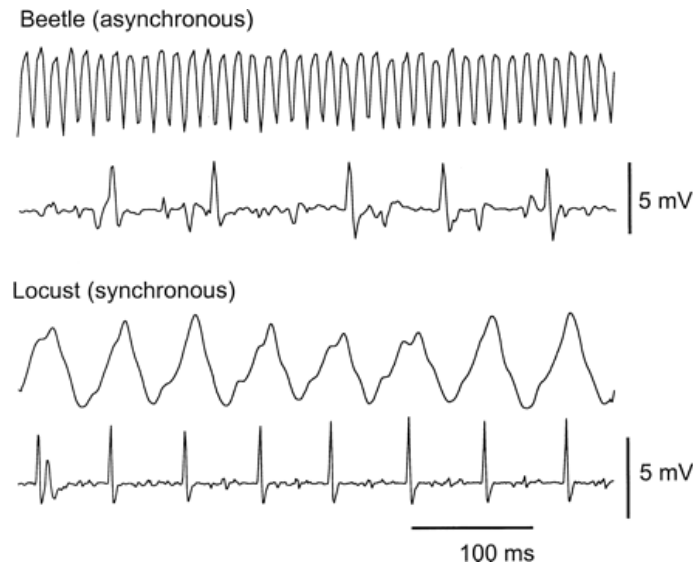


Fig. 5.2 Wing thrust during tethered flight (upper trace) and muscle action potential (lower trace) for an asynchronous (beetle) and synchronous (locust) flight muscle. The asynchronous muscle corresponds to the basalar muscle of the beetle *Cotinis mutabilis* whereas the synchronous muscle corresponds to the metathoracic tergosternal muscle of the locust *Schistocerca americana*. Modified from [Syme and Josephson, 2002].

5.2 Flagellar and ciliary beating

The origin of the eukaryotic flagellum and cilium is over 800 million years ago. These appendages are found in many protozoa and algae (see Fig. 5.3, a-f) and are crucial for cell motility, survival, development, cell feeding and reproduction of microorganisms [Ginger et al., 2008, Bray, 2000, Murase, 1992]. Flagellated organisms may use one (e.g. spermatozoa) or more appendages for propulsion (e.g. the green algae *Chlamydomonas reinhardtii* or *Paramecium tetraurelia*, see Fig. 5.3a-c). Eukaryotic flagella have a complex internal structure. The eukaryotic flagellum is mainly composed of a cytoskeleton superstructure named *axoneme*. This structure has a characteristic ‘9+2’ composition in many eukaryotic organisms, corresponding to 9 peripheral microtubule doublets in a cylindrical arrangement surrounding a central pair of microtubules (see Fig. 5.3g). Additional proteins such as the radial spokes (green) and nexin crosslinkers (pink) connect the center to the peripheral microtubules and prevent free sliding between the

microtubule doublets respectively. Each doublet consists of a 13 pf microtubule (A-tubule) in which dyneins are anchored at regular intervals along the length of the doublets, and a 10 pf microtubule (B-tubule), where neighbouring dynein motors bind to. Axonemal dyneins subdivide into inner (orange) and outer (red) arms, depending on their position (see Fig. 5.3g). Their arrangement is best characterized in *C. reinhardtii*. Outer arms consist of 3 different dynein heavy chains adopting a stacked arrangement whereas inner arms comprise 8 heavy chains: one heterodimer and six monomers [Roberts et al., 2013]. The axonemal structure presents slight variations among different species. Common variations of the ‘9+2’ axoneme are the presence of a permanent link between doublets 1 and 2 for *C. reinhardtii* (Fig. 5.3h,i) or the additional structure of a paraflagellar rod in trypanosomatids (Fig. 5.3j,k). In the last case, this external structure enables the parasite *Trypanosoma brucei* to propulse generating bihelical waves with alternating chirality separated by kinks [Rodríguez et al., 2009].

Early electron-microscope studies demonstrated that the bending of a cilium is accompanied by longitudinal sliding of its peripheral microtubular filaments relative to one another [Satir, 1965, Satir, 1968]. The *sliding mechanism* hypothesis was first directly verified with the observation of the relative motion of nanometer gold beads attached to outer and inner doublets in demembrated sea urchin sperm flagella [Brokaw, 1989]. In the presence of ATP, dyneins drive the sliding of microtubule doublets, generating a sliding force that can slide doublets apart if crosslinkers are removed [Summers and Gibbons, 1971]. Sliding is transformed into bending due to the presence of crosslinker proteins in the structure. Remarkably, this process is carried out in a highly coordinated manner, in such a way that when one team of dyneins in the axoneme is active, the other team remains inactive. In the case of the sperm flagellum, the coordinated mechanism leads to bending waves within a well-defined beat plane [Gaffney et al., 2011]. Coordination between the two teams is currently understood to be a self-organized process due to the coupling of dynein force generation and the geometry of the axoneme [Mitchison and Mitchison, 2010]. However, the precise mechanism is still under debate. Different mechanisms have been proposed to understand how the sliding

forces produced by dynein motors inside the flagellum result in the flagellar beat pattern. Coordinated beating has been hypothesized considering different mechanisms such as dynein activity regulation through local axonemal curvature [Brokaw, 1971, Hines and Blum, 1979], due to the presence of a transverse force (t-force) acting on the axoneme [Lindemann, 1994] or by shear displacements [Camalet et al., 1999, Camalet and Jülicher, 2000, Riedel-Kruse et al., 2007].

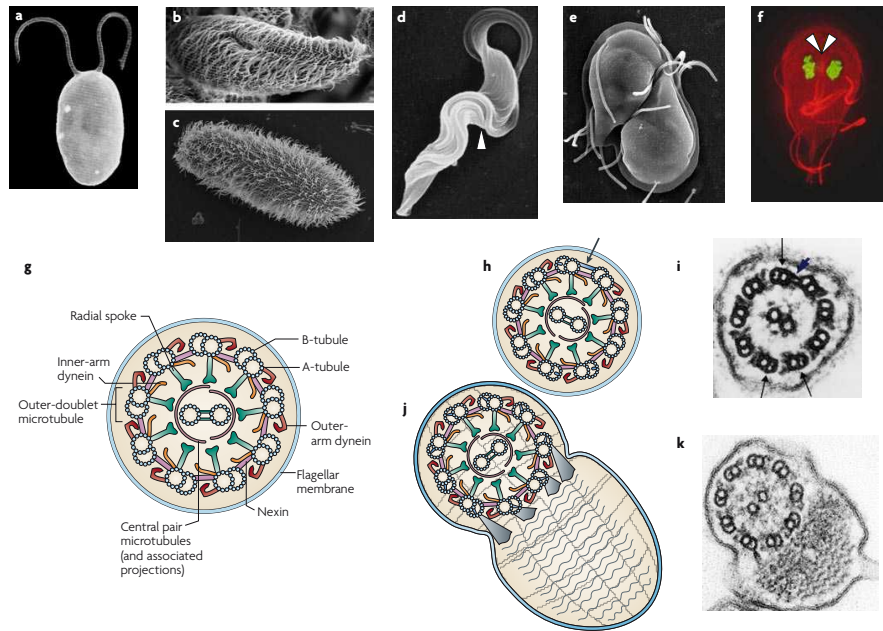


Fig. 5.3 Flagellate diversity. a) *Chlamydomonas reinhardtii*. b) Ventral and c) Dorsal views of *Paramecium tetraurelia*. d) *Trypanosoma brucei* bloodstream trypomastigote. e, f) *Giardia lamblia*, which coordinates duplication and segregation of four flagella pairs during its cell-division cycle. g) Schematic representation of an axonemal section which contains the canonical '9+2' structure, viewed as looking towards the distal end of the flagellum. Panels h-k show common variations of the '9+2' axoneme: h, i) In *C. reinhardtii*, doublets 1 and 2 are linked by a permanent bridge (arrow); j, k) In trypanosomatids a paraflagellar rod is attached along the length of the axoneme. Modified from [Ginger et al., 2008].

5.3 Positive feedback and negative damping

How can positive feedback lead to spontaneous symmetry breaking? Positive feedback loops can also be understood using the concept of negative damping [Jülicher et al., 1997, Howard, 2009]. When moving a spoon in a jar of honey, if we want to move the spoon faster it requires more force due to positive viscous damping. Negative damping would correspond to the inverse situation, namely that when increasing the speed, the spoon would lurch forward, something somehow counterintuitive. We present two different models which account for this effect in symmetric environments where motor assemblies drive positive feedback loops in the system: the two-state rigid model and the ‘tug-of-war’ model.

5.3.1 Two-state rigid model

We first present the case of a rigid motor assembly following Ref. [Jülicher et al., 1997]. We consider an assembly of N motors attached to a common backbone with positions $x_n(t) = X(t) + nq$, $n = 1, \dots, N$, and constant spacing q . The positions $x_n(t)$ are defined in the reference frame of an l -periodic polar filament, to which motors bind and unbind. Here, $X(t)$ denotes the position of the backbone over time respect to some rest position. We choose q/l to be irrational such that the periodicities of motor attachments and the filament are incommensurable. Finally, we associate two possible states $k = 1, 2$ to each motor as discussed in Section 2.6.1, such that they can bind and unbind from the filament with rates $\omega_2(x)$ and $\omega_1(x)$, respectively. The periodic potential landscape corresponding to state k reads $U_k(x)$.

The force that the n -th motor exerts on the backbone will be $f_n = -\partial_x U_k(x_n)$ where $k = 1, 2$. Since the potentials are periodic, the forces f_n depend only on the motor position relative to the potential period. Hence, we can define the cyclic position coordinate $\xi \equiv x \bmod l$ ¹ where $0 \leq \xi < l$. We can define the probability

¹ $a \bmod b = a - b \text{int}(a/b)$ i.e. the remainder of the Euclidean division of a by b . The function $\text{int}(x)$ takes the integer part of x

density of finding a motor at ξ in state k as $P_k(\xi, t)$. In the limit of large N and disordered motor attachments, the sum of the two distributions leads to a constant value i.e. $P_1(\xi, t) + P_2(\xi, t) = 1/l$. This results from the fact that, in an incommensurate structure, each motor can be found at a different position $\xi_n \in [0, l)$ and for large N , the interval becomes homogeneously filled. Since motors are convected during the backbone movement, the time derivative of P_k reads:

$$\frac{dP_k}{dt} = \partial_t P_k + v \partial_\xi P_k \quad (5.1)$$

where $v \equiv \dot{X}$ is the backbone velocity. Without loss of generality, we only study the dynamics of a single probability distribution (e.g. P_1):

$$\partial_t P_1 + v \partial_\xi P_1 = -\omega_1 P_1 + \omega_2 P_2 \quad (5.2)$$

where $\omega_1(\xi)$ and $\omega_2(\xi)$ fulfill Eq. 2.11. On the other hand, force balance determines the velocity of the system:

$$\lambda v = f_{\text{ext}} + f \quad (5.3)$$

where λ is the drag coefficient, f_{ext} is the external force and f is the average active force which reads:

$$f = - \int_0^l d\xi P_1 \partial_\xi U_1 \quad (5.4)$$

where we have taken $U_2 = ct$ and the previous forces are normalized by the total number of motors N . Eq. 5.2 can be solved in the steady state using a power expansion of P_1 as a function of the velocity v :

$$P_1(\xi) = \sum_{m=0}^{\infty} P_1^{(m)} v^m; \quad P_1^{(m)}(\xi) = -\frac{\partial_\xi P_1^{(m-1)}}{\omega_1 + \omega_2} \quad m \geq 1 \quad (5.5)$$

with $P_1^{(0)} = \omega_2 / [(\omega_1 + \omega_2)l]$. The force-velocity behaviour can thus be written as:

$$f_{\text{ext}} = f_\Omega^{(0)} + (\lambda + f_\Omega^{(1)})v + \sum_{m=2}^{\infty} f_\Omega^{(m)} v^m \quad (5.6)$$

where,

$$f_{\Omega}^{(m)} \equiv \int_0^l d\xi P_1^{(m)} \partial_{\xi} U_1 \quad (5.7)$$

Here, the subscript Ω indicates that the coefficients depend on the perturbation amplitude defined in Eq. 2.10. For $\Omega = 0$, there is no spontaneous force $f_{\Omega}^{(0)} = 0$ and $f_{\Omega}^{(1)} > 0$, which indicates that thermal transitions lead to an increasing friction. Only when $\Omega \neq 0$ and U_1 is asymmetric, $f_{\Omega}^{(0)}$ differs from zero and induces spontaneous motion in the system. Let us consider for simplicity the case of symmetric $U_1(\xi)$ and $\theta(\xi)$. In this case, all even coefficients of the force expansion vanish i.e. $f_{\Omega}^{(2n)} = 0$. If no external force is applied to the system we find:

$$0 = (\lambda + f_{\Omega}^{(1)})v + f_{\Omega}^{(3)}v^3 + \mathcal{O}(v^5) \quad (5.8)$$

If $\lambda + f_{\Omega}^{(1)} > 0$, the only solution is $v = 0$. However, if we allow detailed balance to be broken we have $f_{\Omega}^{(1)} < 0$ and at some critical value $\Omega = \Omega_c$ we will have $\lambda + f_{\Omega=\Omega_c}^{(1)} = 0$. If we expand $f_{\Omega}^{(1)}$ around $\Omega = \Omega_c$ we find:

$$f_{\Omega}^{(1)} \simeq -\lambda - \frac{\partial f_{\Omega}^{(1)}}{\partial \Omega} \Big|_{\Omega=\Omega_c} (\Omega - \Omega_c) \quad (5.9)$$

For $\Omega > \Omega_c$ and $\lambda + f_{\Omega}^{(1)} < 0$, we obtain two solutions with finite velocity:

$$v_{\pm} = \pm \left(\frac{1}{f_{\Omega}^{(3)}} \frac{\partial f_{\Omega}^{(1)}}{\partial \Omega} \Big|_{\Omega=\Omega_c} (\Omega - \Omega_c) \right)^{1/2} \quad (5.10)$$

The case $\lambda + f_{\Omega}^{(1)} < 0$, corresponds to an effective negative damping coefficient. In this case, two possible stable moving solutions appear and symmetry breaking occurs in the system since the non-moving state $v = 0$ becomes unstable.

5.3.2 ‘Tug-of-war’ model

Let us imagine a tug-of-war of people where both sides are evenly matched (both teams are equally strong) and that the probability of one person letting go (or slipping on the grass) increases with the load that he or she can withstand. If someone accidentally slips on the grass, the load per motor in the team will increase and thus, the likelihood that a second person lets go will also increase. Eventually, this will lead to a cascade of releases on one side and the winning team will lurch backwards. This example illustrates that load-dependent detachment can lead to positive feedback.

Next we present a simple example to illustrate this effect on a system with molecular motors, following Ref. [Howard, 2009]. Let us consider a collection of N molecular motors that bind and unbind from a polar filament at rates π , ϵ respectively, working against a load F_{ext} . We adopt the sign convention such that for a plus-end-directed motor, a load is negative ($F_{\text{ext}} < 0$). We assume a linear velocity-force relationship, such that each motor produces a force $f(v) = f_0 - \lambda v$, where $\lambda > 0$ is the drag coefficient and f_0 is the stall force of a single motor (Fig. 5.4b). The force balance will read $F_{\text{ext}} = -N_b f$, where N_b is the number of bound motors. We assume that the external force is equally shared by the total number of bound motors such that the load each motor feels is F_{ext}/N_b . On the other hand, we consider the unbinding rate to depend exponentially on the load per motor:

$$\frac{\epsilon(F_{\text{ext}})}{\epsilon_0} = \exp\left(-\frac{F_{\text{ext}}}{N_b f_d}\right) = \exp\left(\frac{f}{f_d}\right) \quad (5.11)$$

where ϵ_0 is the unbinding rate at zero load and f_d is the typical dissociation load at which the unbinding rate grows a factor e . The binding rate will be independent of the external force and thus we consider a constant rate $\pi = \pi_0$. For a given external force F_{ext} the number of bound motors will be $N_b = \eta(F_{\text{ext}})N$, where $\eta(F_{\text{ext}}) = \pi/(\epsilon + \pi)$ is the duty ratio. From the previous considerations, one can derive the following relationships:

$$\frac{dN_b}{d\epsilon} = -\frac{N_b}{\epsilon} \left(1 - \frac{N_b}{N}\right); \quad \frac{d\epsilon}{dF_{\text{ext}}} = -\frac{\epsilon}{N_b f_d} \quad (5.12)$$

Next, let us study the slope of the velocity-force relationship near stall conditions. The slope dF_{ext}/dv reads:

$$\frac{dF_{\text{ext}}}{dv} = N_b \lambda + \frac{dN_b}{dv} (-f_0 + \lambda v) \quad (5.13)$$

By using the chain rule $dN_b/dv = (dN_b/d\epsilon)(d\epsilon/dF_{\text{ext}})(dF_{\text{ext}}/dv)$ and considering that near stall conditions $N_b \simeq N_0$, one can show that $F_{\text{ext}}(v) \simeq -N_0(f_0 - \lambda_d v)$, where λ_d :

$$\lambda_d = \lambda \left[1 - \frac{f_0}{f_d} \left(1 - \frac{N_0}{N}\right)\right] \quad (5.14)$$

Therefore the system feels an apparent friction parameter λ_d which can be negative depending on the parameters of the system (Fig. 5.4c). If $f_d \gg f_0$, $\lambda_d \simeq \lambda > 0$ and the system is damped. That is, if motors are not prone to detach, no instability can occur in the system. This means that, contrary to the high processivity found in intracellular transport ($\eta \sim 1$), motors need to have a low duty ratio to be able to generate dynamic instabilities at a collective level.

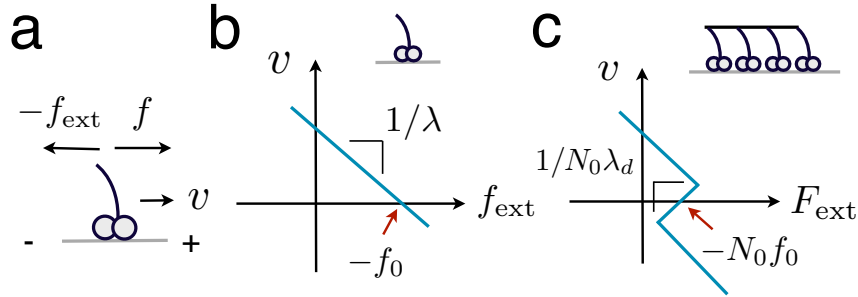


Fig. 5.4 a) A Plus-ended directed motor generates a force $f > 0$ and feels an external load $f_{\text{ext}} < 0$. b) Linear velocity-force relationship for a single motor with a stall force f_0 and damping coefficient $\lambda > 0$ which determines the slope of the curve. c) Nonlinear velocity-force relationship for a collection of motors. The stall force of the system is $N_0 f_0$ and the slope near stall conditions can change sign when damping becomes negative ($\lambda_d < 0$). Figure adapted from [Howard, 2009].

Chapter 6

Spontaneous oscillations of motor assemblies

Early models proposed to understand oscillatory instabilities in motor assemblies were grounded on experimental evidences of muscle contraction [Huxley, 1957, Hill, 1974, Hill, 1975] and were subsequently generalized to the study of eukaryotic flagella [Brokaw, 1975, Brokaw and Rintala, 1975]. Two main approaches have been used: two-state ‘crossbridge’ and ‘stiff motor’ models, which can be considered as two different limits of a more general description that considers the motor-filament interaction and the stiffness of the motors [Guérin et al., 2011, Guérin et al., 2010]. In both cases, oscillations are obtained for non-monotonic velocity-force relationships in the presence of an elastic element. In this section, our purpose will be to study a minimal model to describe such spontaneous oscillations. Following the work of [Jülicher et al., 1997, Jülicher and Prost, 1997], we will use an extension of the two-state model in Section 5.3.1 with the addition of an elastic element. This model has successfully explained many experimental results on biological oscillating systems driven by molecular motors [Camalet et al., 1999, Camalet et al., 2000, Riedel-Kruse et al., 2007, Plaças et al., 2009]. We show that the integro-differential equations in Ref. [Jülicher and Prost, 1997] can be reduced to a set of three ordinary differential equations which capture the main dynamics of the system and exhibit rich nonlinear behaviour. In particular, we will apply the model to a minimal *in vitro* actomyosin system studied in Ref. [Plaças et al., 2009].

6.1 Two-state model with an elastic element

We consider a collection of N molecular motors which are rigidly attached to a common backbone filament and can be in two possible states $k = 1, 2$ as sketched in Fig. 6.1. The dynamics of the system is equivalent to the case described in Section 5.3.1, except from the fact that the backbone is coupled to a spring of elastic modulus KN where K is the elastic modulus per motor. The dynamics of the system reads [Jülicher and Prost, 1997]:

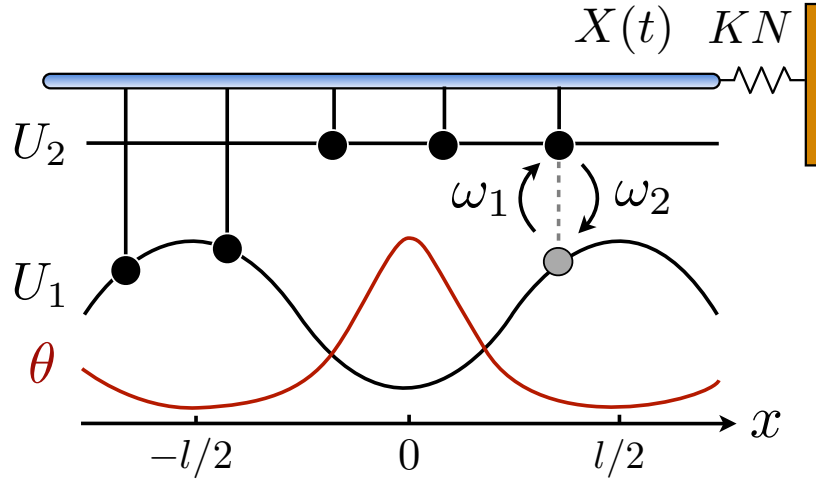


Fig. 6.1 Schematic description of the two-state ratchet model of molecular motors coupled to an elastic element. Motors are rigidly attached to a common backbone (blue) and equally spaced with a distance q incommensurate to the filament periodicity l . Motors detach and attach to the polar filament with rates $\omega_1(x), \omega_2(x)$ respectively, feeling a periodic potential $U_k(x)$ which depends on the state of the motor $k = 1, 2$. Localized active sites are described through the function $\Omega(x)$ which breaks detailed balance in the system. Finally, the backbone is coupled to a spring of elastic modulus KN .

$$\partial_t P_1 + v \partial_\xi P_1 = -\alpha P_1 + \omega_2/l \quad (6.1)$$

$$\lambda v = -KX + F \quad (6.2)$$

where $v \equiv \dot{X}$ is the backbone velocity, λ is the friction coefficient, $\alpha(\xi) \equiv \omega_1(\xi) + \omega_2(\xi)$ and $F = -\int_0^l d\xi P_1 \partial_\xi U_1$ is the active force generated per motor¹. We focus on the dynamics of one probability

¹ Notice that the force per motor is denoted in uppercase now, in contrast to Section 5.3.1

distribution (e.g. P_1) as in Section 5.3.1. Eq. (6.1) describes the dynamics of the probability density P_1 whereas Eq. (6.2) accounts for force balance in the system.

6.2 Three-variable system

Following the work in Ref. [Guérin et al., 2011], we decompose $P_1(\xi, t)$ as an infinite sum of modes $a_n(t)$ and $b_n(t)$:

$$P_1(\xi, t) = \sum_{n=0}^{\infty} [a_n \sin(2\pi n\xi/l) + b_n \cos(2\pi n\xi/l)] \quad (6.3)$$

Since the functions $U_1(\xi), \omega_1(\xi), \omega_2(\xi)$ are periodic, they can be generally described in terms of Fourier series. We will consider the simplest approximation by keeping only the first Fourier mode and defining $g(\xi) = 1 + \cos(2\pi\xi/l)$. We choose a symmetric sinusoidal potential $U_1(\xi) = (U/2)g(\xi + l/2)$ where U is the amplitude of the potential. We also take α to be constant, such that the sum of the transition rates is independent of the spatial coordinate ξ . The transition rates are given by:

$$\begin{aligned} \omega_1(\xi) &= (\beta/2)g(\xi) \\ \omega_2(\xi) &= \alpha - \omega_1(\xi) \end{aligned} \quad (6.4)$$

where α, β are unknown rates. Since biological motors work far from equilibrium, $\omega_1/\omega_2 \simeq \Omega(\xi)$, and thus:

$$\frac{\omega_1}{\omega_2} \simeq \frac{\Omega g(\xi)}{1 - \Omega g(\xi)} \quad (6.5)$$

where $\Omega \equiv \beta/(2\alpha)$ is a dimensionless ATP hydrolysis amplitude and $\Omega \in [0, 1/2)$. Using the orthogonality of the Fourier modes, the active force per motor is simply given by $F = -U\pi a_1/2$. Hence, we obtain an infinite set of ordinary differential equations for the modes $a_n(t), b_n(t), n \geq 0$ and $X(t)$. Remarkably, for constant α , the modes $a_1(t), b_1(t)$ and $X(t)$ are formally decoupled, that is, they evolve independently from the rest (b_0 and a_n, b_n for $n > 1$). The last choice of $\alpha(\xi)$ is known as the constant rate approximation

[Guérin et al., 2011]. The evolution of b_0 is also decoupled from the rest and relaxes exponentially to its steady state value. Non-dimensionalizing with respect to the length scale l , time scale $1/\alpha$ and force density $\lambda\alpha$, the dimensionless governing equations read:

$$\begin{aligned}\dot{\bar{a}}_1 &= -\bar{a}_1 - 2\pi\rho\bar{X}\bar{b}_1 - \mu\bar{a}_1\bar{b}_1 \\ \dot{\bar{b}}_1 &= -\Omega - \bar{b}_1 + 2\pi\rho\bar{X}\bar{a}_1 + \mu\bar{a}_1^2 \\ \dot{\bar{X}} &= -\rho\bar{X} - \frac{\mu}{2\pi}\bar{a}_1\end{aligned}\quad (6.6)$$

and for $n > 1$:

$$\begin{aligned}\dot{\bar{a}}_n &= -\bar{a}_n - 2\pi n\rho\bar{X}\bar{b}_n - n\mu\bar{a}_1\bar{b}_n \\ \dot{\bar{b}}_n &= -\bar{b}_n + 2\pi n\rho\bar{X}\bar{a}_1 + n\mu\bar{a}_1\bar{a}_n\end{aligned}\quad (6.7)$$

where Ω plays the role of the control parameter, $\rho \equiv K/\lambda\alpha$ sets the damping rate of oscillations and $\mu \equiv \pi^2 U/\lambda l^2 \alpha$ is an effective mobility. It is interesting to remark that a similar decoupling occurs for the Markus-Lorenz waterwheel equations [Strogatz, 1994, Kolář and Gumbs, 1992] which share some similarities with Eqs. (6.1) and (6.2). It is noteworthy that all nonlinear terms depend inversely on the friction λ , which plays a major role on the nonlinear nature of the system. Defining the dimensionless active force per motor as $f \equiv F/\lambda\alpha l$ we notice that f is proportional to the first asymmetric mode through $f = -\mu\bar{a}_1/2\pi$. The system has the symmetry $(\bar{X}, -f) \rightarrow (-\bar{X}, f)$, given $W_1(\xi)$ is symmetric. Furthermore, the backbone position \bar{X} far from the initial value is uniquely given by the evolution of f , from Eq. (6.6):

$$\bar{X}(\tau) = \int_0^\infty d\tau' e^{-\rho\tau'} f(\tau - \tau') \quad (6.8)$$

where τ' is the time-lag. Hence, \bar{X} represents the memory of f , i.e. its exponentially weighted past evolution. Through a suitable linear change of variables $\{2\pi\rho\bar{X} + \mu\bar{a}_1, \bar{a}_1, \bar{b}_1 + \Omega\} \rightarrow \{x, y, z\}$ the set of equations (6.6) can be rewritten as :

$$\begin{aligned}\dot{x} &= -\rho x + \mu y \\ \dot{y} &= x(\Omega - z) - y \\ \dot{z} &= -z + xy,\end{aligned}\quad (6.9)$$

where x describes the position of an overdamped particle in an effective system under a forcing term μy . Now the previous symmetry condition is manifested as $(x, y) \rightarrow (-x, -y)$. The dynamics of y and z is the same as in the Lorenz model (for the particular choice of $\beta = 1$ in Ref. [Lorenz, 1963]), however the first equation in (6.9) is different. The system has a single fixed point at the origin. A linear stability analysis around this point gives one negative eigenvalue -1 and two complex conjugated eigenvalues $\gamma \pm i\omega$, where $\gamma = \mu(\Omega - \Omega_c)/2$, $\omega = \sqrt{\rho - \gamma^2}$. $\Omega_c = (1 + \rho)/\mu$ is defined as the critical value of Ω where a Hopf bifurcation takes place, i.e. when $\gamma = 0$. In view of the similarities between Eqs. (6.9) and the Lorenz equations, we investigated the possibility of chaos in the system. We considered the attractor shown in Fig. 6.2, where nearby trajectories tend to locally diverge when found in the two spirals and to locally converge when switching between spirals. The computation of the Lyapunov characteristic exponents

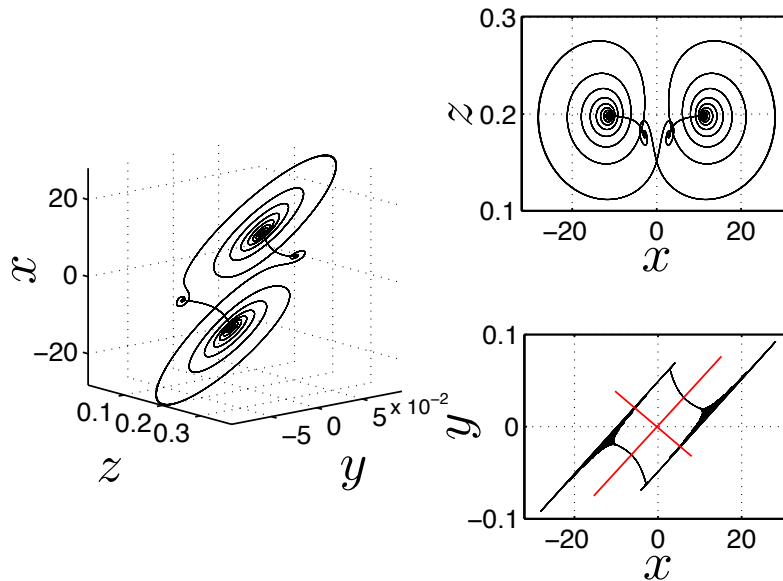


Fig. 6.2 Complex periodic orbit for $\rho = 0.05$, $\mu = 200$ and $\Omega = 0.2$ by solving Eqs. (6.9). We notice that the attractor fulfills the symmetry $(x, y) \rightarrow (-x, -y)$.

for the attractor in Fig. 6.2 was studied numerically by using a *Mathematica* package [Sandri, 1996] based on the algorithms presented in Refs. [Benettin et al., 1980, Eckmann and Ruelle, 1985]. The maximum Lyapunov exponent λ_1 was found to be nearly zero and the remainder exponents were $\lambda_2 \gtrsim \lambda_3 \simeq -0.02$, indicating that the limit set is a periodic orbit. In conclusion, no clear signs of chaotic behaviour were found in the system. Despite the similarities between Eqs. (6.9) and the Lorenz equations, the different terms in the first equation of (6.9) crucially affect the dynamics of the system. Interestingly, as we will discuss next, the system can generally exhibit subharmonic oscillations. Hereinafter, we will focus on the dynamics of \bar{X} rather than x to allow a physical interpretation compatible with empirical observations.

6.3 Comparison with a minimal actomyosin system

We choose the model parameters consistent with the minimal actomyosin system in Ref. [Plaças et al., 2009] which was shown to be successfully described by the two-state model in Ref. [Jülicher and Prost, 1997]. Typical values of KN are found in the range of $10^{-2} - 10^{-1}$ pN/nm [Plaças et al., 2009] and the number of motors are $N \sim 10 - 100$, which gives $K \simeq 10^{-4} - 10^{-2}$ pN/nm, while the friction coefficient was found to be $\lambda \simeq 10^{-2} - 1$ $\mu\text{N}\cdot\text{s}\cdot\text{m}^{-1}$ [Jülicher and Prost, 1997, Bormuth et al., 2009]. We take $\alpha = 10$ s^{-1} and choose Ω much larger than the critical value. By considering $l = 6$ nm, $U = 10k_B T$ we find $\rho \simeq 10^{-2} - 10^2$ and $\mu \simeq 10^3 - 10^5$. Therefore, while the dimensionless damping rate ρ is found to be around the characteristic rate of the system (i.e. ~ 1), the mobility μ is particularly high, thus the system works in a regime where nonlinearities are important. In Fig. 6.3 we study two characteristic types of nonlinear oscillations by solving the reduced system (6.6) (top row) and the complete system (Eqs. (6.1) and (6.2)) (bottom row) for two different set of parameters corresponding to small (Fig. 6.3a) and large (Fig. 6.3b) elastic modulus. Numerical solutions for the complete system are carried out taking $U_1(\xi)$ as a symmetric saw-tooth potential of amplitude U , a constant value for U_2 , a sinusoidal form of the hydrolysis amplitude modu-

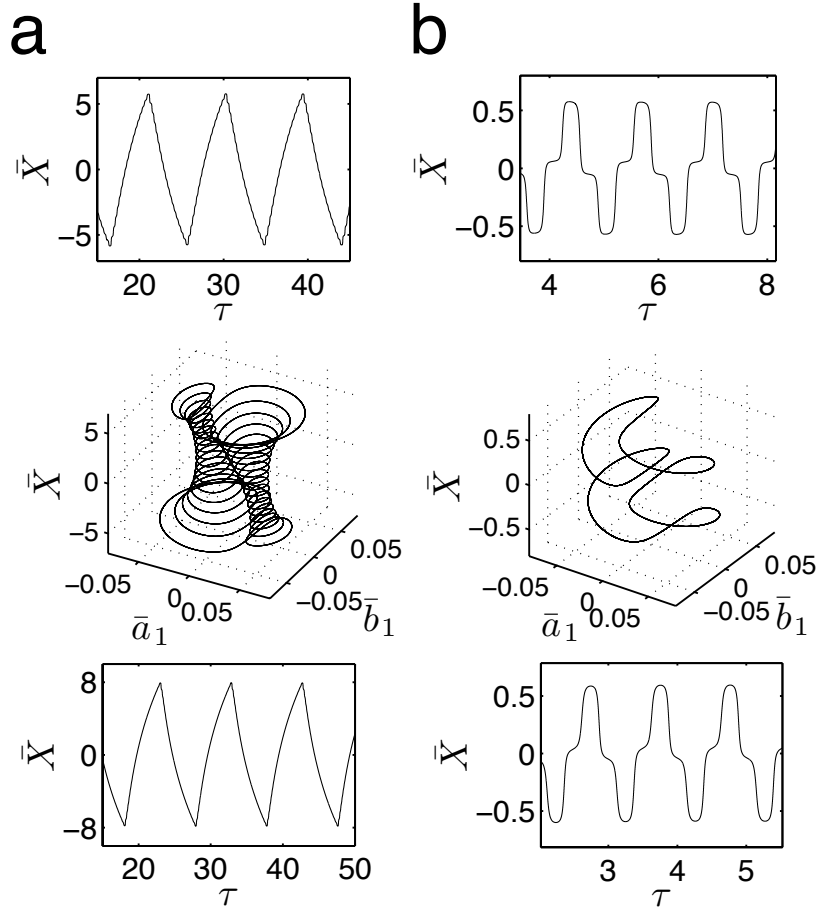


Fig. 6.3 Backbone movement (top) and the corresponding phase-space trajectory (middle) by solving the reduced system (6.6) and backbone movement solving the complete system (Eqs. (6.1) and (6.2)) with a saw-tooth potential of amplitude U , a constant value of U_2 , a sinusoidal form of $\theta(\xi)$ and a constant attachment rate $\omega_2 = \alpha$ (bottom). a) $\rho = 0.7$ and $\mu = 1000$. $\Omega = 0.4$ (top, middle) and $\Omega = 4$, $U = 10k_B T$ and $U_2 = 16k_B T$ (bottom). b) The same for $\rho = 4.5$ and $\mu = 1000$. $\tau \equiv \alpha t$ is the dimensionless time.

lation $\Omega(\xi) = (\Omega/2)g(\xi)$ and a constant attachment rate $\omega_2 = \alpha$. The case (a) corresponds to ~ 1 Hz cusp-like oscillations with peak-to-peak amplitude of ~ 100 nm. On the other hand, case (b) corresponds to ~ 10 Hz oscillations with peak-to-peak amplitude of ~ 10 nm. Notice that despite using a different set of functions to solve the reduced and the complete system, the shape of the oscillations is very similar. Both cases qualitatively agree with

the observed amplitude and frequency measurements reported for spontaneous oscillations in Ref. [Plaçais et al., 2009].

6.4 Subharmonic oscillations

In Fig. 6.4, subharmonic oscillations are shown by solving Eqs. (6.6) (Fig. 6.4a, b, c and d (left)) and the complete system (Fig. 6.4d (right)). The periodic movement of the backbone is characterized by the formation of one (Fig. 6.4c (left)) or two (Fig. 6.4c (right)) subharmonics, where ω_0 is the fundamental frequency of the signal. Remarkably, similar results were found experimentally in Ref. [Plaçais et al., 2009] for large optical trap stiffness where the fundamental frequency was 2.2 Hz and a clear subharmonic peak at approximately $2\omega_0/3$ was observed. Although it was argued that molecular details of the actomyosin interaction could be the reason for this effect, we find that for high mobility values μ and in the limit of large elastic modulus (i.e. $\rho \sim 1 - 10$), the system is generally expected to exhibit periodic motion with two subharmonics and less frequently with only one, as shown in Figs. 6.5 and 6.6.

We identify eight types of staircase shaped oscillations, which exemplify the complex bifurcation scenario. The final steady state of the system is sensitive to the initial conditions as shown in Fig. 6.6, where different basins of attraction are identified. Two types of oscillations exhibit two subharmonics (dark blue and grey diamonds) and one type exhibits a single subharmonic (light blue diamond). It is worth noting that subharmonic oscillations lose the symmetry property $\bar{X}(\tau + \mathcal{T}/2) = -\bar{X}(\tau)$, where \mathcal{T} is the fundamental period of the signal. This property is fulfilled for oscillations in Fig. 6.3 since U_1 is symmetric, however this can be lost for asymmetric U_1 [Jülicher and Prost, 1997]. In this case, a novel symmetry breaking property emerges dynamically due to subharmonic bifurcations of the system. Additionally, the time average of the backbone position in the steady state $\langle \bar{X} \rangle$ is different from zero for subharmonic oscillations and introduces an overall shift, as shown in Figs. 6.4a and d. The latter reflects

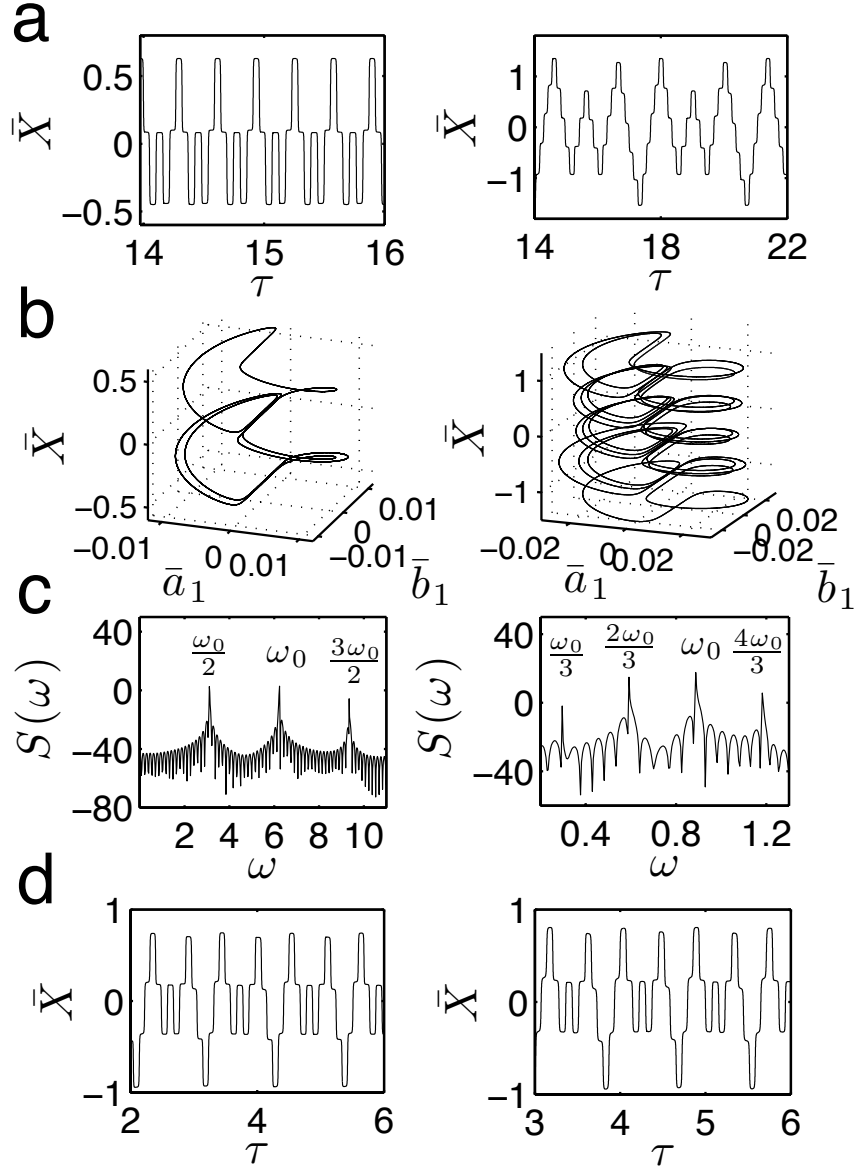


Fig. 6.4 Subharmonic oscillations. a) Backbone time evolution by solving the reduced system for $\Omega = 0.425, \rho = 6, \mu = 63096$ with $\langle \bar{X} \rangle \simeq -0.0045$ (left) and $\Omega = 0.4, \rho = 3, \mu = 6500$ with $\langle \bar{X} \rangle \simeq -0.0115$ (right). b,c) Phase-space trajectories and power spectra $S(\omega)$ in dB for the trajectories in (a) respectively. d) Backbone time evolution by solving the reduced system for $\Omega = 0.4, \rho = 6$ and $\mu = 19000$ with $\langle \bar{X} \rangle \simeq -0.0073$ (left) and by solving the complete system with the same set of functions as in Fig. 6.3, for $\rho = 8.78, \mu = 19038, \Omega = 4, U = 10k_B T$ and $U_2 = 16k_B T$ (right).

asymmetries on the time the backbone spends for positive and negative displacements.

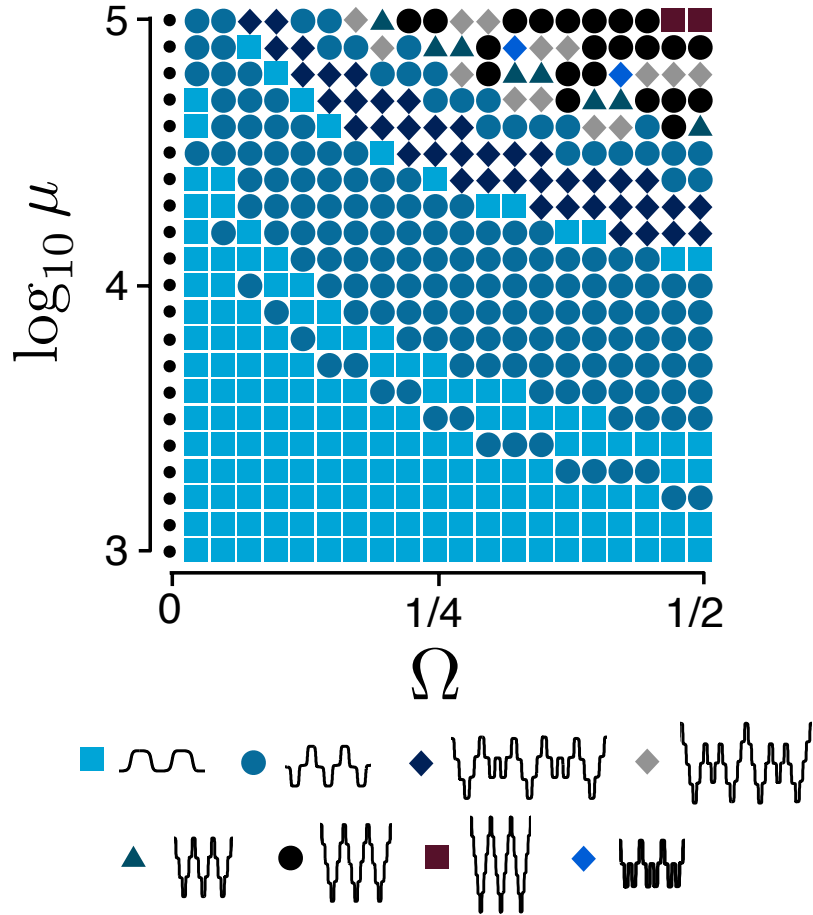


Fig. 6.5 Different types of oscillations in the $\log_{10} \mu$ - Ω parameter space for $\rho = 6$ and the initial condition $(0, 0, 0.074)$ by solving the reduced system. We identify eight types of oscillations in this particular case. Each symbol in the parameter space corresponds to a type of oscillation for a choice of Ω, μ . Subharmonic oscillations (diamonds) are found with two subharmonics (dark blue and grey diamonds) and occasionally with a single subharmonic (light blue diamond). Dots indicate no oscillations.

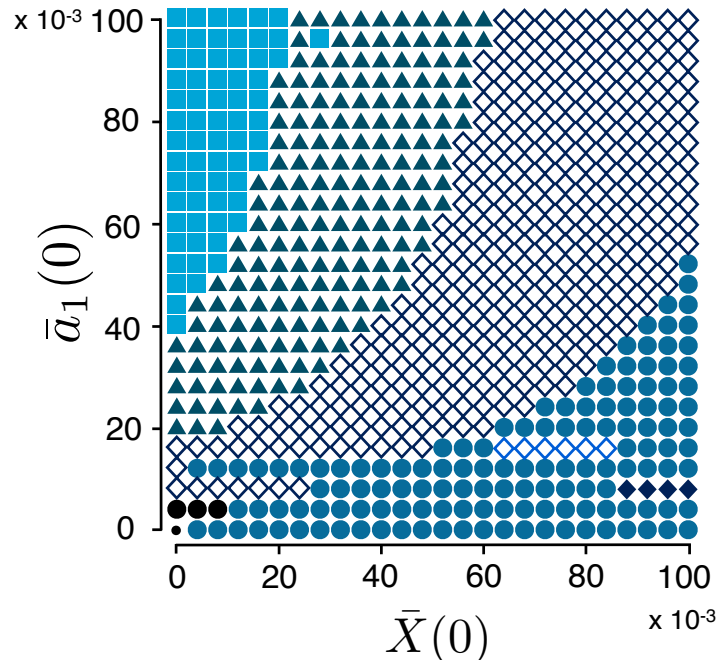


Fig. 6.6 Different domains of attraction by varying the initial conditions $\bar{a}_1(0)$ and $\bar{X}(0)$ and fixing $\bar{b}_1(0) = 0.01$, for $\rho = 6$, $\Omega = 0.4$ and $\mu = 19002$ by solving the reduced system. The symbol and color code is the same as in Fig. 6.5, and empty symbols denote the same type of oscillation with $\bar{X} \rightarrow -\bar{X}$.

6.5 Conclusions

In this chapter we have studied theoretically an actomyosin system coupled to an elastic element, which is able to generate spontaneous oscillations in the presence of ATP via a Hopf bifurcation. This problem mimics the mechanism responsible of the asynchronous wing thrust observed in some insect species. We show that a general theoretical model describing spontaneous oscillations based on an integro-differential system of equations, can be reduced to a simple three-dimensional system. We find that both the complete and reduced systems exhibit subharmonic oscillations in the low friction regime. Remarkably, subharmonic peaks were reported experimentally in the signal power spectrum of a minimal *in vitro* actomyosin system. Hence, we provide an explanation for this phenomenon. Although the reduced description is only exact for

a specific set of functions, direct numerical simulations indicate that the dynamics captured by the reduced system is generic and thus shared by other sets of functions, in particular concerning the occurrence of the referred subharmonic bifurcations. This suggests that a general three-dimensional reduction is inherent to the system, although in general, the corresponding set of variables may not coincide with the explicit ones used in our case.

It is worth stressing that the experiments are subject to strong noise sources, mainly due to the stochastic nature of myosin binding kinetics. This fact is likely to modify in a nontrivial way the amplitude and shape of the subharmonic peaks, by inducing transitions between the different oscillatory regimes, and presumably decreasing the time spent in the subharmonic oscillations in favor of the fundamental frequency oscillations. Furthermore, the studied model is not expected to yield an accurate description of the physical system at molecular level, since the precise forms of the potentials and transition rates are essentially unknown. Nevertheless, the mere fact that the subharmonic peaks are observable under the experimental conditions constitutes by itself a strong evidence of the robustness of this phenomenon. Other types of complex nonlinear behavior of molecular motor assemblies have also been reported in the literature for spontaneous sarcomere dynamics [Günther and Kruse, 2010]. In that case, the assumptions of the model accounted for different physical ingredients and led to notably different nonlinear dynamics, including excitable behaviour and a Ruelle-Takens route to chaos. The results presented here suggest that hydrodynamic friction could be tuned in biological systems in order to suppress undesired multifrequency oscillations.

Acknowledgments

This work was conducted in close collaboration with Dr. H. Gadêlha and Dr. C. Blanch-Mercader.

Chapter 7

Flagellar beating

Over the last half century, intensive experimental and theoretical work has been done to unveil the underlying mechanisms of dynein coordination in axonemal beating. A variety of different mechanisms have been proposed to understand how sliding forces shape the flagellar beat.

In this chapter we will model the eukaryotic flagellum by considering a generalized Euler-elastica filament bundle with passive and active internal forces. Recent studies on the dynamics of flagellar beating used prescribed internal forces [Fu et al., 2008, Gadêlha et al., 2010] or studied the self-organized beating of flagella independently of the specific molecular mechanisms underlying the collective action of dyneins [Camalet et al., 1999, Camalet and Jülicher, 2000, Hilfinger et al., 2009]. Although the latter approaches are general from a physics perspective, they obscure dynein kinetics along the flagellum, which have been shown to be crucial in order to understand several experimental evidences [Brokaw, 1999, Brokaw, 2014, Ginger et al., 2008]. We will use a microscopic bottom-up approach, extending the work in Refs. [Camalet et al., 1999, Riedel-Kruse et al., 2007] by coupling the fully nonlinear action of dyneins to the flagellum. In this way, we will be able to study the saturation of the unstable modes, as a consequence of the nonlinearities arising from the coupling between the flagellum geometry and the dynein activity.

7.1 Continuum flagella equations

We consider a filament bundle composed of two polar filaments subjected to planar deformations. Each filament is modeled as an inextensible, unsharable, homogeneous elastic rod, for which the bending moment is proportional to the curvature and the Young modulus reads E . The filaments are of length L and separated by a constant gap of size b , where $b \ll L$ (Fig. 7.1c). The position of each filament is described in terms of a material curve describing the geometry of the filament bundle centerline $\mathbf{r}(s, t)$. The positions of each polar filament forming the bundle read $\mathbf{r}_{\pm} = \mathbf{r} \pm (b/2)\hat{\mathbf{n}}$, with the orientation of the cross-section at distance s along its length defined by the normal vector to the centerline $\hat{\mathbf{n}} = -\sin\phi\hat{\mathbf{i}} + \cos\phi\hat{\mathbf{j}}$, being $\phi \equiv \phi(s, t)$ the angle between the tangent vector $\hat{\mathbf{s}} \equiv \partial_s \mathbf{r} \equiv \mathbf{r}_s$ and the $\hat{\mathbf{i}}$ direction (taken along the x axis). The subscripts (+) and (-) refer to the upper and lower filaments, respectively (Fig. 7.1c). The shape of the bundle is given at any time by the expression:

$$\mathbf{r}(s, t) = \mathbf{r}(0, t) + \int_0^s (\cos\phi, \sin\phi) ds' \quad (7.1)$$

The geometrical constraint of the filament bundle, originates an arclength mismatch $\Delta(s, t)$ which we shall call ‘sliding displacement’ and that is given by:

$$\Delta(s, t) = \int_0^s (|\partial_s \mathbf{r}_-| - |\partial_s \mathbf{r}_+|) ds' \quad (7.2)$$

For the sake of simplicity, we set any arclength incongruity between the two filaments at the base to zero and we consider the filament clamped at $s = 0$. A similar treatment can be done by assuming basal compliance and other types of boundary conditions at the base (e.g. pivoting or free swimming head); however, we will focus on the nonlinear action of the motors and leave extensions of the work to further studies. If we calculate explicitly Eq. 7.2 we obtain $\Delta(s, t) = b(\phi - \phi_0)$, where $\phi_0 \equiv \phi(0, t)$. We aim to study the active and passive forces generated at each point along the arclength of the filament bundle. We define $\mathbf{f}(s, t) = f(s, t)\hat{\mathbf{s}}$ as the total internal force density generated at s at time t on the plus-filament

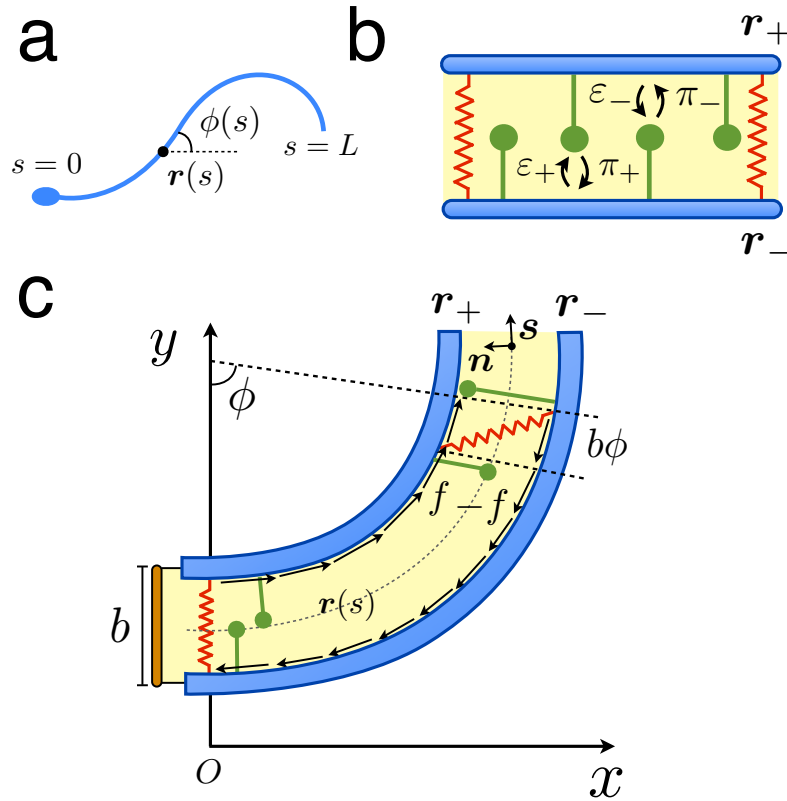


Fig. 7.1 a) Two-dimensional representation of a flagellum, where the centerline $\mathbf{r}(s)$ and tangent angle $\phi(s)$ are parametrized by the arclength parameter s . b) Passive (springs) and active (dynein motors) internal structures in the axoneme. Dyneins in the (+) and (-) filaments compete in a ‘tug-of-war’ and bind/unbind from filaments with rates π_{\pm} and ε_{\pm} respectively. c) Sliding filament mechanism.

due to the action of active and passive forces. By virtue of the action-reaction law, the minus-filament will experience a force density $-\mathbf{f}$ at the same point. Next, consider that N dyneins are anchored at each external filament in a region of characteristic length l_c around s , where l_c is much smaller than the length of the flagellum L , and much larger than the length of the regular intervals dyneins are attached to along the microtubule doublets. We define $n_{\pm}(s, t)$ as the number of bound dyneins in a region of size l_c around s at time t which are anchored in the plus- or minus-filament, respectively. We define a ‘tug-of-war’ of dyneins

at each point s along the flagellum where two groups of N dyneins compete. At the same time, we incorporate an elastic resistance of modulus K between the two filaments describing the presence of crosslinkers. Under these considerations, the internal force density $f(s, t)$ reads:

$$f(s, t) = \rho(n_+F_+ + n_-F_-) - K\Delta \quad (7.3)$$

where $\rho \equiv l_c^{-1}$ is the density of ‘tug-of-war’ units along the flagellum and $F_{\pm}(s, t)$ is the load per motor each group of dyneins experiences due to the action of the antagonistic group. The stresses on the filament bundle are given by a resultant contact force $\mathbf{N}(s, t)$ and resultant contact moment $\mathbf{M}(s, t)$ acting at the point $\mathbf{r}(s, t)$. The internal force density $f(s, t)$ only contributes to the internal moment of the bundle $\mathbf{M}(s, t) = M\hat{\mathbf{k}}$ where $M(s, t)$ reads:

$$M(s, t) = E_b\phi_s - bF \quad (7.4)$$

where $F(s, t) = \int_s^L f(s', t)ds'$ and we have used the approximation $\partial_s\phi_{\pm} \approx \partial_s\phi$, which is valid for bundles characterized by $b \ll L$. The combined bending stiffness of the filament bundle is given by $E_b = 2EI$, where I is the second moment of area of the external rods.

Next, we address the dynamics of dynein. Let us consider a minimal two-state mechanochemical model for dyneins such that two possible states exist $k = 1, 2$, corresponding to microtubule bound or unbound dyneins respectively. Since the sum of bound and unbound motors at s remains constant at all times, we only study the plus- and minus-bound motor distributions $n_{\pm}(s, t)$. Dyneins bind with rates π_{\pm} and unbind with rates ε_{\pm} (Fig. 7.1b). The corresponding bound motor population dynamics will be:

$$\partial_t n_{\pm} = \pi_{\pm} - \varepsilon_{\pm} \quad (7.5)$$

The rates π_{\pm} and ε_{\pm} have the form $\pi_{\pm} = \pi_0(N - n_{\pm})$, $\varepsilon_{\pm} = \varepsilon_0 n_{\pm} \exp(\pm F_{\pm}/f_c)$ where ε_0 and π_0 are constant rates and f_c is the characteristic unbinding force. Here we assume an exponential dependence of the unbinding force on the load. By considering that dyneins fulfill a linear velocity-force relationship with stall

force f_0 and velocity at zero load v_0 , the loads will be defined as $F_{\pm}(s, t) = \pm f_0(1 \mp \Delta_t/v_0)$. Substituting the different definitions, the internal force density $f(s, t)$ reads:

$$f(s, t) = f_0\rho \left(\bar{n} - \frac{n\Delta_t}{v_0} \right) - K\Delta \quad (7.6)$$

where $\bar{n} \equiv n_+ - n_-$ and $n \equiv n_+ + n_-$. For simplicity, we will derive the equations governing the tangent angle ϕ in the limit of small curvature (but possibly large amplitude) such that tension forces can be neglected. The derivation of the full nonlinear elastohydrodynamic equations is given in Appendix E.1. By using resistive force theory in the limit of small curvature, we obtain $\zeta_{\perp}\phi_t = -M_{sss}$, where ζ_{\perp} is the normal drag coefficient (see Appendix E.1). Combining the last expression with Eq. 7.4 we have:

$$\zeta_{\perp}\phi_t = -E_b\phi_{ssss} - bf_{ss} \quad (7.7)$$

Hereinafter we switch to dimensionless quantities keeping the same notation. We non-dimensionalize the arclength with respect to the length scale L , time with respect to the correlation time of the system $\tau_0 = 1/(\varepsilon_0 + \pi_0)$, motor number with respect to N , internal force density with respect to $f_0\rho N$ and sliding displacement with respect to b . The correlation time defines how fast the motors will respond to a change in load. We also define $\text{Sp} = L(\zeta_{\perp}/E_b\tau_0)^{1/4}$, $\mu \equiv Kb^2L^2/E_b$, $\mu_a = bf_0\rho NL^2/E_b$ and $\zeta \equiv b/v_0\tau_0$. The sperm number Sp characterizes the relative importance of elastic forces to viscous drag. The parameter μ denotes the passive sliding resistance, which measures the relative importance of the effective bundle elastic rigidity compared with the elastic crosslinker resistance of the bundle [Gadêlha et al., 2013]. On the other hand, the parameter μ_a denotes the activity of dyneins, measuring the relative importance of motor force generation compared with bending resistance. Finally ζ denotes the ratio of the bundle diameter and the typical deflection induced by the motors. The dimensionless sperm equation in the limit of small curvature reads:

$$\text{Sp}^4\phi_t = -\phi_{ssss} - \mu_a f_{ss} \quad (7.8)$$

where the dimensionless internal force density $f(s, t)$ takes the form:

$$f(s, t) = \bar{n} - \zeta n \Delta_t - \frac{\mu}{\mu_a} \Delta \quad (7.9)$$

and $\Delta = \phi - \phi_0$. Since the base is clamped, $\phi_0 = ct$, and without loss of generality we set $\phi_0 = 0$. Combining Eqs. 7.8 and 7.9 we obtain the nonlinear dynamics of ϕ :

$$\text{Sp}^4 \phi_t = -\phi_{ssss} + \mu \phi_{ss} - \mu_a \bar{n}_{ss} + \mu_a \zeta [n_{ss} \phi_t + 2n_s \phi_{ts} + n \phi_{tss}] \quad (7.10)$$

In the absence of dynein activity (i.e. $\mu_a = 0$), the last expression reduces to the dynamics of an Euler-elastica filament bundle with elastic internal forces [Gadêlha et al., 2013]. Notice that this expression is obtained considering the sliding mechanism and a linear velocity-force relationship for dyneins, but it is independent of dynein kinetics. On the other hand, the dimensionless form of the bound motor population dynamics n_{\pm} reads:

$$\partial_t n_{\pm} = \eta(1 - n_{\pm}) - (1 - \eta)n_{\pm} \exp[\bar{f}(1 \mp \zeta \phi_t)] \quad (7.11)$$

where $\eta \equiv \pi_0/(\pi_0 + \varepsilon_0)$ is the duty ratio of the motors and $\bar{f} \equiv f_0/f_c$ dictates the sensitivity of the unbinding rate on the load.

7.2 Linear stability analysis

The non-moving state of the system is characterized by $\phi = 0$ and $n_{\pm}(s, t) = n_0 \equiv \pi_0/(\pi_0 + \varepsilon_0 e^{\bar{f}})$. This means that the flagellum is aligned with respect to the x -axis and the number of plus- and minus-bound motors is constant in space and time. Next we do a linear stability analysis on Eqs. 7.10, 7.11 defining the corresponding perturbed variables around the base state as $\phi = \delta\phi$ and $n_{\pm} = n_0 + \delta n_{\pm}$. Defining the modulation $\delta n \equiv \delta n_+ = -\delta n_-$ around n_0 and considering $\bar{f} \zeta \phi_t \ll 1$ we obtain:

$$\begin{aligned} \delta n_t &= -\bar{\tau}^{-1} \delta n + (1 - \eta) \zeta \bar{f} e^{\bar{f}} n_0 \phi_t \\ \text{Sp}^4 \phi_t &= -\phi_{ssss} + \mu \phi_{ss} + 2[\mu_a \zeta n_0 \phi_{tss} - \delta n_{ss}] \end{aligned} \quad (7.12)$$

where $\bar{\tau} \equiv n_0/\eta$. We use the ansatz $\phi = \tilde{\phi}(s)e^{\sigma t}$ and $\delta n = \delta\tilde{n}(s)e^{\sigma t}$ where σ is a complex eigenvalue. From the first expression in Eq. 7.12 we get $\delta\tilde{n} = \chi'(\sigma)\tilde{\phi}$, where $\chi'(\sigma)$ is a complex response function:

$$\chi'(\sigma) = \zeta\bar{f}n_0(1 - n_0)\frac{\sigma}{1 + \sigma\bar{\tau}} \quad (7.13)$$

Using Eq. 7.9 and considering $f = \tilde{f}(s)e^{\sigma t}$, we obtain $\tilde{f} = \chi(\sigma)\tilde{\phi}$, where $\chi(\sigma)$ is a second complex response function:

$$\chi(\sigma) = 2\zeta n_0 \left[\bar{f}(1 - n_0)\frac{\sigma - \sigma^2\bar{\tau}}{1 - (\sigma\bar{\tau})^2} - \sigma \right] - \frac{\mu}{\mu_a} \quad (7.14)$$

The latter response functions are a generalization of the results in Ref. [Riedel-Kruse et al., 2007] for a complex eigenvalue σ and are equivalent to the results in Ref. [Bayly and Wilson, 2015]. With the ansatz $\tilde{\phi} \sim \delta\tilde{n} \sim e^{iqs}$ in the second expression of Eq. 7.12, we obtain the characteristic equation:

$$q^4 - \bar{\chi}q^2 + \bar{\sigma} = 0 \quad (7.15)$$

where $\bar{\chi} \equiv \mu_a\chi$, $\bar{\sigma} \equiv \sigma\text{Sp}^4$. Solving Eq. 7.15, we obtain four possible roots:

$$q_i = \pm \left(\frac{\bar{\chi}}{2} \pm \sqrt{\left(\frac{\bar{\chi}}{2}\right)^2 - \bar{\sigma}} \right)^{1/2}, \quad i = 1, \dots, 4 \quad (7.16)$$

where $q_i, \bar{\chi}, \bar{\sigma} \in \mathbb{C}$. Therefore the eigenfunctions read:

$$\tilde{\phi}(s) = \sum_{j=1}^4 \Phi_j e^{iq_j s} \quad (7.17)$$

where $\Phi_j \in \mathbb{C}$. Once $\tilde{\phi}$ is known, $\delta\tilde{n}(s) = \delta N \tilde{\phi}(s) \exp(i\Delta\theta)$ where $\delta N = |\chi'|$ and $\Delta\theta = \arg(\chi')$. Therefore, the evolution of δn is the same as for ϕ except for a phase shift $\Delta\theta$ and an overall change on the amplitude δN , which depends on $\chi'(\sigma)$. This result indicates the presence of a time delay between the action of motors and the response of the flagellum. Indeed, an active force proportional to the time delay of the curvature was proposed as a mechanism to generate bending waves [Brokaw, 1971]. Time delays commonly

arise in systems where molecular motors work collectively as shown in Section 6. In order to find $\tilde{\phi}(s)$, we need to impose the four boundary conditions, obtaining a linear system of equations for $\tilde{\phi}_j$, $j = 1, \dots, 4$ (see Appendix E.2). By setting the determinant of the system to zero, we find the set of complex eigenvalues σ_n , with the corresponding growth rates $\lambda_n = \text{Re}[\sigma_n]$ and frequencies $\omega_n = \text{Im}[\sigma_n]$, which satisfy the boundary conditions, where $\lambda_n, \omega_n \in \mathbb{R}$. We order the set of different eigenvalues according to its growth rate $\lambda_{n+1} > \lambda_n$, such that the first one has the largest growth rate λ_1 . Defining $\mathbf{u} = (\phi, \delta n)^T$, the general solution of the system reads:

$$\mathbf{u}(s, t) = \sum_n A_n \begin{pmatrix} \tilde{\phi}_n \\ \delta \tilde{n}_n \end{pmatrix} e^{\lambda_n t} e^{i\omega_n t} + \text{c.c} \quad (7.18)$$

For $\lambda_n < 0$, $\forall n$, solutions decay exponentially to the non-moving state. On the other hand, when λ_1 becomes positive the system undergoes a Hopf bifurcation and oscillates with frequency ω_1 . Next, we study the marginal stable solutions, i.e. when the maximum growth rate equals zero ($\lambda_1 = 0$). In these cases, we define the critical frequency of oscillation as $\omega_c \equiv |\omega_1|$. Traveling waves propagate from tip to base, a feature already reported for clamped conditions [Camalet et al., 1999, Bayly and Wilson, 2015].

Flagella profiles are shown in Fig. 7.2a and b (top) for low (a) and high (b) viscosity. In Fig. 7.2c, the marginal stability curve (i.e. $\lambda_1 = 0$) in phase space is shown. Intuitively, as Sp is increased the traveling instability occurs for larger motor activity μ_a and the critical frequency of oscillation ω_c typically decreases. For low viscosity ($\text{Sp} = 5$) the wave propagation velocity is slightly oscillatory whereas for high viscosity ($\text{Sp} = 10$) it becomes more uniform (Fig. 7.2a and b, bottom). These results are in agreement with studies on migrating human sperm, where in the limit of high viscosity waves propagated approximately at constant speed [Smith et al., 2009]. For high viscosity, curvature tends to increase from base to tip, finally dropping to zero due to the zero curvature boundary condition at the tail (see Fig. 7.2d and Appendix E.2). This modulation is consistent with experimental studies on human sperm, which show a meandering effect as viscosity is in-

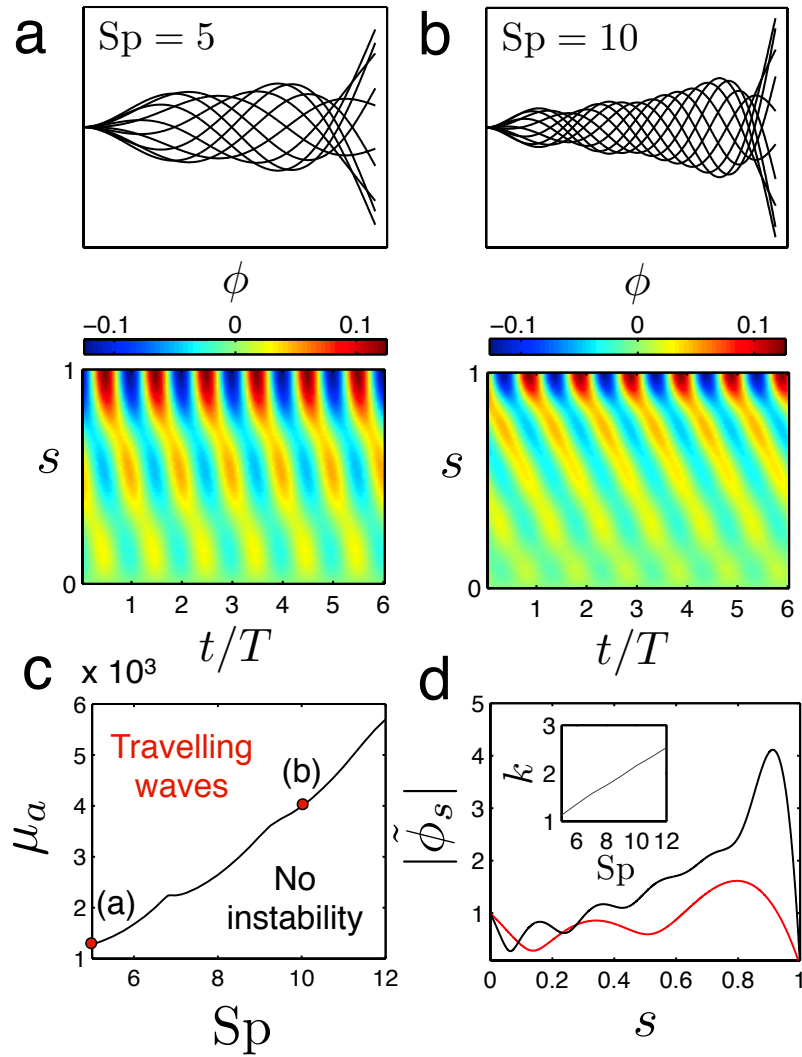


Fig. 7.2 Linear stability analysis. a,b) Clamped head profile solutions with marginal stability (i.e. $\lambda_1 = 0$) for $Sp = 5, 10$ (upper panels) and its tangent angle time evolution (lower panels) where $T = 2\pi/\omega_c$ is the period and $\omega_c \equiv \omega_1$. Amplitudes and angles are arbitrary since they cannot be obtained in the linear analysis. c) Marginal stability curve for the clamped condition for $\mu = 50$, $\zeta = 0.4$, $\eta = 0.14$, $\bar{f} = 2$. Points a and b in parameter space correspond to the profiles in a) and b). d) Curvature modulations as a function of the arclength for $Sp = 5$ (red) and $Sp = 12$ (black). Arbitrary units are used in the y-axis. Inset: Wavenumber k as a function of Sp .

creased. In the latter case, the effect is more pronounced possibly due to external elastic structures such as the outer dense fibers [Smith et al., 2009]. Defining $k \equiv \max |q_i|/2\pi$ as the wavenumber, we obtain that it increases almost linearly with viscosity (Fig. 7.2d, inset). Similar results can be obtained defining k from the covariance matrix (see Section 7.5).

7.3 Parameter choice

Here we present the choice of parameters based on experimental studies on sperm flagella. We first discuss the passive properties of a flagellum. The typical length of a human flagellum is $L \simeq 50 \mu\text{m}$ and the axonemal diameter is found to be $b \simeq 200 \text{ nm}$ [Gaffney et al., 2011]. The bending stiffness of the filament bundle has been reported to be $E_b \simeq 0.9 \cdot 10^{-21} \text{ N}\cdot\text{m}^2$ for sea-urchin sperm [Gadêlha et al., 2013, Gaffney et al., 2011] and $E_b \simeq 1.7 \cdot 10^{-21} \text{ N}\cdot\text{m}^2$ for bull sperm [Riedel-Kruse et al., 2007]. On the other hand, the interdoublet elastic resistance from demembrated flagellar axonemes of *Chlamydomonas* yields an estimated spring constant $2 \cdot 10^{-3} \text{ N/m}$ for $1 \mu\text{m}$ of axoneme [Minoura et al., 1999], thus $K \simeq 2 \cdot 10^3 \text{ N/m}^2$. Finally, typical medium viscosities for sperm flagella range from $\zeta_{\perp} \simeq 10^{-3} \text{ Pa}\cdot\text{s}$ in low viscous media to $\zeta_{\perp} \simeq 1 \text{ Pa}\cdot\text{s}$ in high viscous media [Gadêlha et al., 2010].

Next, we discuss the mechanochemical parameters associated to axonemal dynein. Axonemal dyneins are subdivided in inner and outer arms depending on its position in the axoneme, and can be found in heterodimeric and monomeric forms (see Section 5.2). For the sake of simplicity, we consider identical force generating dynein motor domains acting along the flagellum. The total number of motor domains in a beating flagellum has been estimated to be $\simeq 10^5$ [Ma et al., 2014, Nicastro et al., 2006]. The stall force has been found in the range $f_0 \simeq 1 - 5 \text{ pN}$ [Sakakibara et al., 1999, Hirakawa et al., 2000]. Following Ref. [Riedel-Kruse et al., 2007] we choose the characteristic unbinding force for dynein such that $\bar{f} = 2$. Axonemal dynein is characterized by a low duty ratio

estimated to be $\eta \simeq 0.14$ and speeds at zero load in the range $v_0 \simeq 5 - 7 \mu\text{m/s}$ [Sakakibara et al., 1999, Howard, 2001]. We take the detachment rate at zero load as $\varepsilon_0 \sim 10 \text{ s}^{-1}$. Finally, we need to estimate ρ and N . Considering the length of the human sperm flagellum ($L \simeq 50 \mu\text{m}$) we obtain $\simeq 2 \cdot 10^3$ motors/ μm . In our description, we divide the axoneme in two regions with corresponding dynein teams. Therefore, we have $\rho N \simeq 10^3$ motors/ μm . In order to find ρ , we need to choose a criterion to decide the typical length scale $l_c = \rho^{-1}$ in our coarse-grained description. From Eq. 7.16, we notice that the typical length scale in the system can be given by $l_c \sim L/\sqrt{\mu_a} = \sqrt{E_b/bf_0\rho N}$. Using the previous parameters we get $l_c \sim 1 \mu\text{m}$ and therefore $\rho \sim 1 \mu\text{m}^{-1}$ and $N \sim 10^3$. From the previous considerations, we obtain $\text{Sp} \simeq 4 - 20$, $\mu \simeq 50 - 100$, $\mu_a \sim 10^3$ and $\zeta \simeq 0.4$. The motor activity will be studied in a broad range ($\mu_a \simeq 10^3 - 10^4$) since it plays the role of the main control parameter in our study.

7.4 Nonlinear motor dynamics

In Fig. 7.3a we show two finite amplitude solutions by numerically solving the nonlinear motor dynamics (see Appendix F). Fig. 7.3a (left) corresponds to a case where the system is found close to the Hopf bifurcation, whereas Fig. 7.3a (right) corresponds to a regime far from the bifurcation. We notice that the marginal solution obtained in the linear stability analysis (Fig. 7.2b) gives a very good estimate of the nonlinear profile close to the bifurcation point, although it does not provide the magnitude of ϕ nor δn . Frequencies are found to be ~ 10 Hz comparable to typical sperm frequencies on the order of $\simeq 10 - 20$ Hz [Gaffney et al., 2011] and maximum amplitudes are found to be relatively small, around 10% of the total flagellum length. The color code in Fig. 7.3a indicates the value of the semi-difference of plus- and minus-bound motors δn . Plus-bound motors are predominant in regions of positive curvature ($\phi_s > 0$) along the flagellum and viceversa. Remarkably, less than $\simeq 5\%$ bound dyneins are sufficient to produce $\simeq 1 \mu\text{m}$ amplitude oscillations. In Fig. 7.3b, the time evolution of ϕ and δn is shown at $s = 3/4$ for the cases in Fig. 7.3a, respectively. The tan-

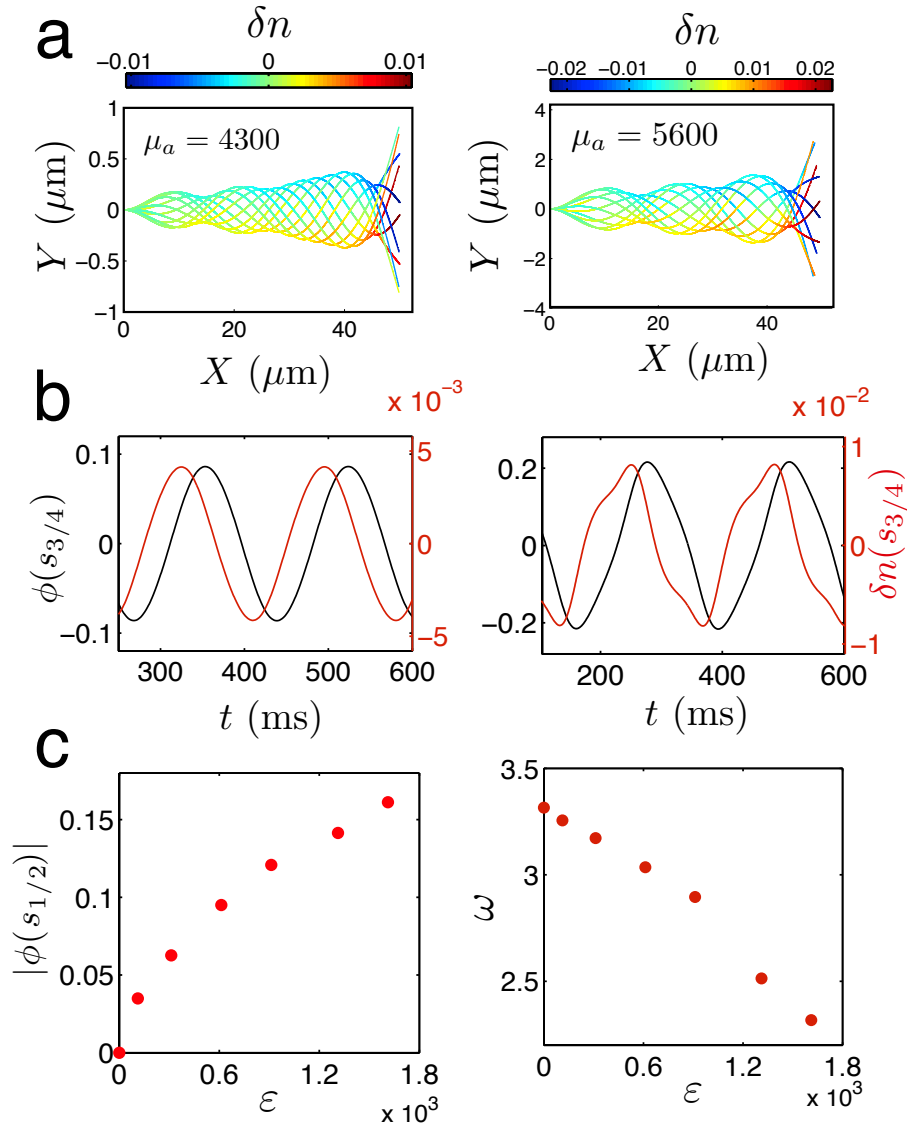


Fig. 7.3 a) Nonlinear flagella profiles for $\mu_a = 4300$ (left) and $\mu_a = 5600$ (right), considering the respective eigenmodes as initial conditions. b) ϕ and δn at $s_0 = 3/4$ for the profiles in (a) respectively. c) Absolute tangent angle in radians at $s = 1/2$ and dimensionless frequency ω as a function of the distance to the bifurcation $\varepsilon = \mu_a - \mu_a^c$. $\text{Sp} = 10$, $\mu = 50$, $\eta = 0.14$, $\zeta = 0.4$, $\bar{f} = 2$.

gent angle ϕ is delayed respect to δn , in agreement with the linear stability analysis. Close to the instability threshold, both signals are very similar since the system is found near the linear regime; however, far from threshold, both signals greatly differ. For high motor activity, both the tangent angle and the fraction of bound dyneins at certain points along the flagellum exhibit cusp-like oscillations (Fig. 7.3b, right). This behaviour is typical of molecular motor assemblies working in the nonlinear regime far from the instability threshold [Jülicher and Prost, 1997]. Experimentally, similar cusp-like shapes of the curvature were found in sea urchin sperm [Ohmuro et al., 2004]. Despite the signals S in Fig. 7.3b (right) are nonlinear, they keep the symmetry $S(t + T/2) = -S(t)$ as a consequence of both plus and minus motor populations being identical, a property also found in spontaneous oscillations of motor assemblies [Jülicher and Prost, 1997]. Finally, in Fig. 7.3c we study how the amplitude and frequency of the oscillations vary with the distance from the bifurcation point $\varepsilon = \mu_a - \mu_a^c$. For small ε , the absolute value of the tangent angle seems to follow a square root dependence, characteristic of a supercritical Hopf bifurcation; however, in the strongly nonlinear regime the curve deviates from this trend. On the other hand, the beating frequency decreases for increasing activity. This fact can be understood in simple terms since the activity μ_a is proportional to $f_0 N$; hence, the larger the activity, the stronger each dynein team becomes. Consequently, the necessary time for a dynein team to win increases, leading to a smaller beating frequency.

7.5 Principal component analysis

In order to analyze the nonlinear solutions we use principal component analysis [Werner et al., 2014, Jolliffe, 2002]. This technique allows us to treat flagellar shapes as multi-feature data sets, which can be projected to a lower dimensional space characterized by principal shape modes. Here we will analyze the data following Ref. [Werner et al., 2014] to study sperm flagella. The covariance matrix C as defined in [Werner et al., 2014] is shown in Fig. 7.4a

for $\mu_a = 4300$ (left) and $\mu_a = 5600$ (right). In both cases, we find anti-correlation between tangent angles which are a distance $\lambda/2$ apart. Hence, a certain wavelength λ can be identified. Interestingly, the number of local maxima along the diagonals in the covariance matrix decreases from $\mu_a = 4300$ to $\mu_a = 5600$, indicating that motor activity tends to eliminate correlations between points along the flagellum. Employing an eigenvalue decomposition of the matrix C , we can obtain the eigenvectors $\mathbf{v}_1, \dots, \mathbf{v}_r$ and their corresponding eigenvalues d_1, \dots, d_r . Without loss of generality, we sort the eigenvalues in descending order $d_1 \geq \dots \geq d_r$. We find that the first two eigenvalues capture $> 99\%$ variance of the data. This fact indicates that our flagellar waves can be suitably described in a two-dimensional shape space, since they can be regarded as single-frequency oscillators. Notice that this would not hold for multifrequency oscillations, where an additional dimension is required (see Section 6). Each flagellar shape can be expressed now as a linear combination of the eigenvectors \mathbf{v}_k :

$$\phi(t) = \sum_{k=1}^r B_k(t) \mathbf{v}_k \quad (7.19)$$

where B_k are the shape scores computed by a linear least-square fit. In Fig. 7.4b (left), the two first eigenvectors v_1, v_2 are shown. In Fig. 7.4b (right), the flagellar shape at a certain time (black line) is reconstructed (dashed grey line) by using the two shape scores B_1, B_2 showing an almost perfect fit. Finally, in Fig. 7.4c we show the shape space trajectories beginning with small amplitude eigenmode solutions. While close to the bifurcation the limit cycle is circular (Fig. 7.4c, left), far from the bifurcation the limit cycle becomes distorted (Fig. 7.4c, right). We conclude that motor activity in the nonlinear regime significantly affects the shape of the flagellum and that linear solutions only provide good estimates sufficiently close to the Hopf bifurcation.

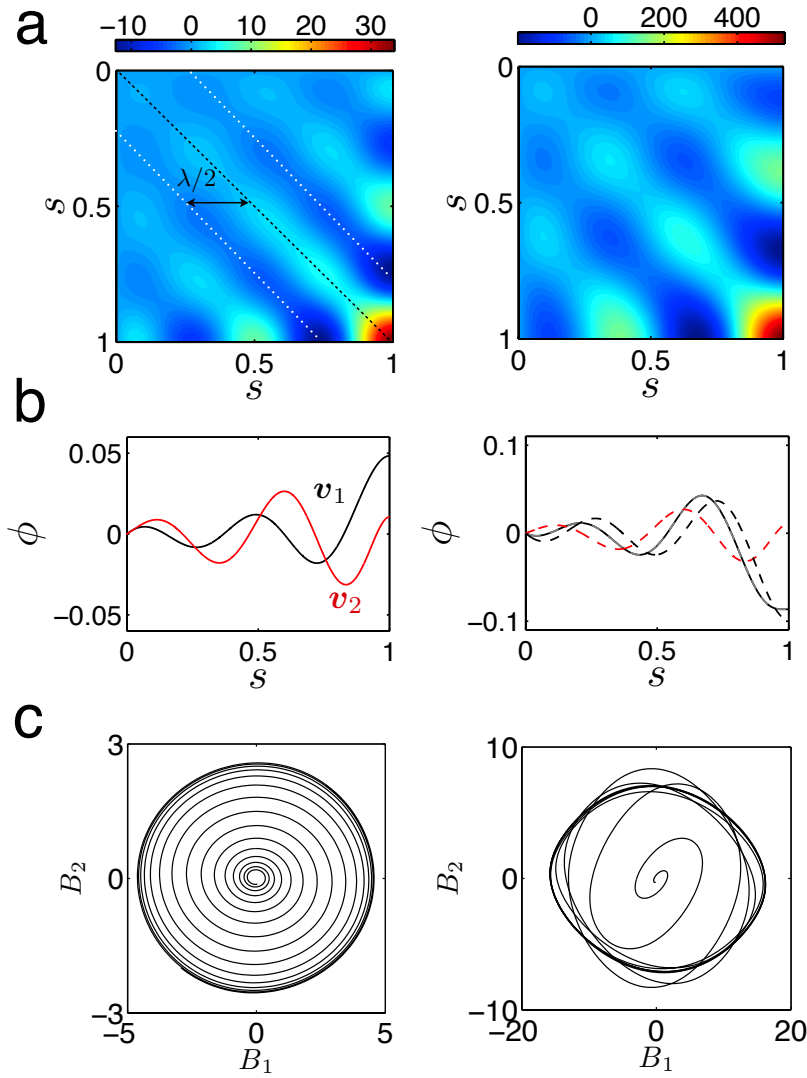


Fig. 7.4 Principal component analysis of flagellar beating. a) Covariance matrix for $\mu_a = 4300$ (left) and $\mu_a = 5600$ (right). The negative correlation at arclength distance $\lambda/2$, gives a characteristic lengthscale of the waves. b) (left) Two principal shape modes v_1, v_2 (black, red), corresponding to the two maximal eigenvalues of the covariance matrix in (a), left. (right) Reconstruction of a flagellar shape (black) by a superposition of the two principal shape modes (grey dashed line) in (a) v_1, v_2 (black and red dashed lines, respectively) at time $t = 1.26$ s. c) Flagellar dynamics in a reduced two-dimensional shape phase space for $\mu_a = 4300$ (left) and $\mu_a = 5600$ (right). $Sp = 10$, $\mu = 50$, $\eta = 0.14$, $\zeta = 0.4$.

7.6 Bending initiation

Finally, bending initiation is an interesting problem that can be studied from the nonlinear equations including various initial conditions. In Fig. 7.5a,b the spatiotemporal transient dynamics are

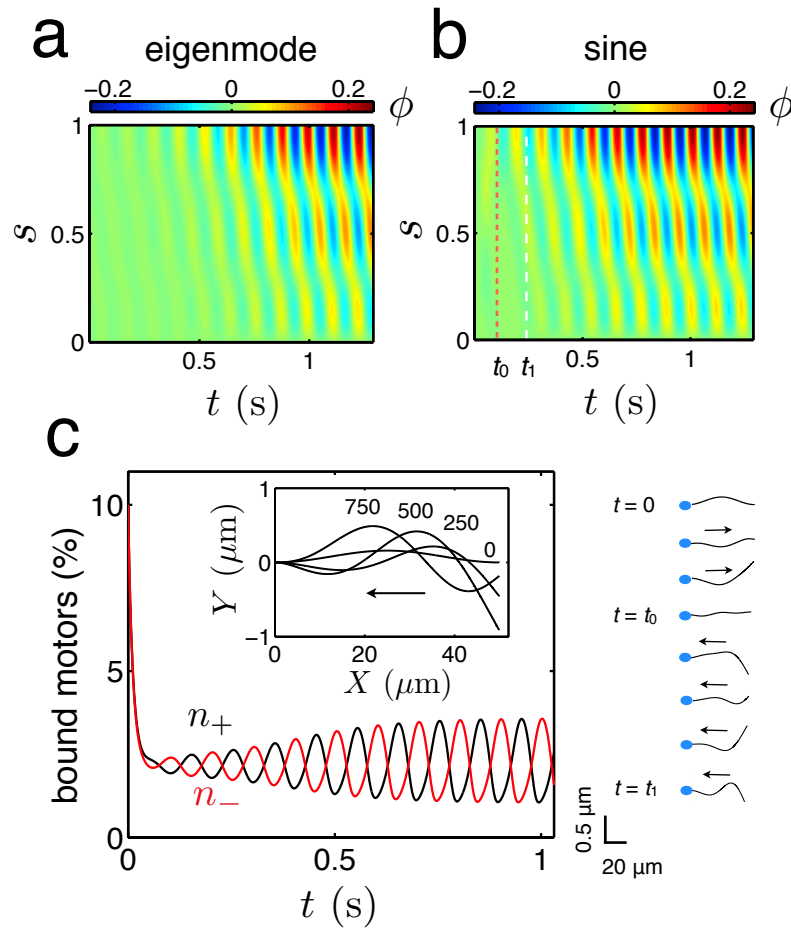


Fig. 7.5 Bending initiation and transient dynamics. a) Spatiotemporal evolution of ϕ for an eigenmode initial condition b) Spatiotemporal evolution of ϕ for a sinusoidal initial condition for the tangent angle with $n_+(0) = n_-(0) = 0.1$ (bottom). c) (Left) Bound motor time evolution for the plus and minus dynein populations at $s = 9/10$ for the case of a sinusoidal initial condition. Inset: Flagella profiles at different times in ms. (Right) Snapshots of the flagellar shape for the sinusoidal initial condition from $t = 0$ to $t = t_1$ (Fig. 7.5b) at equal time intervals. At $t = t_0$, wave interference changes the sense of wave propagation. Arrows indicate the sense of wave propagation. $Sp = 5$, $\mu = 100$, $\mu_a = 2000$, $\eta = 0.14$, $\zeta = 0.4$.

shown for the case of an initial eigenmode solution corresponding to the maximum eigenvalue (a) and an initial sine perturbation in ϕ , with equal constant bound motor densities (b). In case (b) traveling waves propagate in both directions and interfere during the transient dynamics at $t = t_0$ (Fig. 7.5b, 7.5c (right)). However, in the steady state both the eigenmode and sine cases reach the same steady state solution, despite the sinusoidal initial condition being a superposition of eigenmodes. Therefore, we conclude that the fastest growing mode is likely to be the one that takes over in the steady state. In Fig. 7.5c (left) the transient dynamics are shown for plus- and minus-bound dynein populations. Both populations decay exponentially with characteristic time $\bar{\tau}$ to n_0 and begin oscillating in anti-phase around this value, in a ‘tug-of-war’ competition.

7.7 Conclusions

In this chapter we have formulated a set of nonlinear equations describing self-organized flagellar beating, taking into account the coupling of dynein activity with the geometry of the flagellum. Our analysis reveals the spatiotemporal dynamics of dynein kinetics and the flagellum shape for different regimes of motor activity, medium viscosity and flagellum elasticity. We have found that far from the bifurcation, linearized solutions fail to describe the flagellar shape and nonlinear effects arise in the system solely due to motor activity. An important aspect which is not studied explicitly in this work is the sense of traveling wave propagation. For the sake of simplicity, we have used clamped boundary conditions at the head which are known to induce traveling waves which propagate from tip to base [Camalet et al., 1999, Bayly and Wilson, 2015]. It is beyond the scope of our study to determine the effects of different boundary conditions and the role of basal compliance at the head of the flagellum, which are known to crucially affect wave propagation [Riedel-Kruse et al., 2007]. Further work needs to be undertaken to assess the different casuistry in the problem.

Our study provides a deterministic description of flagella; however, real flagella is subject to chemical noise due to the stochastic binding and unbinding of dynein motors. Recently, some studies have provided some insights on this problem by studying a noisy oscillator driven by molecular motors. However, their approach was not spatially extended [Ma et al., 2014]. Our framework can be suitably extended to include chemical noise in the system through Eq. 7.11 by considering a chemical Langevin equation for the bound dynein populations including multiplicative noise [Gillespie, 2000]. From our study, it can be easily deduced that, considering a force-independent unbinding rate, fluctuations of bound motors around the base state have mean $N\eta$ and variance $N\eta(1 - \eta)$, in agreement with the results in Ref. [Ma et al., 2014] where a different model was used. One of the most exciting future challenges in the study of cilia and flagella is the visualization of the spatiotemporal activity of dyneins inside the axoneme. This would reveal how dynein activity couples with flagellum shape and unveil the mechanisms coordinating dynein activity and flagellar beating.

Acknowledgments

This work was conducted in close collaboration with Dr. H. Gad elha in the Wolfson Centre for Mathematical Biology (Mathematical Institute, Oxford).

Chapter 8

General conclusions

In the present thesis we have studied different examples in which cytoskeletal motors self-organize and cooperate in cellular processes.

In the first part, we have carried out a complete theoretical and experimental study on the collective behaviour of single-headed kinesin KIF1A, which constitutes a remarkable example of Brownian motor and a model motor to study intracellular transport.

We have proposed a two-state noise-driven ratchet mechanism to study the collective action of single-headed KIF1A motors *in vitro* extending previous works for the case of vanishing dwell time [Brugués and Casademunt, 2009, Orlandi et al., 2010]. Additionally, by using a lattice approach to describe KIF1A dynamics, we have verified the robustness of the cooperative phenomena found in the Langevin description:

- The presence of finite dwell time in the system reveals non-trivial phenomena associated to a great enhancement of the collective force generation of motors. In simple terms, the combination of several motors in a two-state ratchet enables a switch from a low force noise-driven mechanism ($\sim k_B T l / l_D^2$ with diffusion length $l_D = \sqrt{2D/\omega}$) to a filament-binding mechanism with a high force scale ($\sim U/l$). In order for cooperative effects to emerge, motor positional and internal degrees of freedom must be correlated. The cooperative mechanism of force generation is

robust within a variety of motor-motor interactions, such as repulsive and confining interactions. This effect is able to produce a two-order of magnitude gain on the collective efficiency up to values of $\sim 10^{-2}$. The collective stall force at a given velocity grows faster than proportional to N up to around 5 KIF1A motors. For $N \sim 5 - 10$ the force scaling of KIF1A remains roughly proportional to the number of motors, and for large N the total force produced by the motor ensemble eventually saturates.

- The presence of finite dwell time also reveals staircase shaped velocity-force curves which arise in the high diffusion limit. This effect is a consequence of the inhomogeneous motor density distribution in the cluster and the particular high noise intensity in the system. We find that each plateau corresponds to the recruitment of a new motor to the leading team, and the effect persists for backward movement until the recruitment of the totality of motors.

In order to test the validity of our theoretical predictions on cooperative force generation, we have challenged experimentally single-headed KIF1A motors to extract membrane tubes from GUVs in a minimal *in vitro* setup. Our experimental work has been complemented with *in silico* and mean-field models, which provide a quantitative description of the *in vitro* system:

- We found that single-headed KIF1A motors are capable to collectively extract tubes from GUVs, under similar conditions to previous experiments with conventional kinesin. Hence, our experimental observations validate the theoretical predictions in Chapter 3 on their high cooperativity. Our *in silico* model for longitudinal tube-pulling shows a very good agreement with experiments, providing additional insight on how motors distribute at the tip and all along the tube. While for conventional kinesin the leading cluster was estimated *in silico* to involve $\lesssim 10$ motors [Campàs et al., 2006], here we estimate that $\simeq 15$ KIF1A motors are sufficient for tubulation under similar conditions. This is a remarkable result since the stall force of single-headed

KIF1A is 60 times smaller than that of conventional kinesin.

- Unexpectedly, we found that KIF1A monomers naturally form helical nanotubes. This entails a remarkable capability to collectively exert significant off-axis forces to the point of coiling membrane tubes around MTs. We have shown that a simple mean-field model for KIF1A dynamics captures the essential off-axis dynamics both at a single-motor level and at a collective level. The average single-motor pitch is determined by the MT-motor interactions and the geometry of the MT lattice. The average tube pitch; however, is a collective effect resulting from the competition between the longitudinal and transversal forces generated by the motors.

In the second part, we have focused on the generation of dynamical instabilities driven by molecular motors. Specifically, the spontaneous oscillations in a minimal *in vitro* system and the self-organized beating of flagella have been studied.

In the first case, we have studied in detail a minimal three-variable description for the spontaneous oscillations of collective molecular motors, based on a generic two-state model coupled to an elastic element:

- The three-dimensional reduction is shown to capture the essential nonlinear behaviour of the full set of integro-differential equations. This suggests that a general three-dimensional reduction is inherent to the system even though, in general, the corresponding set of variables may not coincide with the explicit ones used in our case. Moreover, we find that the reduced system shares some similarities with the well known Lorenz model.
- We show that the system can produce different types of nonlinear oscillations which can generally exhibit one or two subharmonics in the limit of large elastic modulus and high mobility. The type of nonlinear oscillations are found to be sensitive to the choice of initial conditions. Interestingly, the emergence of two subharmonics on the spectrum of the backbone signal for large elastic modulus is in remarkable accordance with similar subhar-

monic peaks observed experimentally in analogous conditions [Plaças et al., 2009]. Hence, our study provides a theoretical basis for these experimental observations.

Finally, we have used a theoretical framework for planar flagellar beating providing a nonlinear extension of the works in Refs. [Camalet and Jülicher, 2000, Riedel-Kruse et al., 2007]:

- We have developed a model describing flagellar beating, taking into account the nonlinear coupling between dynein dynamics and flagellum geometry, and formulating a set of nonlinear equations to test how flagellar amplitude and shape vary with dynein activity. Close to the bifurcation, the flagellar profiles obtained using a linear stability analysis are a good approximation to the actual nonlinear profiles. However, far from the bifurcation, linear profiles fail to describe the actual flagellar shapes.
- Far from the bifurcation, we find that the tangent angle dynamics presents relaxation oscillations with cusp-like maxima in some regions along the flagellum. This effect is characteristic of collective molecular motors far from equilibrium coupled to an elastic element [Jülicher and Prost, 1997]. Interestingly, a similar behaviour was found experimentally in sea-urchin sperm [Ohmuro et al., 2004].

Chapter 9

Resum en català

Els enormes progressos de les nanotecnologies durant les últimes dècades han permès un estudi quantitatiu dels fenòmens biològics fins a arribar a la escala d'una sola molècula. La possibilitat de visualitzar, manipular i mesurar fenòmens biològics a escala molecular obre un nou món per a la física, que pot aplicar els seus mètodes de modelització per explicar i predir fenòmens abans inabastables des d'un punt de vista tecnològic. Un clar exemple en són les pinces òptiques i magnètiques, les quals permeten la manipulació de biomolècules i la mesura de forces amb gran precisió. És en aquest marc on disciplines com ara la física estadística de no equilibri, la física no lineal o la ciència de materials tous conflueixen i juguen un paper clau. La complexitat dels sistemes biològics, rau comunament en fenòmens col·lectius en situacions allunyades del equilibri, autoregulats mitjançant xarxes bioquímiques complexes les quals requereixen d'un alt grau d'autoorganització, la qual cosa implica tant fluxes de matèria i energia com d'informació. Tot i així, els nivells d'autoorganització i autoregulació involucrats en funcions cel·lulars tals com la motilitat i el tràfic intern, estan encara molt lluny d'una comprensió quantitativa satisfactòria des d'un punt de vista físic. Tals processos requereixen no només d'una visió qualitativa i descriptiva, sinó també d'una perspectiva físico-matemàtica per a la seva completa comprensió.

El present treball versa sobre l'estudi de l'acció col·lectiva de motors moleculars del citoesquelet, amb la finalitat de contribuir en la comprensió de la generació de força i moviment dins la

cèl·lula. La tesi està estructurada en dues parts: la primera part correspon a l'estudi del transport intracel·lular degut a l'acció cooperativa de motors, en particular, l'estudi es centra en la kinesina monomèrica KIF1A, la qual constitueix un exemple notable de motor Brownià en el context biològic. En primer lloc, es duu a terme un estudi teòric exhaustiu sobre l'acció col·lectiva d'aquests motors, i posteriorment, es validen experimentalment els resultats predits mitjançant experiments d'extracció de tubs de membrana. En la segona part, s'estudia la generació d'instabilitats dinàmiques degudes a l'acció cooperativa de motors moleculars. En particular, es tracten el casos d'oscil·lacions espontànies generades per un sistema *in vitro* d'actina i miosina, i el batec autoorganitzat de flagels degut a l'acció de dineïnes axonèmiques.

Part I: Transport cooperatiu de motors moleculars

Els motors moleculars són proteïnes capaces de transformar energia química en treball mecànic mitjançant la hidròlisi del ATP. Motors com les miosines o les kinesines, són els responsables de la contracció muscular o el transport d'òrgànuls dins la cèl·lula, respectivament. Les kinesines tenen una important labor en processos fonamentals com ara la divisió cel·lular o el transport intracel·lular. Típicament, aquestes proteïnes estan formades per dos dominis motors (forma dimèrica) connectats a un coll que els uneix a la càrrega que transporten. En contacte amb filaments anomenats microtúbuls, aquests motors caminen alternant seqüencialment els seus dominis motors en un mode conegut com *'hand-over-hand'*. No obstant, existeix una classe de kinesina anomenada KIF1A la qual és capaç de generar força únicament amb l'ajuda d'un sol domini motor (forma monomèrica), mitjançant la seva difusió al llarg del microtúbul i funcionant com a motor Brownià. Aquesta kinesina es troba de forma específica en els axons neuronals i s'encarrega de transportar vesícules precursors de la sinàpsi. Les condicions del transport axonal són particularment exigents ja que els motors han de transportar òrgànuls al llarg de grans distàncies (mil·límetres, centímetres o fins i tot metres en alguns organismes). Tot i que la kinesina KIF1A es troba normalment

en la seva forma dimèrica *in vivo*, curiosament s'ha observat que aquesta forma també gaudeix d'un estat difusiu, el qual coexisteix amb un estat processiu en què el motor avança presumiblement utilitzant un mecanisme semblant al de *'hand-over-hand'*. La raó per la qual aquesta kinesina, un motor *a priori* ineficient degut a la presència d'un estat difusiu, està encarregada d'un transport tan exigent com ara el transport axonal, és a hores d'ara una incògnita.

Estudis teòrics de motors moleculars modelitzats mitjançant *ratchets* Brownians o equacions mestres pròpies de la física de no equilibri, han revelat comportaments dinàmics col·lectius no trivials com la presència de cooperativitat o l'aparició de complexitat en forma de caos o fractalitat. Motivats pels anteriors resultats, en el present treball hem estudiat la hipòtesi de que aquests tipus de motors estan particularment adaptats al treball cooperatiu degut a la transmissió de força gràcies a la presència d'un estat difusiu. Per a comprovar l'anterior hipòtesi, hem dut a terme un estudi exhaustiu del comportament col·lectiu de kinesines KIF1A utilitzant una modelització de *ratchets* Brownians amb dos estats: un estat lligat al microtúbul i un estat dèbilment lligat corresponent a l'estat difusiu. Els resultats revelen que la presència de temps d'espera per a capturar l'ATP, augmenta de forma dramàtica l'*stall force* col·lectiva (la força necessària per a aturar el sistema) quan els motors KIF1A treballen conjuntament contra una força externa. En particular, l'augment de l'*stall force* en funció del nombre de motors és no lineal, permetent que 10 motors cooperin per a produir al voltant de 100 vegades la força d'un sol motor.

Posteriorment, ens vàrem disposar a comprovar experimentalment les nostres prediccions teòriques *in vitro*. Per això, vàrem considerar oportú dur a terme experiments biomimètics d'extracció de nanotubs de membrana. En aquests experiments, típicament els motors moleculars s'ancoren en vesícules unilamel·lars gegants. En presència d'ATP i d'una xarxa de microtúbuls amb la qual els motors hi poden interaccionar, aquests cooperen en grups per a extreure tubs de membrana de les vesícules gegants, formant així xarxes de nanotubs de membrana. Els experiments amb la forma monomèrica del motor KIF1A foren satisfactoris i malgrat

la seva ineficiència a nivell individual, els motors varen ser capaços de cooperar per a extreure nanotubs de membrana. Els nostres experiments també varen revelar la sorprenent formació de tubs helicoïdals al voltant de microtúbuls, dels quals en vàrem poder analitzar la seva geometria i dinàmica. Aquest fet insòlit mostra una combinació inesperada de generació col·lectiva de força juntament amb una maniobrabilitat autoorganitzada dels motors. L'estudi s'ha completat amb simulacions *in silico* del sistema i una modelització *mean-field* per a entendre la selecció del angle de les hèlices.

En resum, en la primera part de la tesi hem estudiat l'acció cooperativa de motors monomèrics KIF1A des d'una vessant teòrica i a la vegada experimental, confirmant així la nostra hipòtesi que els motors KIF1A estan particularment adaptats a l'acció cooperativa gràcies a la presència d'un estat difusiu en el seu cicle d'hidròlisi. La sorprenent formació de tubs helicoïdals al voltant de microtúbuls, ens fa especular sobre la possibilitat que la generació de forces transversals pugui ser una estratègia per a evadir possibles obstacles al llarg de l'axó i així assegurar un tràfic axonal fluid. Diverses futures línies de treball són motivades arran dels nostres resultats. A nivell teòric, l'estudi del comportament col·lectiu de motors moleculars en dues dimensions al llarg del microtúbul i la capacitat de maniobra d'aquests grups per a evadir obstacles són dos qüestions fonamentals que poden tenir implicacions directes en l'estudi d'embusos en el tràfic axonal en les neurones. A nivell experimental, seria interessant estudiar fins a quin punt els nostres resultats són extrapolables a la versió dimèrica del motor KIF1A, la qual és la forma rellevant *in vivo*.

Part II: Inestabilitats dinàmiques en agrupacions de motors

En la segona part de la tesi, hem estudiat la generació d'oscil·lacions i la propagació d'ones degut a inestabilitats generades per l'acció d'agrupacions de motors moleculars. Alguns exemples rellevants dins la cèl·lula són les oscil·lacions mitòtiques i meiòtiques,

les oscil·lacions espontànies en cèl·lules auditives, els règims oscil·latoris en la contracció muscular o el batec de cilis i flagels. En el llenguatge de sistemes dinàmics, *feedback loops* positius poden desestabilitzar l'estat immòbil dels sistema generant oscil·lacions o ones que es propaguen en sistemes espacialment estesos. La forma, l'amplitud i el període de les oscil·lacions són posteriorment seleccionats per les no-linearitats específiques del sistema. En particular, hem estudiat la generació d'oscil·lacions mecàniques en estructures del citoesquelet com ara són les oscil·lacions espontànies en un sistema d'actina i miosina o el batec flagel·lar.

En primer lloc, hem estudiat un model genèric, prèviament proposat, en què els motors moleculars són capaços de generar oscil·lacions espontànies en presència d'un element elàstic en el sistema. Aquest model ha descrit satisfactòriament diversos sistemes biològics on els motors moleculars generen oscil·lacions mecàniques. En termes matemàtics, el model consisteix d'un sistema d'equacions integro-diferencials en derivades parcials el qual hem reduït a un sistema simplificat de tres equacions diferencials ordinàries, capturant la dinàmica essencial del sistema. Curiosament, el sistema d'equacions integro-diferencials comparteix certes semblances amb les equacions de Markus-Lorenz, les quals descriuen un exemple de roda hidràulica que presenta caos. L'anterior sistema té la propietat que, per una tria particular de paràmetres, es redueix a les conegudes equacions de Lorenz. En el nostre cas, el sistema mostra certes semblances amb el model de Lorenz encara que no s'ha detectat la presència de caos. Tot i així, el sistema original, així com també el sistema reduït, genera oscil·lacions subharmòniques en el règim d'alta mobilitat (baixa fricció) i mòdul elàstic gran. Sorprenentment, l'aparició d'oscil·lacions subharmòniques es varen detectar prèviament en un sistema *in vitro* d'actina i miosina, utilitzant una trampa òptica la qual exercia una força recuperadora en un filament d'actina, oposant-se a la força generada per les miosines. El nostre estudi doncs, dóna resposta a les oscil·lacions subharmòniques observades experimentalment en un sistema *in vitro* d'actina i miosina.

Finalment, hem estudiat els mecanismes físics del batec flagel·lar i ciliar. La motilitat flagel·lar juga un rol crucial en la super-

vivència, desenvolupament, alimentació i reproducció de diversos microorganismes. Els organismes flagel·lats utilitzen un o més apèndixs per a la seva propulsió. En particular, en el cas d'organismes eucariotes, l'acció de motors moleculars dins els flagels o cilis comporta moviments oscil·lants del mateixos, els quals permeten nedar als microorganismes. L'estructura del citoesquelet que conforma els flagels i cilis eucariotes s'anomena *axonema*. Aquesta estructura té una composició "9+2" característica en la majoria d'organismes eucariotes, corresponent a 9 doblets de microtúbuls perifèrics en disposició cilíndrica envoltant un doblet de microtúbuls centrals. Cada doblet consisteix d'un microtúbul al qual les dineïnes estan ancorades a intervals regulars, i un segon microtúbul a on les dineïnes provinents del doblet veí s'hi enganxen. En presència d'ATP, les dineïnes generen un moviment relatiu dels doblets de microtúbuls, generant una força que pot fer-los lliscar un respecte l'altre en absència de proteïnes que les entreliguin. En presència d'aquestes, el moviment relatiu entre doblets es transforma en flexió. Aquest procés es duu a terme d'una forma altament coordinada, de manera que quan un grup de dineïnes en l'axonema està actiu, l'altre grup resta inactiu. En el cas del flagel espermàtic, aquesta coordinació permet la generació d'ones de flexió definides en un pla. Actualment, la hipòtesi majoritàriament acceptada és que la coordinació és un fenomen autoorganitzat, degut a l'acoplament de l'acció de les dineïnes i la geometria del axonema.

Per tal d'entendre la generació d'ones al llarg d'un flagel eucariota, hem realitzat un estudi teòric en el qual hem introduït explícitament l'acoplament entre l'acció de les dineïnes i la geometria de l'axonema. El nostre enfocament suposa una extensió no lineal d'estudis previs, on la dinàmica dels motors moleculars al llarg del flagel no era incorporada explícitament. En el nostre estudi, hem derivat un sistema d'equacions no lineals les quals permeten estudiar l'evolució espaciotemporal del flagel, així com la dinàmica de les dineïnes arbitràriament lluny de la bifurcació. Per sobre d'una certa activitat crítica dels motors, el flagel genera ones que es propaguen a través d'una bifurcació de Hopf. Prop de la bifurcació, els perfils flagel·lars obtinguts a través de l'anàlisi d'estabilitat lineal són una bona aproximació als perfils dèbilment no lineals.

Per altra banda, l'estudi lluny de la bifurcació revela oscil·lacions *cusp-like* de l'angle tangent les quals difereixen amb l'anàlisi lineal i concorden amb resultats experimentals d'espermatozoides d'ericons de mar. A més a més, també hem analitzat la dinàmica flagel·lar mitjançant una anàlisi de components principals, la qual ens ha permès interpretar les oscil·lacions mitjançant dos únics vectors propis en un espai abstracte de les formes. Finalment, l'estudi de la iniciació del batec flagel·lar per a diferents condicions inicials ens ha permès explorar la dinàmica transitòria, observant en alguns casos, l'interferència d'ones al llarg del flagel.

Appendix A

Analytical VF relationship for KIF1A

In this appendix we present the derivation of the velocity-force relationship for one single-headed KIF1A motor under an external force F in the high diffusion limit. Since KIF1A has been reported to be highly diffusive in the weakly bound state [Okada et al., 2003], this limit is appropriate for this motor. The next arguments are based on Ref. [Orlandi et al., 2010]. We will neglect noise in the U_1 state since sliding velocities are usually high enough in this limit due to low friction. Consequently, the motor will follow a deterministic movement during the power stroke without being excessively perturbed by noise. Conversely, dynamics in the U_2 state will be stochastic since the motor will follow a diffusive movement with coefficient $D = k_B T / \lambda$. The motor will move a distance $\Delta x'$ in a mean time $\tau = 1/\omega$ with probability density:

$$P(\Delta x = \Delta x') = \frac{1}{\sqrt{4\pi D\tau}} \exp\left[-\frac{(\Delta x' + F\tau/\lambda)^2}{4D\tau}\right] \quad (\text{A.1})$$

where $F\tau/\lambda$ is the mean displacement of the motor. We assume a situation where the motor is found in the minimum of the ratchet potential and waits a mean dwell time $\tau_h = 1/\omega^*$ before jumping to the U_2 state. After diffusing for a mean time τ , it will fall back to the U_1 state in a different period of the ratchet. At this point, the motor will follow a deterministic movement until reaching the minimum again. The whole movement defines a *cycle*, and the overall trajectory of the motor can be understood as the sequence of multiple cycles. Therefore, we define the mean displacement $\langle \Delta x \rangle$ as the mean distance the motor travels in a cycle and $\langle \Delta t \rangle$

as the mean time needed to perform this cycle. With the previous definitions, the velocity of the motor reads:

$$V = \frac{\langle \Delta \chi \rangle}{\langle \Delta t \rangle} \quad (\text{A.2})$$

The mean position $\langle \Delta \chi \rangle$ can be expressed as $\langle \Delta \chi \rangle = l \sum_{n=-\infty}^{\infty} n \mathcal{P}(n)$, where $\mathcal{P}(n)$ is the probability of falling at any position between $(n-1)l$ and nl :

$$\langle \Delta \chi \rangle = \sum_{n=-\infty}^{\infty} nl \int_{a+l(n-1)}^{a+ln} P(\Delta x) d\Delta x \quad (\text{A.3})$$

Defining $\alpha \equiv v\tau/(l-a)$, $\beta \equiv 1/\sqrt{4D\tau}$, $\bar{a} \equiv a/l$ and $f \equiv F/\lambda v$, we can rewrite Eq. A.3 as:

$$\langle \Delta \chi \rangle = \frac{\beta}{\sqrt{\pi}} \sum_{n=-\infty}^{\infty} nl \int_{\bar{a}-1}^{\bar{a}} dz \exp[-\beta^2(z+n+\alpha f(1-\bar{a}))^2] \quad (\text{A.4})$$

If we take the limit $\beta \rightarrow 0$ ($D \rightarrow \infty$) we can convert the sum into an integral by means of the change of variable $s = n\beta$. The result is:

$$\langle \Delta \chi \rangle = \frac{l}{\beta\sqrt{\pi}} \int_{\bar{a}-1}^{\bar{a}} dz \int_{-\infty}^{\infty} s \exp[-(s+\beta(z+\alpha f(1-\bar{a})))^2] ds \quad (\text{A.5})$$

Computing the integrals we obtain:

$$\langle \Delta \chi \rangle = \frac{l}{2} [1 - 2\bar{a} - 2f\alpha(1-\bar{a})] \quad (\text{A.6})$$

Similarly, the expression for $\langle \Delta t \rangle$ reads:

$$\begin{aligned} \langle \Delta t \rangle = & \sum_{n=-\infty}^{\infty} \int_{a+l(n-1)}^{nl} \left(\tau + \tau_h - \frac{x}{v - F/\lambda} \right) P(\Delta x) d\Delta x + \\ & + \sum_{n=-\infty}^{\infty} \int_{nl}^{a+nl} \left(\tau + \tau_h + \frac{x}{v \frac{l-a}{a} + F/\lambda} \right) P(\Delta x) d\Delta x \end{aligned} \quad (\text{A.7})$$

Non-dimensionalizing as before, and following the same assumptions we obtain:

$$\langle \Delta t \rangle = \left(\frac{\tau + \tau_h}{1 - f} \right) \frac{1 - \bar{a}}{1 - \bar{a}(1 - f)} \quad (\text{A.8})$$

Finally the motor velocity reads:

$$V(f)_{\beta \rightarrow 0} = v(1 - f) \frac{[1 - 2\bar{a} - 2f\alpha(1 - \bar{a})][1 - \bar{a}(1 - f)]}{2\alpha_\tau(1 - \bar{a})^2} \quad (\text{A.9})$$

where $\alpha_\tau \equiv v(\tau + \tau_h)/(l - a)$. From the last expression we can extract the stall force of the motor:

$$F_s = \lambda v \min \left[1, \frac{f(\bar{a})}{2\alpha} \right] \quad (\text{A.10})$$

The function $f(a) = (1 - 2\bar{a})/(1 - \bar{a})$ is a decaying function of the asymmetry parameter which is 1 at $\bar{a} = 0$ and 0 at $\bar{a} = 1/2$. In this limit $V_1(0)$ depends uniquely on the asymmetry of the ratchet and the time between steps. From Eq. A.10 we find two different stall forces leading to different stall mechanisms. λv is the force needed to drag the motor up the ratchet slope i.e. U/l . This case corresponds to a force which impedes the motor to reach the next minimum. On the other hand, the second stall force $\lambda v f(\bar{a})/2\alpha$ corresponds to the case in which the motor cannot move forward by diffusing to the next period of the track. Substituting the different values we find that the stall force reads $(1 - 2\bar{a})k_B T l / l_D^2$, with the diffusion length $l_D \equiv \sqrt{2D/\omega}$. This fact leads the motor to undertake cycles switching to the diffusive state and falling back to the same period. Finally, we notice the stall force is not affected by the dwell time in this limit.

Appendix B

Simulation of stochastic processes

In this appendix we describe in detail the simulation of Langevin dynamics and the implementation of the Gillespie algorithm.

B.1 Langevin dynamics

We illustrate the procedure used in Section 3.1 to simulate Langevin dynamics [Sancho et al., 1982]. Let us consider an equation describing the stochastic dynamics of a quantity $x(t)$:

$$\frac{dx}{dt} = f(x) + \xi(t) \quad (\text{B.1})$$

where $f(x)$ is a general function of the variable $x(t)$ and $\xi(t)$ is a rapidly fluctuating random term which has zero mean and it is delta correlated in time. Let us consider a small time interval Δ and formally integrate Eq. B.1:

$$x(t + \Delta) = x(t) + \int_t^{t+\Delta} f(x(t'))dt' + \int_t^{t+\Delta} \xi(t')dt' \quad (\text{B.2})$$

For sufficiently small Δ , the function f can be approximated as $f(x(t')) \simeq f(x(t))$ and hence:

$$x(t + \Delta) = x(t) + f(x(t))\Delta + \int_t^{t+\Delta} \xi(t')dt' \quad (\text{B.3})$$

The last term must be evaluated by means of stochastic calculus. Considering the equivalence $\xi(t)dt = \sqrt{2D}dW(t)$, where $W(t)$ is the Wiener process [Gardiner, 1985] and D is the strength of the random term, the stochastic integral reads:

$$\int_t^{t+\Delta} \xi(t')dt' = \sqrt{2D}[W(t+\Delta) - W(t)] = \sqrt{2D\Delta}\gamma \quad (\text{B.4})$$

where γ corresponds to a Gaussian random number with zero mean and variance 1. The Gaussian random number γ can be generated using the Box-Müller formula [Box and Müller, 1958]:

$$\gamma = \sqrt{-\ln \eta_1} \cos(2\pi\eta_2) \quad (\text{B.5})$$

where η_1 and η_2 are two uniformly distributed random numbers taken in the interval $[0,1]$. Finally, the algorithm for the dynamics of $x(t)$ reads:

$$x(t+\Delta) = x(t) + f(x(t))\Delta + \sqrt{-2D\Delta \ln \eta_1} \cos(2\pi\eta_2) \quad (\text{B.6})$$

B.2 Gillespie algorithm

We illustrate the Gillespie algorithm used in Section 3.2.1.2 to simulate KIF1A dynamics on a lattice [Gillespie, 1976]. Let us consider M possible processes (e.g. reactions, transitions) labeled $\sigma = 1, \dots, M$ and let's define the *reaction probability density function* $P(\tau, \sigma)$ where $\tau \in [0, \infty)$. This quantity is defined as follows: $P(\tau, \sigma)d\tau$ is the probability at time t that the next reaction will occur in the differential time interval $(t + \tau, t + \tau + d\tau)$ and will be a σ -process. This probability density has the form:

$$P(\tau, \sigma) = a_\sigma \exp\left(-\sum_{\nu=1}^M a_\nu \tau\right) \quad (\text{B.7})$$

where a_σ is the rate at which the σ -process occurs. The *direct method* [Gillespie, 1976] is a consistent way to simulate multiple stochastic processes. Let us write $P(\tau, \sigma)$ in the following form:

$$P(\tau, \sigma) = P_1(\tau)P_2(\sigma|\tau) \quad (\text{B.8})$$

where $P_1(\tau)d\tau$ is the probability that the next process will occur in the time interval $(t + \tau, t + \tau + d\tau)$, irrespective of which process will be, and $P_2(\sigma|\tau)$ is the probability that the next process will be a σ -process, given that the process occurs at time $t + \tau$. By the addition theorem for probabilities we have:

$$P_1(\tau) = \sum_{\sigma=1}^M P(\tau, \sigma) \quad (\text{B.9})$$

using (B.8) and (B.9) we obtain:

$$P_2(\sigma|\tau) = \frac{P(\tau, \sigma)}{\sum_{\nu=1}^M P(\tau, \nu)} \quad (\text{B.10})$$

Finally using (B.7) we can express the last quantities in terms of the rates a_σ :

$$P_1(\tau) = a \exp(-a\tau) \quad (\text{B.11})$$

$$P_2(\sigma|\tau) = a_\sigma/a \quad (\text{B.12})$$

where $a \equiv \sum_{\sigma=1}^M a_\sigma$. The idea of the method is to first generate a random value τ according to $P_1(\tau)$, and then generate a random number σ according to $P_2(\sigma|\tau)$. The resulting random pair (τ, σ) will be distributed according to $P(\sigma, \tau)$. This means that first we generate a random number to know the necessary time τ for the next process to occur, and next we generate a second random number to know which process will be. The first random value τ can be easily generated by drawing a random number r_1 from the uniform distribution in the unit interval and using:

$$\tau = \frac{1}{a} \ln(1/r_1) \quad (\text{B.13})$$

Finally the random number σ can be generated by drawing a second random number r_2 from the uniform distribution in the unit interval and taking σ to be the integer such that:

$$\sum_{\nu=1}^{\sigma-1} a_\nu < r_2 a \leq \sum_{\nu=1}^{\sigma} a_\nu \quad (\text{B.14})$$

In general a_σ may depend on time, external fields, etc. Therefore a general algorithm will contemplate time dependent rates $a_\sigma(t)$. The algorithm works as follows:

1. At time t_i our system is found in configuration \mathcal{C}_i .
2. Update the values of $a_\sigma(t_i)$ for $\sigma = 1, \dots, N$ and $a(t_i)$.
3. Draw a first uniformly distributed random number $r_1 \in [0, 1]$ to calculate τ using (Eq. B.13).
4. Draw a second uniformly distributed random number $r_2 \in [0, 1]$ to calculate σ using (Eq. B.14).
5. Perform process σ and update the configuration of the system $\mathcal{C}_i \rightarrow \mathcal{C}_{i+1}$.
6. Update the time $t_i \rightarrow t_{i+1} = t_i + \tau$.
7. Go back to step 1.

Appendix C

Cell culture and purification of KIF1A

In this appendix we provide a detailed explanation of the purification protocol for the A382 KIF1A construct used in the experiments in Chapter 4. This protocol was designed by Dr. S. Roth in the FOM Institute AMOLF (The Netherlands). We describe the composition of the mediums and buffers used during the purification process and we detail the different steps: pre-culture, induction, recuperation of the lysate and purification.

C.1 Mediums and buffers

The composition of 1 L LB medium for bacteria was 10 g of Bacto Tryptone, 5 g Yeast extract, 10 g NaCl and ddH₂O to final volume. For the case of 1.5 % agar plates, 15 g of agar was added before autoclaving.

The different buffers used were the lysis buffer (200 mL, pH 8.0), washing buffer (200 mL, pH 7.0) and elution buffer (20 mL, pH 7.0). In Tables C.1 and C.2, the composition of the buffers is shown:

Product	Lysis buffer
Imidazole	20 mM
MgCl ₂	1 mM
NaPi, pH 7.0	50 mM
NaCl	250 mM
Glycerol	10 %
Triton X	0.1 %

Table C.1 Composition of the lysis buffer. Just prior to use, add β -mercaptoethanol 5 mM + 1 tablet of protease inhibitor cocktail / 50 mL

Product	Washing buffer	Elution buffer
Imidazole	20 mM	500 mM
MgCl ₂	1 mM	1 mM
NaPi, pH 7.0	50 mM	50 mM
NaCl	250 mM	250 mM
Glycerol	10 %	10 %

Table C.2 Composition of the washing and elution buffers. Just prior to use, add β -mercaptoethanol 5 mM and MgATP 0.1 mM.

C.2 Protocol

Pre-culture

- Prepare 1L bottle and 2L Erlenmeyer of LB medium and autoclave.
- Transfer 100 mL of LB medium in a 250 mL Erlenmeyer and add ampicillin to 100 μ g/mL final concentration.
- Scrape a transformed single colony with a pipette tip from the agar plates and transfer the pipette tip with bacteria into the 250 mL Erlenmeyer.
- Incubate at 37 °C at 220 rpm overnight.

Induction

- Next day, prewarm the 2L LB medium, add ampicillin (100 μ g/mL) and 25 mL of overnight culture.
- Shake at 210 rpm at 37 °C.

- Check OD 600 every 30 min.
- When OD 600 reaches 0.3, set temperature to 30 °C in a water bath and add IPTG 300 μ M. Let it shake at 160 rpm.
- Induce 4h at 30 °C.
- Transfer the culture into 1L buckets to centrifuge and spin down at 5000 rpm for 30 min at 4 °C.
- Right after the spin, take out the supernatant and resuspend in 50 mL Lysis buffer (add β -mercaptoethanol and protease inhibitor cocktail prior to use).
- Flash freeze in liquid nitrogen.

Recuperation of the lysate

- Prewarm the water bath at 37 °C.
- Take a bucket of ice and place the tube for the centrifuge at 4 °C.
- Thaw quick the lysate in the water bath and place it as soon as it is melted on ice.
- Add lysosyme (1 mg/mL) to break the membrane and a knife tip of DNase (\approx 2 mg).
- Incubate the cell suspension on a shaking platform at 4 °C for 20 min.
- Dip pellets in liquid nitrogen until fully frozen.
- Thaw the pellets by spinning them in a water bath at 37 °C for 5 min.
- Put them back in the shaking platform at 4 °C for 20 min more.
- Freeze and thaw again (as above).
- Pass the cell lysates through a blunt needle (low gauge) a few times to shear genomic DNA. Cell lysates should not be very viscous at the end of the incubation.
- Pour the lysate in tubes for the rotor. Take a sample '0' and balance well.
- Spin down 30 min at 15000 rpm at 4 °C.
- During the spin, prepare a Ni NTA column.
 - Put 2 mL of Ni NTA beads in a 50 mL Falcon.
 - Add 8 mL of lysis buffer, spin 2000 rpm, 1 min at 4 °C.

- Discard the supernatant. Repeat one more time and keep on ice.
- Collect the supernatant from the spin. Take a sample of the supernatant (S) and a sample of the pellet (P).

Purification

- Retrieve the supernatant from the spin and place it on the cleaned Ni NTA beads
- Put in a rotating wheel at 4 °C for 2h.
- 30 min before the end, add MgATP and β -mercaptoethanol to the wash and elution buffers.
- Prepare the tubes for the lysate, the elution and the different washes.
- Run the lysate and the beads through the column and collect the flow through in the different lysate tubes.
- Wash the column with 15 mL washing buffer and collect the flow through in 1mL batches for control purposes.

If labeling:

- Close column.
- Add tris(2-carboxyethyl) phosphine hydrochloride (TCEP) solution 1mM and incubate 30 min.
- Wash 3 times with washing buffer to get rid of the excessive TCEP. Collect flow through in 1mL batches.
- Prepare a stock solution of 8mM labeling molecule (EZ-Link BMCC-biotin or Dylight™ 550 Sulfhydryl reactive dye, Thermo scientific).
- Add the solution of labeling molecule to the protein (1 mL) bound in the column and mix to have a 10X mol excess. Make sure that all the Ni NTA beads are in contact with the reagent by adding phosphate-buffered saline (PBS).
- Incubate 30 min at room temperature.
- Wash three times with washing buffer and collect flow per mL.
- Elute with elution buffer and collect the flow through per mL.

Appendix D

Theoretical description of a tubular helix

In this appendix we describe the geometry and energetics of a tubular helix relevant to the membrane tube extraction experiments presented in Chapter 4.

D.1 Geometry and energetics of a tubular helix

We consider a tubular helix of radius r (tube radius) winding on an imaginary cylinder of radius R (MT radius plus some extra space occupied by the motors, depicted as a dashed circle in Fig. D.1a, left), such that $r + R$ is the distance between the center of the MT and the center of the tube. The helix moves along the z -axis with an angular pitch p which is the distance the helix advances per radian along the z -axis. Each point on the surface of the helix is determined by the vector \mathbf{X} . We can parametrize every point on the helix surface with two variables $\{s, \phi\}$, where s is the arclength following the path of the helix through its center and ϕ is an angle which determines at a given s the position of a point in the circle of radius r . If we call a the angle the helix moves per arclength unit, the distance the helix advances along the z -axis after moving a distance s along the helix will be $p\theta$, where $\theta \equiv as$. If we move an arclength unit, we are moving a distance ap in the z -axis and a distance aR_0 in the axis perpendicular to the z -axis, where $R_0 \equiv R + r$. In this way we find $1 = a^2(R_0^2 + p^2)$. On the other hand, the angle ζ the center of the helix forms respect to the z -axis fulfills (see Fig. D.1b):

$$\tan \zeta = \frac{R_0}{p} \quad (\text{D.1})$$

The position of the center of the left-handed helix is $\mathbf{r}(s) = (R_0 \sin \theta, R_0 \cos \theta, p\theta)$. We can parametrize the surface of the tubular helix $\mathbf{X}(s, \phi)$ as:

$$\mathbf{X}(s, \phi) = \mathbf{r}(s) + r[\mathbf{n}(s) \cos \phi + \mathbf{b}(s) \sin \phi] \quad (\text{D.2})$$

with $\phi \in [0, 2\pi)$, using the orthonormal triad $\{\mathbf{t}, \mathbf{n}, \mathbf{b}\}$ such that $\mathbf{t}(s) = \frac{\partial_s \mathbf{r}}{|\partial_s \mathbf{r}|}$, $\mathbf{n}(s) = \frac{\partial_s \mathbf{t}}{|\partial_s \mathbf{t}|}$ and $\mathbf{b}(s) = \frac{\mathbf{t} \wedge \mathbf{n}}{|\mathbf{t} \wedge \mathbf{n}|}$ (see Fig. D.1a, right). The mean curvature of the surface $H(\phi)$ can be determined through the first and second fundamental forms $g_{\mu\nu}(s, \phi) = \partial_\mu \mathbf{X} \cdot \partial_\nu \mathbf{X}$ and $\Pi_{\mu\nu}(s, \phi) = \partial_{\mu\nu} \mathbf{X} \cdot \mathbf{n}$, $\mu, \nu = s, \phi$; which in a matrix form read:

$$\mathbf{g} = \begin{pmatrix} E & F \\ F & G \end{pmatrix} \quad \mathbf{\Pi} = \begin{pmatrix} L & M \\ M & N \end{pmatrix} \quad (\text{D.3})$$

The mean curvature can be calculated through the expression $H(\phi) = \frac{EN - 2FM + GL}{2 \det(\mathbf{g})}$ [Kamien, 2002, Gray, 1993] which leads to:

$$H(\phi) = \frac{1}{2} \left[\frac{1}{r} + rK(\phi) \right] \quad (\text{D.4})$$

where $K(\phi) = -\frac{C \cos \phi}{r(1 - rC \cos \phi)}$ and $C = \frac{R_0}{R_0^2 + p^2}$ is the curvature of the helical spine curve of the tube. We notice that for $p \rightarrow \infty$ the curvature tends to the one of a cylinder of radius r i.e. $1/2r$. The total surface of a tubular helix of length L and radius r is $2\pi rL$, the same as for a cylinder. Consequently, the surface energy is $2\pi rL\gamma$, and it does not depend on the pitch. Let us define the small quantity $\epsilon \equiv rC$. This quantity is bounded below 1 in the experiments. Considering the first correction up to fourth order in ϵ , the free energy of the system can be approximated as:

$$\mathcal{F} \simeq \frac{\pi\kappa L}{r} \left(1 + \frac{1}{2}\epsilon^2 \right) + 2\pi rL\gamma - FL \quad (\text{D.5})$$

In the limit $p \rightarrow \infty$ (or $\epsilon \rightarrow 0$), we recover the free energy of a cylindrical tube with extraction force $F = 2\pi\sqrt{2\kappa\gamma}$ and diameter $2r = \sqrt{\kappa/\gamma}$. Therefore, we conclude that the last two expressions

for the cylindrical case are accurate to second order in ϵ and yield good approximations to the actual values for the helical tubes.

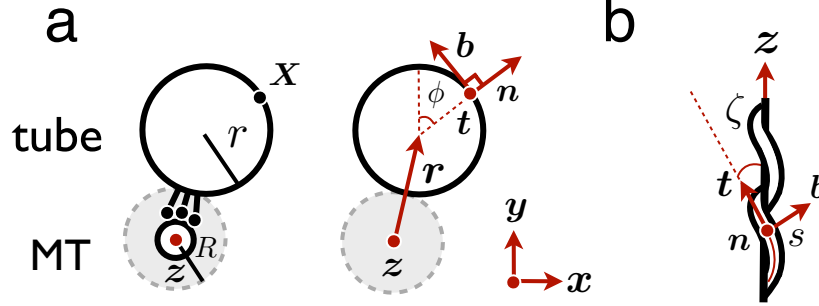


Fig. D.1 Geometry of a tubular helix winding around a MT. a) Sketch of the tube with radius r and the imaginary cylinder of radius R depicted as a dashed circle containing the grey region. The radius of this cylinder corresponds to the radius of the MT plus some extra space occupied by the motors. We associate a orthonormal triad $\{t, n, b\}$ at each point $X(s, \phi)$ on the surface of the helical tube. The vector $r(s)$ defines the position of the nanotube center at s , and the angle ϕ defines a point on the tube surface. b) Helical tube forming a helical angle ζ with respect to the z -axis.

D.2 Superhelical effect on the tube pitch

Let us consider a helical tube of pitch P growing around a MT which has superhelicity of pitch P_{sh} . The angle that the tube will advance per arlength unit will be:

$$a(p') = a(p) + a(p_{sh}) = a(p)(1 + \xi) \quad (\text{D.6})$$

where p' is the angular pitch, p is the angular pitch for a 13pf MT and ξ is the relative increase in angle which reads:

$$\xi = \sqrt{\frac{1 + \cot^2 \zeta}{1 + \cot^2 \zeta_{sh}}} \quad (\text{D.7})$$

where $\cot \zeta_{sh} = p_{sh}/R_0$.

D.3 Estimation of the off-axis force

We can estimate the off-axis force exerted by the motors by using free energy arguments. From Eq. D.5 we find that a lower bound of the excess free energy $\Delta\mathcal{F}$ associated to the winding of the tube reads:

$$\Delta\mathcal{F} \simeq \frac{\pi\kappa L}{2r}\epsilon^2 \quad (\text{D.8})$$

This excess free energy is due to the work KIF1A motors perform in the off-axis direction W_{off} along the tube. This work can be estimated to be:

$$W_{\text{off}} = 2\pi R_{MT} N_w F_{\text{off}} \quad (\text{D.9})$$

where F_{off} is the total off-axis force exerted by the motors and N_w is the winding number. Actually, the above expression underestimates the work by taking the radius of the displacement as that of the microtubule, and not that of the point at the membrane where the force is exerted. The winding number can be expressed in terms of the angle the helix moves per arclength unit a as $N_w = La/2\pi$. Equating the last two expressions we obtain the total off-axis force:

$$F_{\text{off}} = \frac{\pi\kappa\epsilon^{3/2}}{2R_{MT}} \sqrt{1 + \frac{R}{r}} \quad (\text{D.10})$$

In our experiments $\epsilon \simeq 0.04 - 0.5$. Which gives a lower bound of the total off-axis force in the range $F_{\text{off}} \simeq 0.04 - 2$ pN.

Appendix E

Elastohydrodynamic flagella equations

In this appendix we provide the derivation of the nonlinear elastohydrodynamic flagella equations by using a formalism based on the special theory of Cosserat rods [Antman, 1995]. An equivalent derivation can be found in Ref. [Camalet and Jülicher, 2000] using a formalism based on the minimization of an energy functional for the flagellum. Finally we discuss how boundary conditions are obtained considering the case of clamped condition at the base.

E.1 Derivation of the equations

The equilibrium equations for a rod subject to general contact forces $\mathbf{N}(s, t)$ and contact moments $\mathbf{M}(s, t)$ reads [Antman, 1995]:

$$\begin{aligned}\mathbf{N}_s + \mathbf{F}_{ext} &= \mathbf{0} \\ \mathbf{M}_s + \hat{\mathbf{s}} \times \mathbf{N} + \mathbf{L}_{ext} &= \mathbf{0}\end{aligned}\tag{E.1}$$

where \mathbf{F}_{ext} , \mathbf{L}_{ext} are general external forces and torques. The internal moment of the bundle $\mathbf{M}(s, t)$ reads:

$$\mathbf{M} = (E_b \phi_s - bF) \hat{\mathbf{k}}\tag{E.2}$$

where $F(s, t) = \int_s^L f(s', t) ds'$. Differentiating the last expression respect to the arclength we have:

$$\mathbf{M}_s = \hat{\mathbf{s}} \times [(E_b \phi_{ss} + bf) \hat{\mathbf{n}} + \tau \hat{\mathbf{s}}]\tag{E.3}$$

where $\tau(s, t)$ is the tension inside the flagellum. In the absence of external torques ($\mathbf{L}_{\text{ext}} = 0$) and using the second equation in Eq. E.1 we obtain the resultant contact force:

$$\mathbf{N} = -(E_b\phi_{ss} + bf)\hat{\mathbf{n}} + \tau\hat{\mathbf{s}} \quad (\text{E.4})$$

Differentiating the contact force respect to the arclength we have:

$$\mathbf{N}_s = (-E_b\phi_{sss} - bf_s + \phi_s\tau)\hat{\mathbf{n}} + (E_b\phi_s\phi_{ss} + b\phi_sf + \tau_s)\hat{\mathbf{s}} \quad (\text{E.5})$$

Next we consider the flagellum is immersed in a fluid with low Reynolds number and follows a viscous drag force given by resistive force theory. The force \mathbf{F}_{vis} is given by:

$$\mathbf{F}_{\text{vis}} = -\zeta_{\perp}(\mathbf{n} \cdot \mathbf{r}_t)\hat{\mathbf{n}} - \zeta_{\parallel}(\mathbf{s} \cdot \mathbf{r}_t)\hat{\mathbf{s}} \quad (\text{E.6})$$

Using the first equation in Eq. E.1 and considering $\mathbf{F}_{\text{ext}} = \mathbf{F}_{\text{vis}}$ we have:

$$\begin{aligned} \mathbf{r}_t &= \frac{1}{\zeta_{\parallel}}(E_b\phi_s\phi_{ss} + b\phi_sf + \tau_s)\hat{\mathbf{s}} \\ &+ \frac{1}{\zeta_{\perp}}(-E_b\phi_{sss} - bf_s + \phi_s\tau)\hat{\mathbf{n}} \end{aligned} \quad (\text{E.7})$$

Using the fact that $\hat{\mathbf{s}}_t = \phi_t\hat{\mathbf{n}}$ we obtain an equation for ϕ :

$$\begin{aligned} \phi_t &= \frac{1}{\zeta_{\parallel}}\phi_s(E_b\phi_s\phi_{ss} + b\phi_sf + \tau_s) \\ &+ \frac{1}{\zeta_{\perp}}(-E_b\phi_{sss} - bf_{ss} + \phi_{ss}\tau + \phi_s\tau_s) \end{aligned} \quad (\text{E.8})$$

An equation for the tension can be obtained by using the inextensibility condition $\partial_t(\hat{\mathbf{s}} \cdot \hat{\mathbf{s}}) = 2\hat{\mathbf{s}}_t \cdot \hat{\mathbf{s}} = 0$. The differential equation for the tension reads:

$$\begin{aligned} \tau_{ss} - \frac{\zeta_{\parallel}}{\zeta_{\perp}}(\phi_s)^2\tau + E_b\partial_s(\phi_s\phi_{ss}) \\ + b\partial_s(\phi_sf) + \frac{\zeta_{\parallel}}{\zeta_{\perp}}\phi_s(E_b\phi_{sss} + bf_s) = 0 \end{aligned} \quad (\text{E.9})$$

Next we non-dimensionalize the last equations as in Section 7.1. Additionally, we define $\bar{\zeta} \equiv \zeta_{\perp}/\zeta_{\parallel}$ and we non-dimensionalize the

tension with respect to E_b/L^2 . Finally, the dimensionless equations read:

$$\begin{aligned} \text{Sp}^4 \phi_t &= \bar{\zeta} [(\phi_s)^2 (\phi_{ss} + \mu_a f) + \tau_s \phi_s] \\ &\quad - \phi_{ssss} - \mu_a f_{ss} + \phi_{ss} \tau + \phi_s \tau_s \end{aligned} \quad (\text{E.10})$$

$$\tau_{ss} - \frac{1}{\bar{\zeta}} (\phi_s)^2 \tau = -\partial_s (\phi_s \phi_{ss}) - \mu_a \partial_s (\phi_s f) - \frac{\phi_s}{\bar{\zeta}} (\phi_{sss} + \mu_a f_s) \quad (\text{E.11})$$

E.2 Boundary conditions

We need to specify the contact moment and the contact force at the boundaries. At $s = 0$ we have:

$$\begin{aligned} \mathbf{M}_{\text{ext}}|_{s=0} &= [-E_b \phi_s|_{s=0} + bF(0, t)] \hat{\mathbf{k}} \\ \mathbf{N}_{\text{ext}}|_{s=0} &= [E_b \phi_{ss}|_{s=0} + bf(0, t)] \hat{\mathbf{n}} - \tau(0, t) \hat{\mathbf{s}} \end{aligned} \quad (\text{E.12})$$

At $s = L$ we have:

$$\begin{aligned} \mathbf{M}_{\text{ext}}|_{s=L} &= E_b \phi_s|_{s=L} \hat{\mathbf{k}} \\ \mathbf{N}_{\text{ext}}|_{s=L} &= -[E_b \phi_{ss}|_{s=L} + bf(L, t)] \hat{\mathbf{n}} + \tau(L, t) \hat{\mathbf{s}} \end{aligned} \quad (\text{E.13})$$

Next we switch to dimensionless variables where the external contact moment is scaled by E_b/L , and external contact force and tension by E_b/L^2 . At $s = 0$ we have:

$$\begin{aligned} \mathbf{M}_{\text{ext}}|_{s=0} &= [-\phi_s|_{s=0} + \mu_a F(0, t)] \hat{\mathbf{k}} \\ \mathbf{N}_{\text{ext}}|_{s=0} &= [\phi_{ss}|_{s=0} + \mu_a f(0, t)] \hat{\mathbf{n}} - \tau(0, t) \hat{\mathbf{s}} \end{aligned} \quad (\text{E.14})$$

where now $F(s, t) = \int_s^1 f(s', t) ds'$. At $s = 1$ we have:

$$\begin{aligned} \mathbf{M}_{\text{ext}}|_{s=1} &= \phi_s|_{s=1} \hat{\mathbf{k}} \\ \mathbf{N}_{\text{ext}}|_{s=1} &= -[\phi_{ss}|_{s=1} + \mu_a f(1, t)] \hat{\mathbf{n}} + \tau(1, t) \hat{\mathbf{s}} \end{aligned} \quad (\text{E.15})$$

Next we consider the case of small curvature where $\phi_s \ll 1$ and $\tau \approx 0$. At the distant boundary condition we have no applied contact force or contact moment thus $\mathbf{M}_{\text{ext}}|_{s=1} = \mathbf{N}_{\text{ext}}|_{s=1} = \mathbf{0}$. This lead to the conditions $\phi_s|_{s=1} = 0$ and $\phi_{ss}|_{s=1} = -\mu_a f(1, t)$ respectively. The external contact force and contact moment at the base $\mathbf{N}_{\text{ext}}|_{s=0} = \mathbf{F}_{\text{head}}$, $\mathbf{M}_{\text{ext}}|_{s=0} = \mathbf{M}_{\text{head}}$ are given by the specific viscous fluid dynamics assumed. By considering a clamped condition, the base is fixed $\mathbf{r}_t|_{s=0} = 0$, and we obtain the condition $\phi_{sss}|_{s=0} = -\mu_a f_s|_{s=0}$. Additionally, the base is clamped and thus $\mathbf{M}_{\text{ext}}|_{s=0} = 0$. In the linear analysis, the four boundary conditions in Fourier space read:

$$\begin{aligned}\tilde{\phi}(0) &= 0 \\ \tilde{\phi}_{sss}(0) &= -\bar{\chi}\tilde{\phi}_s(0) \\ \tilde{\phi}_s(1) &= 0 \\ \tilde{\phi}_{ss}(1) &= -\bar{\chi}\tilde{\phi}(1)\end{aligned}\tag{E.16}$$

Concerning the constraints on the dynein distribution due to the boundary conditions, at $s = 0$ we have that $\phi_t|_{s=0} = 0$ and thus both plus and minus distributions decay exponentially with characteristic time $\bar{\tau}$ to n_0 at the steady state. For the case of $s = 1$, $\phi_t|_{s=1}$ is different from zero in general, thus the specific boundary conditions for ϕ at the tail constraint the evolution of dynein bound motor distributions.

Appendix F

Integration of the nonlinear flagella equations

In this appendix we provide the numerical algorithm to solve the nonlinear Eqs. 7.10, 7.11 in Chapter 7, numerically. We consider a uniform discretization in the arclength s of the bundle centerline with M intervals of step size $\Delta s = 1/M$. The discrete points are denoted $s_m = (m - 1)\Delta s$, $m = 1, \dots, M + 1$ and the time is discretized as $t_n = n\Delta t$. Any continuous function $X(s, t)$ is denoted X_m^n in the discretized version. The study is done with $\Delta s = 2.5 \cdot 10^{-4}$ and $\Delta t = 5 \cdot 10^{-5}$ (dimensionless units).

F.1 Tangent angle dynamics

We will use a first-order IMEX scheme for the integration of the tangent angle ϕ in the very first time step ($n = 0$) and a second-order IMEX scheme for $n \geq 1$ [Ascher et al., 1995]. After discretization, the problem reduces to a linear system of equations of the form $A\phi^{n+1} = b$, where A is a $(M + 1) \times (M + 1)$ matrix and b and ϕ^{n+1} are $M + 1$ vectors.

In the first time step ($n = 0$) we will use a first order IMEX scheme. The elements of the matrix A corresponding to the rows $m = 3, \dots, M - 1$ take the form:

$$[A]_{mm'} = \delta_{mm'} + \alpha[D_4]_{mm'} - 2\beta([N]_{mm'} - [H]_{mm'}) \quad (\text{F.1})$$

where $\alpha \equiv \Delta t / (\text{Sp}\Delta s)^4$, $\beta \equiv \mu_a \zeta / (2\text{Sp}^4 \Delta s^2)$, D_k are dimensionless operators corresponding to the k -th derivative of second-order in

accuracy, \mathbf{N} is the operator containing the nonlinear terms in Eq. 7.10 and \mathbf{H} is the operator containing the clamped conditions at the head of the flagellum. Standard centered operators are used whenever possible for \mathbf{D}_k , but at the boundaries skewed operators are applied [Tornberg and Shelley, 2004]. The elements of \mathbf{N} for $m = 3, \dots, M - 1$ and $m' = 1, \dots, M + 1$ take the form:

$$[\mathbf{N}]_{mm'} = [\mathbf{G}_2^0(n)]_{mm'} + [\mathbf{G}_0^0(n)]_{mm}[\mathbf{D}_2]_{mm'} + 2[\mathbf{G}_1^0(n)]_{mm}[\mathbf{D}_1]_{mm'} \quad (\text{F.2})$$

where the operators \mathbf{G}_k^0 are diagonal matrices with elements:

$$[\mathbf{G}_k^0(X)]_{mm'} = \delta_{mm'} D_k X_m^n \quad (\text{F.3})$$

where $D_k X_m^n$ is a real number denoting the k -th derivative of the quantity X at point m at time n . The elements of $m = 3, \dots, M - 1$ and $m' = 1, \dots, M + 1$ of the matrix \mathbf{H} reads:

$$[\mathbf{H}]_{mm'} = [\mathbf{G}_2^0(n)]_{mm}[\mathbf{E}]_{mm'} \quad (\text{F.4})$$

where \mathbf{E} is a matrix with ones in the first column and zeros elsewhere. Finally, the elements b_m , $m = 3, \dots, M - 1$ read:

$$b_m = \phi_m^n + \gamma[\mathbf{G}_2^0(\phi)]_{mm} - \delta[\mathbf{G}_2^0(\bar{n})]_{mm} - 2\beta\{[\mathbf{G}_2^0(n)]_{mm}(\phi_m^n - \phi_1^n) + [\mathbf{G}_0^0(n)]_{mm}D_2\phi_m^n + 2[\mathbf{G}_1^0(n)]_{mm}D_1\phi_m^n\} \quad (\text{F.5})$$

where $\gamma \equiv \mu\Delta t/(\Delta s^2\text{Sp}^4)$ and $\delta \equiv \mu_a\Delta t/(\Delta s^2\text{Sp}^4)$. For $n \geq 1$, the elements of the matrix \mathbf{A} corresponding to the rows $m = 3, \dots, M - 1$ take the form:

$$[\mathbf{A}]_{mm'} = \frac{3}{2}\delta_{mm'} + \alpha[\mathbf{D}_4]_{mm'} - 3\beta([\mathbf{N}]_{mm'} - [\mathbf{H}]_{mm'}) \quad (\text{F.6})$$

The elements of \mathbf{N} for $m = 3, \dots, M - 1$ and $m' = 1, \dots, M + 1$ read:

$$[\mathbf{N}]_{mm'} = [\mathbf{G}_2(n)]_{mm'} + [\mathbf{G}_0(n)]_{mm}[\mathbf{D}_2]_{mm'} + 2[\mathbf{G}_1(n)]_{mm}[\mathbf{D}_1]_{mm'} \quad (\text{F.7})$$

where \mathbf{G}_k are diagonal matrices with elements:

$$[\mathbf{G}_k(X)]_{mm'} = \delta_{mm'}(2D_k X_m^n - D_k X_m^{n-1}) \quad (\text{F.8})$$

The elements of \mathbf{H} for $m = 3, \dots, M-1$ and $m' = 1, \dots, M+1$ read:

$$[\mathbf{H}]_{mm'} = [\mathbf{G}_2(n)]_{mm}[\mathbf{E}]_{mm'} \quad (\text{F.9})$$

Finally, the elements b_m , $m = 3, \dots, M-1$ read:

$$\begin{aligned} b_m = & 2\phi_m^n - \frac{1}{2}\phi_m^{n-1} + \gamma[\mathbf{G}_2(\phi)]_{mm} - \delta[\mathbf{G}_2(\bar{n})]_{mm} \\ & + \beta\{[\mathbf{G}_2(n)]_{mm}[-4(\phi_m^n - \phi_1^n) + (\phi_m^{n-1} - \phi_1^{n-1})] \\ & + [\mathbf{G}_0(n)]_{mm}(-4D_2\phi_m^n + D_2\phi_m^{n-1}) \\ & + 2[\mathbf{G}_1(n)]_{mm}(-4D_1\phi_m^n + D_1\phi_m^{n-1})\} \end{aligned} \quad (\text{F.10})$$

The four remaining equations ($m = 1, 2, M, M+1$) are found imposing the four boundary conditions in a similar manner. The boundary conditions will be the same for $n = 0$ and $n \geq 1$ except that we will use the operators \mathbf{G}_k^0 for $n = 0$ instead of \mathbf{G}_k .

F.2 Dynein dynamics

Dynein dynamics is solved by using a simple implicit method on Eq. 7.11. The evolution of n_{\pm} follows:

$$n_{\pm, m}^{n+1} = \frac{n_{\pm, m}^n + \Delta t \eta(1 - n_{\pm, m}^n)}{1 + \Delta t(1 - \eta) \exp(f_{\pm, m}^n)} \quad (\text{F.11})$$

where $f_{\pm, m}^n = \bar{f}[1 \mp \zeta D_t(\phi_m^n - \phi_1^n)]$ and $D_t X_m^n = (X_m^{n+1} - X_m^n)/\Delta t$.

References

- Alberts et al., 2002. Alberts, B., Johnson, A., Lewis, J., Raff, M., Roberts, K., and Walter, P. (2002). *Molecular Biology of the Cell*. Garland Science, New York.
- Amos and Schlieper, 2005. Amos, L. A. and Schlieper, D. (2005). Microtubules and maps. *Adv. Protein Chem.*, 71:257–298.
- Angelova et al., 1992. Angelova, M. I., Soléau, S., Méléard, P., Faucon, J. F., and Bothorel, P. (1992). Preparation of giant vesicles by external ac fields. kinetics and applications. *Progr. Colloid Polym. Sci.*, 89:127–131.
- Antman, 1995. Antman, S. S. (1995). *Nonlinear problems of elasticity*, volume 107 of *Applied Math. Sci.* Springer-Verlag New York.
- Arnold et al., 2011. Arnold, B., Cassady, S. J., VanLaar, V. S., and Berman, S. B. (2011). Integrating multiple aspects of mitochondrial dynamics in neurons: age-related differences and dynamic changes in a chronic rotenone model. *Neurobiol. Dis.*, 41(1):189–200.
- Ascher et al., 1995. Ascher, U. M., Ruuth, S. J., and Wetton, B. T. R. (1995). Implicit-explicit methods for time-dependent partial differential equations. *SIAM J. Numer. Anal.*, 32(3):797–823.
- Bálint et al., 2013. Bálint, S., Verdeny-Vilanova, I., Sandoval-Álvarez, A., and Lakadamyali, M. (2013). Correlative live-cell and superresolution microscopy reveals cargo transport dynamics at microtubule intersections. *Proc. Natl. Acad. Sci. U.S.A.*, 110(9):3375–3380.
- Bayly and Wilson, 2015. Bayly, P. V. and Wilson, K. S. (2015). Analysis of unstable modes distinguishes mathematical models of flagellar motion. *J. R. Soc. Interface*, 12(106):20150124.
- Beeg et al., 2008. Beeg, J., Klumpp, S., Dimova, R., Gracià, R. S., Unger, E., and Lipowsky, R. (2008). Transport of beads by several kinesin motors. *Biophys J.*, 94(2):532–541.
- Benettin et al., 1980. Benettin, G., Galgani, L., Giorgilli, A., and Strelcyn, J. M. (1980). Lyapunov characteristic exponents for smooth dynamical systems and for hamiltonian systems; a method for computing all of them. part 1: Theory. *Meccanica*, 15:21.
- Blanchoin et al., 2014. Blanchoin, L., Boujemaa-Paterski, R., Sykes, C., and Plastino, J. (2014). Actin dynamics, architecture, and mechanics in cell motility. *Physiol. Rev.*, 94(1):235–263.
- Bormuth et al., 2009. Bormuth, V., Varga, V., Howard, J., and Schäffer, E. (2009). Protein friction limits diffusive and directed movements of kinesin motors on microtubules. *Science*, 325(5942):870–873.
- Box and Müller, 1958. Box, G. E. P. and Müller, M. E. (1958). A note on the generation of random normal deviates. *Ann. Math. Statist.*, 29(2):610–611.
- Brady, 1985. Brady, S. T. (1985). A novel brain atpase with properties expected for the fast axonal transport motor. *Nature*, 317(6032):73–75.

- Bray, 2000. Bray, D. (2000). *Cell movements: from molecules to motility*. Garland Science, New York, 2nd edition.
- Brokaw, 1971. Brokaw, C. J. (1971). Bend propagation by a sliding filament model for flagella. *J. Exp. Biol.*, 55(2):289–304.
- Brokaw, 1975. Brokaw, C. J. (1975). Molecular mechanism for oscillation in flagella and muscle. *Proc. Natl. Acad. Sci. U.S.A.*, 72(8):3102–3106.
- Brokaw, 1989. Brokaw, C. J. (1989). Direct measurements of sliding between outer doublet microtubules in swimming sperm flagella. *Science*, 243(4898):1593–1596.
- Brokaw, 1999. Brokaw, C. J. (1999). Computer simulation of flagellar movement vii. conventional but functionally different cross-bridge models for inner and outer arm dyneins can explain the effects of outer arm dynein removal. *Cell Motil. Cytoskeleton*, 42:134–148.
- Brokaw, 2014. Brokaw, C. J. (2014). Computer simulation of flagellar movement x: Doublet pair splitting and bend propagation modeled using stochastic dynein kinetics. *Cytoskeleton*, 71:273–284.
- Brokaw and Rintala, 1975. Brokaw, C. J. and Rintala, D. R. (1975). Computer simulation of flagellar movement. iii. models incorporating cross-bridge kinetics. *J. Mechanochem. Cell Motility*, 3(2):77–86.
- Brugués and Casademunt, 2009. Brugués, J. and Casademunt, J. (2009). Self-organization and cooperativity of weakly coupled molecular motors under unequal loading. *Phys. Rev. Lett.*, 102(11):118104.
- Brugués and Needleman, 2014. Brugués, J. and Needleman, D. (2014). Physical basis of spindle self-organization. *Proc. Natl. Acad. Sci. U.S.A.*, 111(52):18496–18500.
- Brugués et al., 2012. Brugués, J., Nuzzo, V., Mazur, E., and Needleman, D. (2012). Nucleation and transport organize microtubules in metaphase spindles. *Cell*, 149(3):554–564.
- Brunnbauer et al., 2012. Brunnbauer, M., Dombi, R., Ho, T. H., Schliwa, M., Rief, M., and Ökten, Z. (2012). Torque generation of kinesin motors is governed by the stability of the neck domain. *Mol. Cell*, 46(2):147–158.
- Camalet et al., 2000. Camalet, S., Duke, T., Jülicher, F., and Prost, J. (2000). Auditory sensitivity provided by self-tuned critical oscillations of hair cells. *Proc. Natl. Acad. Sci. U.S.A.*, 97(7):3183–3188.
- Camalet and Jülicher, 2000. Camalet, S. and Jülicher, F. (2000). Generic aspects of axonemal beating. *New J. Phys.*, 2:24.
- Camalet et al., 1999. Camalet, S., Jülicher, F., and Prost, J. (1999). Self-organized beating and swimming of internally driven filaments. *Phys. Rev. Lett.*, 82(7):1590–1593.
- Campàs et al., 2006. Campàs, O., Kafri, Y., Zeldovich, K. B., Casademunt, J., and Joanny, J.-F. (2006). Collective dynamics of interacting molecular motors. *Phys. Rev. Lett.*, 97(3):038101.
- Campàs et al., 2008. Campàs, O., Leduc, C., Bassereau, P., Casademunt, J., Joanny, J.-F., and Prost, J. (2008). Coordination of kinesin motors pulling on fluid membranes. *Biophys J.*, 94(12):5009–5017.
- Can et al., 2014. Can, S., Dewitt, M. A., and Yildiz, A. (2014). Bidirectional helical motility of cytoplasmic dynein around microtubules. *eLife*, 3:e03205.
- Carter, 2013. Carter, A. P. (2013). Crystal clear insights into how the dynein motor moves. *J. Cell Sci.*, 126:705–713.
- Chao et al., 1982. Chao, J., Turner, J. A., and Sturgess, J. M. (1982). Genetic heterogeneity of dynein-deficiency in cilia from patients with respiratory disease. *Am. Rev. Respir. Dis.*, 126(2):302–305.
- Chowdhury, 2006. Chowdhury, D. (2006). Collective effects in intra-cellular molecular motor transport: Coordination, cooperation and competition. *Physica (Amsterdam)*, 372A(84).
- Chrétien and Wade, 1991. Chrétien, D. and Wade, R. H. (1991). New data on the microtubule surface lattice. *Biol. Cell.*, 71(1-2):161–174.
- Conde and Cáceres, 2009. Conde, C. and Cáceres, A. (2009). Microtubule assembly, organization and dynamics in axons and dendrites. *Nat. Rev. Neurosci.*, 10:319–332.

- Cotterill, 2002. Cotterill, R. M. J. (2002). *Biophysics: An Introduction*. J. Wiley & Sons Ltd.
- Derényi et al., 2002. Derényi, I., Jülicher, F., and Prost, J. (2002). Formation and interaction of membrane tubes. *Phys. Rev. Lett.*, 88(23):238101.
- DeWitt et al., 2012. DeWitt, M. A., Chang, A. Y., Combs, P. A., and Yildiz, A. (2012). Cytoplasmic dynein moves through uncoordinated stepping of the aaa+ ring domains. *Science*, 335(6065):221–225.
- Eckmann and Ruelle, 1985. Eckmann, J.-P. and Ruelle, D. (1985). Ergodic theory of chaos and strange attractors. *Rev. Mod. Phys.*, 57:617.
- Engelhardt and Ljubimowa, 1939. Engelhardt, W. A. and Ljubimowa, M. N. (1939). Myosine and adenosinetriphosphatase. *Nature*, 144:668–669.
- Evans et al., 1996. Evans, E., Bowman, H., Leung, A., Needham, D., and Tirrell, D. (1996). Biomembrane templates for nanoscale conduits and networks. *Science*, 273(5277):933–935.
- Evans, 1996. Evans, M. R. (1996). Bose-einstein condensation in disordered exclusion models and relation to traffic flow. *Europhys. Lett.*, 36(1):13–18.
- Ferguson and Camilli, 2012. Ferguson, S. M. and Camilli, P. D. (2012). Dynamins, a membrane-remodelling gtpase. *Nat. Rev. Mol. Cell. Biol.*, 13:75–88.
- Feynman, 1963. Feynman, R. P. (1963). *The Feynman Lectures on Physics*, volume 1. Addison-Wesley, Massachusetts, USA.
- Fu et al., 2008. Fu, H. C., Wolgemuth, C. W., and Powers, T. R. (2008). Beating patterns of filaments in viscoelastic fluids. *Phys. Rev. E*, 78(4):041913.
- Fujita and Ishiwata, 1998. Fujita, H. and Ishiwata, S. (1998). Spontaneous oscillatory contraction without regulatory proteins in actin-filament-reconstituted fibers. *Biophys J.*, 75(3):1439–1445.
- Furuta et al., 2013. Furuta, K., Furuta, A., Toyoshima, Y. Y., Amino, M., Oiwa, K., and Kojima, H. (2013). Measuring collective transport by defined numbers of processive and nonprocessive kinesin motors. *Proc. Natl. Acad. Sci. U.S.A.*, 110(2):501–506.
- Gadêlha et al., 2013. Gadêlha, H., Gaffney, E. A., and Goriely, A. (2013). The counter-bend phenomenon in flagellar axonemes and cross-linked filament bundles. *Proc. Natl. Acad. Sci. U.S.A.*, 110(30):12180–12185.
- Gadêlha et al., 2010. Gadêlha, H., Gaffney, E. A., Smith, D. J., and Kirkman-Brown, J. C. (2010). Nonlinear instability in flagellar dynamics: a novel modulation mechanism in sperm migration? *J. R. Soc. Interface*, 7(53):1689–1697.
- Gaffney et al., 2011. Gaffney, E. A., Gadêlha, H., Smith, D. J., Blake, J. R., and Kirkman-Brown, J. C. (2011). Mammalian sperm motility: observation and theory. *Annu. Rev. Fluid Mech.*, 43(1):501–528.
- García-Ojalvo and Sancho, 1999. García-Ojalvo, J. and Sancho, J. M. (1999). *Noise in spatially extended systems*. Springer-Verlag, New York.
- Gardiner, 1985. Gardiner, C. W. (1985). *Handbook of stochastic methods*. Springer-Verlag, New York.
- Gibbons and Rowe, 1965. Gibbons, I. R. and Rowe, A. J. (1965). Dynein: a protein with adenosine triphosphate activity from cilia. *Science*, 149(3682):424–426.
- Gillespie, 1976. Gillespie, D. T. (1976). A general method for numerically simulating the stochastic time evolution of coupled chemical reactions. *J. Comp. Phys.*, 22:403–434.
- Gillespie, 2000. Gillespie, D. T. (2000). The chemical langevin equation. *J. Chem. Phys.*, 113(1):297–306.
- Ginger et al., 2008. Ginger, M. L., Portman, N., and McKean, P. G. (2008). Swimming with protists: perception, motility and flagellum assembly. *Nat. Rev. Microbiol.*, 6(11):838–850.
- Gray, 1993. Gray, A. (1993). *Modern differential geometry of curves and surfaces*. CRC Press.
- Greulich et al., 2007. Greulich, P., Garai, A., Nishinari, K., Schadschneider, A., and Chowdhury, D. (2007). Intracellular transport by single-headed kinesin kif1a: Effects of single-motor mechanochemistry and steric interactions. *Phys. Rev. E*, 75:041905.

- Grill et al., 2005. Grill, S. W., Kruse, K., and Jülicher, F. (2005). Theory of mitotic spindle oscillations. *Phys. Rev. Lett.*, 94(10):108104.
- Gross et al., 2007. Gross, S. P., Vershinin, M., and Shubeita, G. T. (2007). Cargo transport: two motors are sometimes better than one. *Curr. Biol.*, 17(12):R478–486.
- Guérin et al., 2011. Guérin, T., Prost, J., and Joanny, J.-F. (2011). Dynamical behaviour of molecular motor assemblies in the rigid and crossbridge models. *Eur. Phys. J. E Soft Matter*, 34(6):1–21.
- Guérin et al., 2010. Guérin, T., Prost, J., Martin, P., and Joanny, J.-F. (2010). Coordination and collective properties of molecular motors: theory. *Curr. Opin. Cell. Biol.*, 22(1):14–20.
- Gunning, 2008. Gunning, P. (2008). *Tropomyosin*, volume 644 of *Advances in experimental medicine and biology*. Landes Bioscience and Springer Science+Business Media, LLC.
- Günther and Kruse, 2010. Günther, S. and Kruse, K. (2010). Spontaneous sarcomere dynamics. *Chaos*, 20(4):045122.
- Gurel et al., 2014. Gurel, P. S., Hatch, A. L., and Higgs, H. N. (2014). Connecting the cytoskeleton to the endoplasmic reticulum and golgi. *Curr. Biol.*, 24(14):R660–R672.
- Hackney, 1996. Hackney, D. D. (1996). The kinetic cycles of myosin, kinesin, and dynein. *Annu. Rev. Physiol.*, 58:731–750.
- Hammond et al., 2009. Hammond, J. W., Cai, D., Blasius, T. L., Li, Z., Jiang, Y., Jih, G. T., Meyhöfer, E., and Verhey, K. J. (2009). Mammalian kinesin-3 motors are dimeric in vivo and move by processive motility upon release of autoinhibition. *PLoS Biol.*, 7(3):e1000072.
- Hancock, 2014. Hancock, W. O. (2014). Bidirectional cargo transport: moving beyond tug of war. *Nat. Rev. Mol. Cell. Biol.*, 15(9):615–628.
- Hänggi and Marchesoni, 2009. Hänggi, P. and Marchesoni, F. (2009). Artificial brownian motors: controlling transport on the nanoscale. *Rev. Mod. Phys.*, 81(1):387.
- Hao and Scholey, 2009. Hao, L. and Scholey, J. M. (2009). Intraflagellar transport at a glance. *J. Cell Sci.*, 122:889–892.
- Hartman and Spudich, 2012. Hartman, M. A. and Spudich, J. A. (2012). The myosin superfamily at a glance. *J. Cell Sci.*, 125:1627–1632.
- Helfrich, 1973. Helfrich, W. (1973). Elastic properties of lipid bilayers: theory and possible experiments”. *Z. Naturforsch C.*, 28(11):693–703.
- Hendricks et al., 2010. Hendricks, A. G., Perlson, E., Ross, J. L., Schroeder3rd, H. W., Tokito, M., and Holzbaaur, E. L. F. (2010). Motor coordination via tug-of-war mechanism drives bidirectional vesicle transport. *Curr. Biol.*, 20(8):697–702.
- Hilfinger et al., 2009. Hilfinger, A., Chattopadhyay, A. K., and Jülicher, F. (2009). Non-linear dynamics of cilia and flagella. *Phys. Rev. E*, 79(051918).
- Hill, 1974. Hill, T. L. (1974). Theoretical formalism for the sliding filament model of contraction of striated muscle. part i. *Prog. Biophys. Mol. Biol.*, 28:267–340.
- Hill, 1975. Hill, T. L. (1975). Theoretical formalism for the sliding filament model of contraction of striated muscle. part ii. *Prog. Biophys. Mol. Biol.*, 29(2):105–159.
- Hines and Blum, 1979. Hines, M. and Blum, J. J. (1979). Bend propagation in flagella. ii. incorporation of dynein cross-bridge kinetics into the equations of motion. *Biophys J.*, 25(3):421–441.
- Hirakawa et al., 2000. Hirakawa, E., Higuchi, H., and Toyoshima, Y. Y. (2000). Processive movement of single 22s dynein molecules occurs only at low atp concentrations. *Proc. Natl. Acad. Sci. U.S.A.*, 97(6):2533–2537.
- Hirokawa et al., 2009. Hirokawa, N., Noda, Y., Tanaka, Y., and Niwa, S. (2009). Kinesin superfamily motor proteins and intracellular transport. *Nat. Rev. Mol. Cell. Biol.*, 10(10):682–696.
- Hirokawa and Takemura, 2005. Hirokawa, N. and Takemura, R. (2005). Molecular motors and mechanisms of directional transport in neurons. *Nat. Rev. Neurosci.*, 6:201–214.
- Holzbaaur and Goldman, 2010. Holzbaaur, E. L. F. and Goldman, Y. E. (2010). Coordination of molecular motors: from in vitro assays to intracellular dynamics. *Curr. Opin. Cell. Biol.*, 22(1):4–13.

- Howard, 2001. Howard, J. (2001). *Mechanics of Motor Proteins and the Cytoskeleton*. Sinauer Associates.
- Howard, 2009. Howard, J. (2009). Mechanical signaling in networks of motor and cytoskeletal proteins. *Annu. Rev. Biophys.*, 38:217–234.
- Huxley, 1957. Huxley, A. F. (1957). Muscle structure and theories of contraction. *Prog. Biophys. Biophys. Chem.*, 7:255–318.
- Huxley and Niedergerke, 1954. Huxley, A. F. and Niedergerke, R. (1954). Structural changes in muscle during contraction: interference microscopy of living muscle fibers. *Nature*, 173(4412):971–973.
- Huxley and Hanson, 1954. Huxley, H. and Hanson, J. (1954). Changes in the cross-striations of muscle during contraction and stretch and their structural interpretation. *Nature*, 173(4412):973–976.
- Ishiwata et al., 2010. Ishiwata, S., Shimamoto, Y., and Suzuki, M. (2010). Molecular motors as an auto-oscillator. *HFSP J.*, 4(3-4):100–104.
- Ishiwata et al., 2007. Ishiwata, S., Shimamoto, Y., Suzuki, M., and Sasaki, D. (2007). Regulation of muscle contraction by Ca^{2+} and adp: focusing on the auto-oscillation (spoc). *Adv. Exp. Med. Biol.*, 592:341–358.
- Jolliffe, 2002. Jolliffe, I. T. (2002). *Principal Component Analysis*. Springer-Verlag, New York.
- Jülicher et al., 1997. Jülicher, F., Ajdari, A., and Prost, J. (1997). Modeling molecular motors. *Rev. Mod. Phys.*, 69(4):1269–1282.
- Jülicher and Prost, 1997. Jülicher, F. and Prost, J. (1997). Spontaneous oscillations of collective molecular motors. *Phys. Rev. Lett.*, 78(23):4510–4513.
- Jülicher and Seifert, 1994. Jülicher, F. and Seifert, U. (1994). Shape equations for axisymmetric vesicles: A clarification. *Phys. Rev. E*, 49(5):4728–4731.
- Kamien, 2002. Kamien, R. D. (2002). The geometry of soft materials: a primer. *Rev. Mod. Phys.*, 74:953.
- Kapitein et al., 2005. Kapitein, L. C., Peterman, E. J. G., Kwok, B. H., Kim, J. H., Kapoor, T. M., and Schmidt, C. F. (2005). The bipolar mitotic kinesin eg5 moves on both microtubules that it crosslinks. *Nature*, 435(7038):114–118.
- Katz, 2010. Katz, A. M. (2010). *Physiology of the heart*. Wolters Kluwer, Lippincott Williams & Wilkins, 5th edition.
- Khelifa et al., 2014. Khelifa, B. M., Coutton, C., Zouari, R., Karaouzène, T., Rendu, J., Bidart, M., Yassine, S., Pierre, V., Delaroche, J., Hennebicq, S., Grunwald, D., Escalier, D., Pernet-Gallay, K., Jouk, P. S., Thierry-Mieg, N., Touré, A., Arnoult, C., and Ray, P. F. (2014). Mutations in *dnah1*, which encodes an inner arm heavy chain dynein, lead to male infertility from multiple morphological abnormalities of the sperm flagella. *Am. J. Hum. Genet.*, 94(1):95–104.
- Klopfenstein et al., 2002. Klopfenstein, D. R., Tomishige, M., Stuurman, N., and Vale, R. D. (2002). Role of phosphatidylinositol(4,5)biphosphate organization in membrane transport by the *unc104* kinesin motor. *Cell*, 109(3):347–358.
- Kolář and Gumbs, 1992. Kolář, M. and Gumbs, G. (1992). Theory for the experimental observation of chaos in a rotating waterwheel. *Phys. Rev. A*, 45(2):626.
- Kolomeisky and Fisher, 2007. Kolomeisky, A. B. and Fisher, M. E. (2007). Molecular motors: A theorist’s perspective. *Annu. Rev. Phys. Chem.*, 58:675–695.
- Korten et al., 2010. Korten, T., Månsson, A., and Diez, S. (2010). Towards the application of cytoskeletal motor proteins in molecular detection and diagnostic devices. *Curr. Opin. Biotechnol.*, 21(4):477–488.
- Koster et al., 2003. Koster, G., VanDuijn, M., Hofs, B., and Dogterom, M. (2003). Membrane tube formation from giant vesicles by dynamic association of motor proteins. *Proc. Natl. Acad. Sci. U.S.A.*, 100(26):15583–15588.
- Krug, 1991. Krug, J. (1991). Boundary-induced phase transitions in driven diffusive systems. *Phys. Rev. Lett.*, 67(14):1882–1885.
- Kruse and Jülicher, 2005. Kruse, K. and Jülicher, F. (2005). Oscillations in cell biology. *Curr. Opin. Cell. Biol.*, 17(1):20–26.

- Kühne, 1859. Kühne, W. (1859). Untersuchungen über bewegungen und veränderungen der contractilen substanzen. *Archiv für Anatomie, Physiologie, und wissenschaftliche Medizin*, pages 748–835.
- Kull et al., 1996. Kull, F. J., Sablin, E. P., Lau, R., Fletterick, R. J., and Vale, R. D. (1996). Crystal structure of the kinesin motor domain reveals a structural similarity to myosin. *Nature*, 380(6574):550–555.
- Lakadamyali, 2014. Lakadamyali, M. (2014). Navigating the cell: how motors overcome roadblocks and traffic jams to efficiently transport cargo. *Phys. Chem. Chem. Phys.*, 16(13):5907–5916.
- Langevin, 1908. Langevin, P. (1908). Sur la théorie du mouvement brownien. *C. R. Acad. Sci. (Paris)*, 146:530–533.
- Lauga and Powers, 2009. Lauga, E. and Powers, T. R. (2009). The hydrodynamics of swimming microorganisms. *Rep. Prog. Phys*, 72(9):096601.
- Leduc et al., 2004. Leduc, C., Campàs, O., Zeldovich, K. B., Roux, A., Jolimaitre, P., Bourel-Bonnet, L., Goud, B., Joanny, J.-F., Bassereau, P., and Prost, J. (2004). Cooperative extraction of membrane nanotubes by molecular motors. *Proc. Natl. Acad. Sci. U.S.A.*, 101(49):17096–17101.
- Lehman et al., 1994. Lehman, W., Craig, R., and Vibert, P. (1994). Ca^{2+} -induced tropomyosin movement in *limulus* thin filaments revealed by three-dimensional reconstruction. *Nature*, 368(6466):65–67.
- Lehman et al., 2001. Lehman, W., Rosol, M., Tobacman, L. S., and Craig, R. (2001). Troponin organization on relaxed and activated thin filaments revealed by electron microscopy and three-dimensional reconstruction. *J. Mol. Biol.*, 307(3):739–744.
- Leibler and Huse, 1993. Leibler, S. and Huse, D. A. (1993). Porters versus rowers: a unified stochastic model of motor proteins. *J. Cell Biol*, pages 1357–1368.
- Lindemann, 1994. Lindemann, C. B. (1994). A "geometric clutch" hypothesis to explain oscillations of the axoneme of cilia and flagella. *J. Theor. Biol.*, 168(2):175–189.
- Lipowsky et al., 2001. Lipowsky, R., Klumpp, S., and Nieuwenhuizen, T. M. (2001). Random walks of cytoskeletal motors in open and closed compartments. *Phys. Rev. Lett.*, 87(10):108101.
- Lodish et al., 2000. Lodish, H., Berk, A., Lawrence-Zipursky, S., Matsudaira, P., Baltimore, D., and Darnell, J. (2000). *Molecular Cell Biology*. W. H. Freeman, 4th edition.
- Lorenz, 1963. Lorenz, E. N. (1963). Deterministic nonperiodic flow. *J. Atmos. Sci.*, 20:130–141.
- Loughran and Walls, 2011. Loughran, S. T. and Walls, D. (2011). Purification of poly-histidine-tagged proteins. *Methods Mol Biol.*, 681:311–335.
- Ma et al., 2014. Ma, R., Klindt, G. S., Riedel-Kruse, I. H., Jülicher, F., and Friederich, B. M. (2014). Active phase and amplitude fluctuations of flagellar beating. *Phys. Rev. Lett.*, 113(4):048101.
- Magnasco, 1993. Magnasco, M. O. (1993). Forced thermal ratchets. *Phys. Rev. Lett.*, 71(10):1477–1481.
- Malgaretti et al., 2012. Malgaretti, P., Pagonabarraga, I., and Frenkel, D. (2012). Running faster together: huge speed up of thermal ratchets due to hydrodynamic coupling. *Phys. Rev. Lett.*, 109(16):168101.
- Malgaretti et al., 2013. Malgaretti, P., Pagonabarraga, I., and Rubí, J. M. (2013). Confined brownian ratchets. *J. Chem. Phys.*, 138(19):194906.
- Mallik et al., 2005. Mallik, R., Petrov, D., Lex, S. A., King, S. J., and Gross, S. P. (2005). Building complexity: an in vitro study of cytoplasmic dynein with in vivo implications. *Curr. Biol.*, 15(23):2075–2085.
- Mandelkow and Mandelkow, 2002. Mandelkow, E. and Mandelkow, E. M. (2002). Kinesin motors and disease. *Trends Cell. Biol.*, 12(12):585–591.
- McMahon and Mills, 2004. McMahon, H. T. and Mills, I. G. (2004). Cop and clathrin-coated vesicle budding: different pathways, common approaches. *Curr. Opin. Cell. Biol.*, 16(4):379–391.

- Millecamps and Julien, 2013. Millecamps, S. and Julien, J. P. (2013). Axonal transport deficits and neurodegenerative diseases. *Nat. Rev. Neurosci.*, 14(3):161–176.
- Minoura et al., 1999. Minoura, I., Yagi, T., and Kamiya, R. (1999). Direct measurement of inter-doublet elasticity in flagellar axonemes. *Cell Struct. Funct.*, 24(1):27–33.
- Mitchison and Mitchison, 2010. Mitchison, T. J. and Mitchison, H. M. (2010). How cilia beat. *Nature*, 463:308–309.
- Morfini et al., 2007. Morfini, G., Pigino, G., Opalach, K., Serulle, Y., Moreira, J. E., Sugimori, M., Llinás, R. R., and Brady, S. T. (2007). 1-methyl-4-phenylpyridinium affects fast axonal transport by activation of caspase and protein kinase c. *Proc. Natl. Acad. Sci. U.S.A.*, 104(7):2442–2447.
- Müller et al., 2008. Müller, M. J. I., Klumpp, S., and Lipowsky, R. (2008). Tug-of-war as a cooperative mechanism for bidirectional cargo transport by molecular motors. *Proc. Natl. Acad. Sci. U.S.A.*, 105(12):4609–4614.
- Mullins et al., 1998. Mullins, R. D., Heuser, J. A., and Pollard, T. D. (1998). The interaction of arp2/3 complex with actin: nucleation, high affinity pointed end capping, and formation of branching networks of filaments. *Proc. Natl. Acad. Sci. U.S.A.*, 95(11):6181–6186.
- Murase, 1992. Murase, M. (1992). *The dynamics of cellular motility*. J. Wiley and Sons, New York.
- Needleman and Brugués, 2014. Needleman, D. and Brugués, J. (2014). Determining physical principles of subcellular organization. *Dev. Cell*, 29(2):135–138.
- Neri et al., 2011. Neri, I., Kern, N., and Parmeggiani, A. (2011). Totally asymmetric simple exclusion process on networks. *Phys. Rev. Lett.*, 107(068702).
- Neri et al., 2013. Neri, I., Kern, N., and Parmeggiani, A. (2013). Exclusion processes on networks as models for cytoskeletal transport. *New J. Phys.*, 15(085005):54pp.
- Nicastro et al., 2006. Nicastro, D., Schwartz, C., Pierson, J., Gaudette, R., Porter, M. E., and McIntosh, J. R. (2006). The molecular architecture of axonemes revealed by cryo-electron tomography. *Science*, 313(5789):944–948.
- Nishinari et al., 2005. Nishinari, K., Okada, Y., Schadschneider, A., and Chowdhury, D. (2005). Intracellular transport of single-headed molecular motors kif1a. *Phys. Rev. Lett.*, 95(11):118101.
- Ohmuro et al., 2004. Ohmuro, J., Mogami, Y., and Baba, S. A. (2004). Progression of flagellar stages during artificially delayed motility initiation in sea urchin sperm. *Zool. Sci.*, 21(11):1099–1108.
- Okada et al., 2003. Okada, Y., Higuchi, H., and Hirokawa, N. (2003). Processivity of the single-headed kinesin kif1a through biased binding to tubulin. *Nature*, 424(6948):574–577.
- Okada and Hirokawa, 1999. Okada, Y. and Hirokawa, N. (1999). A processive single-headed motor: kinesin superfamily protein kif1a. *Science*, 283(5405):1152–1157.
- Okada and Hirokawa, 2000. Okada, Y. and Hirokawa, N. (2000). Mechanism of the single-headed processivity: diffusional anchoring between the k-loop of kinesin and the c terminus of tubulin. *Proc. Natl. Acad. Sci. U.S.A.*, 97(2):640–645.
- Okada et al., 1995. Okada, Y., Yamazaki, H., Sekine-Aizawa, Y., and Hirokawa, N. (1995). The neuron-specific kinesin superfamily protein kif1a is a unique monomeric motor for anterograde axonal transport of synaptic vesicle precursors. *Cell*, 81(5):769–780.
- Oldfors et al., 2004. Oldfors, A., Tajsharghi, H., Darin, N., and Lindberg, C. (2004). Myopathies associated with myosin heavy chain mutations. *Acta Myol.*, 23(2):90–96.
- Orlandi et al., 2010. Orlandi, J. G., Blanch-Mercader, C., Brugués, J., and Casademunt, J. (2010). Cooperativity of self-organized brownian motors pulling on soft cargoes. *Phys. Rev. E*, 82:061903.
- Parmeggiani et al., 2003. Parmeggiani, A., Franosch, T., and Frey, E. (2003). Phase coexistence in driven one-dimensional transport. *Phys. Rev. Lett.*, 90(8):086601.
- Parmeggiani et al., 1999. Parmeggiani, A., Jülicher, F., Ajdari, A., and Prost, J. (1999). Energy transduction of isothermal ratchets: Generic aspects and specific examples close to and far from equilibrium. *Phys. Rev. E*, 60:2127–2140.

- Plaçaïs et al., 2009. Plaçaïs, P.-Y., Balland, M., Guérin, T., Joanny, J.-F., and Martin, P. (2009). Spontaneous oscillations of a minimal actomyosin system under elastic loading. *Phys. Rev. Lett.*, 103(15):158102.
- Pringle, 1977. Pringle, J. W. S. (1977). *Insect flight muscle*. North-Holland, Amsterdam.
- Rai et al., 2013. Rai, A. K., Rai, A., Ramaiya, A. J., Jha, R., and Mallik, R. (2013). Molecular adaptations allow dynein to generate large collective forces inside cells. *Cell*, 152(1-2):172–182.
- Raucher and Sheetz, 1999. Raucher, D. and Sheetz, M. P. (1999). Characteristics of a membrane reservoir buffering membrane tension. *Biophys J.*, 77(4):1992–2002.
- Ray et al., 1993. Ray, S., Meyhöfer, E., Milligan, R. A., and Howard, J. (1993). Kinesin follows the microtubule's protofilament axis. *J. Cell Biol.*, 121(5):1083–1093.
- Reimann, 2002. Reimann, P. (2002). Brownian motors: noisy transport far from equilibrium. *Phys. Rep.*, 361(2-4):57–265.
- Riedel-Kruse et al., 2007. Riedel-Kruse, I. H., Hilfinger, A., Howard, J., and Jülicher, F. (2007). How molecular motors shape the flagellar beat. *HFSP J.*, 1(3):192–208.
- Roberts et al., 2013. Roberts, A. J., Kon, T., Knight, P. J., Sutoh, K., and Burgess, S. A. (2013). Functions and mechanics of dynein motor proteins. *Nat. Rev. Mol. Cell. Biol.*, 14(11):713–726.
- Rodríguez et al., 2009. Rodríguez, J. A., López, M. A., Thayer, M. C., Zhao, Y., Oberholzer, M., Chang, D. D., Kisalu, N. K., Penichet, M. L., Helguera, G., Bruinsma, R., Hill, K. L., and Miao, J. (2009). Propulsion of african trypanosomes is driven by bihelical waves with alternating chirality separated by kinks. *Proc. Natl. Acad. Sci. U.S.A.*, 106(46):19322–19327.
- Roux et al., 2001. Roux, A., Cappello, G., Cartaud, J., Prost, J., Goud, B., and Bassereau, P. (2001). A minimal system allowing tubulation with molecular motors pulling on giant liposomes. *Proc. Natl. Acad. Sci. U.S.A.*, 99(8):5394–5399.
- Sakakibara et al., 1999. Sakakibara, H., Kojima, H., Sakai, Y., Katayama, E., and Oiwa, K. (1999). Inner-arm dynein c of chlamydomonas flagella is a single-headed processive motor. *Nature*, 400(6744):586–590.
- Sanchez et al., 2011. Sanchez, T., Welch, D., Nicastro, D., and Dogic, Z. (2011). Cilia-like beating of active microtubule bundles. *Science*, 333(6041):456–459.
- Sancho et al., 1982. Sancho, J. M., Miguel, M. S., Katz, S. L., and Gunton, J. D. (1982). Analytical and numerical studies of multiplicative noise. *Phys. Rev. A*, 26(3):1589–1609.
- Sandri, 1996. Sandri, M. (1996). Numerical calculation of lyapunov exponents. *Math. J.*, 6(3):78–84.
- Satir, 1965. Satir, P. (1965). Studies on cilia ii. examination of the distal region of the ciliary shaft and the role of the filaments in motility. *J. Cell Biol.*, 26(3):805–834.
- Satir, 1968. Satir, P. (1968). Studies on cilia iii. further studies of the cilium tip and a 'sliding filament' model of ciliary motility. *J. Cell Biol.*, 39(1):77–94.
- Schlüter et al., 1997. Schlüter, K., Jockusch, B. M., and Rothkegel, M. (1997). Profilins as regulators of actin dynamics. *Biochim. Biophys. Acta*, 1359(2):97–109.
- Schnitzer et al., 2000. Schnitzer, M. J., Visscher, K., and Block, S. M. (2000). Force production by single kinesin motors. *Nat. Cell. Biol.*, 2(10):718–723.
- Schroeder3rd et al., 2012. Schroeder3rd, H. W., Hendricks, A. G., Ikeda, K., Shuman, H., Rodionov, V., Ikebe, M., Goldman, Y. E., and Holzbaur, E. L. F. (2012). Force-dependent detachment of kinesin-2 biases track switching at cytoskeletal filament intersections. *Biophys J.*, 103(1):48–58.
- Shaklee et al., 2010. Shaklee, P. M., Bourel-Bonnet, L., Dogterom, M., and Schmidt, T. (2010). Nonprocessive motor dynamics at the microtubule membrane tube interface. *Biophys J.*, 98(1):93–100.
- Shaklee et al., 2008. Shaklee, P. M., Idema, T., Koster, G., Storm, C., Schmidt, T., and Dogterom, M. (2008). Bidirectional membrane tube dynamics driven by nonprocessive motors. *Proc. Natl. Acad. Sci. U.S.A.*, 105(23):7993–7997.
- Shao and Gao, 2006. Shao, Q. and Gao, Y. Q. (2006). On the hand-over-hand mechanism. *Proc. Natl. Acad. Sci. U.S.A.*, 103(21):8072–8077.

- Smith et al., 2009. Smith, D. J., Gaffney, E. A., Gadêlha, H., Kapur, N., and Kirkman-Brown, J. C. (2009). Bend propagation in the flagella of migrating human sperm, and its modulation by viscosity. *Cell Motil. Cytoskeleton*, 66(4):220–236.
- Smoluchowski, 1912. Smoluchowski, M. (1912). Experimentell nachweisbare, der üblichen thermodynamik widersprechende molekular-phänomene. *Phys. Zeitschur.*, 13:1069–1080.
- Soppina et al., 2014. Soppina, V., Norris, S. R., Dizaji, A. S., Kortus, M., Veatch, S., Peckham, M., and Verhey, K. J. (2014). Dimerization of mammalian kinesin-3 motors results in superprocessive motion. *Proc. Natl. Acad. Sci. U.S.A.*, 111(15):5562–5567.
- Sparacino et al., 2011. Sparacino, J., Lamberti, P. W., and Arizmendi, C. M. (2011). Shock detection in dynamics of single-headed motor proteins kif1a via jensen-shannon divergence. *Phys. Rev. E*, 84:041907.
- Spitzer, 1970. Spitzer, F. (1970). Interaction of markov processes. *Adv. Math.*, 5(2):246–290.
- Spudich and Watt, 1971. Spudich, J. A. and Watt, S. (1971). The regulation of rabbit skeletal muscle contraction. i. biochemical studies of the interaction of the tropomyosin-troponin complex with actin and the proteolytic fragments of myosin. *J. Biol. Chem.*, 246(15):4866–4871.
- Straub, 1943. Straub, F. B. (1943). Actin ii. *Stud. Inst. Med. Chem. Univ. Szeged.*, 3:23–37.
- Strogatz, 1994. Strogatz, S. H. (1994). *Nonlinear Dynamics and Chaos*. Perseus Books Publishing.
- Summers and Gibbons, 1971. Summers, K. E. and Gibbons, I. R. (1971). Adenosine triphosphate-induced sliding of tubules in trypsin-treated flagella os sea-urchin sperm. *Proc. Natl. Acad. Sci. U.S.A.*, 68(12):3092–3096.
- Svoboda and Block, 1994. Svoboda, K. and Block, S. M. (1994). Force and velocity measured for single kinesin molecules. *Cell*, 77(5):773–784.
- Sweeney and Houdusse, 2010. Sweeney, H. L. and Houdusse, A. (2010). Structural and functional insights into the myosin motor mechanism. *Annu. Rev. Biophys.*, 39:539–557.
- Syme and Josephson, 2002. Syme, D. A. and Josephson, R. K. (2002). How to build fast muscles: synchronous and asynchronous designs. *Integr. Comp. Biol.*, 42(4):762–770.
- Tabb et al., 1998. Tabb, J. S., Molyneaux, B. J., Cohen, D. L., Kuznetsov, S. A., and Langford, G. M. (1998). Transport of er vesicles on actin filaments in neurons by myosin v. *J. Cell Sci.*, 111(Pt 21):3221–3234.
- Thompson and Langford, 2002. Thompson, R. F. and Langford, G. M. (2002). Myosin superfamily evolutionary history. *Anat. Rec.*, 268(3):276–289.
- Tomishige et al., 2002. Tomishige, M., Klopfenstein, D. R., and Vale, R. D. (2002). Conversion of unc104/kif1a kinesin into a processive motor after dimerization. *Science*, 297(5590):2263–2267.
- Tornberg and Shelley, 2004. Tornberg, A.-K. and Shelley, M. J. (2004). Simulating the dynamics and interactions of flexible fibers in stokes flow. *J. Comp. Phys.*, 196(1):8–40.
- Tortora and Derrickson, 2013. Tortora, G. J. and Derrickson, B. H. (2013). *Principles of anatomy and physiology*. J. Wiley and Sons, New York, 14th edition.
- Tripathi, 2010. Tripathi, G., editor (2010). *Cellular and Biochemical Sciences*. I. K. International Publishing House.
- Uemura et al., 2002. Uemura, S., Kawaguchi, K., Yajima, J., Edamatsu, M., Toyoshima, Y. Y., and Ishiwata, S. (2002). Kinesin-microtubule binding depends on both nucleotide state and loading direction. *Proc. Natl. Acad. Sci. U.S.A.*, 99(9):5977–5981.
- Vale et al., 1985. Vale, R. D., Reese, T. S., and Sheetz, M. P. (1985). Identification of a novel force-generating protein, kinesin, involved in microtubule-based motility. *Cell*, 42(1):39–50.
- van Kampen, 1981. van Kampen, N. G. (1981). *Stochastic processes in physics and chemistry*. North-Holland, Amsterdam.
- Vershinin et al., 2007. Vershinin, M., Carter, B. C., Razafsky, D. S., King, S. J., and Gross, S. P. (2007). Multiple-motor based transport and its regulation by tau. *Proc. Natl. Acad. Sci. U.S.A.*, 104(1):87–92.

- Vogel et al., 2009. Vogel, S. K., Pavin, N., Maghelli, N., Jülicher, F., and Tolić-Nørrelykke, I. M. (2009). Self-organization of dynein motors generates meiotic nuclear oscillations. *PLoS Biol.*, 7(4):e1000087.
- Waterman-Storer and Salmon, 1998. Waterman-Storer, C. M. and Salmon, E. D. (1998). Endoplasmic reticulum membrane tubules are distributed by microtubules in living cells using three distinct mechanisms. *Curr. Biol.*, 8(14):798–806.
- Waugh, 1982. Waugh, R. E. (1982). Surface viscosity measurements from large bilayer vesicle tether formation. ii. experiments. *Biophys J.*, 38(1):29–37.
- Werner et al., 2014. Werner, S., Rink, J. C., Riedel-Kruse, I. H., and Friederich, B. M. (2014). Shape mode analysis exposes movement patterns in biology: flagella and flatworms as case studies. *PLoS ONE*, 9(11):e113083.
- Wickstead and Gull, 2007. Wickstead, B. and Gull, K. (2007). Dyneins across eukaryotes: A comparative genomic analysis. *Traffic*, 8(12):1708–1721.
- Yajima and Cross, 2005. Yajima, J. and Cross, R. A. (2005). A torque component in the kinesin-1 power stroke. *Nat. Chem. Biol.*, 1(6):338–341.
- Yildiz et al., 2004. Yildiz, A., Tomishige, M., Vale, R. D., and Selvin, P. R. (2004). Kinesin walks hand-over-hand. *Science*, 303(5658):676–678.
- Zot and Potter, 1987. Zot, A. S. and Potter, J. D. (1987). Structural aspects of troponin-tropomyosin regulation of skeletal muscle contraction. *Annu. Rev. Biophys. Biochem. Chem.*, 16:535–559.